Assessment of the surface functionalization of SPION and DND nanomaterials for cellular uptake and fluorescence imaging

Dissertation zur Erlangung des naturwissenschaftlichen Doktorgrades der Julius-Maximilians-Universität Würzburg

vorgelegt von

Thomas Sowik
aus Herne

Würzburg 2014

Eingereicht bei der Fakultät für Chemie und Pharmazie am

_____

Gutachter der schriftlichen Arbeit

1. Gutachter: Prof. Dr. U. Schatzschneider

2. Gutachter: Prof. Dr. A. Krüger

Prüfer des öffentlichen Promotionskolloquiums

1. Prüfer: Prof. Dr. U. Schatzschneider

2. Prüfer: Prof. Dr. A. Krüger

3. Prüfer: _____

Datum des öffentlichen Promotionskolloquiums

_____

Doktorurkunde ausgehändigt am

_____

Acknowledgements

There have been many people who supported me in accomplishing this work, not only scientifically, but also as friends walking this path together with me. I am very grateful for their help and I would like to thank particularly the following people:

Prof. Dr. Ulrich Schatzschneider for the opportunity to work in his group.

Prof. Dr. Anke Krüger for her willingness to act as the co-examiner for this thesis.

Prof. Dr. Martin Kamp and *Prof. Dr. Georg Krone* for the opportunity to measure TEM with them and learning a lot about this technique.

Dr. Andreas Steffen and *Dr. Robert Edkins* for performing luminescence studies on my compounds and materials and for taking the time to teach me the basics of photophysics and photochemistry.

Dr. Tessa Lühmann for fluorescence microscopy and cell culture.

Thomas Kampf for measuring relaxations on my SPIONs and for answering all my questions regarding MRI.

Stefan Wachtler und *Thomas Meinhardt* for sharing their precious nanodiamond with me and helping me with all problems concerning this chapter.

Dr. Andreas Schmidt and *Dr. Ferdinand Jamitzky* for their non-chemical point of view regarding science, the many hours of discussing all kinds of things, and their awesome friendship.

Luisa Hiersch, Fabian Schönfeld, Stefan Wachtler, Adrian Kissinger, Manuel Brasch, Sebastian Fricke, Alexander Probst, Caroline Bischof, Andreas Hochrein-Margeit, Sandra Bobersky, Hendrik Pfeiffer, Johanna Niesel, Sandesh Pai, and *Christoph Nagel* for making the past years an unforgettable time.

The saddest aspect of life right now is that science gathers knowledge faster than society gathers wisdom

Isaac Asimov

Table of Contents

Abbreviations

AAS	atom absorption spectrometry
ALST1	allatostatin 1
Aoa	aminoxy acetic acid
Boc	butyloxycarbonyl
CuAAC	copper(I)-catalysed 1,3-dipolar azide-alkyne cycloaddition
CVD	chemical vapour deposition
Cy5	cyanine5
DAPI	4,5-diamindino-2-phenylindole
DIPEA	*N*,*N*-diisopropylethylamine
DLS	dynamic light scattering
DMSO	dimethylsulfoxide
EDX	energy dispersion X-ray spectroscopy
EPR	enhanced permeability and retention
ESI	electron spray ionization
Fmoc	9-fluorenyloxymethylcarbonyl
HBTU	2-(1*H*-benzotriazole-1-yl)-1,1,3,3-tetramethyluronium hexafluorophosphate
HOBT	1-hydroxy-benzotriazole
HPLC	high pressure liquid chromatography
hrSEM	high-resolution scanning electron microscopy
ISC	intersystem crossing
MLCT	metal-to-ligand charge transfer
MPI	magnetic particle imaging
MRI	magnetic resonance imaging
NIR	near-infrared
N-V center	nitrogen vacancy center
PEG	polyethylene glycol
PITC	phenylisothiocyanate
QDots	quantum dots
SERS	surface enhanced Raman spectroscopy
SOC	spin-orbit coupling
SPECT	single photon emission computed tomography
SPPS	solid-phase peptide synthesis

TEA	triethylamine
TEOS	triethylorthosiliane
TGF	transforming growth factor
TIS	triisopropylsilane
TNT	1,3,5-trinitrotoluene
VPF	vascular permeability factors
TGA	thermogravimetric analysis

1 Introduction

1.1 Synthesis and properties of nanoparticles

The field of particle-based nanoscience has attracted a lot of attention during the past two decades. Nanoparticles of all sizes based on organic and inorganic materials have been investigated for a wide range of applications as catalysts, surface modifications, contrast agents for bioimaging, biosensors, and platforms for drug delivery.[1-6] One of their advantages compared to molecular compounds is the versatility in shape and size, influencing physical and chemical properties alike. Furthermore, nanometer-sized particles have a higher volume-to-surface ratio than bulk materials, leading to higher drug payloads and bigger catalytically active surfaces.[5] Further important tunable factors of nanoparticles are chemical composition, shape, mechanical features, surface coating, and functionalization (Fig. 1.1)

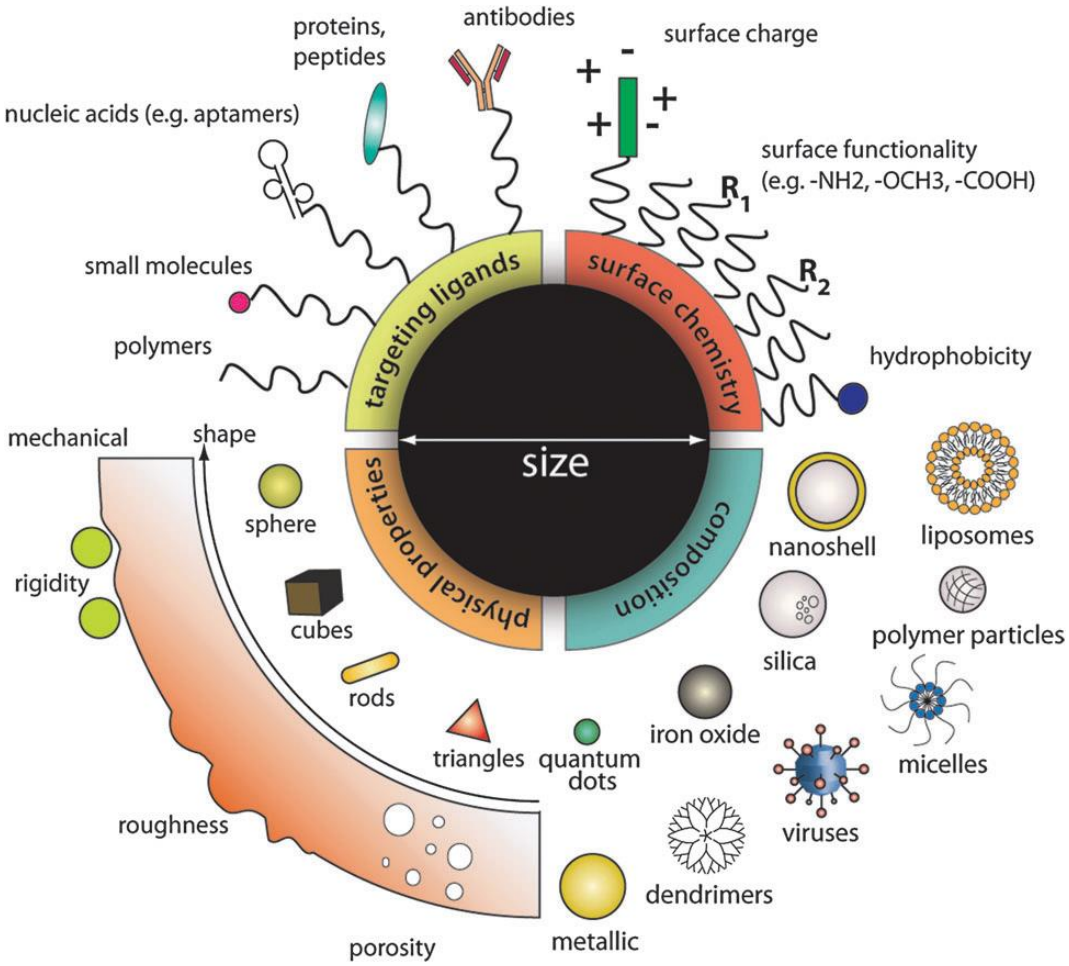

Fig. 1.1: Important features of nanoparticles like composition, shape, surface modification, coating, and mechanical features. Republished with permission of *The Royal Society of Chemistry* from[7].

Although a broad range of nanoparticles with different sizes and shapes are known, their synthesis was developed by empirical means, which had not led to a higher level of mechanistic understanding, yet. However, synthetic procedures can be categorized into three classes:

- Co-precipitation:
  Precipitation of poorly soluble products from aqueous solutions followed by decomposition to its oxides. It includes three phases: nucleation, growth, and agglomeration. The distinction of these processes is nearly impossible, thus the exact mechanism of co-precipitation is still not completely understood.[8-9]

- Sol-gel method:
  It is based on the hydrolysis and condensation of alkoxide-based precursors. This method has applications in the field of nanoparticles, but also in coating and polymer chemistry. The sol-gel method can be subdivided into six steps. First, a stable solution of the alkoxide or metal precursor is produced, which is called sol. Second, by polycondensation or polyesterification, gel building is induced. During *syneresis*, the gel transforms into a solid mass, accompanied by gel contraction and expulsion of solvent form the gel pores. Afterwards, remaining solvent is removed in an anhydrousing process, determining many of the gels physical and mechanical properties. The gel is now called monolith. The monolith surface still contains a vast amount of hydroxyl groups that have to be removed in a dehydration process to improve its stability. This is accomplished by calcination at up to 800 °C. The last step is used to prepare dense ceramics and glasses. The monolith is heated up to temperatures higher than 800 °C. This leads to a total collapse of the material's pores leading to volatilation of remaining organic species. [9-12]

- Microemulsion and solvothermal processing:
  Microemulsion is a homogeneous solution of water, oil, surfactant, and amine- or alcohol-based co-surfactant. However, the orientation of the surfactant is not random but it rather forms spherical aggregates due to ion-dipole interactions with the co-surfactant, similar to micelles. The co-surfactant minimizes repulsion between the positively charged surfactant heads. When metal cations are present and reduced to the elemental metal, nanoparticles are formed by using the micelles as a kind of template. However, limitations of this method are the stability and solubility of metal salts and reduction agents.[9, 13-14] In solvothermal processing, reactions are performed in a sealed vessel. Thus, solvents can be heated to

higher temperatures than their ambient pressure boiling point. They can become supercritical, exhibiting both characteristics of fluids and gases. Not all solvothermal reactions make use of superfluids. Still, benefits include a lack of surface tension and much better solubility of reactants. Unlike co-precipitation and sol-gel methods, the products of solvothermal reactions are usually crystalline and do not require post-annealing treatment.[9, 15-17]

1.2 Characteristics of nanoparticles in biological systems

The use of nanoparticles for treatment, diagnosis, monitoring, and manipulation of biological systems has recently been referred to as nanomedicine. Research in this field includes the delivery and targeting of therapeutic, and diagnostic agents. These involve the identification of biological targets such as cells and receptors, which are related to specific clinical conditions. The choice of an appropriate nanocarriers is important to achieve the required biological response while minimizing detrimental side effects. Mononuclear phagocytes, dendritic, endothelial, and cancers cells are key targets.[18] In addition, nanoparticles also have seen application in imaging as contrast agents for magnetic resonance imaging (MRI), as tracers for magnetic particle imaging (MPI), surface enhanced Raman spectroscopy (SERS), and fluorescence imaging.[5, 18-19] However, nanoparticle behaviour in biological systems cannot be generalized, as its features like stability, intracellular and extracellular distribution, toxicity, and clearance change depending on size, morphology, composition, and surface functionalization.

In general, the lymphatic and blood vessels provide a complete but uncontrolled access to every tissue in living eukaryotic organisms. Intravenous administration of nanoparticles leads to fast clearance from the circulation system by liver and spleen macrophages. This site-specific but passive clearance is due to opsonisation, which is the deposition of blood opsonic factors like fibronectin and immunoglobulins which meditate recognition by the macrophages. Thus, size and surface features play a significant role in the opsonisation process and clearance kinetics. Particles with a size > 200 nm get cleared faster as they are more efficient in triggering macrophage recognition. However, smaller particles can undergo aggregation processes *in vivo*, leading to an increased effective particle size, also influencing the clearance kinetic. Furthermore, nanoparticles with a hydrodynamic radius < 10 nm show enhanced rate of renal clearance.[20] The key to control nanoparticle clearance is surface modification. Most common is coating with polyethylene glycol (PEG) or related polymers. This reduces protein aggregation and surface opsonisation, and thus macrophage recognition. Further modifications are based on

polydentate phosphine coatings for longer serum stability or glutathione coatings for faster renal clearance.[18, 20-23]

Another important phenomenon of nanoparticle accumulation in eukaryotic organisms is the enhanced permeability and retention (EPR) effect. This can be observed in inflammatory and especially tumour tissue. Nowadays, the knowledge about tumour-selective or tumour-specific targeting mechanisms is limited. However, the EPR effect in solid tumour tissue is one of the few specific characteristics. It is predominantly observed for biocompatible macromolecules and nanoparticles.[24] Solid tumours show elevated levels of vascular permeability factors like bradykinin, nitric oxide and the vascular permeability factor (VPF). This results in higher degrees of extravasation. In contrast, low-molecular chemotherapeutics do not discriminate between healthy and tumour tissue and their systemic distribution depends on diffusion-dependent equilibrium.[25] As a result, macromolecules with a molecular weight higher than 30 kDa show a 10x higher accumulation in tumour than in healthy tissue.[24-27].

Once a small tumour mass has formed, the tumour tissue starts excreting angiogenetic factors inducing blood vessel growth (neovascularization). The resulting imbalance of angiogenic regulators such as growth factors and matrix metalloproteinases make tumour vessels disorganized and dilated with numerous pores, showing enlarged gap junctions between endothelial cells and compromised lymphatic drainage.[28] Thus, particle with a size between 30 to 250 nm can passively accumulate in tumour tissue (Fig. 1.2).[18, 24-25, 28-32]

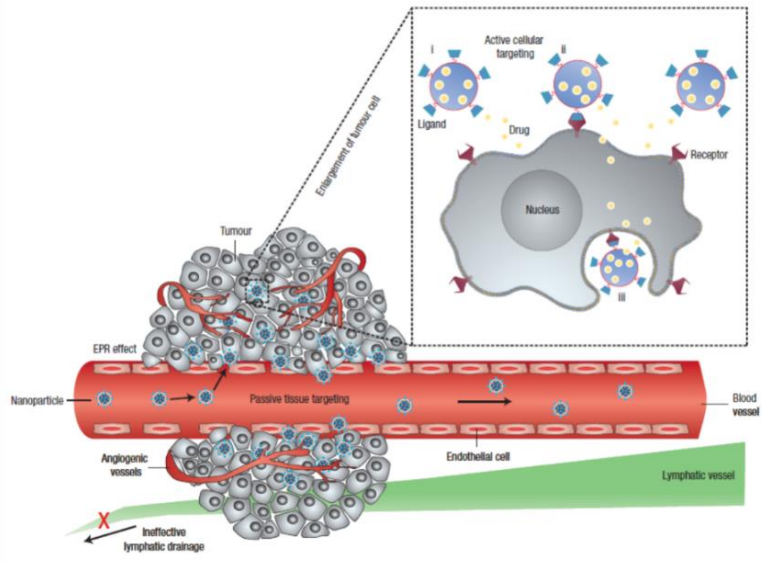

Fig. 1.2: Schematic image of the EPR effect. Particles injected into blood vessels accumulate passively in tumour tissue due to fenestration. These fenestration is generated by an imbalance of angiogenic regulators during tumour growth, leading to disorganized blood vessels. Furthermore, the lymphatic drainage is compromised, hindering the clearance of nanoparticles from tumour tissue. Combination of EPR effect and active targeting moieties on the nanoparticle surface can yield a highly specific tumour. Reprinted by permission of *Macmillan Publishers Ltd*: *Nature Nanotechnology*[29], Copyright 2007.

1.3 Diagnostic and therapeutic applications of nanoparticles

1.3.2 Silica-based nanoparticles

Silicon is the second most abundant element in the earth's crust and a trace element in organisms. Especially the water-soluble form silicic acid $Si(OH)_4$ is of high importance for biological systems. Silicon deficiency produces defective collagenous connective tissue formation and defects in bone growth, leading to a general retarded growth.[33-34] Silicon is most abundant in osteoblast cells at the mineralization sites in growing bone and is involved in collagen biosynthesis. Especially the activity of the enzyme prolyl hydroxylase, which is involved in the synthesis of procollagen, is highly dependent on the silicon concentration.[35] Furthermore, it is also supposed to take part in aluminium homeostasis, preventing organisms from aluminium intoxication.[36-38]

Elemental silicon itself is inert and shows no significant toxicity in organisms. Silicic acid itself shows no significant toxicity, either. Orally administered, it is absorbed by the intestines and excreted via the urine. However, long-time inhalation of silicon particles, like SiO_2 dust, can lead to silicosis. This fibrosis of the lung tissue is induced by chronic irritation due to creation of active oxygen species by the small particles.[39] In 1968, *Stöber* et al. reported a technique to synthesize monodisperse silica microspheres.[40] This sol-gel synthesis, also known as the *Stöber* process, is a base-catalysed polymerisation of silicic acid to polysilicic acid (Fig. 1.3).

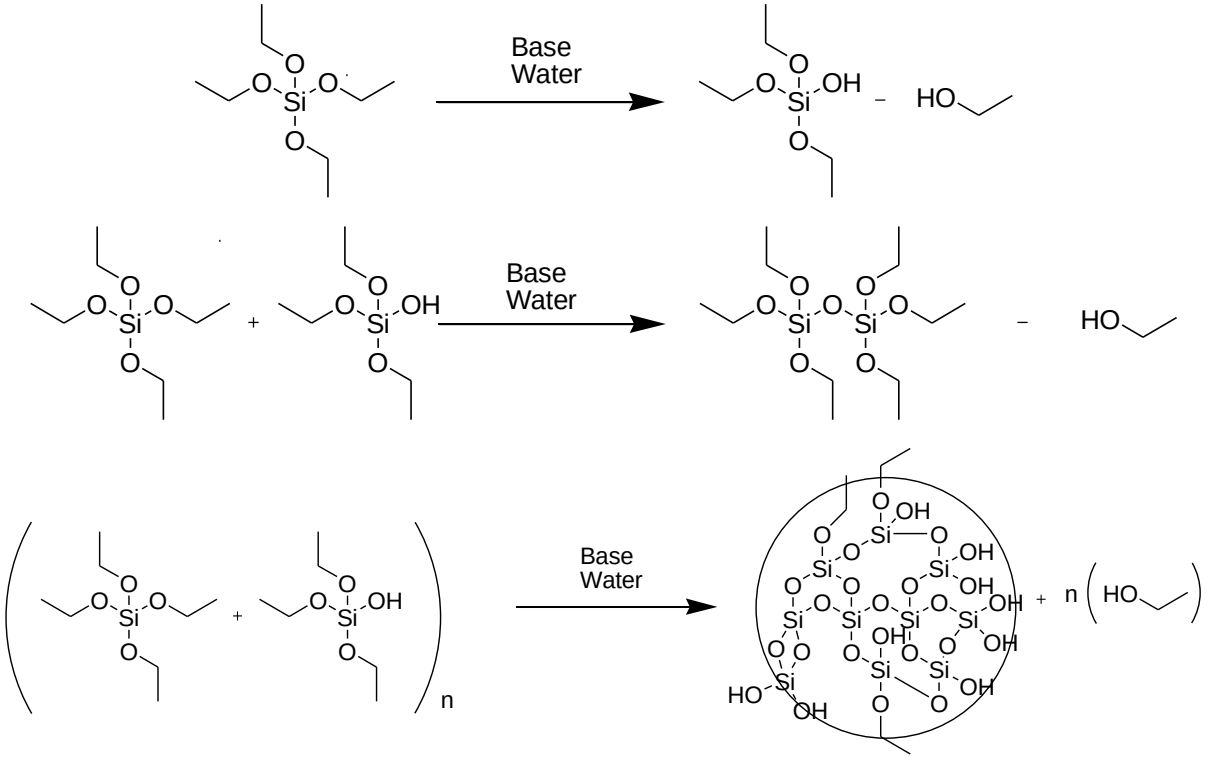

Fig. 1.3: Base-catalysed polymerisation of tetraethylorthosilicate to polysilicic acid with a spherical morphology according to the *Stöber process*.

However, silica nanoparticles are not the only silicon-containing nanoparticle systems. Silicon quantum dots (QDots) have emerges as a potent replacement of selenium and cadmium containing QDots for biotechnological purposes.[41-43] Today, the *Stöber* process is still a crucial technique for the synthesis of silica nanoparticles, although it has been modified and improved to give three different types of nanoparticle systems (Fig. 1.4):

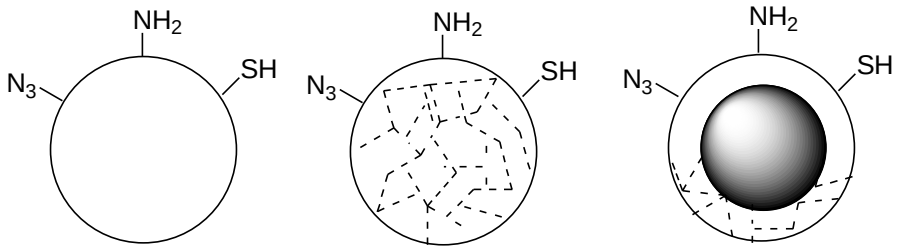

Fig. 1.4: Three silica nanoparticle systems: "solid" silica nanoparticles (left) present functional groups on the surface (amine, azide, thiole) which enable a vast range of modifications. Mesoporous silica nanoparticles (middle) remain this feature and add internal cavities which can adsorb or encapsulate compounds. Silica core-shell particles (right) are hybrid material that combine physical properties of an inorganic core with protection by either "solid" or mesoporous silica shell.

- "Solid" silica nanoparticles

  Synthesized by the original *Stöber* process, they can undergo various surface modifications introducing groups like amines, azides, and thioles, enabling covalent surface modification with proteins, antibodies, organic molecules, and metal complexes.[44-45]

- Mesoporous nanoparticles

  They are comprised of a honeycomb-like structure, containing channels that are able to adsorb or encapsulate a significant amount of molecules like drugs, peptides, or DNA.[46] Therefore, mesoporous nanoparticles have been extensively studied as carrier systems for drug delivery.[46-51] In addition, mesoporous silica particles retain the ability of surface functionalization as described for "solid" silica nanoparticles above. The combination of both these properties gives rise to systems that are able to release drugs depending on chemical or physical environmental parameters like temperature, pH value, or Ca^{2+} concentration.[52-54]

- Core-shell particles

  Core-shell particles have a mostly inorganic core which is encapsulated by a silica shell. This shell can be either "solid" or mesoporous and acts mainly as protection of the core against degradation or agglomeration. However, the silica shell features are comparable to

the different types of silica particles. Thus, highly complex systems can be designed with tuneable physical properties due to the inorganic core and a vast range of options for surface modification due to the silica shell.[55-59]

1.3.3 Carbon-based nanomaterials and nanodiamond

Carbon-based nanomaterials can be grouped into three different types which are of high interest: graphene, carbon nanotubes and nanodiamond. Graphene is a two-dimensional sheet of sp^2-bonded carbon atoms which can be viewed as a large polyaromatic molecule.[60-61] Carbon nanotubes consists of curved sheets of graphene which forms three-dimensional structures like wires or spheres. The spheres are referred to as fullerenes.[62-64] These have promising electrochemical properties due to their extensive conjugated π-systems. In contrast, nanodiamond consists of sp^3-hybridized carbon atoms and shows properties different from bulk diamond like tunable electronic properties by doping with other elements leading to semi-conductor or quasi-metallic features (Fig. 1.5).[65]

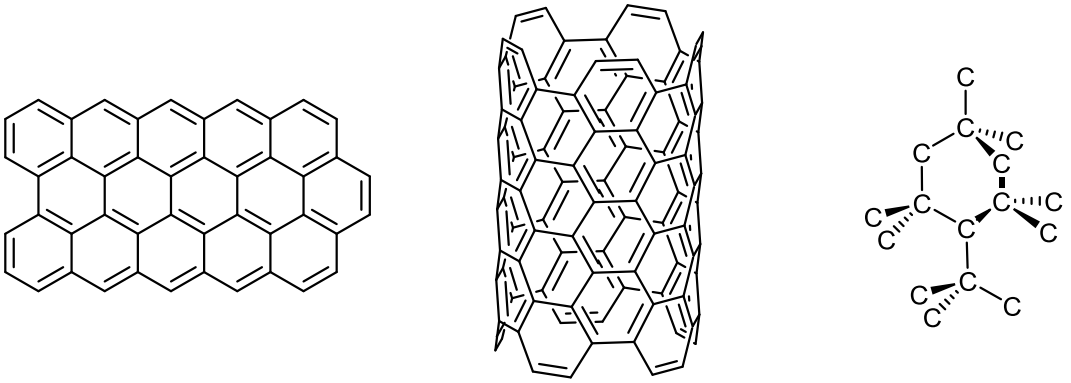

Fig. 1.5: Molecular structure of graphene (left). When curved, graphene forms nanotubes (middle). In contrast, the molecular structure of diamond based on extensive network of covalently linked sp^3-carbon atoms.

Furthermore, graphene, carbon nanotubes and nanodiamond have differing biological properties. Graphene shows the lowest, nanodiamond the highest cell uptake. Furthermore, graphene and carbon nanotubes have similar cytotoxicity, although nanotubes are more easily taken up by cells than graphene.[66] In contrast, nanodiamond shows neither cytotoxicity nor toxicity in model organisms like *C. elegans* and are supposed to be biologically inert.[66-68] However, *Boukherroub* et. al. found that nanodiamond toxicity in cells and embryos of higher organisms like *Xenopus laevis* depends on surface functionalization. Thus, particles with carboxylic groups on the surface have a much higher toxicity than particles with amine or hydroxyl groups.[69] However, different scientific groups collected contradictory data on the

cytotoxicity and toxicity in higher organisms.[66-74] Nonetheless, nanodiamond is the most promising carbon-based nanomaterial for biological and nanomedical applications. Extreme conditions like high temperature and pressure are necessary to synthesize nanodiamond.[75-76]

- Shock-wave synthesis

  An external explosion generates a localized area of high pressure up to 30 GPa, heating up a reaction vessel filled with graphite and copper.[77-78] The nanodiamond obtained are polycrystalline, nano-sized particles covert by graphitic materials.[65]

- Detonation synthesis

  Another method is detonation synthesis, which was developed in the early 1960s.[79] In contrast to shock-wave synthesis, 2,4,6-trinitrotoluene (TNT) and hexogen are used as the starting materials and the energy source at the same time.[80] The explosion in a reaction vessel generates temperatures up to 3000 K and a pressure between 20 and 30 GPa. After detonation, the pressure drops much faster than the temperature. Therefore, cooling is crucial to prevent formation of sp^2-hybridized graphite-like structures. Depending on the coolant, *anhydrous synthesis* (protective gas cooling) and *wet synthesis* (water cooling) are distinguished. Both methods yield nanodiamond with different chemical und physical parameters with respect to size and surface modification (Fig. 1.6).[79, 81] Other less important ways to synthesize nanodiamond are the substrate-free chemical vapour deposition (CVD) and the milling of synthetic or natural microdiamond.[82-83]

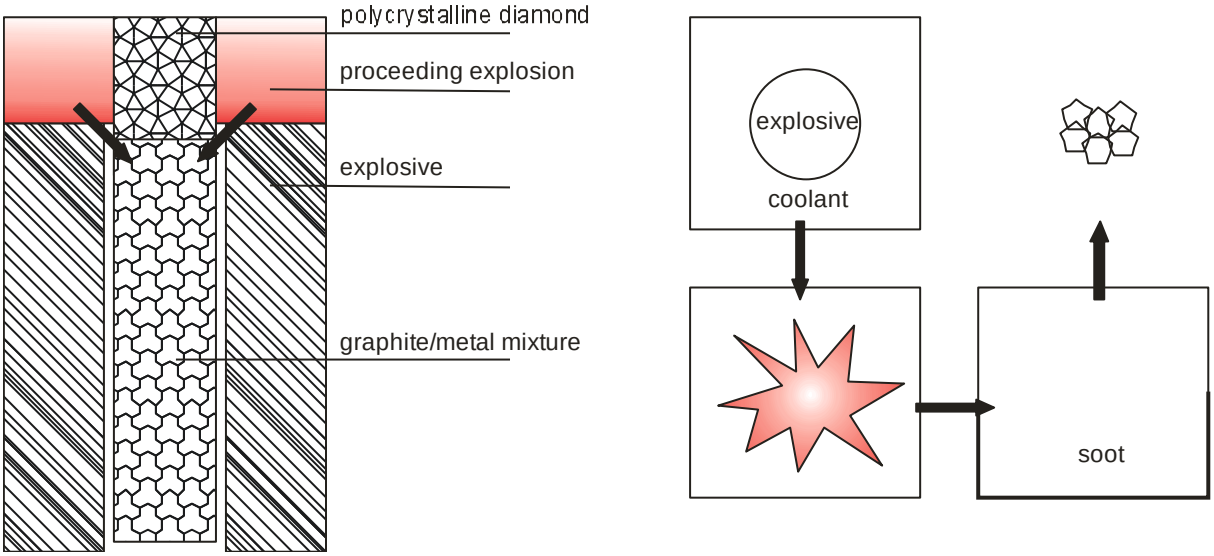

Fig. 1.6: Synthesis of nanodiamond by shock-wave (left) yielding highly sintered polycrystalline powders. The detonation synthesis (right) yields agglomerates of very small particles.[65]

The key for nanodiamond functionalization is in the understanding of the diamond surface structure. Approximately 15% of the diamond carbon atoms are exposed to the surface.[84] The carbon binding sites are saturated by functional groups like hydroxyl, carboxyl, and ketone groups, or graphitic double bonds and lactones. Therefore, the diamond surface is quite heterogenic and needs to be homogenized first to reduce undesired side reactions. Common reactions include oxidation, reduction, halogenation, hydration, and graphitization (Fig. 1.7). [65, 75, 85-91]

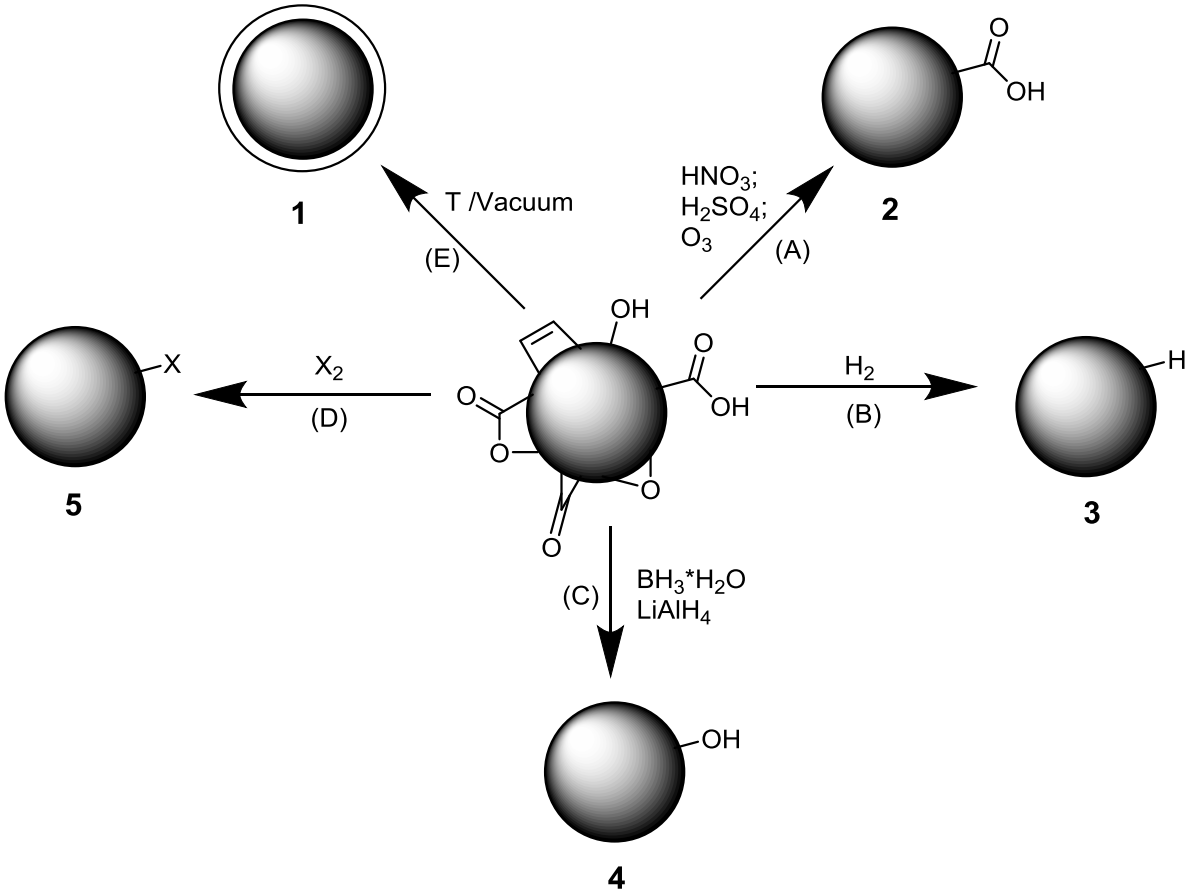

Fig. 1.7: Surface homogenisation of nanodiamond. (A) Oxidation with nitric or sulfonic acid leads to carboxylic group surface functionalization. (B) Hydration with H_2 gas leads to hydrogen termination of the carbon atoms. (C). Reduction with lithium aluminium hydride or borane leads to hydroxyl group surface functionalization. (D) Halogenation with halogens ($X_2 = F_2$ or Cl_2) leads to halogen termination. (E) During graphitization, all functional groups are removed from the surface, leading to surface termination by double bonds.

After homogenization, a several reactions are available for further functionalization. Thus, peptides, proteins, antibodies, organic drugs and metal complexes can be attached to the diamond surface, enabling a vast variety of possible applications. For example, such materials can be used as solid support for heterogeneous catalysis or solid-phase peptide synthesis.[75, 92-99] To obtain azide surface functionalization, the thermally treated nanodiamond (**1**) is reacted

with 4-(2-chlorethyl) benzenediazonium tetrafluoroborate (**6**) to give detonation nanodiamond with chlorine surface functionalization (**7**). Subsequently, **7** is reacted with sodium azide to yield azide-functionalized detonation nanodiamond (**8**). By treating these with sodium boronhydride, azide groups are partially reduced to amines, generating a detonation nanodiamond with a mixed azide and amine surface functionalization (**9**) (Fig. 1.8).[75, 97] Besides covalent surface functionalization, non-covalent surface modification is also possible using strong polar intermolecular interaction to immobilize proteins and peptides by adsorption.[65, 91, 100]

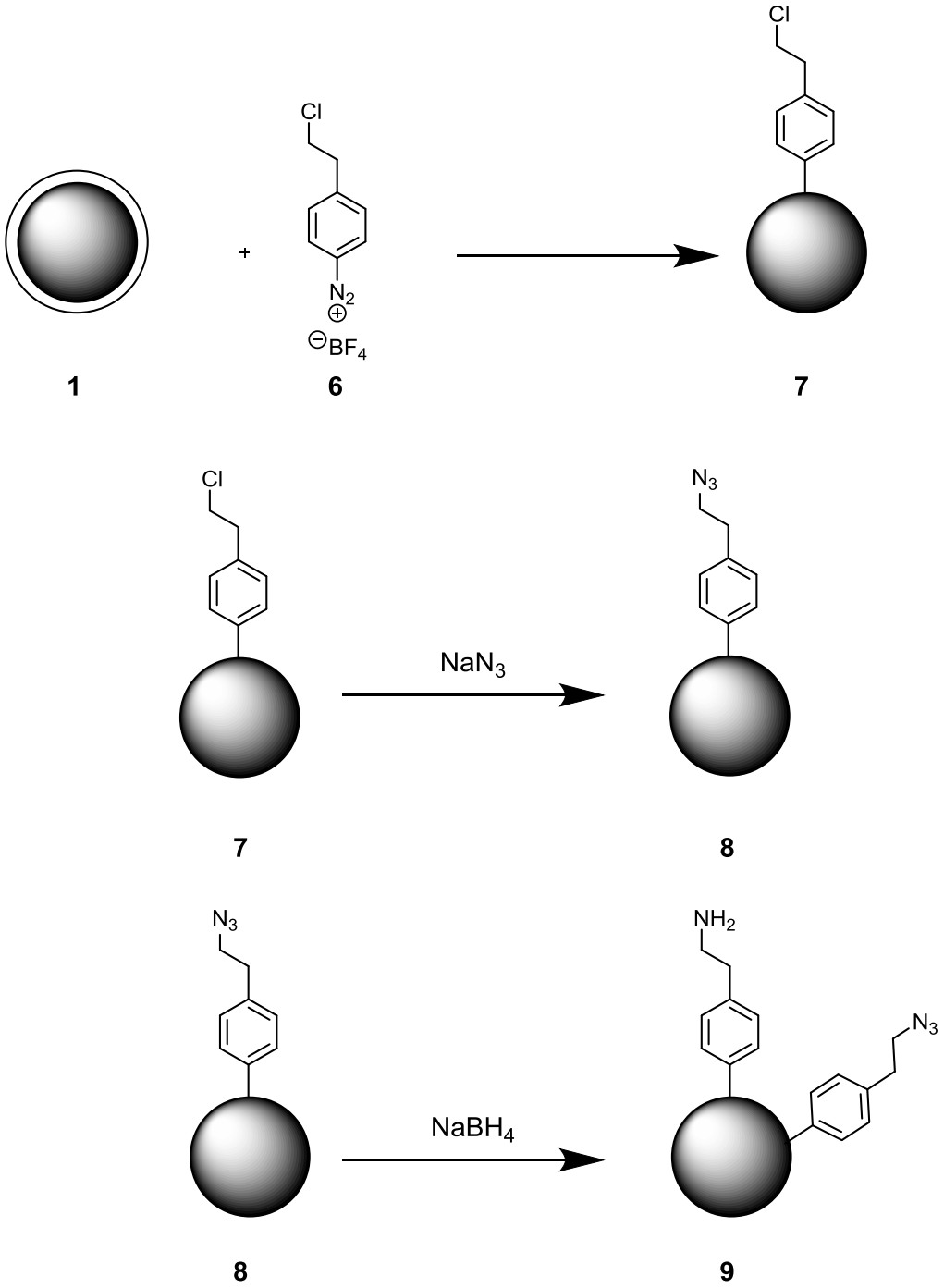

Fig. 3.8: Synthesis of mixed amine- and azide-functionalized detonation nanodiamond.

Macro-, micro- and nanodiamond contains impurities from the synthesis. The most common impurity is nitrogen. It is either incorporated as single isolated nitrogen atom called C centres, as pairs of adjacent N-N units known as A centres, or in larger assemblies such as four nitrogen atoms surrounding a vacancy known as B centres (Fig. 1.9).[95, 101]

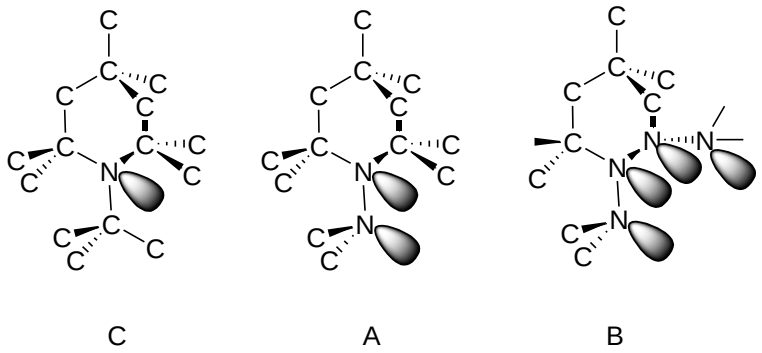

Fig. 1.9: Types of defects in the nanodiamond lattice. The C defect is an isolated nitrogen atom. The A defect is a pair of nitrogen atoms. The B defect is a group of at least 4 nitrogen atoms surrounding a vacancy site.

This so called nitrogen-vacancy centres (N-V centre of type C) are of significant interest for biotechnological and biomedical applications, as they show fluorescence in the visible range with high quantum yield and no photobleaching.[95, 102-103] The energy level structure of the N-V centre is an electron spin triplet for the ground state ^{3}A and the excited state ^{3}E. Furthermore, due to the spin-spin interaction in the diamond crystal the states are split into $m_s = 0$ and $m_s = \pm 1$ sublevels (Fig. 1.10).[95, 104]

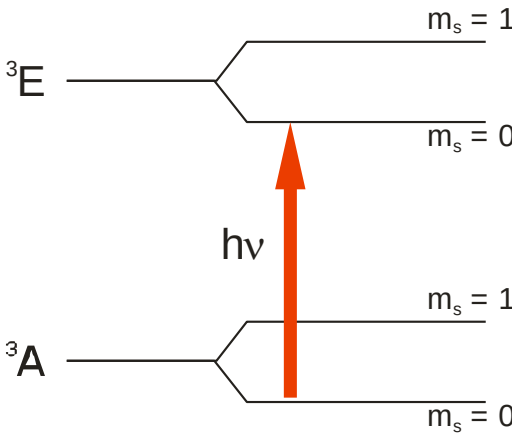

Fig. 1.10: Ground state and first excited state of the N-V centre. Transition from the ground state to the first excited state is induced by UV-light (hν).

A transition from the ground state to the first excited state is induced by UV-light. Upon decay, the N-V centres emit a characteristic, highly heterogeneous fluorescence spectrum in the visible or near IR spectrum consisting of a zero-phonon line and accompanied by broad phonon sidebands.[95] Furthermore, it is possible to distinguish between neutral (N-V^0), positively (N-

V^+) and negatively charged (N-V^-) Nitrogen-vacancy sites.[95, 105-107] The N-V defects can be introduced by damaging the diamond lattice using an electron beam with an energy of 1 to 2 MeV and afterwards annealing at 800 °C under vacuum.[74-75, 95, 98].

1.3.4 Superparamagnetic iron oxide nanoparticles

Superparamagnetic iron oxide nanoparticles (SPIONs) are composed of magnetite (Fe_3O_4), maghemite (γ-Fe_2O_3), or hematite (α-Fe_2O_3).[108] SPIONs can be synthesized by co-precipitation, microemulsion, and sol-gel synthesis (see Chapter 1.1).[8, 108-111] However, the most common method, based on co-precipitation, was developed by *Massart* in 1981.[112] When mixed in an aqueous solution, ferrous (Fe^{2+}) and ferric (Fe^{3+}) ions in a 1:2 stoichiometry under basic conditions react to give a black precipitate of monodisperse magnetite SPIONs by co-precipitation. The colloidal stability of SPIONs is controlled by hydrophobic-hydrophilic, magnetic, and van-der-Waals interactions. In general, nanometer-sized particles tend to agglomerate to minimize the surface or interfacial energy due to van-der-Waals forces. When reaching micrometer size, further aggregation is driven by magnetic dipole-dipole interactions. These particles are able to agglomerate further by applying an external magnetic field.[108, 113] To prevent this kind of agglomeration, surface modification is the key to enable applications in biotechnology and drug delivery. Most often surfaces are modified using biodegradable polymers like dextran, chitosan, cellulose, PEG, or fatty acids.[114] Also, silica can be used to generate core-shell particles (see Chapter 1.3.2). In general, SPIONs show no or low cytotoxicity. However, results from cytotoxicity assays show a low rate of reproducibility. This is due to the aggregation of the SPIONs with proteins and additives in the cell medium, causing protein denaturation and decomposition, thus generating toxic species. Therefore, preincubation of SPIONs with medium is necessary to generate reproducible data in such assays.[115-117] These results indicate the possibility of *in vivo* toxicity due to extensive opsonisation and protein interaction, leading to conformational changes of proteins and exposure of possible antigen sites.[118-120] Although the data of *in vivo* studies of SPIONs is insufficient, they have been established in a various of applications as separation and isolation of biomolecules like DNA, peptides, and proteins, drug delivery, solid support for peptide or DNA synthesis, cell separation, and MRI.[121-124] SPIONs are of special interest for MRI due to their superparamagnetism. The phenomenon of superparamagnetism was first described by *Bean* in 1955.[125] Ferromagnetic particles are assigned to three different categories depending on their size. Large particles consist of many domains. Their initial magnetization is due to motion of domain walls. On the other hand, very small particles consist of only one single domain. However, they accomplish their initial magnetization due to coherent rotation of the

magnetic moment against anisotropies in the particle. The third, and for MRI most important category, consist of only one domain and the thermal energy is sufficient to equilibrate the magnetization and overcome the energy of the potential anisotropic barrier. These particles possess long range order of magnetization and thus are superparamagnetic.[125-126] When a magnetic field B_0 is applied, protons align due to the *Zeeman* effect, building up a macroscopic magnetization M.[127] M consists of two components, the longitudinal magnetisation M_l and the transversal magnetization M_t (Fig. 1.11).

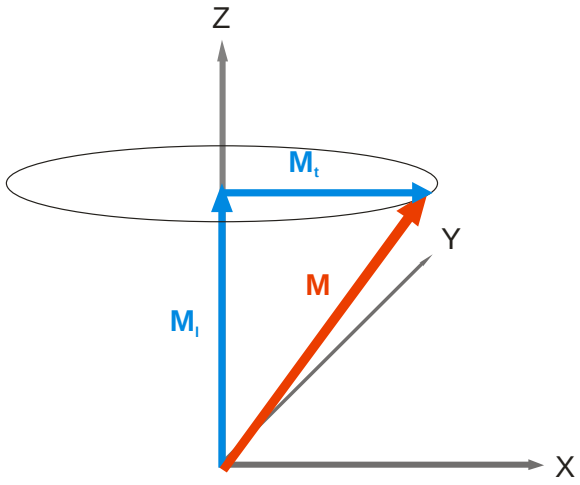

Fig. 1.11: Schematic presentation of the magnetization M, which results from vector addition of M_l and M_t.

This equilibrium is perturbed by application of a transverse radiofrequency pulse which can interact with the *Lamor* frequency of the proton. Upon return to equilibrium, two independent relaxation processes are operative to generate an MR image. The longitudinal relaxation or spin-lattice relaxation T_1 describes the time which is needed to restore 67% of the initial longitudinal magnetization. The transversal relaxation or spin-spin relaxation T_2 describes the time which is needed to reduce the transversal magnetization by 37%.[127-128] The contrast of a MR image depends on the relaxation times T_1 or T_2, the proton concentration in the tissue, instrumental parameters, and the presence of contrast agents. The ability of a contrast agent to decrease the relaxation T is called relaxivity r. In clinical applications, most used MRI contrast agents are based on Gd^{3+} complexes, which decrease T_1 by direct coordination of water to the Gd^{3+} centre. Thus, a positive contrast is observed in the MR image.[129] In contrast, the applied magnetic field B_0 induces a magnetic dipole μ in the SPIONs. When water diffuses into the outer sphere of a magnetic particle, the relaxation of the protons is perturbed by the induced magnetic dipole μ, leading to a shortening of T_2. In the MR image, results in a negative contrast (Fig 1.12). [128, 130] Nowadays, various SPION preparations are available or in clinical trial as MRI contrast agents (Tab. 1.1).[130-131]

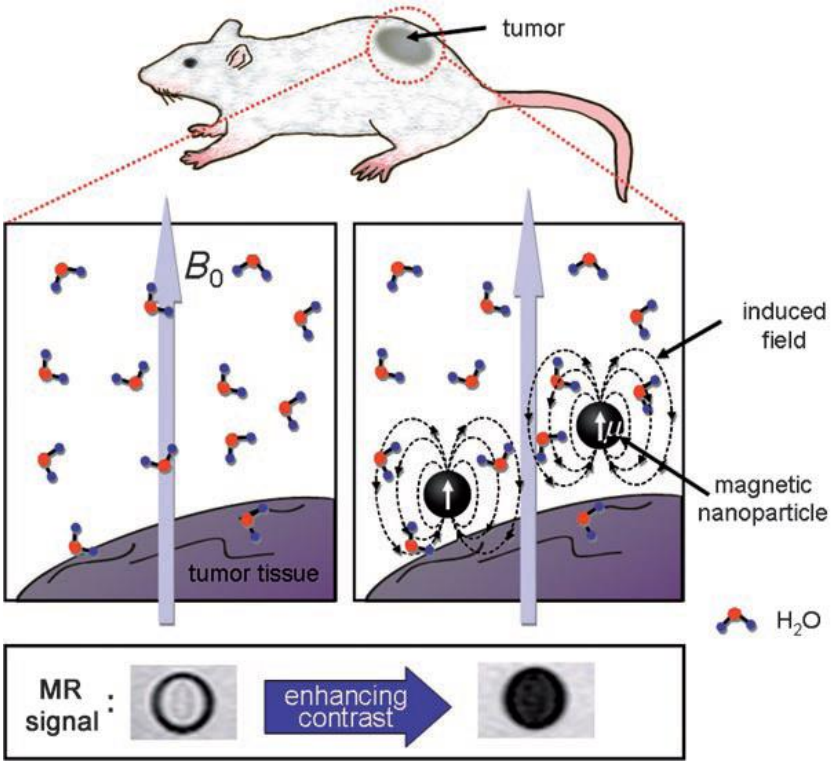

Fig. 1.12: MR contrast effect of SPIONs. In a magnetic field B_0, a magnetic dipole moment μ is generated which perturbs the water molecules aligned along B_0. This causes a darkening in the MR image, a so-called negative contrast. Republished with permission of *John Wiley and Sons Inc* from[130].

Tab. 1.1: Characteristics of a selection of SPIONs for MRI used in the clinics or clinical trials. The size gives the hydrodynamic radius measured by DLS. The relaxivity r_2 was measured at 1.5 T.

Name	**Company**	**Coating**	**Size [nm]**	**r_2 [$mM^{-1}s^{-1}$]**	**Application**
Ferrumoxides AMI-25	Guerbet, Advanced Magnetics	Dextran T10	120-180	120	liver imaging
Ferrumoxytol	Advanced Magnetics	Carboxylmethyl-Dextran	30	89	macrophage imaging
Supravist SHU-555C	Schering	carboxydextran	21	38	blood pool agent
ferristen Abdoscan	GE-Healthcare	sulfonated styrene-dibenzylvinyl copolymere	3500	-----	oral GI-imaging
VSOP-C184	Ferropharm	citrate	7	33.4	blood pool agent

Summarizing, SPIONs are a potent tool in magnetic resonance imaging. However, possible toxicity and metabolization are neither fully investigated nor completely understood. Furthermore, there are no specifically targeting SPIONs yet, as the targeting of Ferrumoxytol and Ferrumoxides is achieved by naturally occurring macrophage uptake of nanoparticles and delivery into liver for metabolization (see Chapter 1.2).

1.4 Bioactive peptides

1.4.1 Solid-phase peptide synthesis

Solid-phase peptide synthesis (SPPS) has become the method of choice for synthesizing peptides and small proteins. *Merrifield* developed the technique in the 1960s using a solid support and an orthogonal protecting group strategy for the *N*-terminus and the amino acid side chain groups. While the *N*-terminus is protected as *tert*-butoxy carbonyl (Boc), labile to trifluoroacetic acid during elongation steps of the synthesis, the peptide is released from the solid support by hydrofluoric acid, based on the differences in acid lability of the N^{α} protection group.[132-134] Today, the so-called Fmoc strategy is preferred over *Merrifield*'s Boc strategy, as it does not require the highly toxic hydrofluoric acid. In the Fmoc strategy, the N^{α} group of the amino acid is protected by fluoren-9-ylmethyloxycarbonyl (Fmoc) which is cleaved off with piperidine (Fig. 1.13).

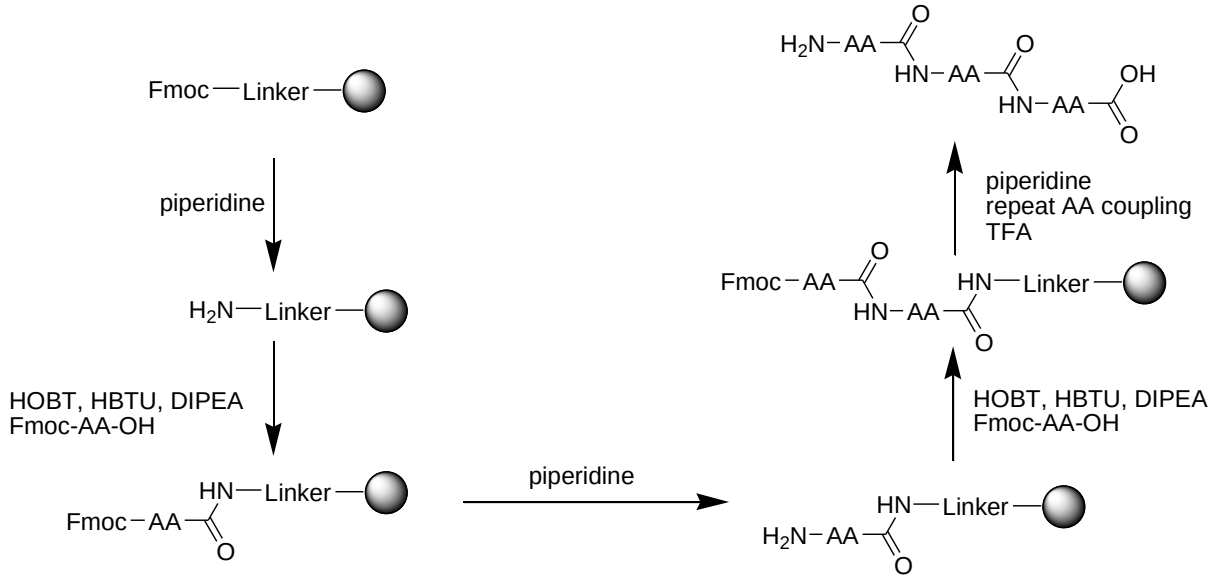

Fig. 1.13: Schematic protocol of Fmoc solid-phase peptide synthesis. Fmoc is removed by piperidine; the coupling is then performed by using the coupling reagents HOBT, HBTU and DIPEA. The side chain protecting groups are removed in the final step as the peptide is cleaved from the solid support using TFA.

The amino acid side chain groups are protected by specific acid-labile protecting groups. Thus, the peptide remains on the solid support during sequential elongation and Fmoc cleavage. Finally, all protection groups are removed and the peptide is cleaved from the solid support by using trifluoroacetic acid.[134-136] During the past 50 years a countless number of synthetic protocols have been developed for peptides containing cysteine und methionine, cyclic peptides, peptides with disulfide bridges and even peptides consisting of unnatural amino acid derivatives.[134, 137-140]

1.4.3 Tumour targeting peptides

Uncontrolled proliferation is in general the hallmark of cancer. During tumour development, cells accumulate several mutations in their genome which inhibit apoptosis, increase the proliferation rate, and reactivate telomerases to avoid the *Hayflick*-limit and gain immortality.[141] However, this can be achieved by a various number of different mutations leading to different compromised cellular signal transduction pathways. Thus, cancer is a highly individual disease which is not only defined by its organ or tissue of origin, but also by the number of different accumulated mutations.[142-143] Compromised signal transduction pathways are attractive targets for specific cancer targeting, as signal receptors on the cell membrane or receptor ligands are overexpressed. Utilizing this difference between the biochemical phenotype of cancer and healthy tissue, a selectivity can be achieved which is impossible to achieve for classic chemotherapeutics.[144-146] In this work, two peptides for active tumour targeting are considered. The first one is the TGF-β_1 binding peptide (**10**) with the sequence LPLGNSH which has a high affinity to the signal transduction ligand TGF-β_1 in phage display (Fig. 1.14).[147]

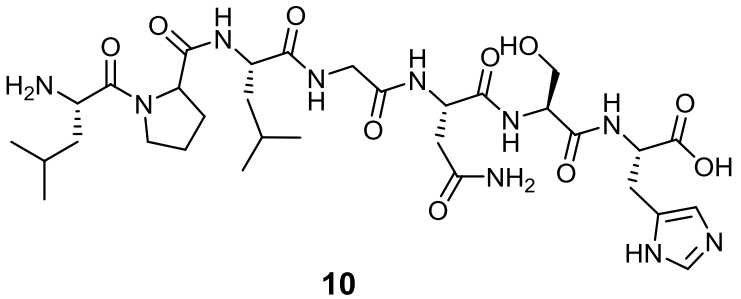

10

Fig. 1.14: Molecular structure of TGF-β_1 binding peptide (**10**) with the amino acid sequence LPLGNSH.

Transforming growth factors (TGF) are a signal transduction ligand class with over 40 members. They share many structural and functional similarities. The TGF-β superfamily members are crucial in nearly every cellular process. They mediate early embryonic

development, cell growth, differentiation, cell motility, and apoptosis. Furthermore, TGF-β signalling has the ability to potentially inhibit tumours of epithelial origin, including breast and colon carcinoma. However, these tumours most often develop resistances against TGF-β due to accumulation of defects in the TGF-β signalling pathways, leading to TGF-β overexpression and neoplasia.[148-150] TGF-β ligands initiate signalling by binding to a tetrameric receptor complex consisting of Type I and II serine/threonine kinase receptors. This activation transduces the signal to downstream components like Smad and members of the Ras/mitogen-activated protein kinase. Moreover, TGF-β is able to use multiple intersecting pathways to modulate downstream cellular events.[148] Therefore, a lot of scientific effort is directed at the study of the TGF-β signalling pathways and utilizing them for cancer therapy. For example, it has been reported that overexpression of TGF-β_1 allows the tumour to escape from immune surveillance and that antibodies neutralizing TGF-β_1 prevents fibrosis in solid tumours.[151-152] Thus, peptides which bind to TGF-β_1 are of special interest in the context of tumour targeting and treatment. The second peptide is allatostatin 1, a neuropeptide hormone with the sequence APSGAQRLYGFGL (ALST1; **11**) (Fig. 1.15).

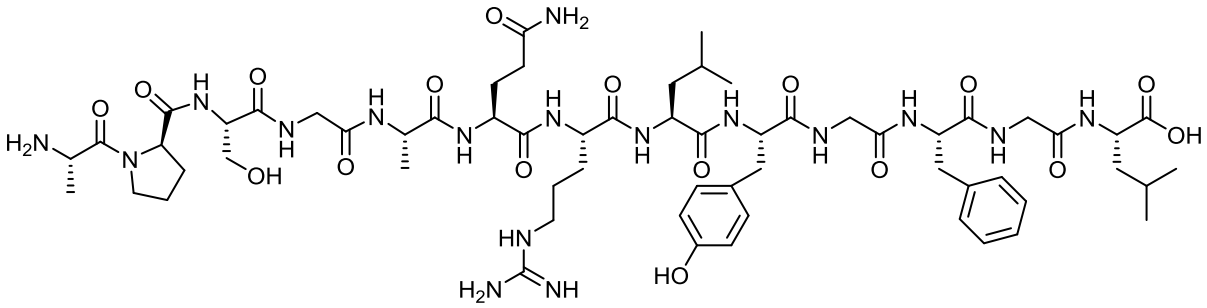

11

Fig. 1.15: Molecular structure of allatostatin 1 (ALST1) with the amino acid sequence APSGAQRLYGFGL.

Allatostatins are insect neuropeptide hormone hormones which control juvenile hormone production. They are crucial for normal development, metamorphosis, and reproduction of most insect species and an interesting target in insecticide research.[153-154] However, ALST1 also shows interesting bioactivity in mammalian cells. *Ishikawa* et al. and *Biju* et al. independently showed that QDots conjugated with ALST1 are highly efficient internalized into cells by clathrin-mediated endocytosis and into the cell nucleus.[155-156] Furthermore, allatostatin receptors in insects show significant sequence and functional similarity with the G-protein-coupled galanin and somastatin receptors in mammals.[157-158] Galanin and somastatin are neuropeptide hormones like ALST1. They are overexpressed with their corresponding receptors in neuroendocrinic tumours where they influence tumour proliferation.[159-160] Typical

neuroendocrinic tumours are endocrinic pancreatic tumours, pheocromocytomas, neuroblastomas, and ganglioneuromas.[161] Thus, ALST1 is suggested to be a potential vector for targeted therapy for these difficult to treat tumours.[155]

1.5 Metal complexes as luminescent probes in biotechnology

Fluorescence-based techniques have become the most powerful imaging tool in cell biology and related fields.[162] Coupled with microscopes or appropriate detectors, a high sensitivity and resolution can be achieved in *in vitro* assays or in imaging of cellular structures.[163-164] A potential fluorescent probe has to fulfil several criteria to be useful in biotechnology (Tab. 1.2).[165-166]

Tab.1.2: Essential properties and physical criteria for luminophores to be usable in cell imaging.[165-166]

Essential property	**Description**
Stability and solubility	Compound must be soluble and stable in aqueous buffer and cell medium
Toxicity	Compound must be non-toxic over the course of experiment and should not show phototoxicity
Uptake	Compound must be taken up without addition of chemical agents to increase cell membrane permeability. Often this requires high lipophilicity of the compound
Localisation	Compound should have preferential localization in certain organelle of the cell
Physical criteria	
Radiation tissue penetration	The compound must be excitable and emit at wavelengths which can transit through the tissue to be imaged. UV light has poor tissue penetration and may also cause cell damage. Typically, red shifted excitation and emission profiles are advantageous, with near IR (NIR) showing the best tissue penetration
Stokes shift	Large Stokes shift are preferred to prevent compound from autoquenching and distinguish it from autofluorescence
Lifetime τ	High lifetimes enable separation of compound fluorescence ($\tau \approx 100$ ns) from autofluorescence ($\tau << 10$ ns)

Only radioisotope imaging techniques exceed the fluorescence methods in sensitivity. However, fluorescence techniques are preferred over ionizing radiation due to the benign nature of visible light.[167] Most fluorophores for cell imaging are organic compounds. Shortcomings include short fluorescence lifetimes, small Stokes shifts, and photobleaching, when compared to luminescent metal complexes.[165, 168] Typical metals in luminescent complexes for cell imaging are Pt(II), Ru (II), Ir(III), and Re(I). As a d^8 metal, Pt(II) adopts a square-planar geometry. The presence of strong-field ligands is important in the design of emissive platinum(II) complexes to ensure that metal-centred d–d states, which are highly distorted compared to the ground state, are displaced to higher energies, as they have a deactivating effect.[169] Many of the highly luminescent Pt(II) complexes are based on cyclometallating ligands like arylpyridines as well as bidentate ligands like *acac* or amino acids (1.16).[170-171] Pt(II) complexes are used in time-resolved luminescence cell microscopy.[172]

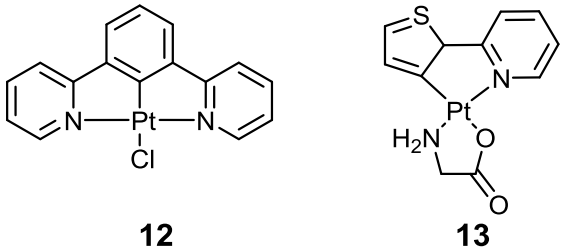

12 **13**

Fig. 1.16: Examples of luminescent Pt(II) complexes.

In comparison to Pt(II), Ir(III), Ru(II), and Re(I) are low-spin d^6 metal ions that adopt a distorted octahedral geometry. Thus, the ligand exchange rate is low which is crucial for moderating the toxicity of heavy metal complexes.[165] Furthermore, they have large Stoke shifts (hundreds of nm), long luminescence lifetimes (100 ns to ms), and a low rate of photobleaching.[173-175] These ions are typically coordinated by polypyridyl ligands, which are strong π-acceptors, leading to metal-to-ligand charge-transfer (MLTC) (Fig 1.17).[162] The participation of the metal ion in the excited states facilitates spin–orbit coupling (SOC) pathways in such complexes. This accelerates the rate of intersystem crossing (ISC) from the singlet electronic excited states S_1, which are initially populated upon absorption of light, to the triplet states. It also promotes the T_1 to S_0 radiative transition to the ground state. This process is strongly forbidden in most purely organic molecules. The complex therefore displays emission from the triplet excited state T_1, and is formally a phosphorescent molecule in the sense that $\Delta S \neq 0$.[176] Especially Re(I) compounds with *fac*-tricarbonyl and polypyridyl-like ligands are of special interest. On the one hand, toxicity of Re(I) is low and toxic effects are mostly due to the aromatic ligand systems and therefore tuneable.[165]

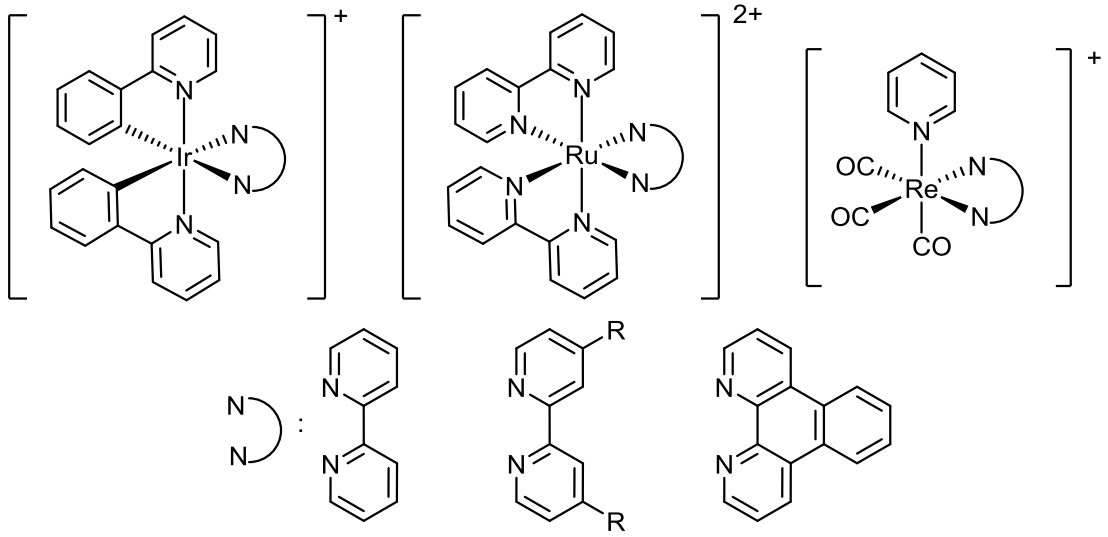

Fig. 1.17: Typical structures of Ir(III), Ru(II), and Re(I) luminophores.

On the other hand, the neutral complexes show absorption and emission maxima around 350 and 370 nm with lifetimes τ of hundreds of ns and quantum yields Φ in the order of 0.1%.[175] Furthermore, Re has applications in radiotherapy and imaging, first as an electron emitter in ^{188}Re and second as a model for ^{99m}Tc for single photon emission computed tomography (SPECT). Thus, a single compound is able to combine nuclear imaging and fluorescence applications.[177-178]

The ligand 2-phenyl-1*H*-imidazo[4,5-*f*][1,10]phenanthroline (**14**) and its analogue 4-(1*H*-imidazo[4,5-*f*][1,10]phenanthrolin-2-yl)benzaldehyde (**15**) are known to have fluorescence properties. However, with an excitation is in the UV range, the molecules are not suitable for cell imaging. This problem can be solved by coordination to a metal centre, shifting the excitation into the visible part. Furthermore, **15** can be attached to peptides or nanoparticles using oxime ligation, utilizing stable imine formation between an aldehyde and aminoxy acetic acid (Fig. 1.18).[179-183]

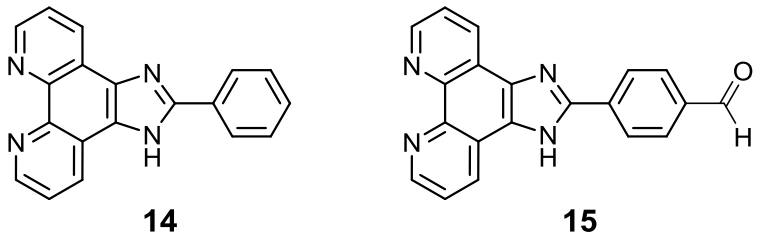

Fig. 1.18: Molecular structure of the ligands **14** and **15**. Compound **15** can form a stabile imine via oxime ligation with aminoxy acetic acid.

2 Motivation

Nanoscience is an upcoming scientific field which merges physics, chemistry, and medicine to utilize nano-sized constructs for various applications. For example in nanomedicine, the surface functionalization of nanoparticles with bio-active molecules like proteins and peptides plays a crucial role for drug delivery. However, these systems are often poorly characterized with regard to surface functionalization. Thus, in the first part of this work, analytical methods were to be developed for the characterization of nanoparticles with amine, azide, and peptide surface modification. For this purpose, the neuropeptide hormone allatostatin 1 (ALST1) and related tyrosine- and phenylalanine-substituted model peptides were to be synthesized and conjugated to azide-functionalized silica nanoparticles using the copper(I)-catalyzed cycloaddition of azides and terminal alkynes (CuAAC). Different analytical approaches based on UV/Vis spectroscopy and HPLC were then to be evaluated for their potential to quantify nanoparticle surface modifications. In the second part of the work, azide-functionalized silica-coated superparamagnetic iron oxide nanoparticles (SPIONs) were to be synthesized and conjugated with the ALST1 peptide as a potential vector for active targeting of neuroendocrinic tumours. Their potential as magnetic resonance imaging (MRI) contrast agents was to be investigated with a focus on the effect of different surface modifications like peptides or organic fluorescent dyes. Finally, the particles were to be tested *in vitro* for their potential of cell internalization. In the third part of the work, manganese(I) and rhenium(I) complexes were to be synthesized and investigated for their potential as alternatives to organic luminescent dyes. These were then to be conjugated to detonation nanodiamond (DND), which is a biologically inert carrier system. ALST1 was to be conjugated to the nanodiamond as well, since it enhances cellular uptake when conjugated to nanoparticles. Then, this material was also to be applied to cell cultures to investigate its cell uptake properties and the potential of the metal complexes as a luminescent probes for fluorescent cell imaging in comparison to the commercially available organic dye cyanine 5 (Cy5).

3 Results and discussion

3.1 Synthesis and characterization of metal complexes

3.1.1 Synthesis of 2-phenyl-1*H*-imidazo[4,5-*f*][1,10]phenanthroline

2-Phenyl-1*H*-imidazo[4,5-*f*][1,10]phenanthroline (**14**) was synthesized by heating a solution of ammonium acetate in water, 1,10-phenanthroline-5,6-dione (**16**), and benzaldehyde (**17**) to reflux in concentrated acetic acid for 3 h (Fig 3.1).[179-181, 184] The compound 1,10-phenanthroline-5,6-dione (**16**) was synthesized according to literature procedure.[185]

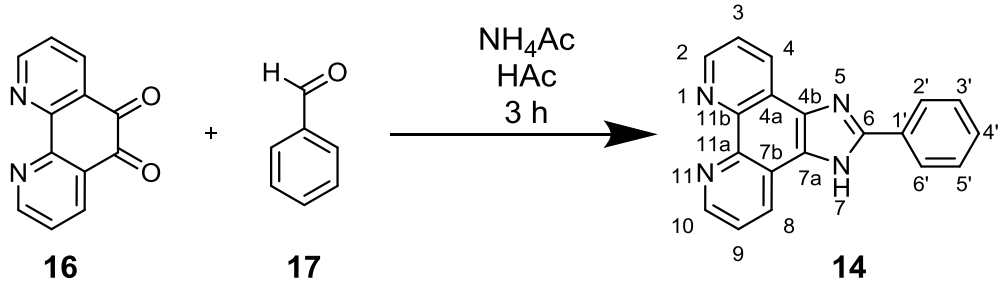

Fig. 3.1: Synthesis of 2-phenyl-1*H*-imidazo[4,5-*f*][1,10]phenanthroline (**14**).

After cooling to room temperature, the product was precipitated with 25% aqueous ammonia, filtered off, washed with water several times, and dried in vacuum to give a yellow solid with a yield of 49%. The ^{1}H-NMR spectrum shows a quintet at 2.50 ppm, a broad signal at 3.35 ppm and a set of signals from 7.75 to 9.05 ppm (Fig 3.2). The signal at 2.50 ppm is due to the DMSO-d_6 and the signal at 3.35 ppm from residual water in the solvent used. The multiplet from 7.52 to 7.62 ppm with an integral of 3H is assigned to the protons at positions 3', 4', and 5' of compound **14**. The doublet of doublets at 7.84 ppm with a ^{3}J of 4.35 Hz and an integral of 2H is assigned to the protons at position 3 and 9.

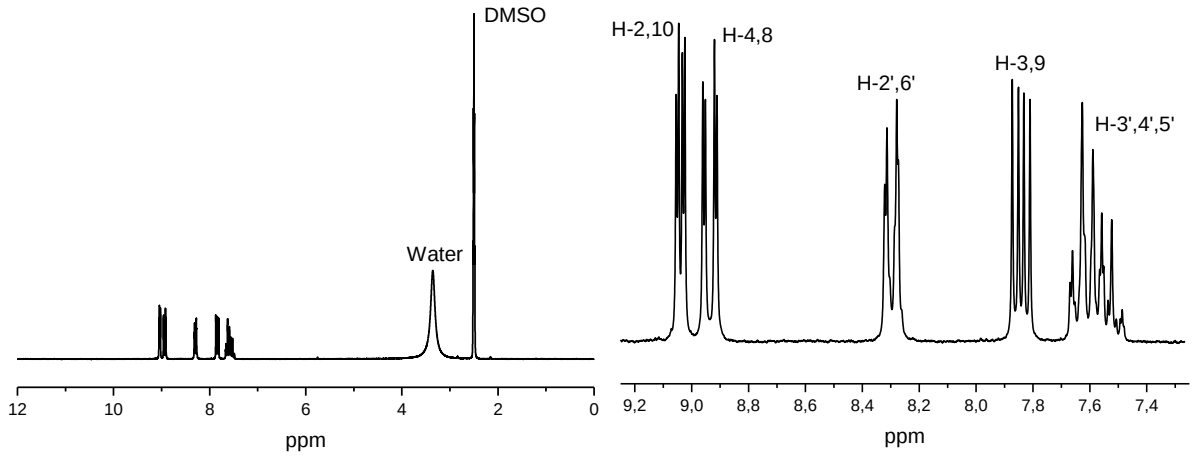

Fig. 3.2: 200 Hz ^{1}H-NMR spectrum of 2-phenyl-1*H*-imidazo[4,5-*f*][1,10]phenanthroline (**14**) in DMSO-d_6.

The doublet of doublets at 8.28 ppm with an integral of 2H, a ^{3}J of 8.41 Hz, and a ^{4}J of 1.53 Hz, is due to the protons at 2' and 6' position. The doublet of doublets at 8.94 ppm with an integral of 2H, a ^{3}J of 8.13 Hz and ^{4}J of 1.75 Hz is assigned to the protons at positions 4 and 8. The doublet of doublets with an integral of 2H at 9.04 ppm, a ^{3}J was 4.33 Hz and the ^{4}J was 1.73 Hz is assigned to the protons at positions 2 and 10. The IR spectrum shows a broad signal around 3064 cm^{-1} and further peaks at around 1546, 1459 and 802 cm^{-1} (Fig. 3.3). The very broad signal at 3064 cm^{-1} is assigned to a combination of the N-H deformation vibration as well as the aromatic C-H stretching vibrations. Furthermore, the sharp signals around 1546 and 1459 cm^{-1} are due to the aromatic C=C stretching vibrations.

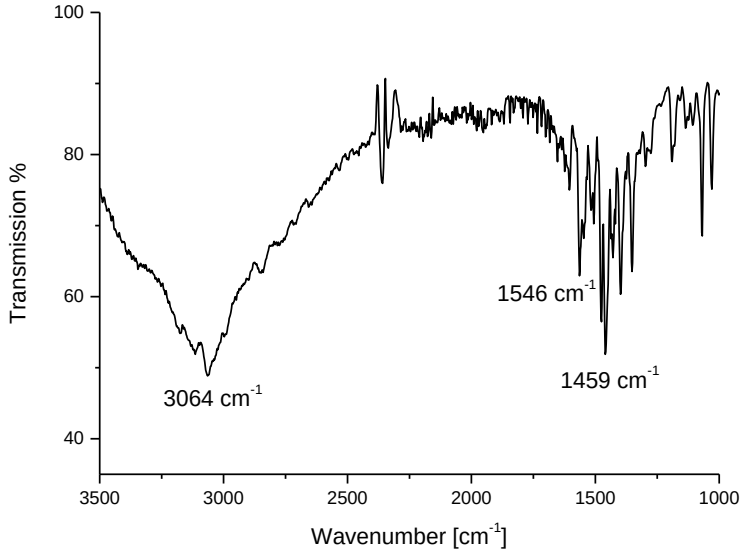

Fig. 3.3: ATR IR spectrum of compound 2-phenyl-1*H*-imidazo[4,5-*f*][1,10]phenanthroline (**14**).

The positive mode ESI mass spectrum shows signals at 297.11, 319.09 and 615.20. These signals are assigned to $[M+H]^{+}$, $[M+Na]^{+}$, and $[2M+Na]^{+}$.The CHN analysis demonstrates the purity of the compound with measured values within a maximum of ± 0.5% from the expected ones.

3.1.2 Synthesis of 4-(1*H*-imidazo[4,5-*f*][1,10]phenanthrolin-2-yl)benzaldehyde

4-(1*H*-imidazo[4,5-*f*][1,10]phenanthrolin-2-yl)benzaldehyde (**15**) was synthesized by heating a solution of ammonium acetate in water and terephthalaldehyde (**18**) in concentrated acetic acid to reflux for 3 h while slowly adding 1,10-phenanthroline-5,6-dione (**16**) (Fig. 3.4). During the reaction a red solid precipitated, which was filtered off after cooling to room temperature. However, it turned out that the red solid was 2-(4-(1*H*-imidazo[4,5-*f*][1,10]phenanthrolin-2-

yl)phenyl)-1*H*-imidazo[4,5-*f*][1,10]-phenanthroline (**19**) and not compound **15** (see chapter 7 for ^{1}H NMR Data). After addition of 25% aqueous ammonia to the remaining reaction mixture, an orange solid precipitated which was filtered off, washed with water several times, and dried in vacuum to give an orange powder with a yield of 48%.

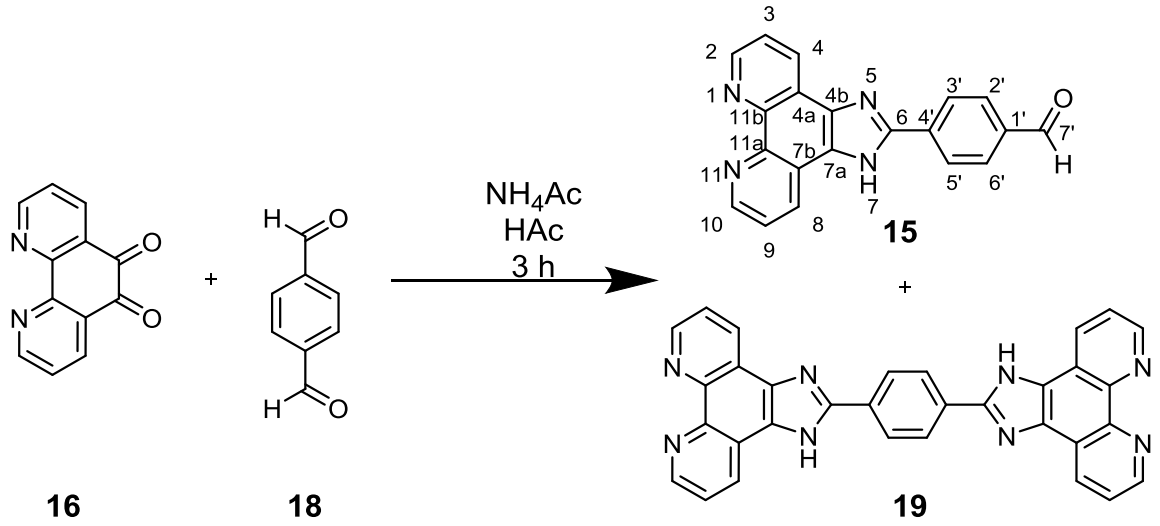

Fig. 3.4: Synthesis of 4-(1*H*-imidazo[4,5-*f*][1,10]phenanthrolin-2-yl)benzaldehyde (**15**) with 2-(4-(1*H*-imidazo[4,5-*f*][1,10]phenanthrolin-2-yl)phenyl)-1*H*-imidazo[4,5-*f*][1,10]-phenanthroline (**19**) formed as a by-product.

The ^{1}H-NMR spectrum of compound **15** shows a quintet at 2.50 ppm, a broad signal at 3.35 ppm, five sets of signals from 7.75 to 9.05 ppm and a singlet at 10.09 ppm (Fig 3.5). The signal at 2.50 ppm is assigned to the DMSO-d_6 and the signal at 3.35 ppm is due to residual water.

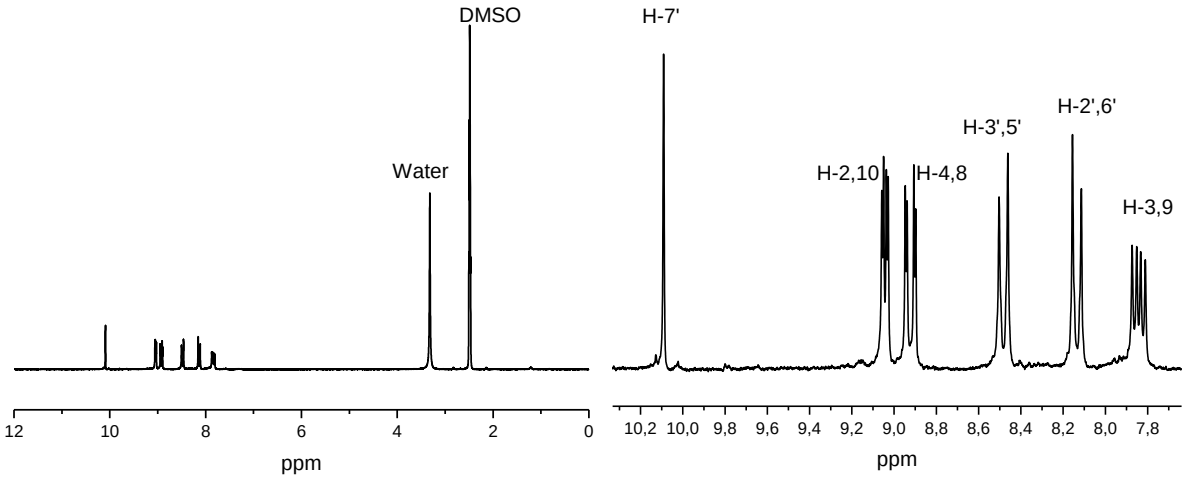

Fig. 3.5: 200 Hz ^{1}H-NMR spectrum of 4-(1*H*-imidazo[4,5-*f*][1,10]phenanthrolin-2-yl)benzaldehyde (**15**) in DMSO-d_6.

The quartet at 7.84 ppm with ^{3}J of 4.34 Hz and an integral of 2H is assigned to the protons at position 3 and 9. At 8.13 ppm, the doublet with an integral of 2H and ^{3}J coupling of 8.41 Hz is assigned to the protons at 2' and 6' position. The signals at 8.48 ppm with a ^{3}J of 8.27 Hz and an integral of 2H is assigned to the protons at 3' and 5' positions. The doublet of doublets at 8.91 ppm with an integral of 2H and ^{3}J of 8.13 Hz and ^{4}J of 1.75 Hz is assigned to the protons at positions 4 and 8. The doublet of doublets with an integral of 2H at 9.04 ppm with ^{3}J of 4.33 Hz and the ^{4}J of 1.73 Hz are due to the protons at position 2 and 10. The singlet at 10.09 ppm with an integral of 1H is assigned to the aldehyde proton at position 7'. The IR spectrum shows a broad signal around 3064 cm^{-1} and a sharp signal at 1693 cm^{-1} (Fig. 3.6). The broad signal around 3046 cm^{-1} is assigned to a combination of the N-H as well as the aromatic C-H stretching vibrations. Furthermore, the sharp signal at 1693 cm^{-1} is assigned to the aldehyde C=O stretching vibration. The positive mode ESI mass spectrum showed a signal at 325.10. This signal is assigned to $[M+H]^{+}$. The CHN analysis demonstrates the purity of the compound with measured values within a maximum of ± 0.5% from the expected ones.

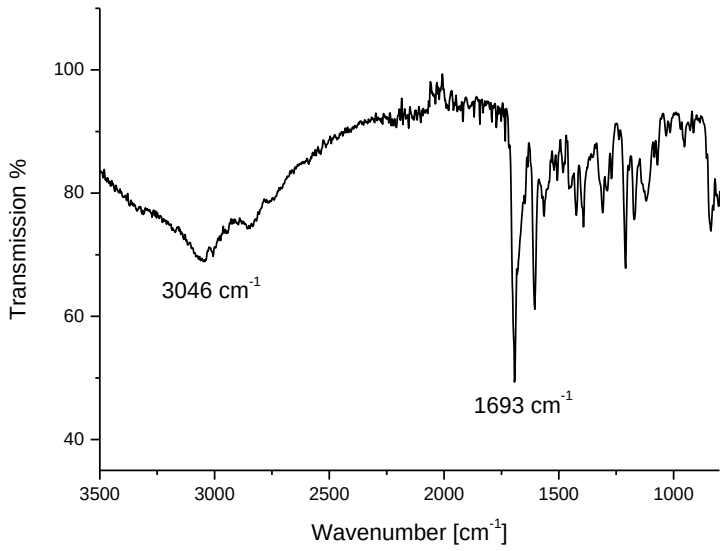

Fig. 3.6: ATR IR spectrum of 4-(1*H*-imidazo[4,5-*f*][1,10]phenanthrolin-2-yl)benzaldehyde (**15**).

3.1.3 Synthesis of bromo(tricarbonyl)(2-phenyl-1*H*-imidazo[4,5-*f*][1,10]phenanthroline) manganese(I)

Bromo(tricarbonyl)(2-phenyl-1*H*-imidazo[4,5-*f*][1,10]phen-anthroline) manganese(I) (**20**) was synthesized by heating compound **14** and manganese pentacarbonyl bromide in ethanol to reflux for 5 h (Fig. 3.7).

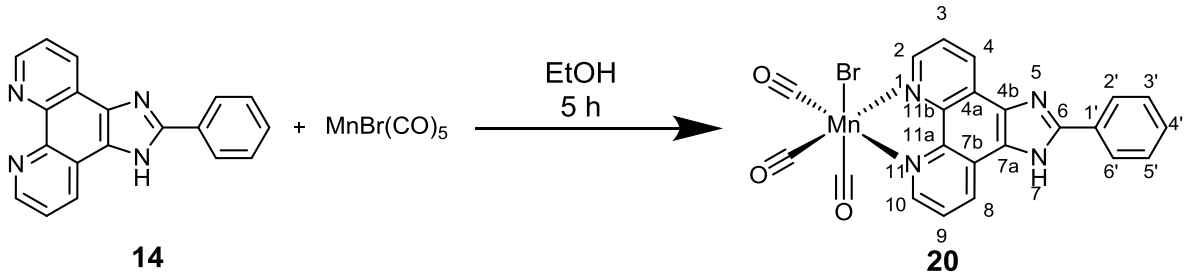

Fig. 3.7: Synthesis of bromo(tricarbonyl)(2-phenyl-1H-imidazo[4,5-f][1,10]phen-anthroline) manganese(I) (**20**).

After cooling to room temperature, the yellow precipitate was filtered off and washed several times with water and ethanol. Afterwards, it was dried in vacuum to get a bright yellow solid with a yield of 61%. In addition to the solvent and residual water signals, the ^{1}H-NMR spectrum shows five sets of signals from 7.75 to 9.05 ppm (Fig 3.8).

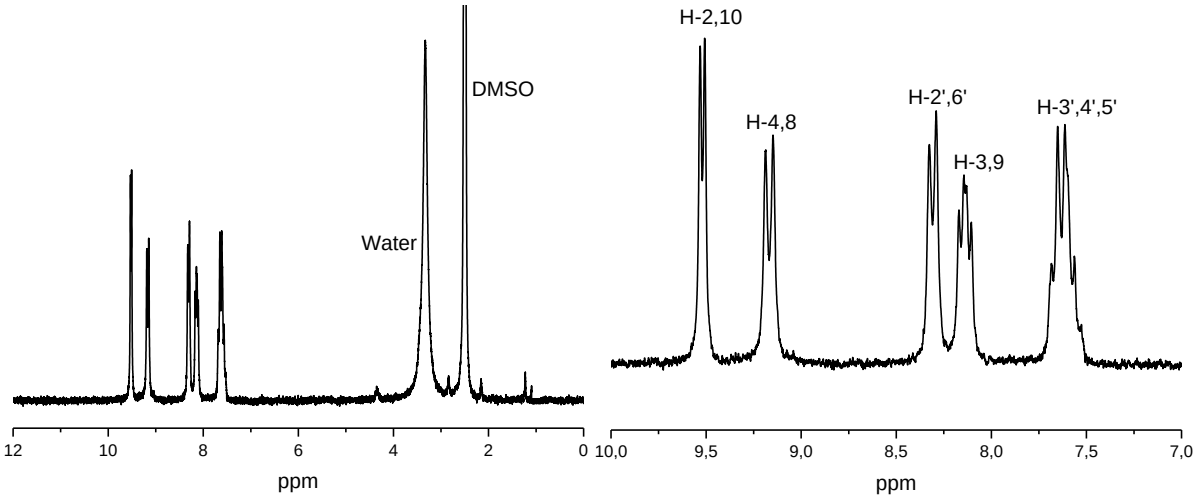

Fig. 3.8: 200 Hz ^{1}H-NMR spectrum of bromo(tricarbonyl)(2-phenyl-1*H*-imidazo[4,5-*f*][1,10]phen-anthroline) manganese(I) (**20**) in DMSO-d_6.

The multiplet from 7.56 to 7.68 ppm with an integral of 3H is assigned to the protons at positions 3', 4', and 5'. The doublet of doublets at 8.12 ppm with an integral of 2H and a ^{3}J of 4.36 Hz is assigned to the protons at position 3 and 9. The doublet at 8.33 ppm with an integral of 2H and ^{3}J of 7.13 Hz is assigned to the protons at positions 2' and 6'. The doublet at 9.16 ppm with an integral of 2H and ^{3}J of 7.64 Hz is assigned to the protons at positions 4 and 8. The doublet with an integral of 2H at 9.51 ppm with ^{3}J of 4.73 is assigned to the protons at

position 2 and 10. In comparison to compound **14**, the signals shifted to higher ppm values. The IR spectrum shows a broad signal around 3141 cm^{-1} and three sharp signals between 1909 and 2024 cm^{-1} (Fig. 3.9). The signal at around 3141 cm^{-1} are due to a combination of the N-H as well as the aromatic C-H stretching vibrations. Furthermore, the signals at 2024, 1934, and 1909 cm^{-1} are the characteristic stretching vibrations for complexes with carbonyl ligands. The signal at 2024 cm^{-1} is assigned to the symmetric and the signals at 1934 and 1909 cm^{-1} are assigned to the asymmetric carbonyl stretching vibrations. In positive mode ESI mass spectrometry, compound **20** shows a signal at 950.97. This signal is assigned to $[2M\text{-}Br]^+$. The CHN analysis demonstrates the purity of the compound with measured values within a maximum of ± 0.5% from the expected ones.

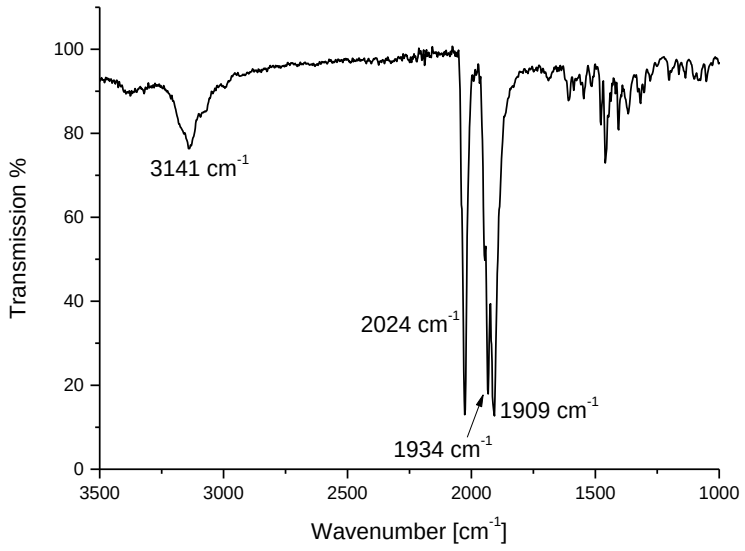

Fig. 3.9: ATR IR spectrum of bromo(tricarbonyl)(2-phenyl-1*H*-imidazo[4,5-*f*][1,10]phenanthroline) manganese(I) (**20**)

3.1.4 Synthesis of bromo(tricarbonyl)(4-(1*H*-imidazo[4,5-*f*][1,10]phenanthrolin-2-yl)benzaldehyde) manganese(I)

The synthesis of bromo(tricarbonyl)(4-(1*H*-imidazo[4,5-*f*][1,10]phenanthrolin-2-yl)benzaldehyde) manganese(I) (**21**) was carried out as described for compound **20** (Fig. 3.10). The yield was 63%.

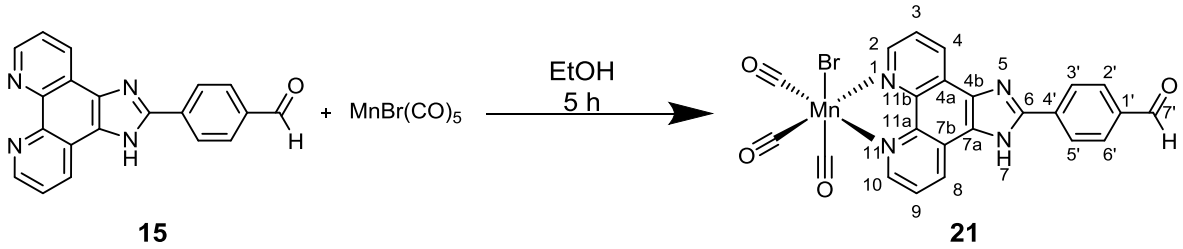

Fig. 3.10: Synthesis of bromo(tricarbonyl)(4-(1*H*-imidazo[4,5-*f*][1,10]phenanthrolin-2-yl)benzaldehyde) manganese(I) (**21**).

No properly resolved ^{1}H-NMR spectrum could be recorded for compound **21**, regardless of the solvent and experimental conditions. In addition to the solvent peaks of DMSO-d_6 and water, there were only a total of five very broad resonances in the range of 7.5 to 10.5 ppm (Fig. 3.11). The broad resonances show maxima at 8.03, 8.56, 9.16, 9.41, and 10.03 ppm. As the broad signals overlap with each other and show no signal splitting, neither signal integrals, nor coupling constants could be determined.

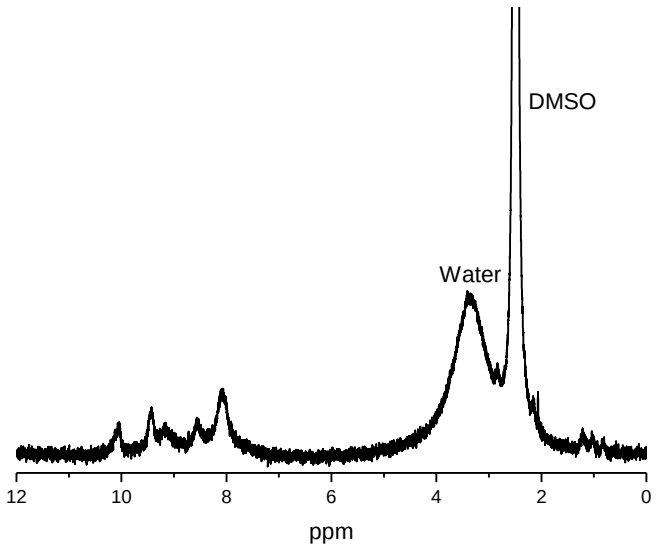

Fig. 3.11: 200 Hz ^{1}H-NMR spectrum of bromo(tricarbonyl)(4-(1*H*-imidazo[4,5-*f*][1,10]phenanthrolin-2-yl)benzaldehyde) manganese(I) (**21**) in DMSO-d_6.

The IR spectrum shows dominant signals at 2024, 1924, 1911, and 1691 cm^{-1} (Fig. 3.12). The peaks at 2024, 1924, and 1911 cm^{-1} is assigned to the different carbonyl stretching vibrations of the complex. The signal at 2024 cm^{-1} is assigned to the symmetric and the signals at 1924 and 1911 cm^{-1} are assigned to the asymmetric carbonyl stretching vibrations. Furthermore, the signal at 1691 cm^{-1} is due to the stretching vibration of the aldehyde C=O group.

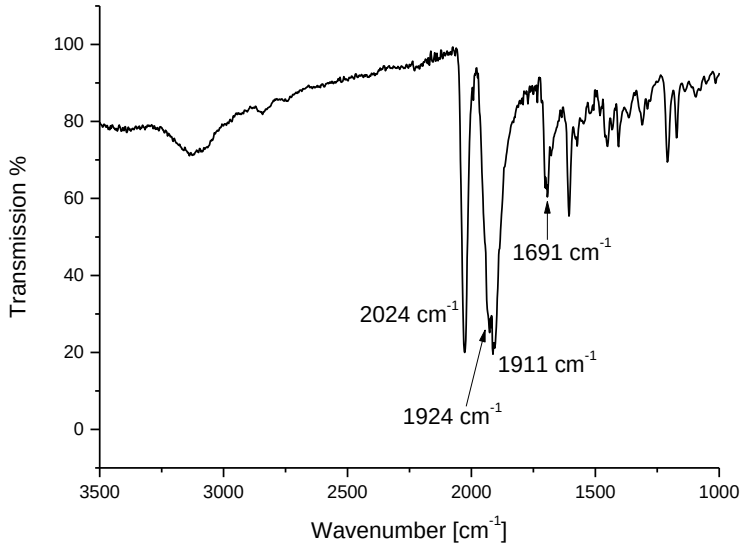

Fig. 3.12: ATR IR spectrum of bromo(tricarbonyl)(4-(1*H*-imidazo[4,5-*f*][1,10]phenanthrolin-2-yl)benzaldehyde) manganese(I) (**21**).

The positive mode ESI mass spectrum shows a signal at 379.03. This signal is assigned to $[M\text{-}Br^{-}\text{-}3CO]^{+}$, indicating lability of the carbonyl ligands due to their elimination. The CHN analysis demonstrates the purity of the compound with measured values within a maximum of ± 0.5% from the expected ones.

3.1.5 Synthesis of bromo(tricarbonyl)(2-phenyl-1*H*-imidazo[4,5-*f*][1,10]phenanthroline) rhenium(I)

Bromo(tricarbonyl)(2-phenyl-1*H*-imidazo[4,5-*f*][1,10]phenanthroline) rhenium(I) (**22**) was synthesized by heating compound **14** and rhenium pentacarbonyl bromide in toluene to reflux for 20 hours (Fig. 3.13). After cooling to room temperature, the yellow precipitate was filtered off and washed several times with water and ethanol. Afterwards, it was dried in vacuum to get a bright yellow-greenish solid with a yield of 33%. %. In addition to the solvent and residual water signals, the ^{1}H-NMR spectrum shows five sets of signals from 7.50 to 9.60 ppm (Fig 3.14).

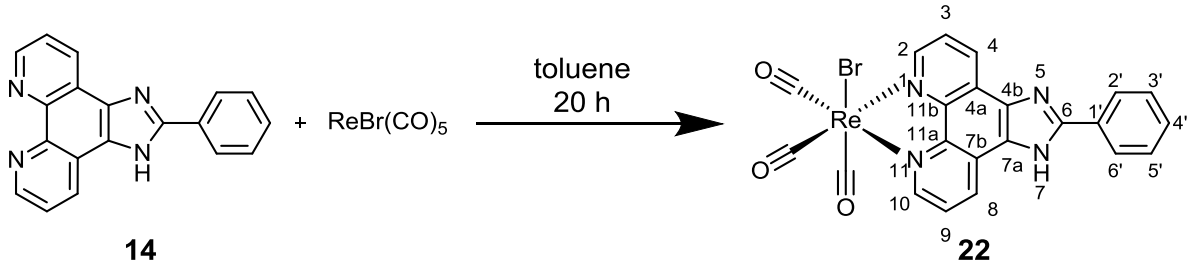

Fig. 3.13: Synthesis of bromo(tricarbonyl)(2-phenyl-1*H*-imidazo[4,5-*f*][1,10]phenanthroline) rhenium(I) (**22**).

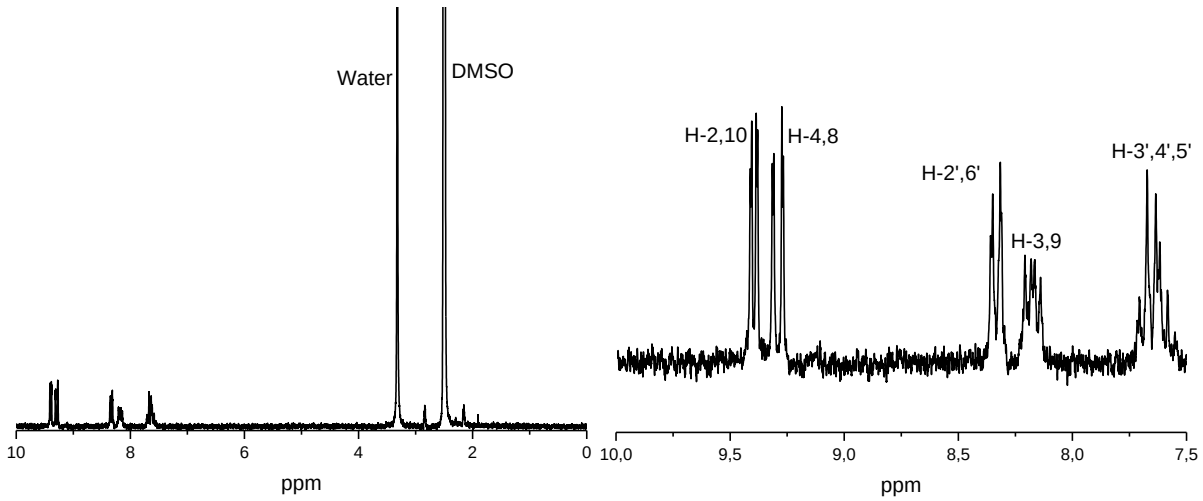

Fig. 3.14: 200 Hz ^{1}H-NMR spectrum of bromo(tricarbonyl)(2-phenyl-1*H*-imidazo[4,5-*f*][1,10]phenanthroline) rhenium (**22**) in DMSO-d_6.

In analogy to compound **20**, the multiplet from 7.58 to 7.70 ppm with an integral of 3H is assigned as the protons at positions 3', 4', and 5'. The doublet of doublets at 8.17 ppm with an integral of 2H is due to the protons at position 3 and 9. The doublet at 8.30 ppm with an integral of 2H and a coupling constant ^{3}J of 6.69 Hz is assigned to the protons at 2' and 6' positions. The doublet at 9.29 ppm with an integral of 2H, ^{3}J of 8.29 Hz and ^{4}J of 1.25 Hz is assigned to

the protons at positions 4 and 8. The doublet with an integral of 2H at 9.49 ppm, with ^{3}J of 5.13 Hz, and ^{4}J of 1.25 Hz is due to the protons at positions 2 and 10. The IR spectrum shows a broad signal at around 3137 cm^{-1}, one sharp signal at 2021 and one broad and intense signal at 1882 cm^{-1} (Fig. 3.15). The peak at about 3137 cm^{-1} is assigned to a combination of the N-H as well as the aromatic C-H stretching vibrations. Furthermore, the signals at 2021 cm^{-1} and the broad signal at 1882 cm^{-1} are the characteristic stretching vibrations for complexes with carbonyl ligands. The signal at 2021 cm^{-1} is assigned to the symmetric and the signal at 1882 cm^{-1} is due to the asymmetric carbonyl stretching vibrations. The positive mode ESI mass spectrum shows signals at 567.04, 595.05, and 668.95. These are assigned to $[M\text{-}Br]^{+}$, $[M\text{-}Br+N_2]^{+}$, and $[M+Na]^{+}$. The CHN analysis demonstrates the purity of the compound with measured values within a maximum of ± 0.5% from the expected ones.

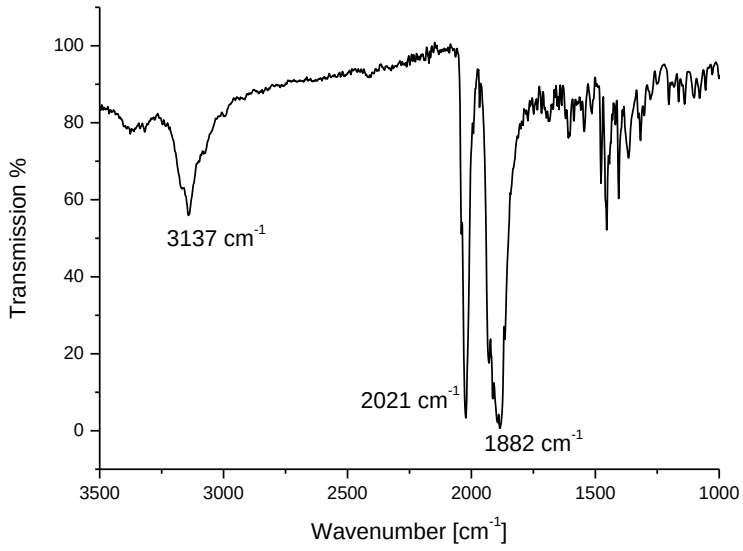

Fig. 3.15: ATR IR spectrum of bromo(tricarbonyl)(2-phenyl-1*H*-imidazo[4,5-*f*][1,10]phenanthroline) rhenium(I) (**22**).

3.1.6 Synthesis of bromo(tricarbonyle)(4-(1*H*-imidazo[4,5-*f*][1,10]phenanthrolin-2-yl)benzaldehyde) rhenium(I)

In analogy to compound **22**, bromo(tricarbonyle)(4-(1*H*-imidazo[4,5-*f*][1,10]phenanthrolin-2-yl)benzaldehyde) rhenium(I) (**23**) was synthesised by heating compound **15** and rhenium pentacarbonyl bromide in toluene to reflux for 15 hours (Fig. 3.16).

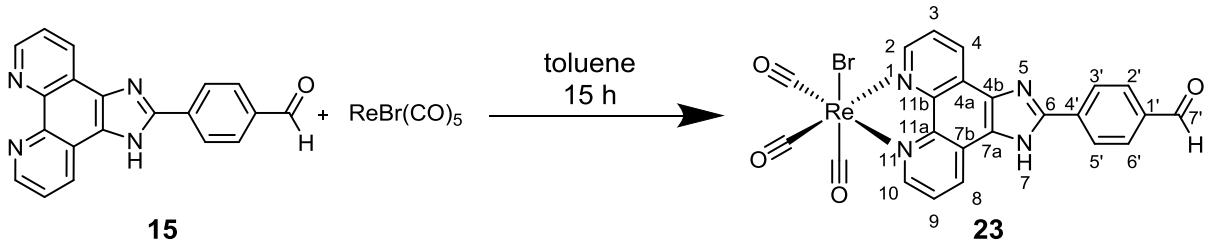

Fig. 3.16: Synthesis of bromo(tricarbonyle)(4-(1*H*-imidazo[4,5-*f*][1,10]phenanthrolin-2-yl)benzaldehyde) rhenium(I) (**23**).

In addition to the solvent and residual water signals, the ^{1}H-NMR spectrum shows five sets of signals from 8.00 to 10.50 ppm (Fig 3.17). The multiplet from 8.16 to 8.22 ppm with an integral of 4H is an overlap of a doublet and a quartet. These signals are assigned to the protons at position 3 and 9 (quartet) as well as 2' and 6' (doublet). The doublet at 8.54 ppm with an integral of 2H and ^{3}J of 8.03 Hz is due to the protons at positions 3' and 6'. The doublet of doublets at 9.29 ppm with an integral of 2H, ^{3}J of 8.31 Hz, and ^{4}J of 1.25 Hz is assigned to the protons at positions 4 and 8. The doublet of doublets with an integral of 2H at 9.42 ppm, ^{3}J of 5.13 Hz, and ^{4}J of 1.27 Hz is assigned to the protons at position 2 and 10. The singlet with an integral of 1H at 10.13 ppm is assigned to the aldehyde proton at position 7'. The IR spectrum showed a set of signals around 3216, 2017, 1900, 1693, and 1608 cm^{-1} (Fig. 3.18).

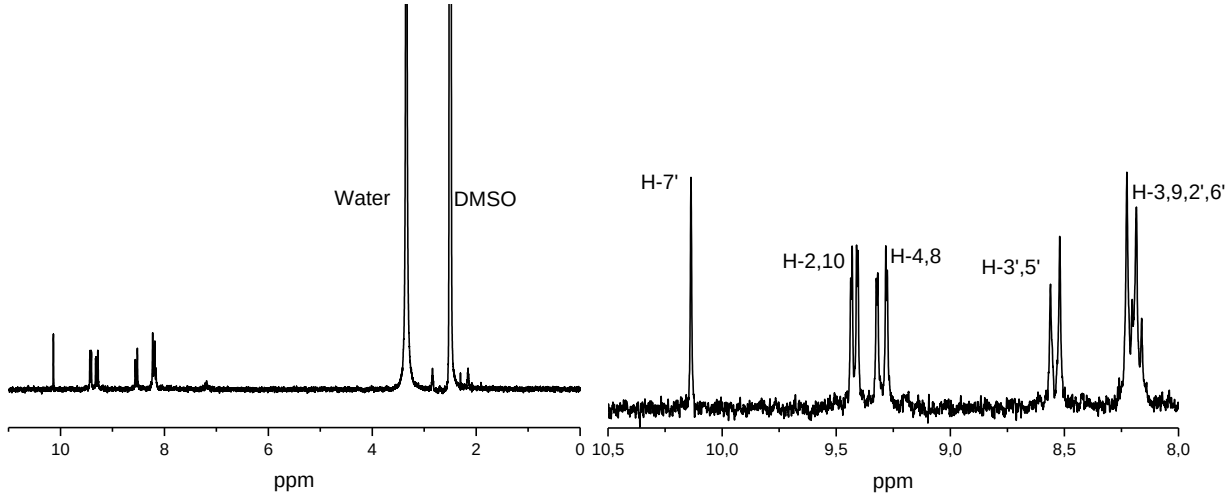

Fig. 3.17: 200 Hz ^{1}H-NMR spectrum bromo(tricarbonyle)(4-(1*H*-imidazo[4,5-*f*][1,10]phenanthrolin-2-yl)benzaldehyde) rhenium(I) (**23**) in DMSO-d_6.

The IR spectrum shows a set of signals around 3216, 2017, 1900, 1693, and 1608 cm^{-1} (Fig. 3.18). In analogy to the previously discussed manganese- and rhenium carbonyl compounds **20**, **21**, and **22**, the signals at around 3216 cm^{-1} is assigned to the combined C-H and N-H stretching vibrations.

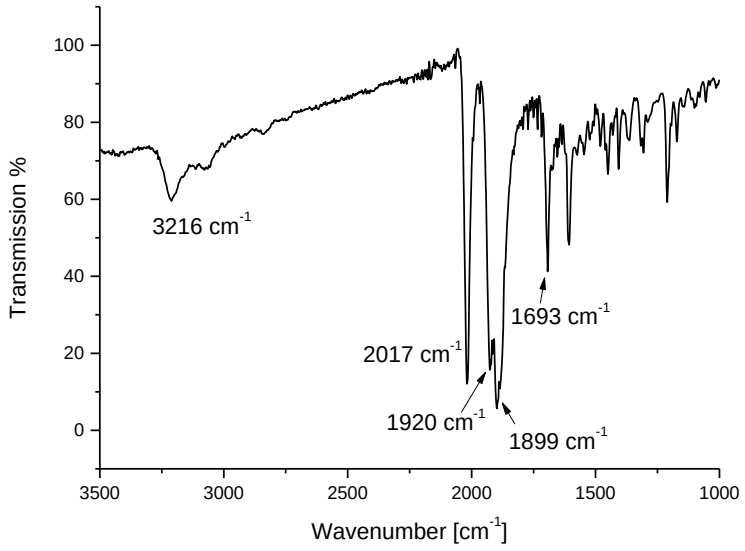

Fig. 3.18: ATR IR spectrum of bromo(tricarbonyle)(4-(1*H*-imidazo[4,5-*f*][1,10]phenanthrolin-2-yl)benzaldehyde) rhenium(I) (**23**).

The signals at 2017, 1920 and 1899 cm^{-1} is assigned to the symmetrical and asymmetrical carbonyl stretching vibrations. The signal at 1693 cm^{-1} is characteristic for aldehyde carbonyl groups. Furthermore, the signal at 1608 cm^{-1} is assigned to the C=C stretching vibration. The positive mode ESI mass spectrum shows a signal at 697.65, which is due to $[M+Na]^+$. The CHN analysis demonstrates the purity of the compound with measured values within a maximum of ± 0.5% from the expected ones.

3.1.7 UV/Vis absorption and stability of complexes

2-Phenyl-1*H*-imidazo[4,5-*f*][1,10]phenanthroline (**14**) and 4-(1*H*-imidazo[4,5-*f*][1,10]phenanthrolin-2-yl)benzaldehyde (**15**) are yellow to orange in colour in the solid state. The UV/Vis spectrum of compound **14** in methanol/dichloromethane (1:1, v/v) shows two absorption maxima at 276 and 307 nm, while compound **15** in methanol/dichloromethane (1:1, v/v) has several absorption maxima at 283, 305, and 327 nm (Fig. 3.19). **15** shows a bathochromic shift of the absorption bands in comparison to **14**. This is due to the electron withdrawing effect of the aldehyde group.

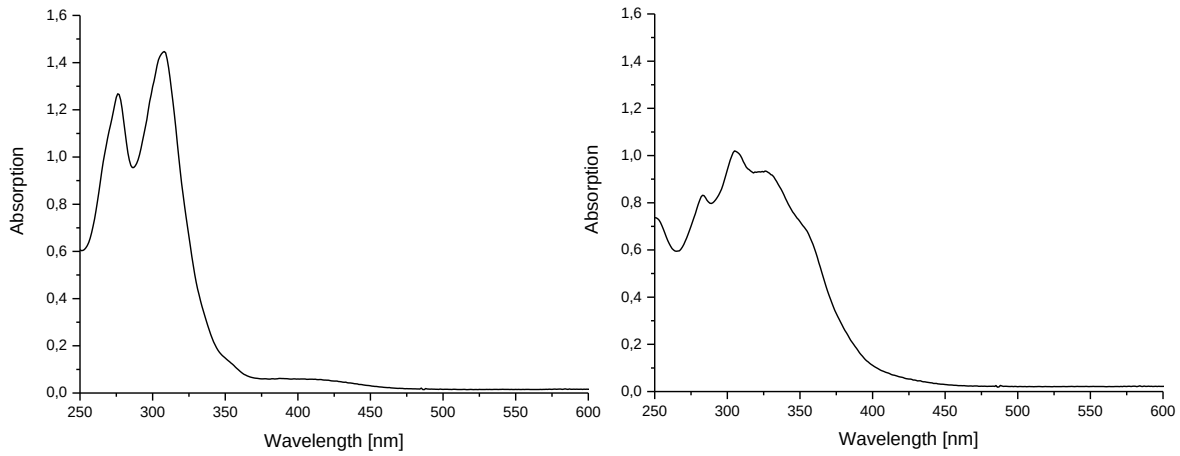

Fig. 3.19: UV/Vis absorption spectra of **14** (left) and **15** (right) in methanol/dichloromethane (1:1, v/v). **14** shows absorption maxima at 276 and 307 nm, and **15** shows absorption maxima at 283, 305, and 327 nm.

In the solid state, manganese complexes **20** and **21**.are yellow. In methanol/dichloromethane (1:1 v/v) **20** shows three absorption maxima at 280, 305, and 422 nm, while **21** has absorption maxima at 289, 328, and 428 nm (Fig. 3.20).

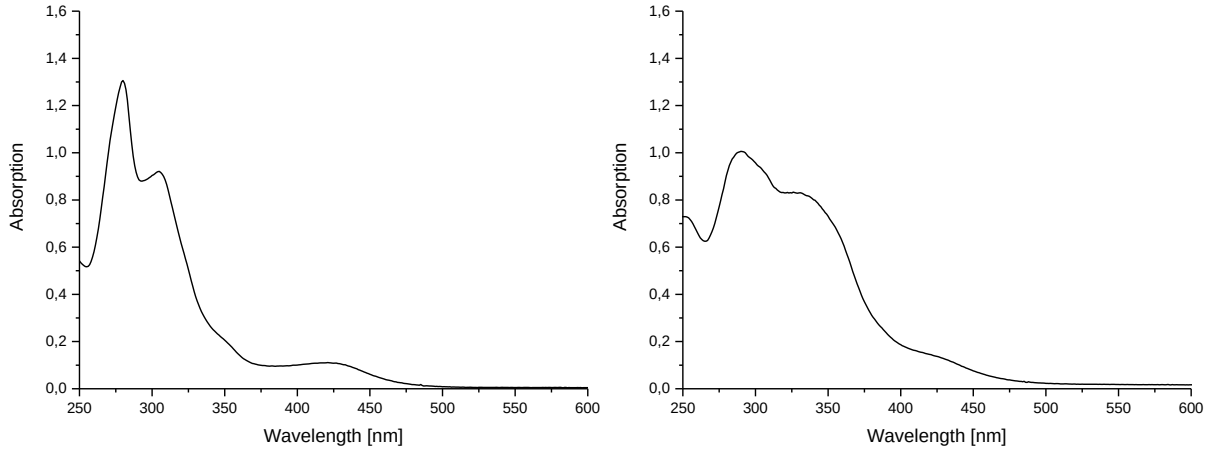

Fig. 3.20: UV/Vis absorption spectra of **20** (left) and **21** (right) in methanol/dichloromethane (1:1, v/v). **20** shows absorption maxima at 280, 305 and 422 nm, and **21** shows absorption maxima at 289, 328, and 428 nm.

Absorption below 300 nm is due to the absorption of the aromatic ligand system. The absorption bands at 305 nm and at about 425 nm are most likely due to MLTC of the manganese centre to the aromatic ligand system. The absorption at 328 is likely due to LLTC of the bromo ligand to the aromatic ligand system.[186] Upon exposure of **20** to 365 nm light, the absorption at 280, 310, 350 and 415 nm decreases rapidly over a time of 54 min indicating decomposition of the compound (Fig.3.21). Furthermore, the absorption band at 310 shifts to 302 nm after the first 30 sec of illumination with light at 365 nm.

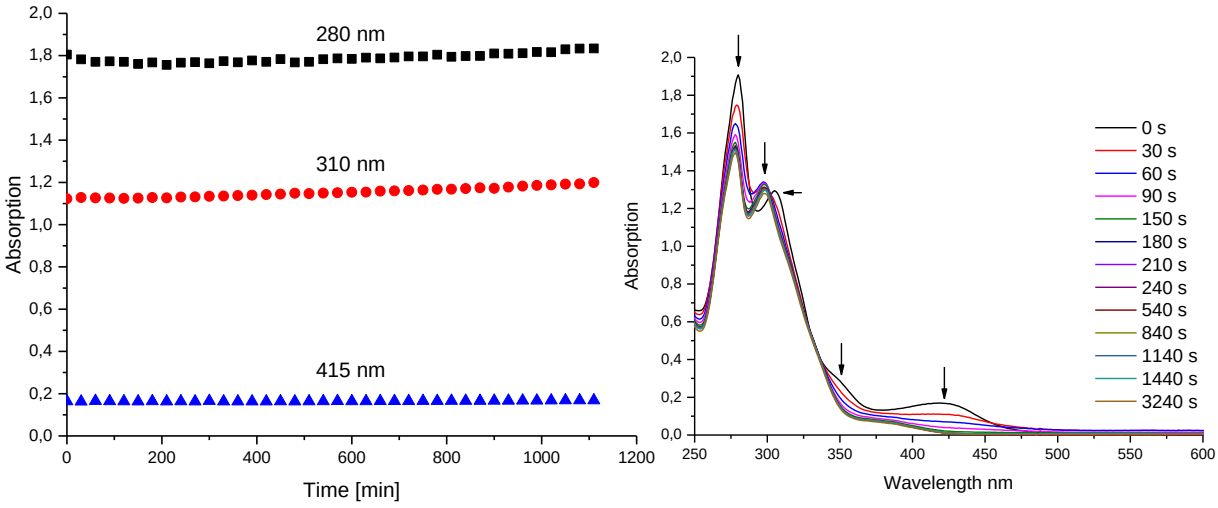

Fig. 3.21: Absence of change of **20** at 280, 310, and 415 nm when kept in the dark for up to 1100 min. Illumination of **20** at 365 nm causes rapid decrease of the absorption bands at 280, 305, 350, and 415 nm over 54 min.

As expected, upon exposure of **21** to 365 nm light, the absorption at 290, 340, and 420 decrease rapidly over a time of 62 min indicating decomposition of the compound (Fig.3.21). Furthermore, the absorption band at 310 shifts to 302 nm after the first 30 sec of illumination with light at 365 nm. Compound **21** showed similar results when irradiated with UV light at 365 nm, indicating decomposition of compound **21**. (Fig. 3.22).

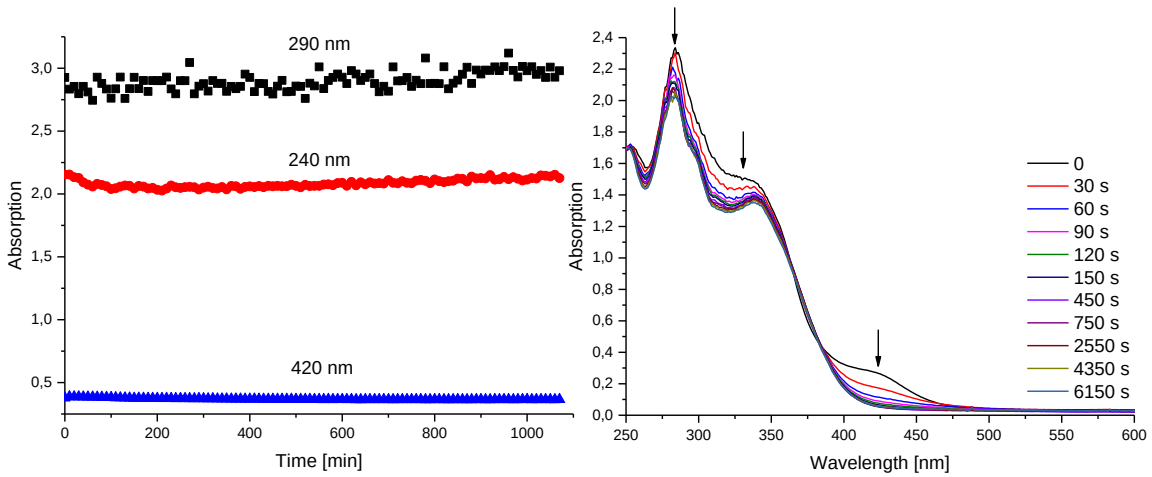

Fig. 3.22: Absence of change of **21** in at 290, 340, and 420 nm when kept in the dark for up to 1100 min. Illumination of **21** at 365 nm causes rapid decrease of the absorption bands at 280, 305, 350, and 415 nm over 110 min.

Manganese carbonyl complexes are known to release carbon monoxide ligands upon illumination. [44, 187-189] However, this instability makes **20** and **21** unsuitable as luminophores The rhenium complexes **22** and **23** are greenish-yellow in the solid state. In methanol/dichloromethane (1:1 v/v) **22** shows four absorption maxima at 280, 304, 350 and 415 nm, while **23** has three broad absorption signals with maxima at 292, 331, and 415 nm. The absorption spectra of **22** and **23** are very similar to **20** and **21** (Fig. 3.23). Upon exposure of **22** to 365 nm light, the absorption spectrum shows no changes over a cause of 192 min (Fig.3.24). The increase of absorption over the cause of the experiment is due to slow evaporation of solvent from the cuvette. Upon exposure of **23** to 365 nm light, the absorption spectrum shows no changes over a cause of 247 min (Fig.3.25). The rhenium complexes **22** and **23** are stable in solution and upon illumination with UV light, making them suitable as potential luminescence probes.

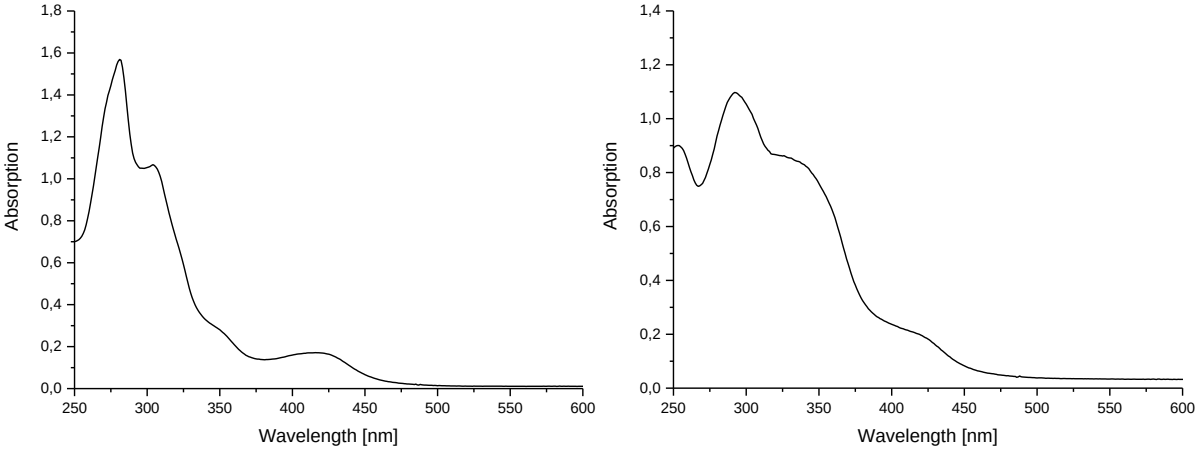

Fig. 3.23: UV/Vis absorption spectra of **22** (left) and **23** (right) in methanol/dichloromethane (1:1, v/v). **22** shows absorption maxima at 280, 304, 350 and 415 nm, and **23** shows absorption maxima at 292, 331, and 415 nm.

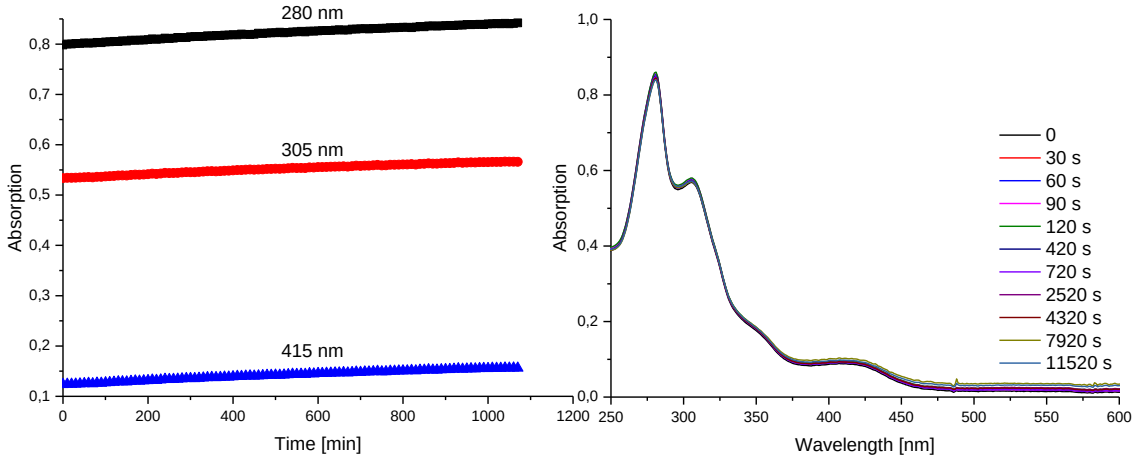

Fig. 3.24: Absence of change of **22** at 280, 305, and 415 nm when kept in the dark for up to 1100 min. Illumination of **20** at 365 nm causes no changes in the absorption spectrum over 194 min.

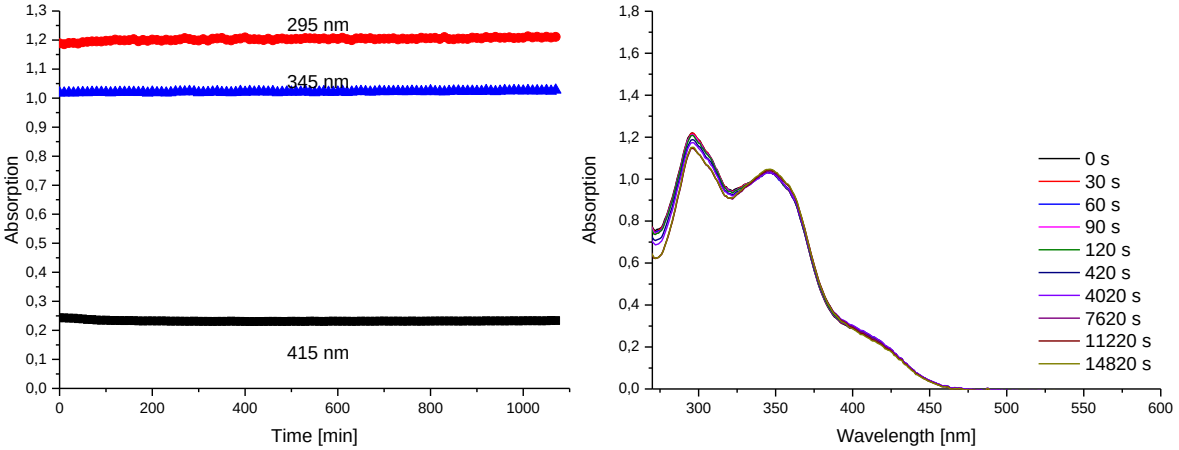

Fig. 3.25: Absence of change of **23** at 295, 335, and 415 nm when kept in the dark for up to 1100 min. Illumination of **23** at 365 nm causes no changes in the absorption spectrum over 247 min.

3.1.8 Luminescence properties of [ReBr(CO)$_3$(L*)] and organic dye Cy5

When ligands **14** and **15** in methanol/dichloromethane (1:1 v/v) are excited at 365 nm, **14** shows a blue-violet and **15** a bright turquoise luminescence. At the same wavelength, rhenium complexes **22** and **23** respectively show bright orange and yellow luminescence (Fig. 3.26).

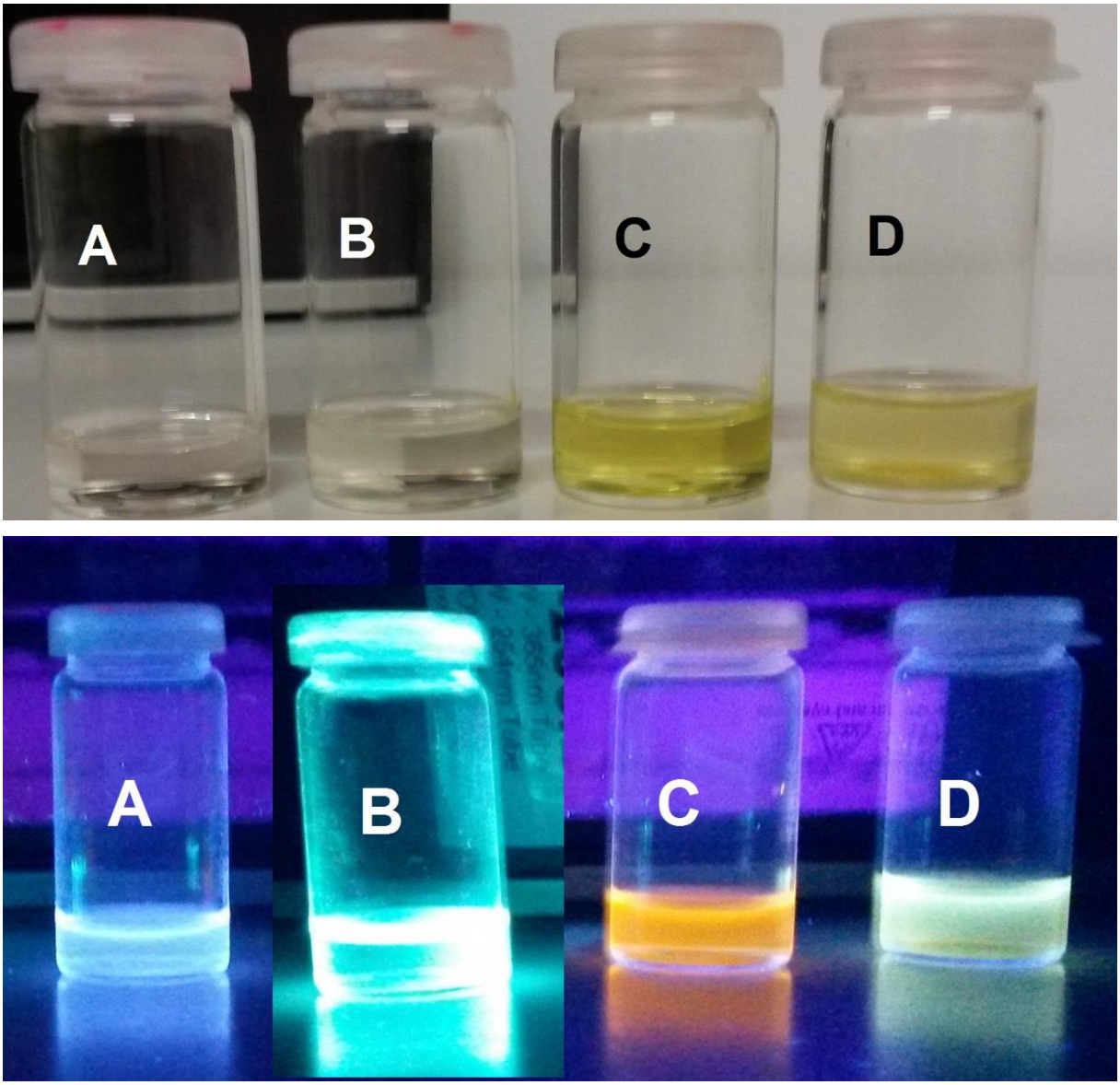

Fig. 3.26: Colour of **14** (A), **15** (B), **22** (C), and **23** (D) upon exposure to daylight (top) and upon excitation at 365 nm.

Upon excitation at 415 nm, rhenium complex **22** shows a broad emission at 612 nm. (Fig. 3.27). Furthermore, the quantum yield Φ and life time τ were measured in degassed methanol/dichloromethane (1:1 v/v) using the time-correlated single-photon counting (TCSPC) method (Tab. 3.1). These photophysical data are compared to the organic dye cyanine 5 (Cy5) (Fig. 3.28) [190-191]

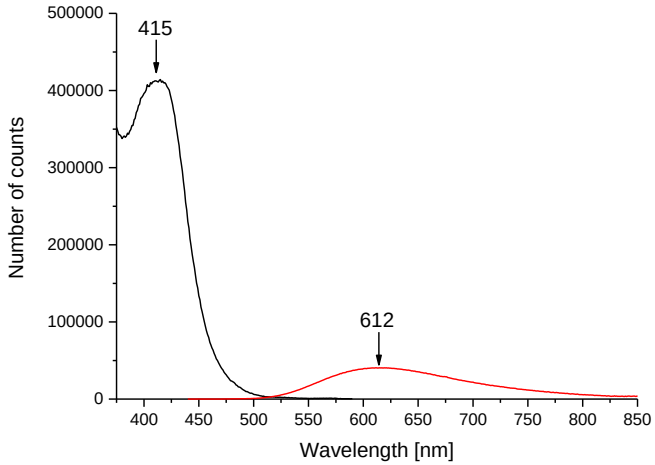

Fig. 3.27: Absorption spectrum (black) and emission spectrum (red) of **22** (λ_{Ex} = 415 nm) in degassed methanol/dichloromethane (1:1 v/v).

Tab. 3.1: Photophysical properties of **22** and Cy5. The data for the latter were taken from the literature.[190-191]

Property	**Compound 19**	**Cy5**
λ_{Ex} [nm]	415	646
λ_{Em} [nm]	612	670
ε [$Lmol^{-1}cm^{-1}$]	1700	250000
Φ	0.05	0.28
τ [ns]	455	1

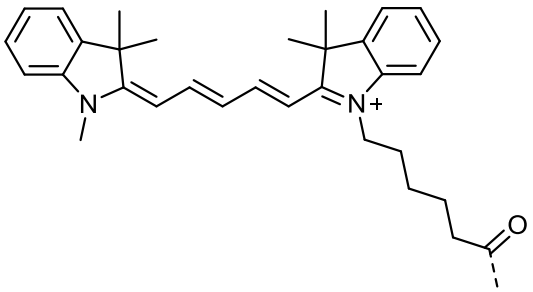

Fig. 3.28: Molecular structure of cyanine 5 (Cy5).

Complex **22** is excited at 415 and emits at 612 nm, while Cy5 is excited at 646 and emits at 670 nm. Thus, **22** has a Stoke shift of 197 nm, avoiding overlap of excitation and emission spectrum as observed for Cy5, which has a Stokes shift of 24 nm. However, Cy5 has a 147x higher emission coefficient ε than **22**. The quantum yield Φ of Cy5 is 6x higher than **22**. However, the lifetime τ of **22** is 455x higher than Cy5. Such a long lifetime is an indication for phosphorescence.[192-193]

3.2 Synthesis and characterization of bioactive peptides

3.2.2 Synthesis of TGF-β1 binding peptide

TGF-β_1 belongs to a superfamily of signal transduction ligands. The TGF-β signalling pathway is involved in apoptosis, proliferation, and differentiation.[148-150] TGF-β receptors and ligands are overexpressed in many kinds of tumours. Therefore, peptide **10** is a promising candidate as a vector for active tumour targeting. It was synthesized with free N- and C- termini via a Fmoc SPPS strategy on a H-(L)-His(Trt)-2CT resin (Fig. 3.29).

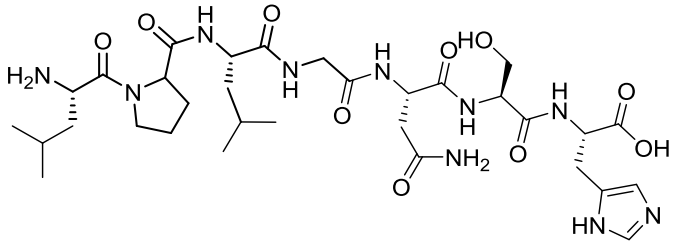

10

Fig. 3.29: Sequence of TGF-β_1 binding peptide (**10**).

The analytical HPLC trace after test cleavage shows three peaks at R_t = 5.58, 13.21, and 18.78 min with the second one of dominant intensity (Fig. 3.30). Thus, in addition to the injection peak at 5.58 min, there is only a minor species at R_t = 18.78 min. The identity of the main product at R_t = 13.21 min was established by positive mode ESI mass spectrometry. It shows a signal at 737.38 which is assigned to $[M+H]^+$.

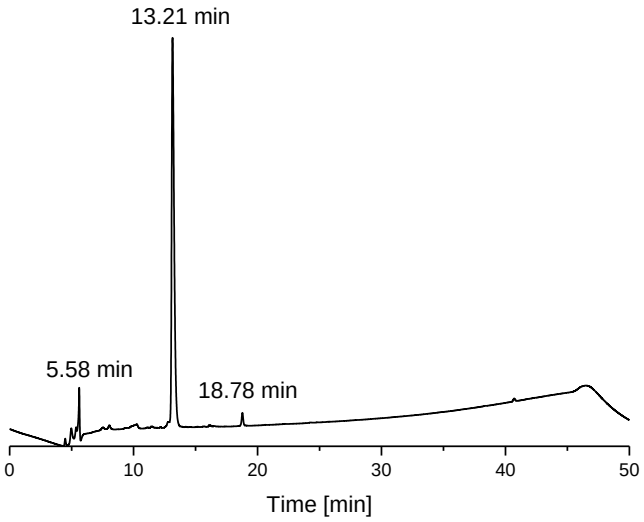

Fig. 3.30: HPLC trace at 220 nm of peptide **10**.

3.2.3 Synthesis of neuropeptide hormone ALST1-hexynoic acid conjugate

The neuropeptide hormone ALST 1 (**11**) is crucial for normal development, metamorphosis, and reproduction of most insect species and was found to promote transportation of nanoparticles into cells and cell nuclei. Furthermore, it shows homology to human galanin and somastatin, which are overexpressed in many difficult-to-treat neuroendocrinic tumours.[154, 156, 159-160] Thus, ALST1 is a promising candidate as a vector for active tumour targeting. Therefore, Peptide **24** was synthesized via an Fmoc SPPS strategy on a Wang Amide MBHA resin giving an amide-capped *C*-terminus. Furthermore, hexynoic acid was conjugated to the *N*-terminus, enabling copper(I) catalysed 1,3-dipolar cycloaddition with azides (Fig. 3.31).[194]

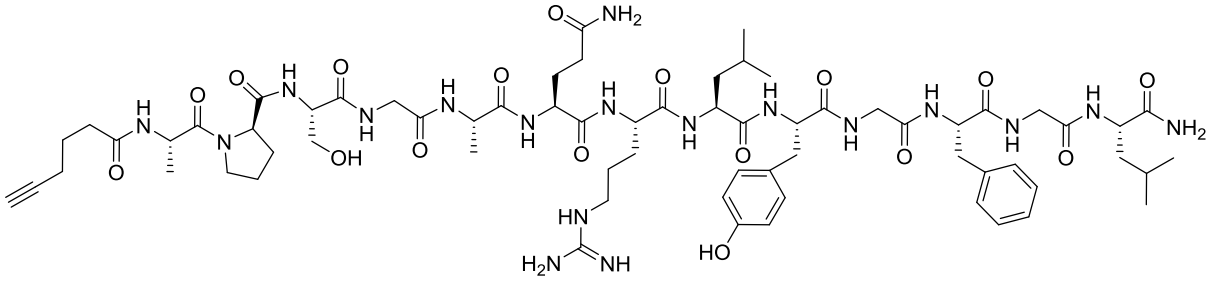

24

Fig. 3.31: Sequence of the synthesized ALST1-hexynoic acid conjugate (**24**).

The analytical HPLC trace of **24** after purification by preparative HPLC, shows two peaks at R_t = 6.21 and 21.54 min, with the second one of dominant intensity (Fig. 3.32). The latter one is accompanied by several minor species. It was not possible to remove them by preparative HPLC. The peak at 6.21 min is assigned to the injection peak. The identity of the main product at R_t = 21.54 min was established by positive mode ESI mass spectrometry. It shows two signals at 726.37 and 1429.75 which are assigned to $[M+H+Na]^{2+}$ and $[M+H]^{+}$ respectively.

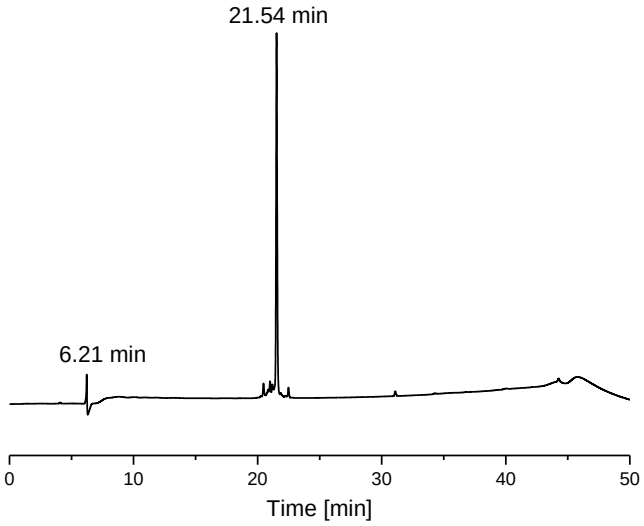

Fig. 3.32: HPLC trace at 220 nm of peptide **24**.

3.3 Analytical methods for peptide characterization on nanoparticle surfaces

3.3.1 Synthesis of azide-functionalized silica nanoparticles

Azide-functionalized silica nanoparticles (**25**) are synthesized according to the *Stöber* process.[40] Thus, tetraothosilicate (TEOS), the surfactant benzethonium chloride, (3-azidopropyl)triethylsilane and sodium hydroxide were mixed in water and stirred for 24 h. By addition of methanol, a white precipitate was obtained. It was washed and dried in vacuum to yield the product as a white solid.[44] The ATR IR spectrum of the material shows a weak signal at 2105 cm^{-1} and an intense, broad signal at 1064 cm^{-1} (Fig. 3.33).

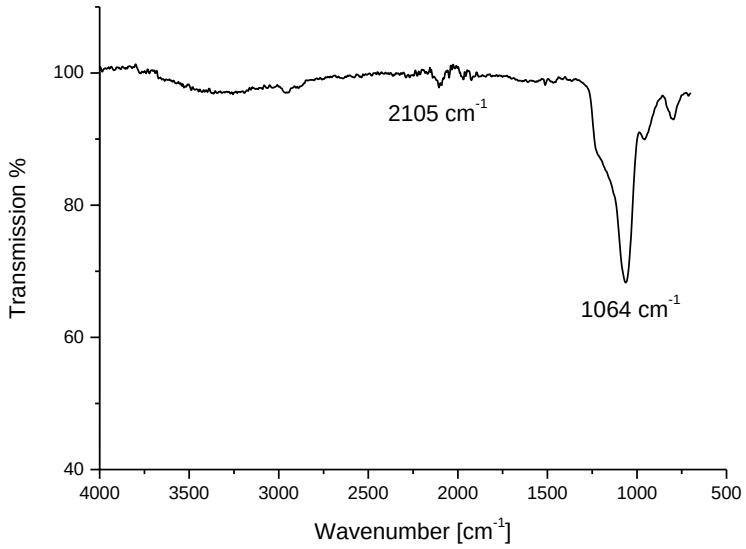

Fig 3.33: ATR IR spectrum of azide-functionalized silica nanoparticles (**25**).

The signal at 2105 cm^{-1} is assigned to the stretching vibration of the azide. However, the signal is weak, indicating a low surface loading. The signal at 1064 cm^{-1} is due to the Si-O stretching vibration. A qualitative demonstration for the presence of the azide groups on the surface was performed using the *Kaiser* test.[195] Thus, material **25** is treated with sodium boron hydride in anhydrous methanol to reduce the azide groups to primary amines (**25a**). Subsequently, ninhydrine (**26**) was added to form Schiff bases. Upon elimination of water, aminoninhydrine (**30**) is formed, dimerising with another molecule of **26** to *Ruhemann's* blue (**31**) (Fig. 3.34) During the Kaiser test, the boronhydride-reduced silica particles (**25a**) turn blue, showing the presence of amino groups.(Fig. 3.35).

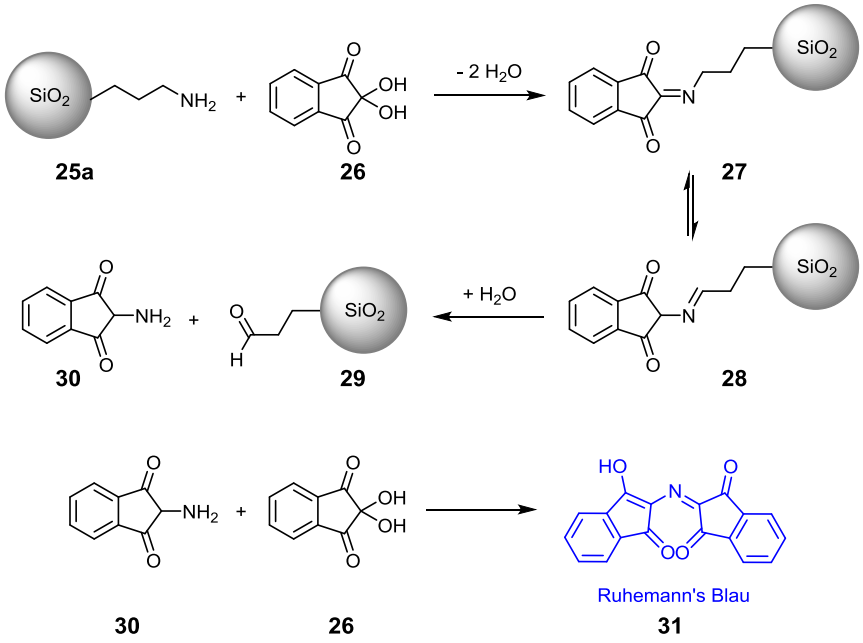

Fig. 3.34: Formation of *Ruhemann's* blue (**31**) during the Kaiser test with primary amines presented on a silica nanoparticle surface.

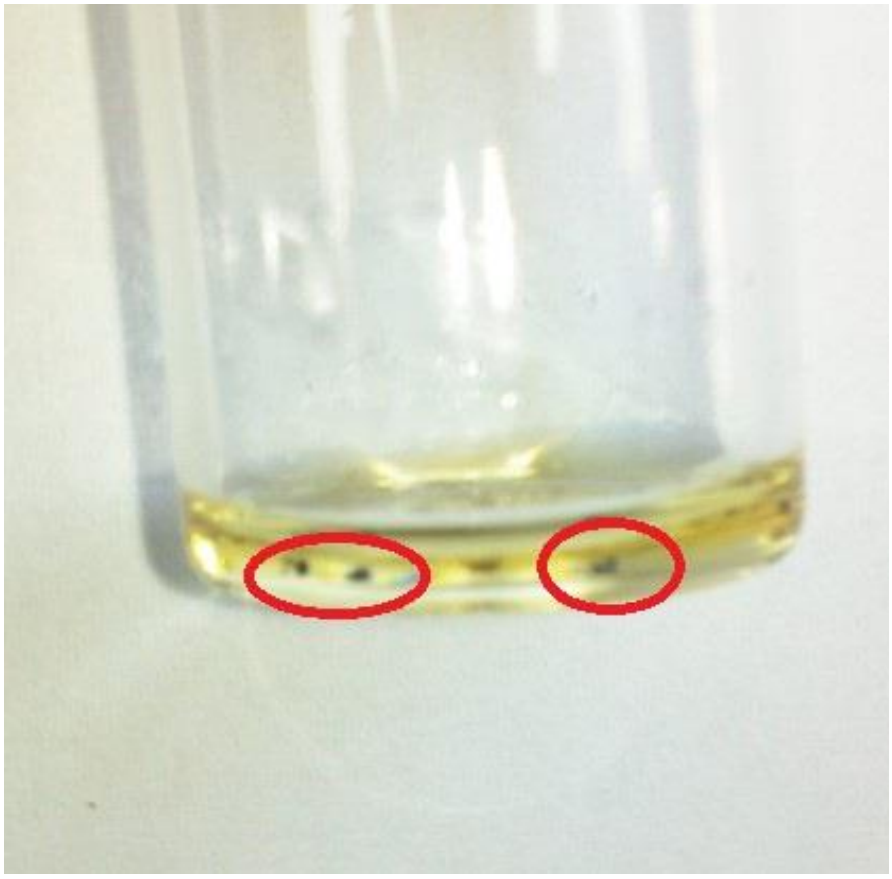

Fig. 3.35: Suspension of boronhydride-reduced azide-functionalized silica nanoparticles in a mixture of ninhydrine, phenol and pyridine in ethanol according to *Kaiser* test protocol.[195] The blue particle agglomerates are marked with red circles.

For hrSEM, the azide-functionalized silica nanoparticles were suspended in ethanol. One single drop of the suspension was applied on a carbon grid and it was dried by exposure to the air. Then, the grid was introduced into the electron microscope and images were recorded showing white, spherical particles (Fig. 3.36). Using the hrSEM images, the main particle size distribution was determined, ranging from 40 to 60 nm, with an average size of 48.2 nm (Fig. 3.37).

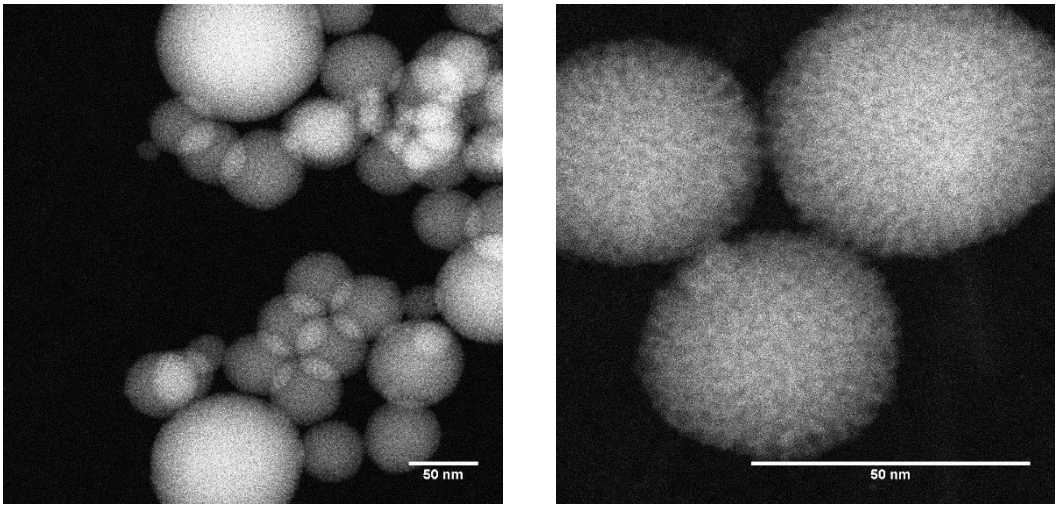

Fig. 3.36: hrSEM of azide-functionalized silica nanoparticles (**23**) in two different magnifications.

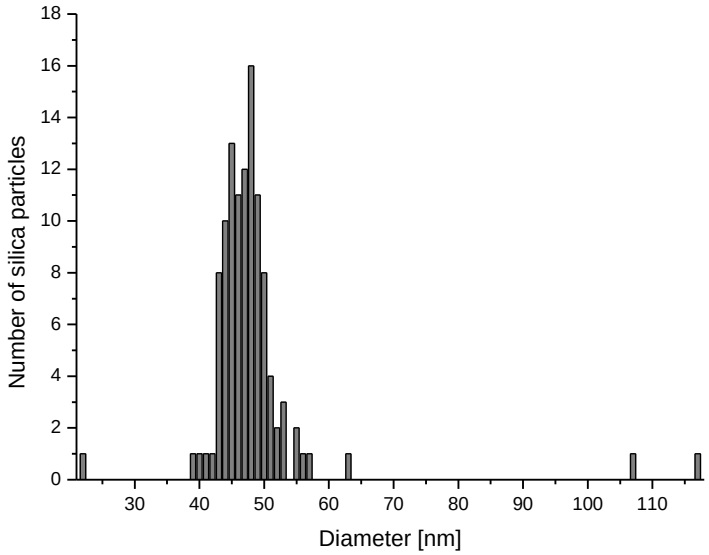

Fig. 3.37: Size distribution of **25**. The average size is 48.2 nm. N = 110.

3.3.2 Determination of surface loading of azide-functionalized silica nanoparticle

In SPPS, the α-amino groups are protected by Fmoc. During deprotection, piperidine deprotonates the fluorine ring to generate a cyclopentadiene-like intermediate. This further reacts to form dibenzofulvene, which is scavenged by piperidine (Fig. 3.38). Dibenzofulvene as well as the dibenzofulvene piperidine adduct absorb UV light strongly. This allows monitoring of the deprotection process and determination of the amount of amines.[137]

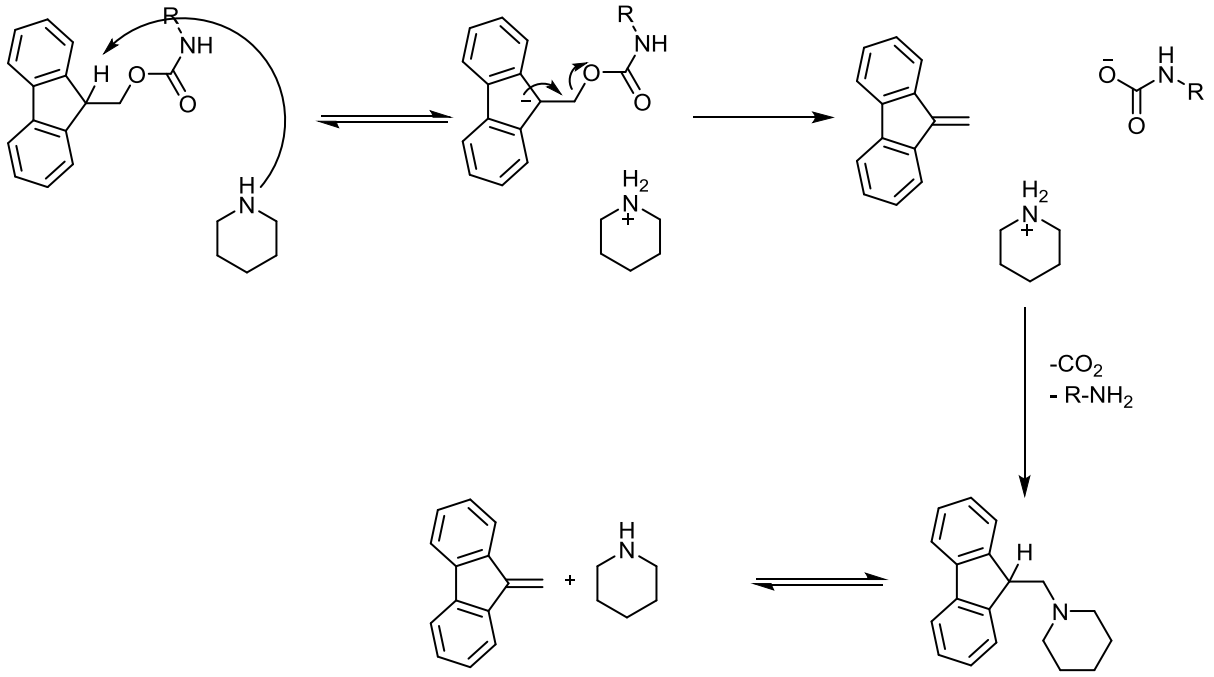

Fig 3.38: Mechanism of Fmoc deprotection. The dibenzofulvene and dibenzofulvene piperidine adduct have a very high UV absorption.

Utilizing this reaction for nanoparticles might allow indirect determination of azide surface loading. Thus, the azide-functionalized silica nanoparticles (**25**) were first reduced with sodium boronhydride to generate amine-functionalized silica nanoparticles (**25a**). Then, they were reacted with Fmoc-Rink Amide linker (**25b**) according to SPPS protocol to yield Fmoc-Rink Amide linker-functionalized silica nanoparticles (**25c**) (Fig. 3.39)[137, 139-140] The ATR IR spectrum of **25c** shows signals at 2105, 1659 and 1056 cm^{-1}(Fig. 3.40). The signal at 2105 cm^{-1} is assigned to the stretching vibrations of the azide groups, which are inaccessible to boronhydride reduction. The signal at 1659 cm^{-1} is assigned as the stretching vibrations of the two amide bonds of the Fmoc Rink Amide linker, while the signal at 1056 cm^{-1} is assigned to the stretching vibrations of the Si-O bonds.

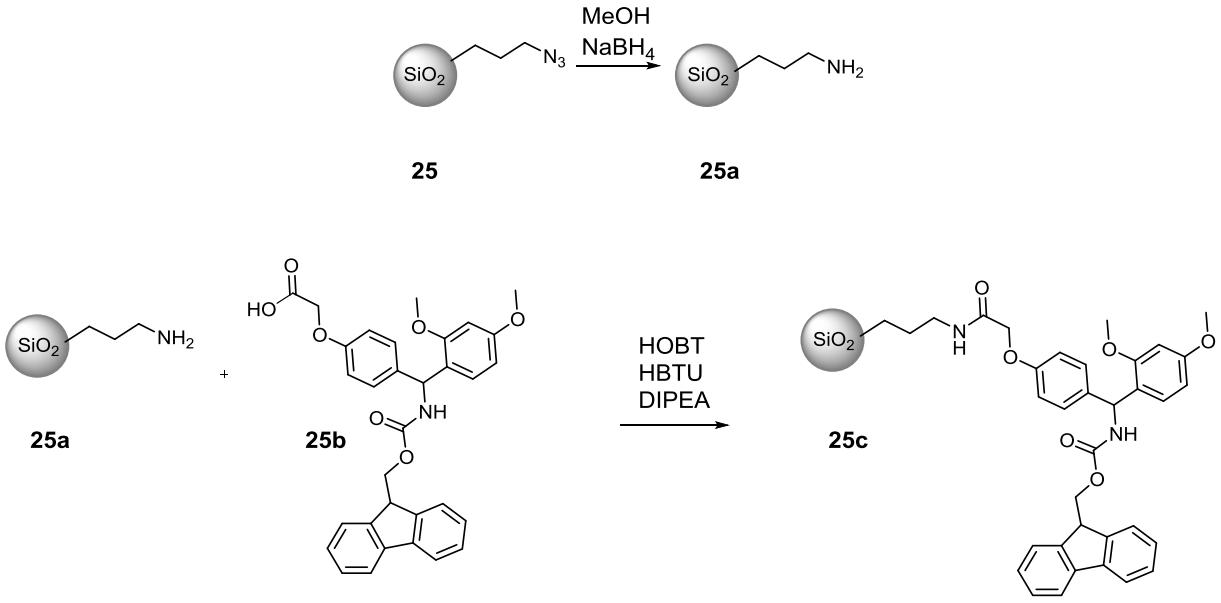

Fig 3.39: Reduction of **25** with sodium boronhydride to amine-functionalized silica nanoparticles (**25a**) and subsequent conjugation with Fmoc Rink Amide linker (**25b**) according to SPPS protocol to yield **25c**.

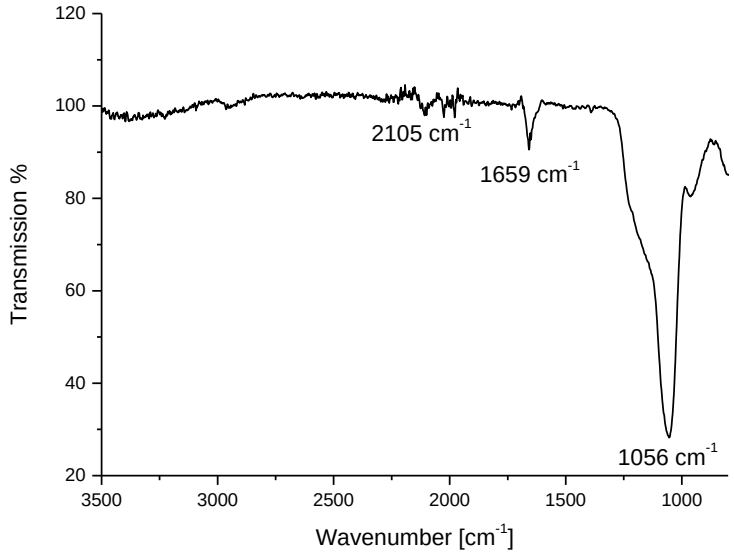

Fig. 3.40: ATR IR spectrum of Fmoc-Rink Amide linker-functionalized silica nanoparticles (**25c**).

For the determination of the azide surface loading, a calibration curve for the Fmoc deprotection had to be generated. Thus, commercially available Fmoc-Rink Amide MBHA resin with a surface loading of 0.68 mmol/g was used, since it has a great similarity to the Fmoc-Rink Amide silica nanoparticle (**23b**). For deprotection, the material was mixed with piperidine in DMF (30%, v/v) and shaken for 30 min. Then, the sample was centrifuged and the absorption of the supernatant, containing dibenzofulvene and dibenzofulvene piperidine adduct, at 301 nm was measured (Fig. 3.41).

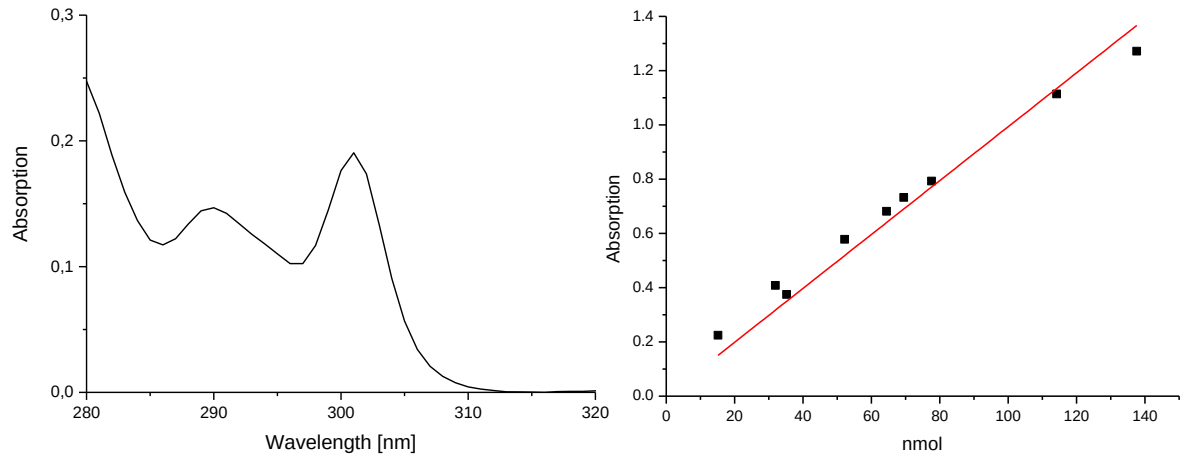

Fig. 3.41: Baseline-corrected UV/Vis spectrum of boronhydride-reduced azide-functionalized silica nanoparticle modified with Fmoc-Rink Amide linker and deprotected with a solution of piperidine in DMF (30%, v/v) (left). Calibration curve for determination of amine groups on the nanoparticle surface measured by UV/Vis spectroscopy at 301 nm (right).

Thus, a fixed amount of Fmoc-Rink Amide linker-functionalized silica nanoparticles were added to a solution of 30% piperidine in DMF, mixed, and centrifuged. A small amount of the supernatant was then diluted with 30% piperidine in DMF and the absorption at 301 nm was measured with a UV/Vis spectrometer. However, the spectra showed a baseline A < 0. Thus, the determined amine surface loading is considered be lower than the real loading. Using the calibration curve, the loading was then determined (Tab. 3.4)

Tab. 3.2: Determination of azide loading of reduced azide functionalised silica nanoparticles (**23**). The values were determined using a calibration curve shown in Fig.3.40. The fitting function is f(x) = 0.00933x.

m (particles) [mg]	**Absorption (λ_{301})**	**n [nmol]**	**surface loading azide [µmol/g]**
1.89	0.32	34.3	18.1
3.94	0.41	44.2	11.2
2.81	0.42	45.2	16.1
5.77	0.57	61.8	10.7

The average azide surface loading of the azide-functionalized silica nanoparticles (**25**) was determined as 14.0 ± 3.6 µmol/g. There is only little literature concerning about the surface loading of functional groups on nanoparticle surfaces. Mostly, the loading of adsorbed or encapsulated functional molecules on mesoporous nanoparticles is determined by their release

from the material, using inherent fluorescence or catalytic activity of the functional molecules.[196-197] The group of *Schatzschneider* et al. assessed the loading of the metal complex $[Mn(CO)_3(tpm)]^+$ attached via copper(I)-catalysed 1,3-dipolar azide-alkyne cycloaddition to the silica particle surface using data from CHN analysis and atom absorption spectrometry (AAS). Thus, the total azide loading was determined as 410 µmol/g and the $[Mn(CO)3(tpm)]^+$ surface loading was determined as approximately 90 µmol/g.[44] Comparing both approaches, the data correspond in the range of surface loading with each other.

3.3.3 Peptide analysis on nanoparticle surface utilizing *Pauly* reaction

3.3.3.1 *Pauly* reaction of tyrosine, phenylalanine, and glycine

The *Pauly* reaction is sensitive for tyrosine and histidine residues in proteins and peptides and was developed and patented in 1904.[198] It is based on the covalent modification of the aromatic ring of tyrosine and histidine by diazo sulfanilic acid, resulting in formation of an azo dye with deep red colour and an absorption maximum at about 485 nm (Fig. 3.42).

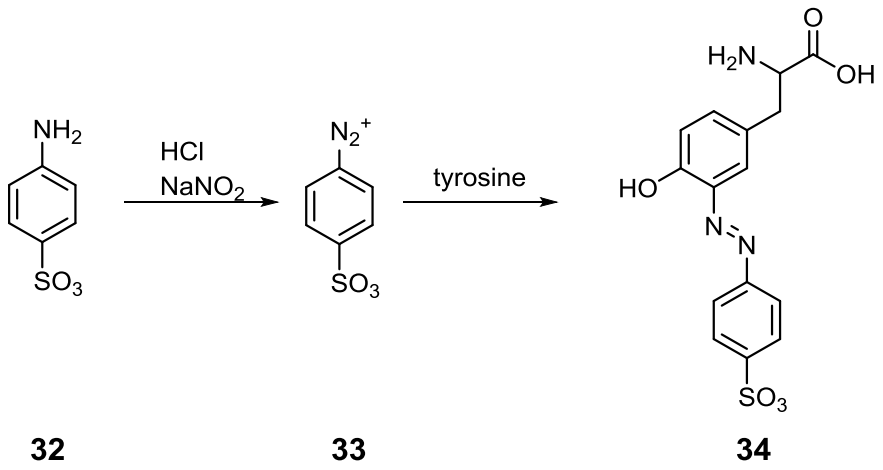

Fig. 3.42: Reaction of sulfanilic acid (**32**) with sodium nitrate in acidic solution leads to diazo sulfanilic acid (**33**) which reacts with tyrosine to azotyrosine (**34**).

The neuropeptide hormone ALST1 with the sequence APSGAQRLYGFGL contains two aromatic amino acid residues, tyrosine (Y) and phenylalanine (F). Only tyrosine is able to react with diazo sulfanilic acid. As an initial test, glycine, serving as a non-aromatic negative control, phenylalanine serving as an aromatic negative control, and tyrosine serving as a positive control were reacted with diazo sulfanilic acid according to *Pauly* reaction protocol. The resulting azo dye was then quantified by UV/Vis spectroscopy. The reaction of glycine with diazo sulfanilic acid leads to a product with strong absorption s at 270, 360, and 394 nm, but no significant absorption around 500 nm even when very high concentrations of the reagents are used. The

solution appears yellow in colour. The absorptions are assigned to unreacted sulfanilic acid, the diazo sulfanilic acid and some other unknown reaction product. Phenylalanine gave identical results. However, the tyrosine solution resulted in a deep red colour upon treatment with sulfanilic acid, showing absorption at 485 nm. This signal is assigned to azotyrosine (Fig. 3.43). However, when the amount of added tyrosine is plotted against the absorption of azotyrosine at 485 nm, a sigmoidal curve is obtained. (Fig. 3.44).

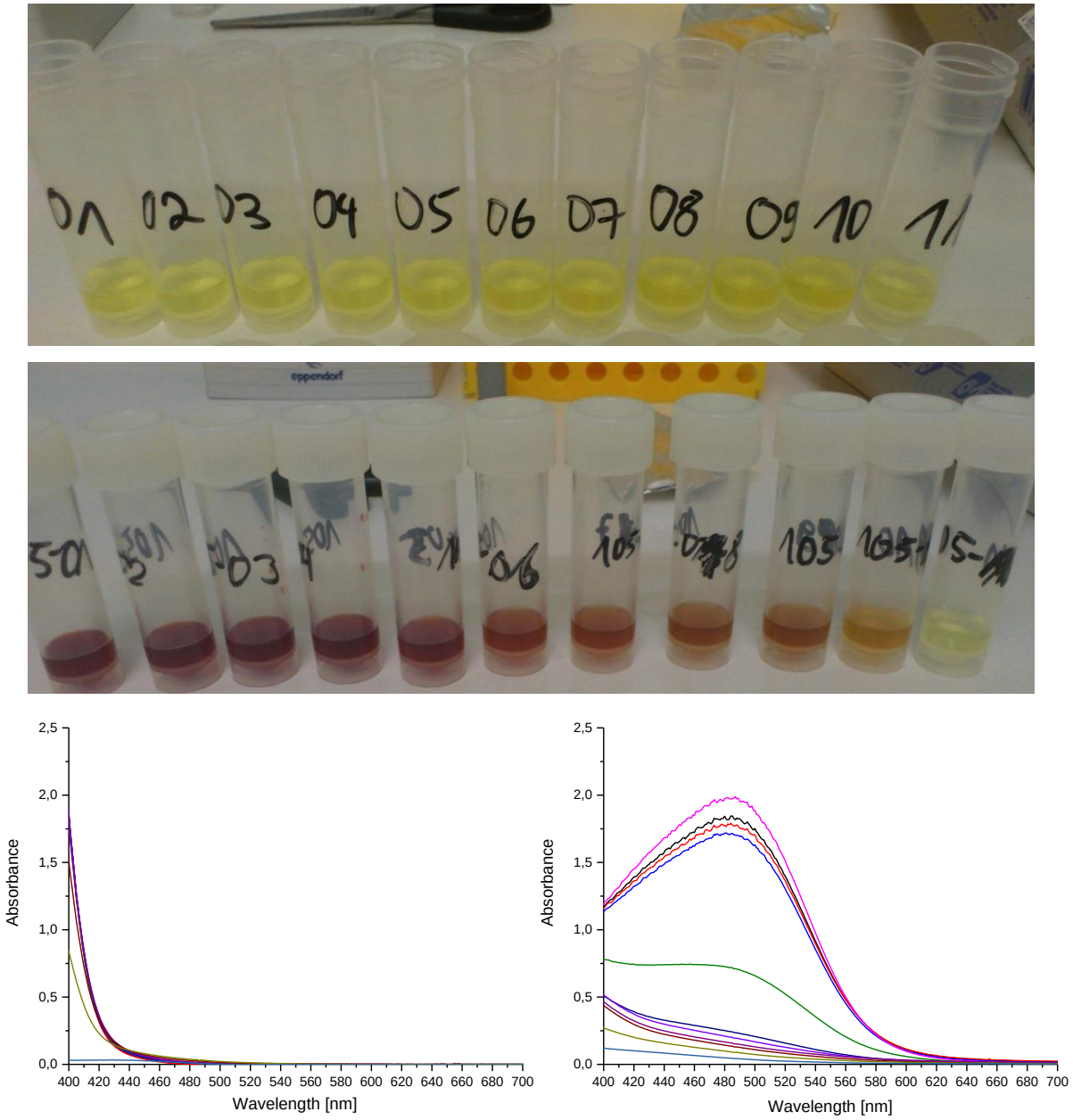

Fig. 3.43: Top: glycine/phenylalanine react with diazo sulfanilic acid to a yellow solution, regardless of amino acid concentration, 1 mg/ml (01) – 0 mg/ml (11) in 0.1 mg/ml steps. Middle: tyrosine reacts with diazo sulfanilic acid to a red solution. Colour intensity depends on the tyrosine concentration, 1 mg/ml (01) – 0 mg/ml (11) in 0.1 mg/ml steps. Left graph: change in absorption of solution in *Pauly* reaction upon increasing glycine/phenylalanine concentration. Right graph: change in absorption of solution in *Pauly* reaction upon increasing tyrosine concentration.

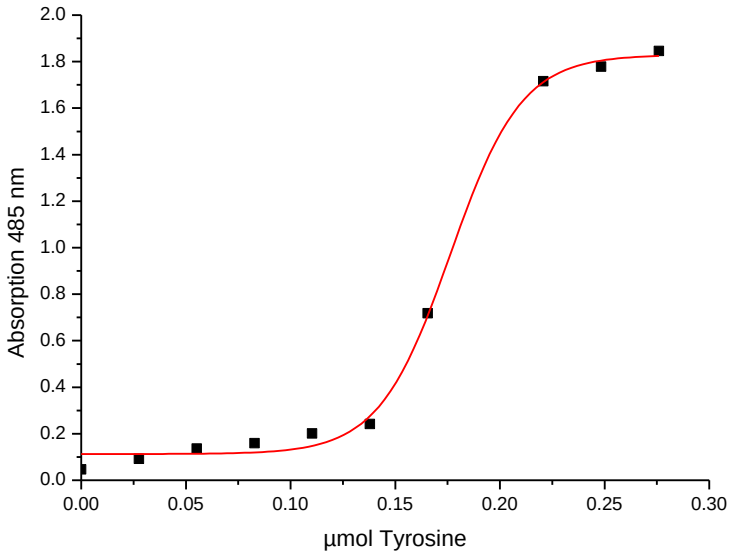

Fig. 3.44: Change of absorption at 485 nm with increasing amount of tyrosine used in *Pauly* reaction.

During the *Pauly* reaction, the amount of sodium nitrate, sulfanilic acid, and sodium carbonate added to the tyrosine solution was kept constant, only the amount of tyrosine was varied in the range of 0 to 30 µmol. However, the absorption of azotyrosine is pH-sensitive, since the tyrosine OH group has a pK_s value of 10.4. In *Pauly* reaction conditions at low tyrosine concentration, the OH group is deprotonated leading to a decrease in absorption of azotyrosine. With increasing tyrosine concentration the pH value of the solution decreases due to the carboxylic group of the amino acid, shifting the OH group to the protonated form and increasing the absorption of azotyrosine.[199]

3.3.3.2 *Pauly* reaction of ALST1 and related model peptides

To investigate the potential detection of tyrosine-containing peptides in aqueous solution by *Pauly* reaction, four model hexapeptides were prepared based on the *C*-terminal sequence of ALST1 (Fig. 3.45). In the first sequence, hexynoic acid-LYGFGL^{NH2} (**24a**), both phenylalanine and tyrosine are incorporated. It will serve as a positive control. In the second sequence, hexynoic acid-LYGGGL^{NH2} (**24b**), phenylalanine was replaced by glycine. It acts as a positive control to investigate potential effects of phenylalanine during *Pauly* reaction. The third sequence, hexynoic acid-LGGFGL^{NH2} (**24c**), tyrosine was replaced by glycine. It acts as a negative control. The fourth sequence is hexynoic acid-LTGVGL^{NH2} (**24d**). Here, tyrosine was replaced by threonine and phenylalanine was replaced by valine. This became necessary since all attempts to replace both tyrosine and phenylalanine by glycine failed, since accumulation of

non-polar amino acids causes problems with sequence assembly due to aggregation.[137-138, 140] The model peptides were synthesized by manual SPPS, purified by HPLC, and characterized by HPLC and ESI mass spectrometry. The data is summarized in Tab. 3.3.

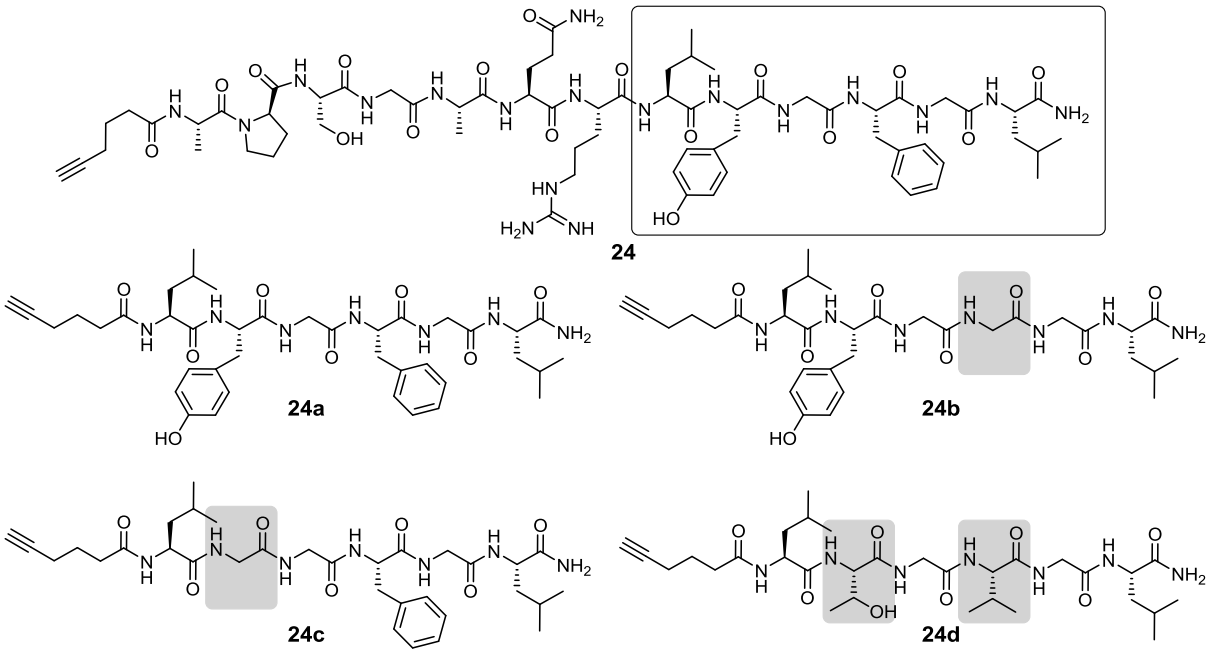

Fig. 3.45: The sequence of hexynoic acid-ALST1 (**24**) and the *C*-terminal model hexapeptides.

Tab 3.3: Analytical data and characterization of ALST1 model hexapeptides **24a**, **24b**, **24c**, and **24d**.

Sequence	**R_t [min]**	**R_f**	**ESI^+ (*m/z*)**	**Assignment**
Hexynoic acid-LYGFGL^{NH2} (**24a**)	25.46	3.62	784.40	$[M+Na]^+$
			1545.81	$[2M+Na]^+$
Hexynoic acid-LYGGGL^{NH2} (**24b**)	21,77	2.90	694.35	$[M+Na]^+$
			1365.72	$[2M+Na]^+$
Hexynoic acid-LGGFGL^{NH2} (**24c**)	30.89	4.05	678.36	$[M+Na]^+$
			1333.72	$[2M+Na]^+$
Hexynoic acid-LTGVGL^{NH2} (**24d**)	33.17	4.44	674.38	$[M+Na]^+$
			1325.77	$[2M+Na]^+$

Upon treatment of **24a** with sulfanilic acid and sodium nitrate according to the *Pauly* reaction protocol, the colour of the solution changes from colourless to deep orange. The UV/Vis spectrum of the product has absorptions at 435 and 485 nm which are due to azotyrosine (Fig 3.46). When the amount of added **24a** is plotted against the absorption of azotyrosine at 435 nm, a linear curve is obtained (3.47).

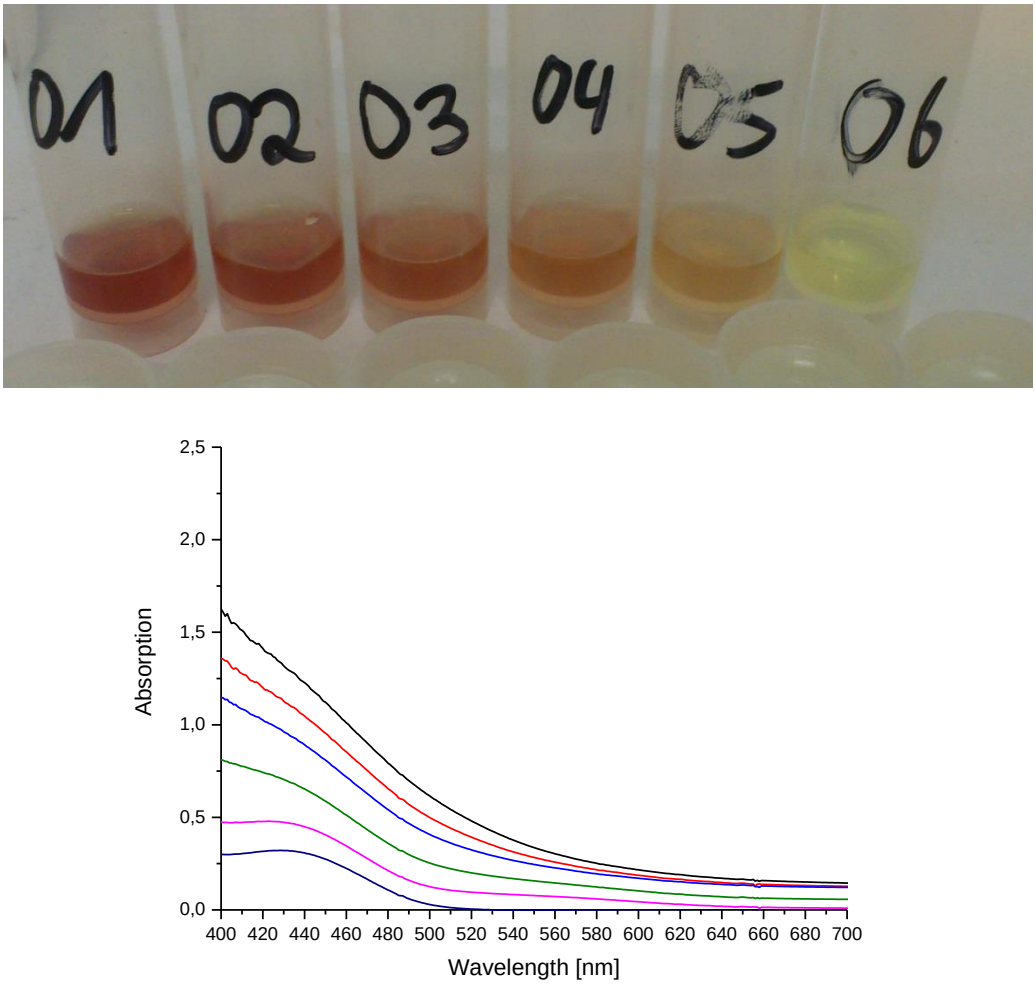

Fig. 3.46: Top: **24a** reacts with diazo sulfanilic acid to from a colourless to a red solution. The colour intensity changes upon the used concentration of **24a** from 0.5 mg/ml (01) to 0 mg/ml (06) in 0.1 mg/ml steps. Graph: change in absorption of solution in *Pauly* reaction upon increasing **24a** concentration.

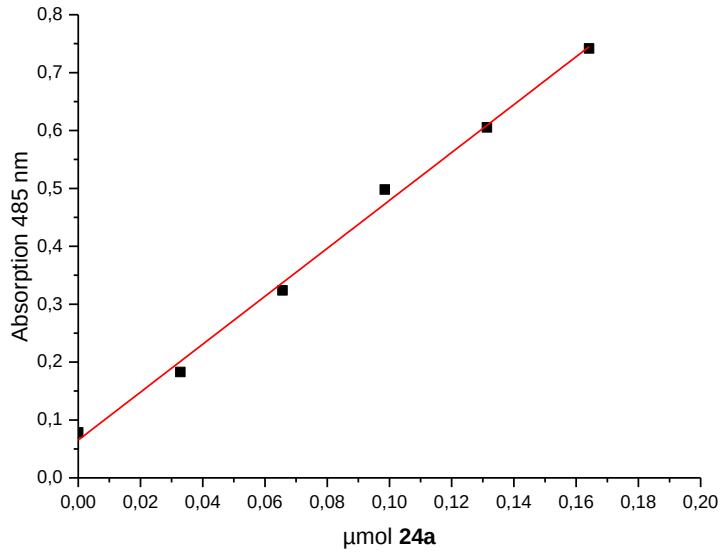

Fig. 3.47: Change of absorption at 435 nm with increasing concentration of **24a** in the *Pauly* reaction. The amount of substance of **24a** is plotted against the absorption at 435 nm.

Upon treatment of **24b** and **24** with sodium nitrate and sulfanilic acid according to the Pauly protocol, the solutions turned from colourless to orange-red, identically to **24a** discussed before (see Chapter 7). Upon treatment of **24c** with sodium nitrate and sulfanilic acid according to the *Pauly* protocol, the solutions turned from colourless to yellow (Fig.3.48). When the amount of added **24c** is plotted against the absorption of azotyrosine at 435 nm, a linear curve is obtained (Fig. 3.49). Upon treatment of **24d** with sodium nitrate and sulfanilic acid according to the *Pauly* protocol, the solutions turned also from colourless to yellow, identically to **24c** discussed before (see Chapter 7).

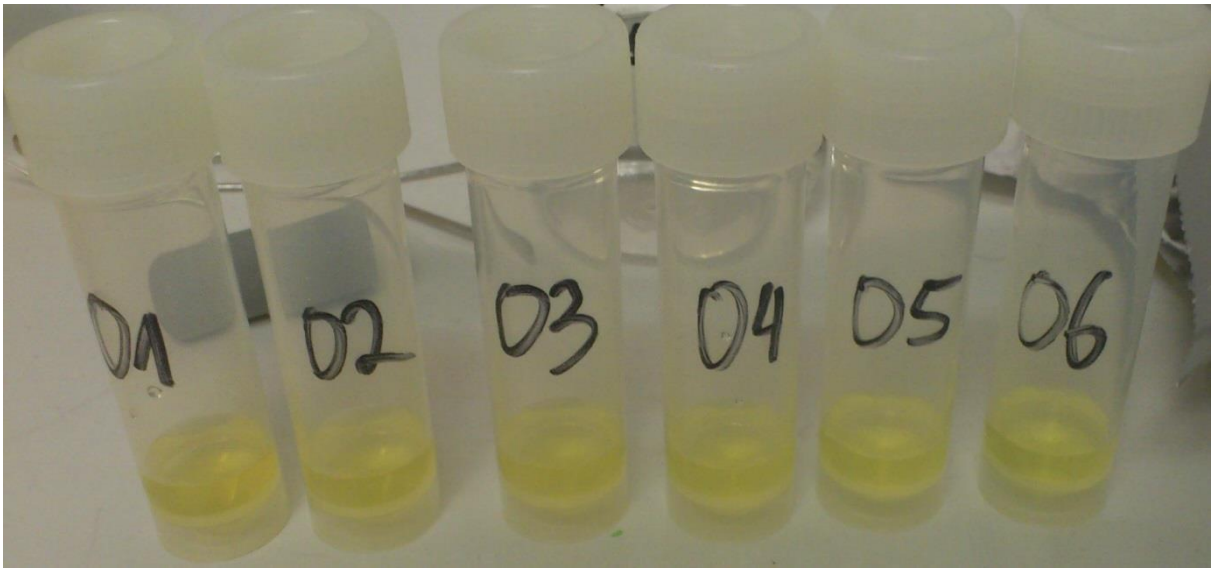

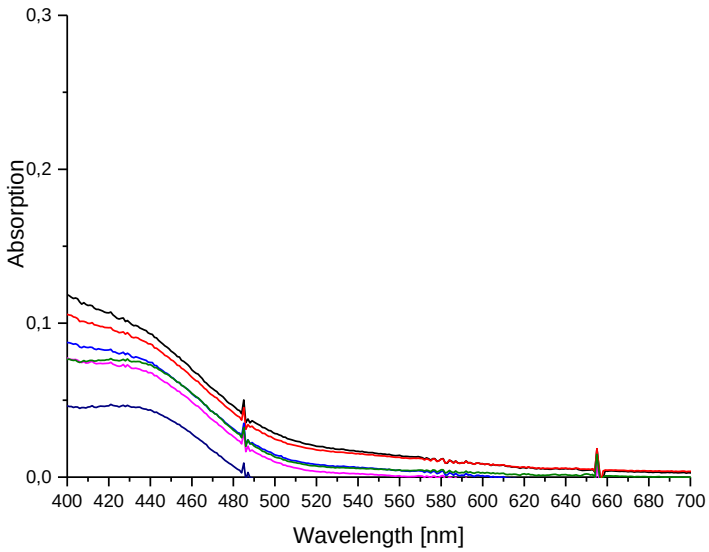

Fig. 3.48: Top: **24c** reacts with diazo sulfanilic acid to from a colourless to a yellow solution. The colour intensity does not change in dependence of used concentrations of **24c** from 0.5 mg/ml (01) to 0 mg/ml (06) in 0.1 mg/ml steps. Graph: change in absorption of solution in *Pauly* reaction upon increasing **24c** concentration.

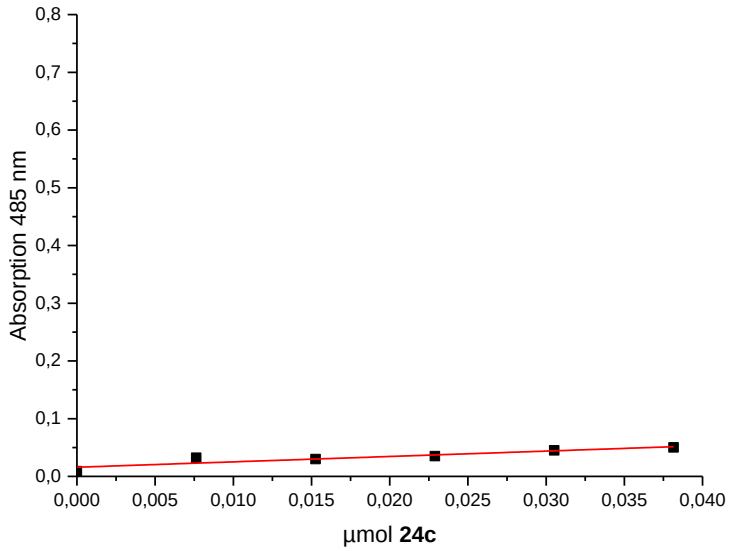

Fig. 3.49: Change of absorption at 435 nm with increasing concentration of **24c** in the *Pauly* reaction. The amount of substance of **24c** is plotted against the absorption at 435 nm.

Using the calibration curve for tyrosine shown in Figure 3.44, it should be possible to determine the concentration of tyrosine-containing peptides by the *Pauly* reaction and UV/Vis spectroscopy. However, comparing the calibration curve of tyrosine in the range of 0 to 2.75 µmol with the calibration curves of peptides **24**, **24a**, and **24b** shows that this is not the case (Tab. 3.4).

Tab. 3.4: Comparison of the *Pauly* reaction calibration curves of tyrosine, and peptides **24**, **24a**, **24b**, **24c**, and **24d**. The interception point with the y-axis is y(0). The slope of the curve is b.

Sequence	**y(0)**	**b [µmol]**
Tyrosine (0 µmol - 2.75 µmol)	0.051 ± 0.004	1.371 ± 0.051
ALST1 hexynoic acid conjugate (**24**)	0.059 ± 0.010	4.859 ± 0.271
Hexynoic acid-LYGFGL^{NH2} (**24a**)	0.065 ± 0.013	4.139 ± 0.134
Hexynoic acid-LYGGGL^{NH2} (**24b**)	0.025 ± 0.002	5.260 ± 0.401
Hexynoic acid-LGGFGL^{NH2} (**24c**)	0.016 ± 0.004	0.932 ± 0.185
Hexynoic acid-LTGVGL^{NH2} (**24d**)	0.021 ± 0.001	0.512 ± 0.046

For using the calibration curve of tyrosine to determine the concentration of tyrosine-containing peptides by the *Pauly* reaction and UV/Vis spectroscopy, their calibration curves should be identical and therefore have matching intersection points with the y-axis y(0) and

slopes b. The calibration curves for tyrosine and peptides **24**, and **24a** have similar y(0) ranging from 0.05 to 0.065, but different slopes with 1.371 for tyrosine and 4.859 for **24** and 4.139 for **24a**. Thus, it is not possible to determine the concentration of **24** and **24a** with the calibration curve of tyrosine, since the calibration curves do not match. The calibration curve of **24b** shows a lesser y(0) with 0.025 and a higher b with 5.260 than the tyrosine calibration curve. Thus, it is also not possible to determine the concentration of **24b** using the calibration curve of tyrosine. The tyrosine-free peptides **24c** and **24d** show in their calibration curves y(0) about 0.02 and a slope < 1. The effectivity of the *Pauly* reaction depends on the accessibility of tyrosine and thus on the peptide sequence it is incorporated in. Due to this, it is not possible to use a calibration curve of tyrosine for quantitative determination of the concentrations of tyrosine-containing peptides, but a calibration curve for each individual peptide is required.[199]

3.3.3.3 *Pauly* reaction of ALST1- and related model peptide-functionalized silica nanoparticles

The peptides ALST1, LYGFGL^{NH2}, LYGGGL^{NH2}, LGGFGL^{NH2}, and LTGVGL^{NH2} were conjugated to azide-functionalized silica nanoparticles (**25**) using the copper(I)-catalysed 1,3-dipolar cycloaddition of azides and terminal alkynes (CuAAC). During the reaction, 1,2,3-triazoles linkages are formed.[200-201] TBTA was used in the reaction to stabilizes Cu(I) during the reaction.[202-204] Azide functionalized silica particles were shaken for 2 d with a solution of hexynoic acid-functionalized peptide, Cu(I), and TBTA in degassed triethylamine (TEA) to yield the product as a white powder (Fig. 3.50, Fig. 3.51).

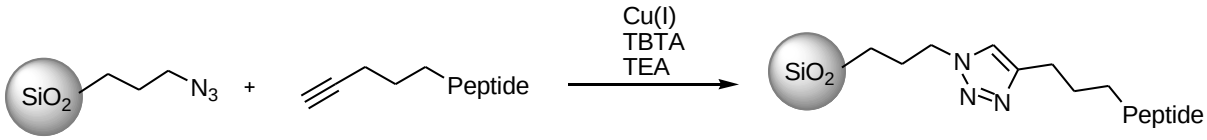

Fig. 3.50: Conjugation of hexynoic acid-functionalized peptide with azide functionalized silica nanoparticle utilizing the copper(I)-catalysed 1,3-dipolar cycloaddition of azides and terminal alkynes. For stabilisation of copper(I), TBTA was used.

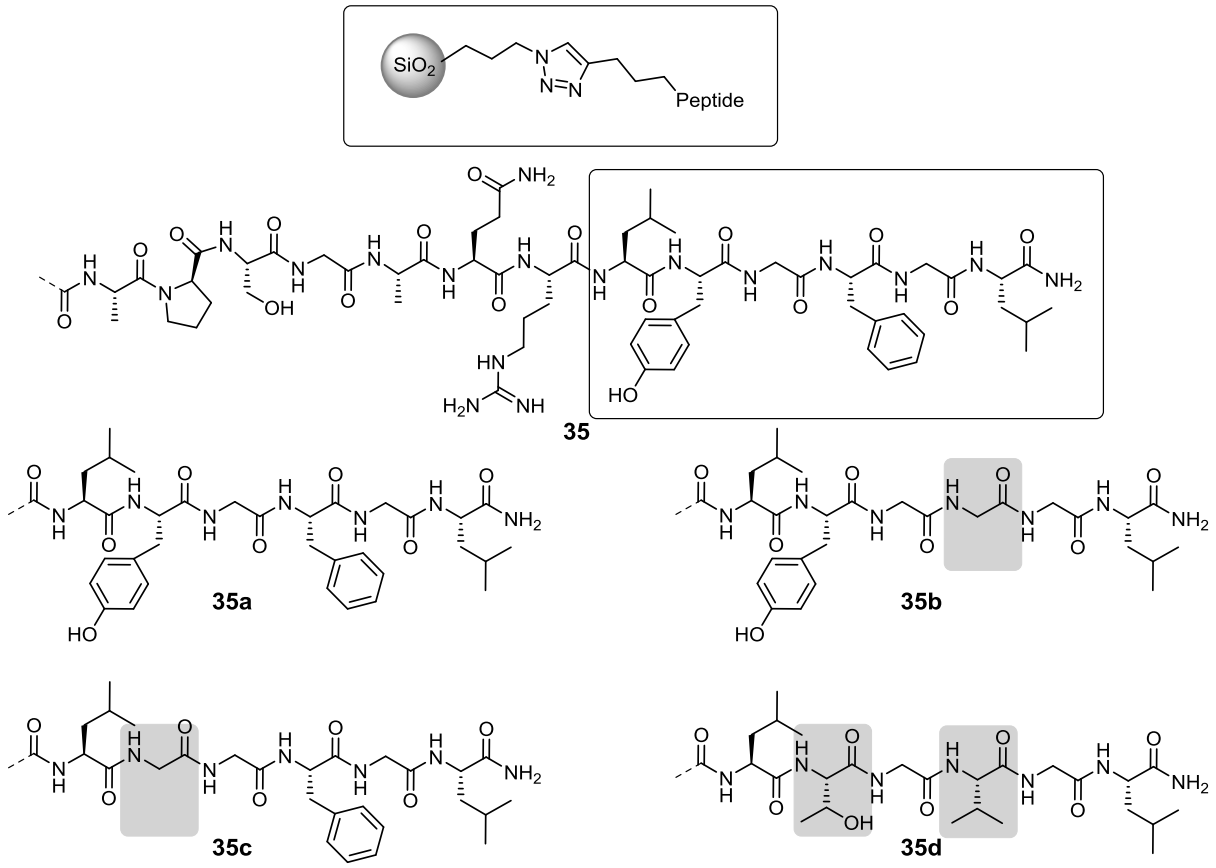

Fig. 3.51: Peptide functionalized silica nanoparticles via copper(I)-catalysed 1,3-dipolar cycloaddition of azides and terminal alkynes.

The peptide-functionalized nanoparticles show signals at 2956, 2892, 2099 cm, as well as a number of weak signals in the range of 1662 cm^{-1} to 1462 cm^{-1}. Furthermore, a very strong signal at 1046 cm^{-1} is observed (Fig. 3.52). These peaks are found for all five materials (**35**, **35a**, **35b**, **35c**, and **35d**).

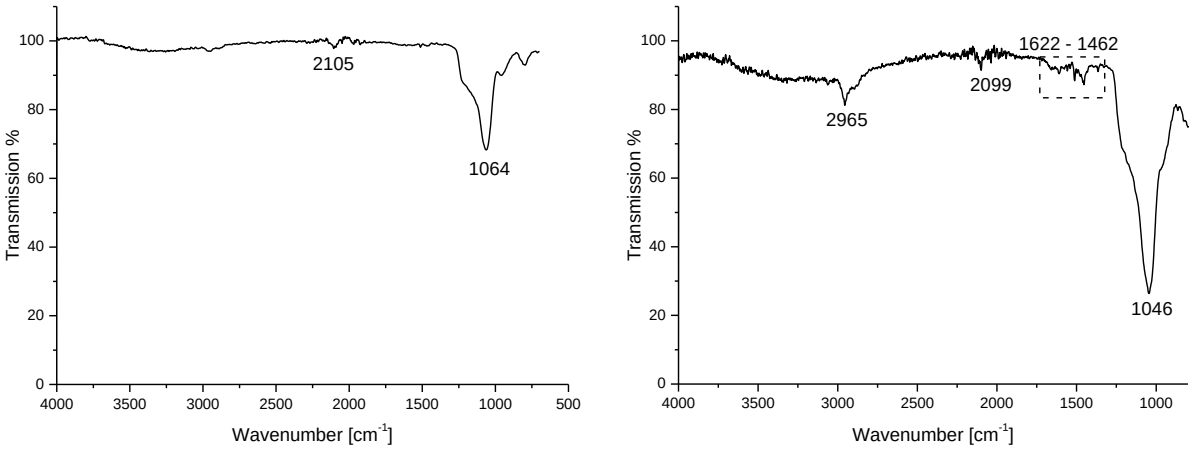

Fig. 3.52: ATR IR spectrum of azide-functionalised silica nanoparticle (**35**) (left) in comparison to peptide-functionalized silica nanoparticle (**35a**, **35b**, **35c**, and **35d**) (right).

The signals at 2956 and 2892 cm^{-1} are assigned to the C-H and C-C stretching vibrations of the peptide. The signal at 2099 cm^{-1} is assigned to inaccessible azide groups in the particle core. The signals at 1662 to 1462 cm^{-1} are assigned to the stretching vibrations of peptide amide bonds and deformation vibrations of methylene groups in the peptide side chains. CHN analysis of the peptide-functionalised silica nanoparticles show increased amount of carbon, hydrogen, and nitrogen in comparison to the azide-functionalised silica nanoparticles (Tab. 3.5).

Tab. 3.5: CHN analysis data for azide-functionalized silica nanoparticles (**25**) and peptide-functionalized silica nanoparticles.

Compound	**C-%**	**H-%**	**N-%**
25	15.43	2.97	1.87
35	24.70	4.08	2.23
35a	27.90	4.06	4.91
35b	25.62	4.00	2.96
35c	30.15	4.04	6.07
35d	25.80	3.81	2.14

The peptide-functionalized silica nanoparticles show an average difference ΔC-% of 11.40, ΔH-% of 1.02, and ΔN-% of 1.79 in comparison to the azide functionalized silica nanoparticles, indication a successful conjugation of the peptide to the nanoparticle surface. TEM demonstrates, that conjugation with peptides according to copper(I)-catalysed 1,3-dipolar cycloaddition of azides and terminal alkynes had no influence on the particles spherical geometry and size (Fig. 3.53). All sample constructs show a particle sizes between 40 and 60 nm. Due to the recorded analogue pictures, an accurate measurement is however very difficult.

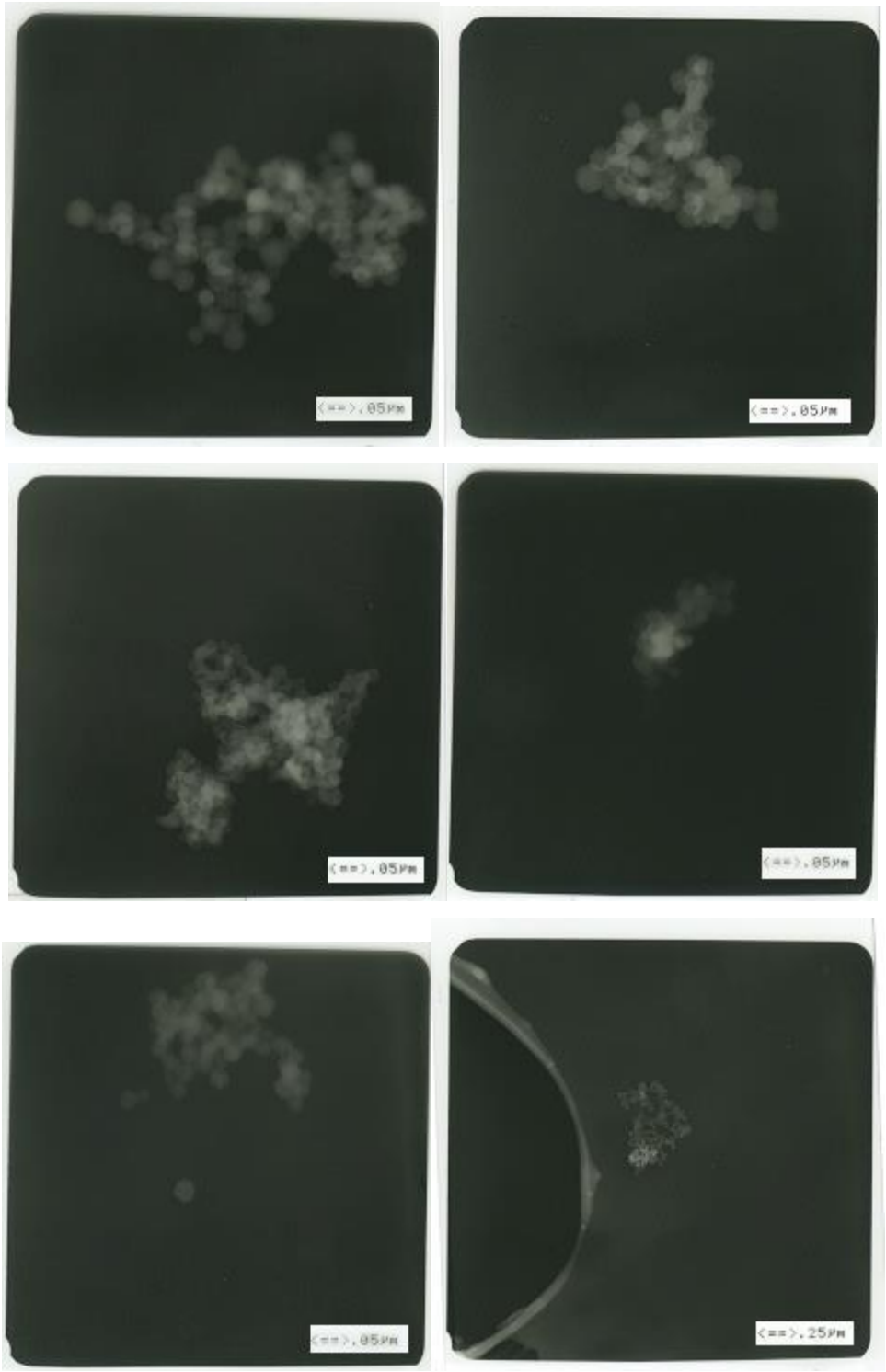

Fig: 3.53: TEM images of **25** (upper left), **35a** (upper right), **35b** (middle left), **35c** (middle right), **35d** (lower left), and **35** (lower right, particles can be observed next to TEM grid artifact).

Then, the peptide-functionalized silica nanoparticles were treated with sulfanilic acid and sodium nitrate according to the *Pauly* reaction protocol to investigate its applicability on these peptide-modified systems. Unfortunately, the particles formed no stable suspension, thus making UV/Vis spectroscopy impossible. Still, the tyrosine-containing peptide-functionalized

silica nanoparticle **35**, **35a**, and **35b** show a change in colour from white to red upon treatment with sulfanilic acid in acidic solution, while the tyrosine-free peptide-functionalized silica nanoparticles **35c** and **35d** show no change in colour (Fig.3.54). This indicates a successful conjugation of the peptides to the nanoparticle surface.

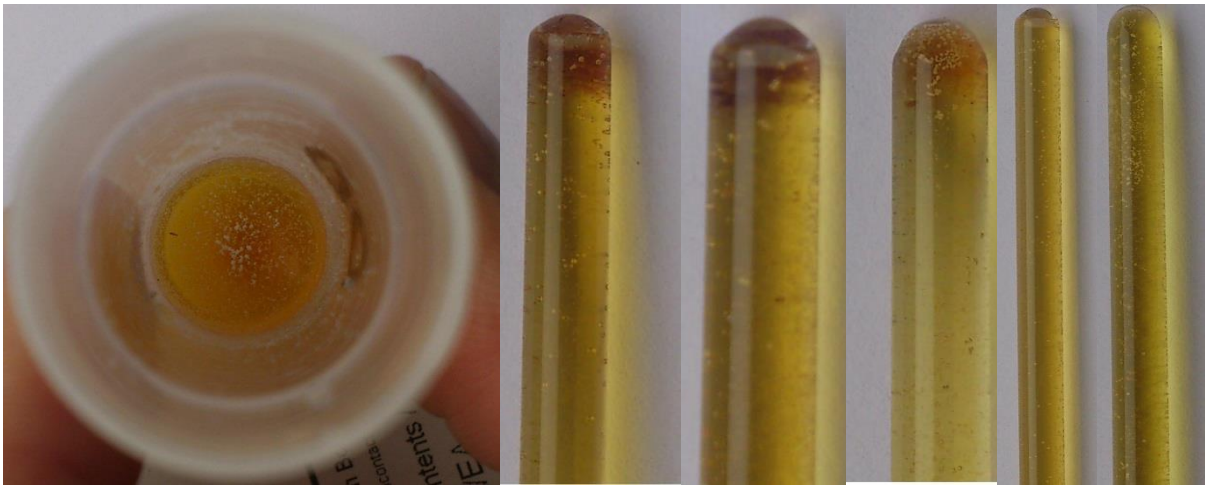

Fig. 3.54: Peptide-functionalized silica nanoparticles upon treatment according to the *Pauly* reaction protocol. The depict order (left to right) is: azide functionalized silica nanoparticles (**25**), **35** (SilicaNP-APSGAQRLYGFGL^{NH2}), **35a** (SilicaNP-LYGFGL ^{NH2}), **35b** (SilicaNP-LYGGGL ^{NH2}), **35c** (SilicaNP-LGGFGL ^{NH2}), and **35d** (SilicaNP-LTGVGL ^{NH2}).

3.3.4 Amino acid analysis of peptide-functionalized nanoparticles with HPLC

3.3.4.1 Amino acid analysis using HPLC

The analysis of the amino acid content of peptides by chromatographic methods is difficult, since most amino acids do not show large UV/Vis absorption. Thus, derivatization is necessary to detect and identify them properly. The first method established was based on the separation of amino acids by ion-exchange chromatography and post-column derivatization with ninhydrine.[205] However, with the development of potent reverse-phase HPLC techniques, the need for pre-column derivatization methods increased, leading to derivatization with dansyl chloride or *o*-phthaldialdehyde. Due to the strong UV absorption of these derivatives, a detection limit < 1 pmol has become possible. However, the derivatives suffered from poor stability and the inability to modify secondary amines. The derivatization with phenylisothiocyanate (PITC) avoids many of these problems, since it leads to quantitative phenylthiocarbamyl amino acid derivatives (Fig. 3.55).[206-207]

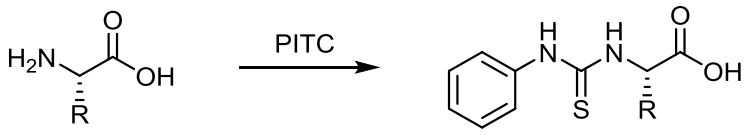

Fig. 3.55: Formation of phenylthiocarbamyl amino acid derivatives from PITC and a primary amino acid.

The phenylthiocarbamyl amino acid show a strong absorption at 254 nm with a detection limit of 1 pmol.[206] To establish a method for peptide analysis on functionalized nanoparticles, the R_t and R_f values of the amino acid building blocks in ALST1 and its model peptides (see chapter 3.3.3.2) were determined using a *Dionex Ultimate 3000* HPLC equipped with a ReproSil 100 C18 5 µm column. Thus, glycine, phenylalanine, tyrosine, alanine, serine, glutamic acid, proline, leucine, arginine, threonine, and valine were reacted with PITC and analysed by HPLC at 254 nm using the ramp gradient method defined in Chapter 5.1.2. Furthermore, the injected amount of phenylthiocarbamyl amino acid derivative was varied to construct calibration curves for the single amino acids. The results are summarized in Table 3.6. The individual phenylthiocarbamyl amino acid derivatives show in the linear calibration curves different slopes (Calibration factor [$nmol^{-1}$]. This is due to the variable extinction coefficients of the adducts.

Tab. 3.6: Retention times R_t, retention factors R_f and calibration factor of phenylthiocarbamyl amino acid derivatives measured by.

Amino acid	**R_t**	**R_f**	**calibration factor [$nmol^{-1}$]**
A	21.09	2.61	6.99
E	18.79	2.22	12.20
F	28.35	3.85	12.34
G	18.14	2.10	14.65
L	27.35	3.70	8.37
P	20.19	2.45	16.47
R	16.52	1.83	12.96
S	17.63	2.02	10.71
T	19.11	2.22	16.51
V	25.03	3.22	15.87
Y	23.48	3.02	6.62

3.4.4.2 Peptide analysis using HPLC

For peptide analysis, the amide bonds first need to be cleaved before derivatization by heating the peptide to 110 °C in 6 M hydrochloric acid for 24 h. Furthermore, during this process asparagine and glutamine are transformed to aspartic acid and glutamic acid.[205-208] Thus, ALST1 hexynoic acid conjugate (**24**) and its derivatives (**24a** - **24b**) were digested in concentrated hydrochloric acid at 110 °C and subsequently derivatized with PITC. The resulting

mixture of phenylthiocarbamyl amino acid derivatives was analysed by HPLC using the ramp gradient defined in Chapter 5.1.2 at 254 nm. For evaluation, the amounts of the amino acids were calculated using the calibration factors displayed in Table 3.6 and the absorption of the individual signals. Then, the values were normalized on the amino acid with the fewest amount, rounded to whole numbers, and compared to the expected amino acid ratio of the used peptide sequence. The HPLC trace at 254 nm of hexynoic acid-LYGFGL^{NH2} (**24a**) shows after digestion and derivatized with PITC eight signals (Fig. 3.56). The results are summarized in Table 3.7.

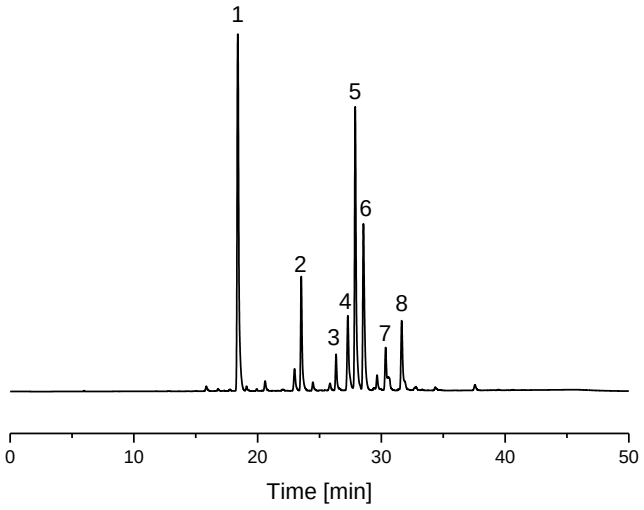

Fig. 3.56: HPLC trace at 254 nm of peptide **24a** after digestion with hydrochloric acid and derivatization with PITC.

Tab. 3.7: Summarized results of amino acid analysis by HPLC of peptide **24a**.

Peak	R_t [min]	R_f	Assignment [a]	Amount [nmol] [a]	Normalized [b]
1	18.39	2.11	glycine	332	2
2	23.58	2.99	tyrosine	193	1
3	26.32	3.45			
4	27.20	3.60			
5	27.82	3.71	leucine	405	2
6	28.53	3.83	phenylalanine	220	1
7	30.41	4.14			
8	31.60	4.34			

[a] assigned according to Table 3.6; [b] rounded values.

The amino acid analysis by HPLC of peptide **24a** shows a normalized amino acid ratio of 2:2:1:1 as it is expected for the sequence LYGFGL^{NH2}. The HPLC trace at 254 nm of hexynoic acid-LYGFGL^{NH2} (**24b**) shows after digestion and derivatized with PITC eight signals (Fig. 3.57). The results are summarized in Table 3.8.

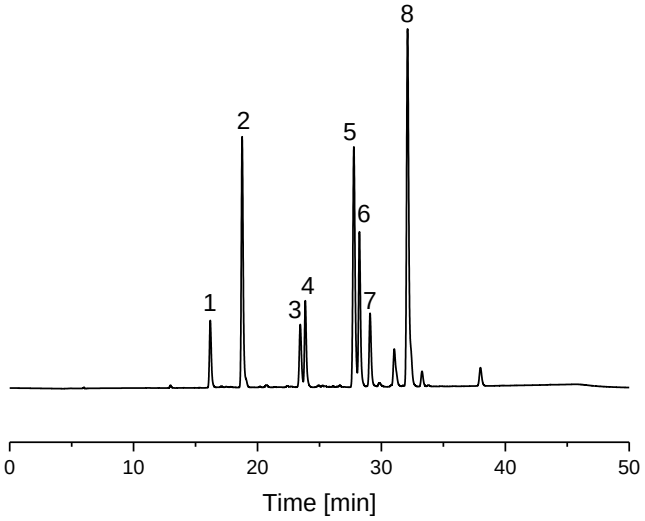

Fig. 3.57: HPLC trace at 254 nm of peptide **24b** after digestion with hydrochloric acid and derivatization with PITC.

Tab. 3.8: Summarized results of amino acid analysis by HPLC of peptide **24b**.

Peak	R_t [min]	R_f	Assignment [a]	Amount [nmol] [a]	Normalized [b]
1	16.09	1.68			
2	18.72	2.12	glycine	63	1
3	23.32	2.88			
4	23.82	2.96	tyrosine	68	
5	27.77	3.62			1
6	28.26	3.71	leucine	51	1
7	29.13	3.84	(phenylalanine)	(22)	
8	32.03	4.32			

[a] assigned and calculated according to Table 3.6; [b] rounded values.

The amino acid analysis by HPLC of peptide **24b** shows a normalized amino acid ratio of 1:1:1, but a ratio of 3:2:1 it is expected for the sequence LYGGGL^{NH2}. This result indicates an incomplete digestion, as the outer amino acid of the sequence leucine shows the highest amount of substance and the amino acids glycine and tyrosine show a much lesser amount of substance

than expected. Thus, signals 5 and 6 might be peptide fragments. Signal 7 is assigned to phenylalanine, which is not incorporated in peptide **24b**, and thus due to impurities. The HPLC trace at 254 nm of hexynoic acid-LGGFGL^{NH2} (**24c)** shows after digestion and derivatized with PITC six signals (Fig. 3.58). The results are summarized in Table 3.9.

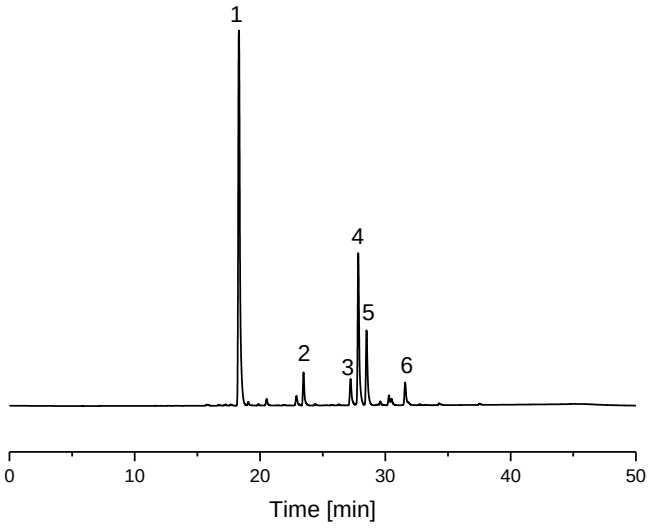

Fig. 3.58: HPLC trace at 254 nm of peptide **24c** after digestion with hydrochloric acid and derivatization with PITC.

Tab. 3.9: Summarized results of amino acid analysis by HPLC of peptide **24c**.

Peak	R_t [min]	R_f	Assignment [a]	Amount [nmol] [a]	Normalized [b]
1	18.31	2.12	glycine	301	3
2	23.49	3.00	(tyrosine)	(50)	
3	27.20	3.64			
4	27.84	3.74	leucine	198	2
5	28.53	3.86	phenylalanine	111	1
6	31.60	4.39			

[a] assigned and calculated according to Table 3.6; [b] rounded values.

The amino acid analysis by HPLC of peptide **24c** shows a normalized amino acid ratio of 3:2:1 as expected for the sequence LGGFGL^{NH2}. However, a tyrosine signal is observed which is assigned to impurities. The HPLC trace at 254 nm of hexynoic acid-LTGVGL^{NH2} (**24d**) shows after digestion and derivatized with PITC eleven signals (Fig. 3.59). The results are summarized in Table 3.10.

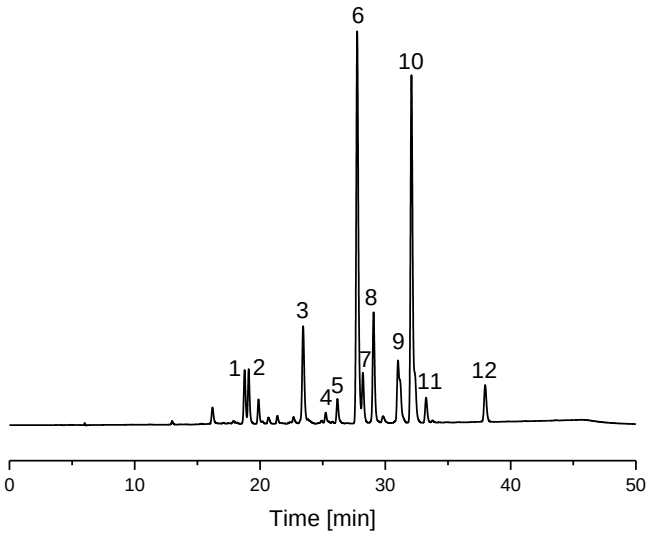

Fig. 3.59: HPLC trace at 254 nm of peptide **24d** after digestion with hydrochloric acid and derivatization with PITC.

Tab. 3.10: Summarized results of amino acid analysis by HPLC of peptide **24d**.

Peak	R_t [min]	R_f	Assignment [a]	Amount [nmol] [a]	Normalized [b]
1	18.71	2.11	glycine	12	6
2	19.02	2.16	threonine	10	5
3	23.42	2.90			
4	25.24	3.20	valine	2	1
5	26.15	3.35			
6	27.83	3.63			
7	28.29	3.71	leucine	18	9
8	29.04	3.83	(phenylalanine)	(26)	
9	31.00	4.16			
10	32.03	4.33			
11	33.33	4.55			
12	38.00	5.32			

[a] assigned and calculated according to Table 3.6; [b] rounded values.

The amino acid analysis by HPLC of peptide **24d** shows a normalized amino acid ratio of 9:6:5:1, but a ratio of 3:2:1 it is expected for the sequence LTGVGL^{NH2}. This result indicates an incomplete digestion, as the outer amino acid of the sequence leucine shows the highest amount of substance and the amino acids glycine and threonine and especially valine show a

much lesser amount of substance than expected. Again, a signal for phenylalanine is observed which is assigned to impurities. The HPLC trace at 254 nm of hexynoic acid-APSGAQRLYGFGL^{NH2} (**24**) shows after digestion and derivatized with PITC ten signals of dominant intensity (Fig. 3.60). The results are summarized in Table 3.11.

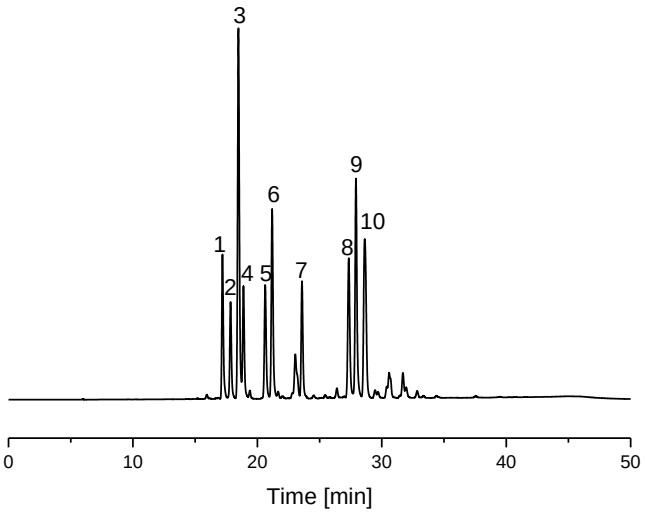

Fig. 3.60: HPLC trace at 254 nm of peptide **24** after digestion with hydrochloric acid and derivatization with PITC.

Tab. 3.10: Summarized results of amino acid analysis by HPLC of peptide **24d**.

Peak	R_t [min]	R_f	Assignment [a]	Amount [nmol] [a]	Normalized [b]
1	17.19	1.86	arginine	86	2; (1)
2	17.82	1.97	serine	85	1; (1)
3	18.47	2.07	glycine	179	4; (2)
4	18.88	2.14	glutamate/glutamine	86	2; (1)
5	20.62	2.43	proline	45	1; (1)
6	21.19	2.53	alanine	177	4; (2)
7	23.59	2.93	tyrosine	116	3; (1)
8	27.34	3.55			
9	27.92	3.65	leucine	172	4; (2)
10	28.62	3.79	phenylalanine	83	2; (1)

[a] assigned and calculated according to Table 3.6; [b] rounded values. Normalized on proline; (phenylalanine).

The amino acid analysis by HPLC of peptide **24** shows a normalized amino acid ratio of 4(G) : 4(A) : 4(L) : 3(Y) : 2(R) : 2(F) : 1(S) : 1(E) : 1(P), but a ratio of 3(G) : 2(A) : 2(L) : 1(Y) : 1(R) : 1(F) : 1(S) : 1(E) : 1(P) is expected for the sequence APSGAQRLYGFGL^{NH2}. However, when

phenylalanine is used for normalizing the results, a ratio of 2(G) : 2(A) : 2(L) : 1(Y) : 1(R) : 1(F) : 1(S) : 1(E) : 1(P) is found, matching the expected one quite well. However, it is mentioned in literature that proline shows a lesser reliability for quantification after acidic hydrolysis and pre-column derivatization with PITC.[209-210] Thus, phenylalanine is a better choice for normalization.

3.4.4.3 Peptide analysis of functionalized silica nanoparticles with HPLC

Azide-functionalized silica nanoparticle (**25**) was treated with hydrochloric acid at 110 °C for 24 h. Subsequently, the solvent was evaporated and the residue treated with PITC. The particles were centrifuged and the supernatant analysed by HPLC at 254 nm, showing a set of 9 signals (Tab. 3.11)

Tab. 3.11: Retention times R_t, retention factors R_f of signals obtained after digestion and derivatization with PITC of azide-functionalized silica nanoparticle.

Peak	**R_t [min]**	**R_f**
1	15.48	1.59
2	18.81	2.15
3	22.40	2.75
4	26.78	3.49
5	28.08	3.71
6	30.06	4.04
7	31.10	4.21
8	36.85	5.18
9	39.13	5.56

These signals are assigned to impurities and side reactions during treatment with PITC. Especially signals 2 and 5 are problematic, since their R_f match glycine and leucine. After acidic hydrolysis and treatment with PITC, the residue was suspended in ethanol and investigated by TEM (3.61). The image shows spherical particles, indicating stability of the silica particles under the harsh hydrolytic conditions. Material **35a** was hydrolysed and treated with PITC as described before. For evaluation, the amounts of the amino acids were calculated using the calibration factors displayed in Table 3.6 and the absorption of the individual signals. Then, the values were normalized on the amino acid with the fewest amount, rounded to whole numbers, and compared to the expected amino acid ratio of the peptide sequence assumed to be

conjugated to the nanoparticle surface and the results discussed in Chapter 3.4.4.2 for the individual peptides upon acid hydrolysis and PITC derivatization. The HPLC trace at 254 nm shows a set of 16 signals. The results are summarized in Table 3.12.

Fig. 3.61: TEM image of **25** after digestion with 6 M HCl at 110 °C for 24 h and treatment with PITC.

Tab. 3.12: Summarized results of amino acid analysis by HPLC of material **35a**.

Peak	**R_t [min]**	**R_f**	**Assignment [a]**	**Amount [nmol][a]**	**Normalized [b]**
1	15.84	1.70			
2	17.94	2.07	glycine	32	2
3	20.85	2.55			
4	22.46	2.83			
5	23.14	2.94	tyrosine	17	1
6	25.85	3.41			
7	26.78	3.56			
8	27.49	3.69	leucine	39	2
9	28.88	3.80	phenylalanine	69	4
10	29.37	3.92			
11	29.99	4.01			
12	31.04	4.11			
13	32.27	4.29			
14	34.27	4.50			
15	34.25	4.84			
16	36.85	5.28			

[a] assigned and calculated according to Table 3.6; [b] rounded values.

The amino acid analysis by HPLC of material **35a** shows a normalized amino acid ratio of 4:2:2:1. However, an amino acid ratio of 2:2:1:1 is expected for the sequence $LYGFGL^{NH2}$ attached to the silica nanoparticles surface. The increased amount of phenylalanine is probably due to impurities and by-products generated during hydrolysis and derivatization, which have the same R_t than the amino acid. Nonetheless, the data indicate a successful conjugation of peptide **24a** to the nanoparticle surface. Then, material **35b** was hydrolysed and treated with PITC as described before. The HPLC trace at 254 nm shows a set of 14 signals. The results are summarized in Table 3.13.

Tab. 3.13: Summarized results of amino acid analysis by HPLC of material **35b**.

Peak	**R_t [min]**	**R_f**	**Assignment [a]**	**Amount [nmol] [a]**	**Normalized [b]**
1	15.74	1.69			
2	18.01	2.07	glycine	7	2
3	20.90	2.57			
4	22.48	2.84			
5	23.15	2.95			
6	23.48	3.01	tyrosine	4	1
7	25.99	3.44			
8	26.78	3.57			
9	27.47	3.69	leucine	8	2
10	28.15	3.80			
11	28.89	3.93			
12	30.18	4.15			
13	31.10	4.31			
14	32.28	4.51			

[a] assigned and calculated according to Table 3.6; [b] rounded values.

The amino acid analysis by HPLC of material **35b** shows a normalized amino acid ratio of 2:2:1, not matching the expected amino acid ratio of 3:2:1 for the sequence $LYGGGL^{NH2}$ attached to the silica nanoparticles surface. However, this results correspond with the found ones for peptide **24b** when hydrolysed and treated with PITC (see Chapter 3.4.4.2), indicating incomplete hydrolysis of the peptide attached to the nanoparticle surface. Material **35c** was hydrolysed and treated with PITC as described before. The HPLC trace at 254 nm shows a set of 14 signals. The results are summarized in Table 3.14.

Tab. 3.14: Summarized results of amino acid analysis by HPLC of material **35c**.

Peak	R_t [min]	R_f	Assignment [a]	Amount [nmol] [a]	Normalized [b]
1	15.67	1.67			
2	17.96	2.06	glycine	18	1
3	20.83	2.55			
4	22.46	2.83			
5	26.73	3.56			
6	27.42	3.68	leucine	38	2
7	28.08	3.79	phenylalanine	59	3
8	29.87	4.10			
9	30.19	4.15			
10	31.02	4.29			
11	32.21	4.50			
12	34.18	4.83			
13	36.75	5.27			
14	39.12	5.68			

[a] assigned and calculated according to Table 3.6; [b] rounded values.

Material **35c** shows an increased phenylalanine signal upon hydrolysis and treatment with PITC, corresponding with the findings for material **35a** before. Furthermore, it shows a signal for leucine which is higher than expected. This is due to impurities provided by the nanoparticle itself upon hydrolysis and treatment with PITC (see Tab. 3.11). Thus, a normalized amino acid ratio of 3(F) : 2(L) : 1(G) is found, which matches not the expected ratio of 3(G) :2 (L) :1 (F) for the peptide sequence $LYGGGL^{NH2}$ attached to the silica nanoparticle surface. Nonetheless, due to the found data it is assumed that peptide **24c** is attached to the surface of the silica nanoparticles. Material **35d** was hydrolysed and treated with PITC as described before. The HPLC trace at 254 nm shows a set of 17 signals. The results are summarized in Table 3.15.

Tab. 3.15: Summarized results of amino acid analysis by HPLC of material **35d**.

Peak	**R_t [min]**	**R_f**	**Assignment [a]**	**Amount [nmol] [a]**	**Normalized [b]**
1	15.65	1.67			
2	18.00	2.07	glycine	6	3
3	19.31	2.29	threonine	2	1
4	19.86	2.38			
5	20.85	2.55			
6	22.46	2.83			
7	25.42	3.33	valine	3	2
8	25.98	3.43			
9	26.78	3.56			
10	27.46	3.68	leucine	10	5
11	28.14	3.80			
12	28.88	3.92			
13	30.18	4.15			
14	31.10	4.30			
15	32.34	4.51			
16	36.09	5.15			
17	39.01	5.65			

[a] assigned and calculated according to Table 3.6; [b] rounded values.

A normalized amino acid ratio of 5(L) : 3(G) : 2(V) : 1(T) is found, matching not the expected ratio of 2(L) : 2(G) : 1(V) : 1(T) for the peptide sequence LTGVGL^{NH2} attached to the silica nanoparticle surface. However, this result corresponds with results found for peptide **24d** upon hydrolysis and treatment with PITC (see Chapter 3.4.4.2), indicating incomplete digestion of the peptide sequence. Thus, it is assumed that peptide **24d** was conjugated successfully to the silica nanoparticle surface. Material **35** shows a set of 21 signals in the HPLC trace at 254 nm after hydrolysis with 6 M hydrochloric acid and treatment with PITC (Tab. 3.16).

Tab. 3.16: Summarized results of amino acid analysis by HPLC of material **35d**.

Peak	R_t [min]	R_f	Assignment [a]	Amount [nmol] [a]	Normalized [b]
1	15.64	1.66			
2	16.66	1.84	arginine	10	1
3	17.41	1.97	serine	9	1
4	17.94	2.06	glycine	22	2
5	18.43	2.14	glutamate	10	1
6	20.10	2.43	proline	7	(1)
7	20.81	2.55	alanine	63	7
8	22.46	2.83			
9	23.14	2.94	tyrosine	11	1
10	25.80	3.40			
11	26.59	3.53			
12	27.34	3.66	leucine	24	3
13	28.08	3.79	phenylalanine	64	7
14	28.76	3.91			
15	29.93	4.10			
16	30.98	4.28			
17	32.16	4.48			
18	36.66	5.25			
19	38.34	5.54			
20	38.88	5.63			
21	39.70	5.77			

[a] assigned and calculated according to Table 3.6; [b] rounded values.

Material **35** shows an increased phenylalanine signal upon hydrolysis and treatment with PITC, corresponding with the findings for material **35a** and **35c** before. The signal for alanine is also increased as well. Furthermore, the signal for leucine is also higher as expected, corresponding with the results found for material **25** upon acidic hydrolysis and treatment with PITC (Tab 3.11). Thus, the amino acid analysis by HPLC of material **35** shows a normalized amino acid ratio of 2(G) : 7(A) : 2(L) : 3(1) : 2(1) : 7(F) : 1(S) : 1(E) : 1(P) and a ratio of 3(G) : 2(A) : 2(L) : 1(Y) : 1(R) : 1(F) : 1(S) : 1(E) : 1(P) is expected for the sequence APSGAQRLYGFGL^{NH2}. Serine was used for normalization, since proline shows a poor reliability for quantification after acidic hydrolysis and pre-column derivatization with PITC.[209-210] Nonetheless, the ratio matches well with the expected one, indicating a successful conjugation of the peptide to the

nanoparticle surface. The digestion of peptide functionalized silica nanoparticles with hydrochloric acid and subsequent derivatization with PITC and HPLC analysis of the phenylthiocarbamyl amino acids is a potent method for amino acid analysis of peptide-functionalized silica nanoparticles. However, the method suffers of side reactions and incomplete digestion. Especially the amino acids alanine, phenylalanine and leucine overlap with other signals coming from side reactions due to the nanoparticle, leading to unclear and difficult-to-interpret results.

3.3.5 Comparison of amino acid analysis with the results of azide-surface loading determination and *Pauly* reaction

In the previous chapters, three methods for analysing nanoparticle surface functionalization were explored. Initially, surface loading on azide-functionalized silica nanoparticles was determined by reduction of the azide to amine groups with sodium boronhydride and subsequent derivatization with the Fmoc-Rink Amide linker. Then, Fmoc was cleaved off with piperidine and the generated dibenzofulvene and its piperidine adduct were quantified by UV/Vis spectroscopy using a calibration curve. This method allows a quantification down to nanomolar concentrations. However, although sodium boronhydride was used in a large excess, some azide groups may remain unreduced. Thus, the loadings determined are only the lower limit of surface azide groups (see Chapter 3.3.2).

Next, a colourimetric approach based on the *Pauly* reaction was utilized to investigate peptides attached to nanoparticle surfaces. It is based on the reaction of tyrosine with sulfanilic acid to a red azotyrosine dye. However, this method has two major disadvantages. First, UV/Vis measurements on nanoparticles is highly dependent on their capability to form a stable suspension in the reaction solvent. However, this was not the case for the silica nanoparticles to be studied. Second, it is limited to particles which do not have an intense colour, as it might otherwise overlay the red azotyrosine. Nonetheless within these limits, the *Pauly* reaction has potential as a fast qualitative method to demonstrate the successful attachment of tyrosine- or histidine- containing peptides on nanoparticle surfaces (see Chapter 3.3.3).

Finally, the peptide-functionalized silica nanoparticles were hydrolysed with hydrochloric acid, releasing the individual amino acids, and subsequent derivatized with PITC. The reaction mixture was analysed with HPLC. The resulting phenylthiocarbamyl amino acids have an absorption at 254. Due to the high sensitivity to picomolar concentrations, an as sterile as possible environment is necessary to avoid protein contamination of the sample. Furthermore, this method yields complex HPLC traces due to side reactions of the nanoparticle,

contaminations with other proteins from dust or naturally ubiquitous bacteria and incomplete digestion and fragmentation of the peptides. Thus, a HPLC system optimized for trace analysis is required to ensure reproducible retention times and retention factors (see Chapter 3.3.4).

The results of azide surface loading determination, the *Pauly* reaction, and amino acid analysis are correlated with each other in Table 3.17. The results of the *Pauly* reaction and HPLC amino acid analysis correspond with each other regarding the presence of the amino acid tyrosine, showing the red colour in the *Pauly* reaction, and the signal with R_f = 3.00 in the HPLC trace. The peptide surface loading was determined using the amount of material used for a single experiment and the amount of the amino acids calculated using the calibration factor from Table 3.6 as well as the UV absorption of the individual peaks from the corresponding HPLC trace. However, when the loading of the azide-functionalized silica nanoparticles is determined and compared to the peptide loading, an incomplete conjugation of peptide to nanoparticle surface by copper(I)-catalysed dipolar alkyne-azide cycloaddition is observed. Material **35a** has 34% of free azide groups left after conjugation to the corresponding peptide by CuAAC. Materials **35**, **35b** and **35c** have 64 to 73% azide groups left after conjugation to the corresponding peptides by CuAAC, and material **35d** has 94% of free azide groups remaining after conjugation to the corresponding peptide by CuAAC. However, this might also be because of the observed incomplete digestion of the peptide sequence. Taken together, these results indicate that the effectivity of CuAAC of alkyne-terminated peptides to azide-functionalized nanoparticles depends on the amino acid sequence of the peptides.

Tab. 3.17: Correlation of results of *Pauly* reaction, azide loading determination, and peptide sequence analysis using HPLC

Compound	Tyrosine *Pauly* [a]	Tyrosine HPLC [b]	Azide Loading [nmol] Fmoc [c]	Peptide Loading [nmol] HPLC [d]	$\Delta_{Loading}$ [%] [e]
35	positive	positive	59.06 ± 15.36	15.86 ± 3.76	73
35a	positive	positive	40.54 ± 10.54	26.85 ± 6.97	34
35b	positive	positive	25.39 ± 6.60	8.16 ± 4.94	68
35c	negative	negative	50.08 ± 13.03	18.07 ± 6.80	64
35d	negative	negative	51.06 ± 13.26	3.07 ± 0.54	94

[a] Formation of the red dye azotyrosine indicating presence of tyrosine and is marked as positive. [b] Presence of the tyrosine signal with an R_f around 3.00 is marked as positive. [c] Loading of azide groups determined for used material in amino acid analysis by HPLC according to Chapter 3.3.1. [d] Loading calculated of the amount of substance found in the amino acid analysis using HPLC by applying the calibration curves. [e] Difference of determined loading of azide groups and attached peptide in %.

3.5 Bifunctionalized silica coated superparamagnetic iron oxide nanoparticles for imaging purposes

3.5.1 Synthesis and characterization of bifunctionalized silica coated superparamagnetic iron oxide nanoparticles

Superparamagnetic iron oxide nanoparticles are used as T_2 contrast agents for magnetic resonance imaging (MRI) and as tracers for magnetic particle imaging (MPI). However, their distribution is usually systemic, only controlled by passive accumulation in tumours, spleen, liver and kidneys. Thus, there is a need for actively targeting MRI contrast agents. Therefore, silica-coated super paramagnetic iron oxide nanoparticles with amine and azide surface functionalization were prepared ($^{Amine;Azide}$Silica@SPION **36**). To enable and cell uptake studies based on fluorescence microscopy, $^{Amine;Azide}$Silica@SPION **36** was reacted with the cyanine dye Cy5-NHS ester to yield Cy5-functionalised silica-coated iron oxide nanoparticles with free surface azide groups ($^{Cy5;Azide}$Silica@SPION **36a**). Subsequently, $^{Cy5;Azide}$Silica@SPION **36a** was conjugated with the ALST1-hexynoic acid conjugate (**24**) using CuAAC to obtain dual-functionalized Cy5/ALST1 silica coated iron oxide nanoparticles ($^{Cy5;ALST1}$Silica@SPION **36b**). As a negative control, $^{Cy5;Azide}$Silica@SPION **36a** was also conjugated with hexyne by CuAAC to obtain dual-functionalized Cy5/butyl-capped silica coated iron oxide nanoparticles ($^{Cy5;butyl\text{-}capped}$Silica@SPION **36c**) (Fig. 3.62). The amine- and azide- surface loading of material $^{Amine;Azide}$Silica@SPION **36** was determined by conjugating them with Fmoc-Rink Amide linker, subsequent cleavage and determination of the dibenzofulvene and its piperidine adduct by UV/Vis spectroscopy, and calculating the amount of amine groups using the calibration curve determined in Chapter 3.3.2. The azide loading was assessed by reduction of the surface azide to amine groups with sodium boronhydride, subsequent derivatization with Fmoc-Rink Amide linker and cleavage of Fmoc by piperidine as described before. From the calibration curve, the total amount of amine and azide groups was calculated. The difference of the total amount of surface amine groups and the amine groups of the non-reduced particles give the amount of azide groups (Tab. 3.18). The morphology and diameter was determined by TEM (Fig.3.63). The functionalized silica-coated iron oxide nanoparticles $^{Amine;Azide}$Silica@SPION **36**, $^{Cy5;Azide}$Silica@SPION **36a**, $^{Cy5;ALST1}$Silica@SPION **36b**, and $^{Cy5;butyl\text{-}capped}$Silica@SPION **36c** all have a diameter of around 14 nm.

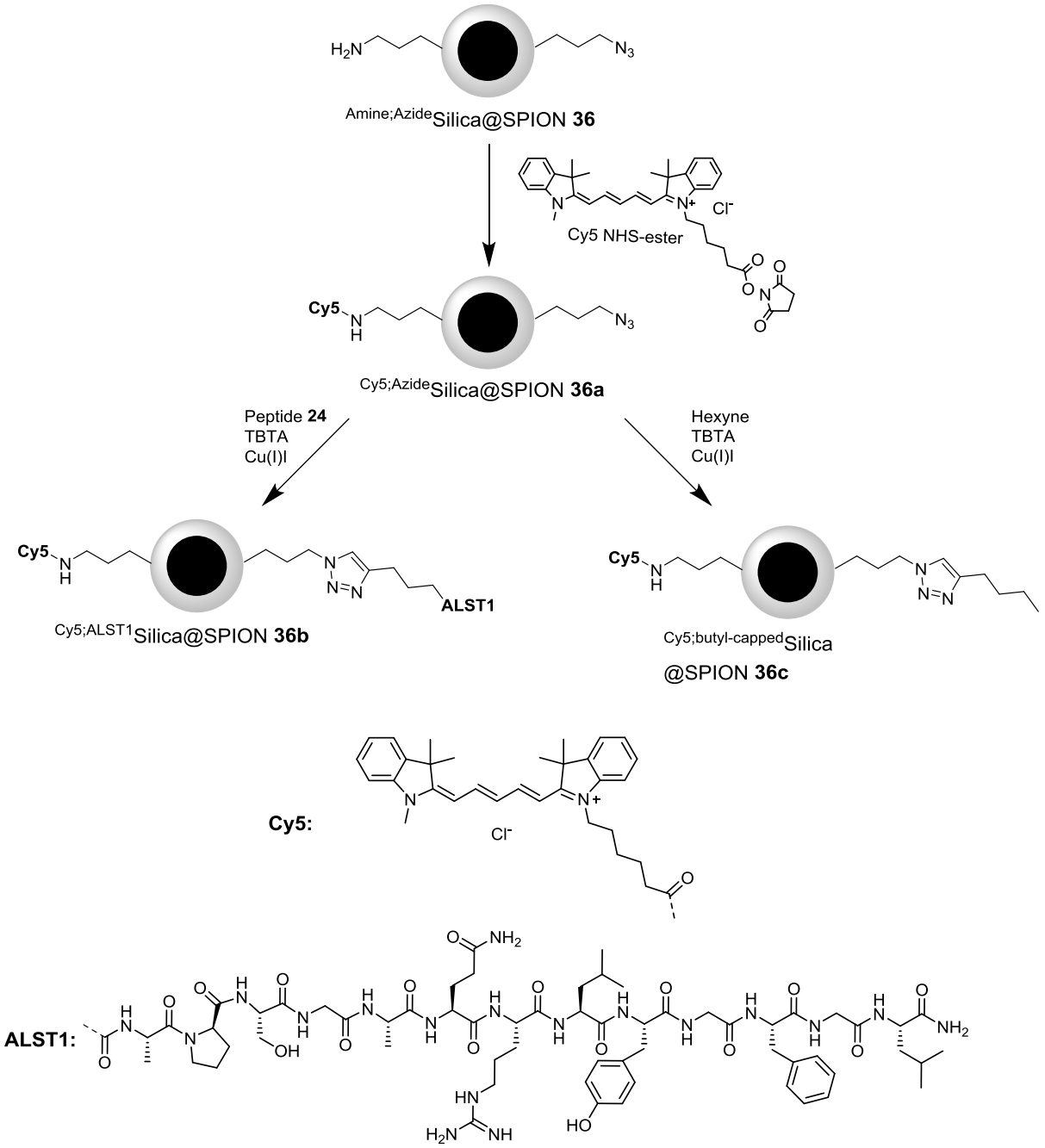

Fig. 3.62: Synthesis of bi-functionalized silica-coated iron oxide nanoparticles.

Tab. 3.18: Amine and Azide surface loading of compound $^{Amine;Azide}$Silica@SPION **36**.

$^{Amine;Azide}$Silica@SPION **36**	**Loading [µmol/g]**
Amines and reduced azides	82.3 ± 2.1
Amine	61.0 ± 1.8
Azide	21.3 ± 3.9

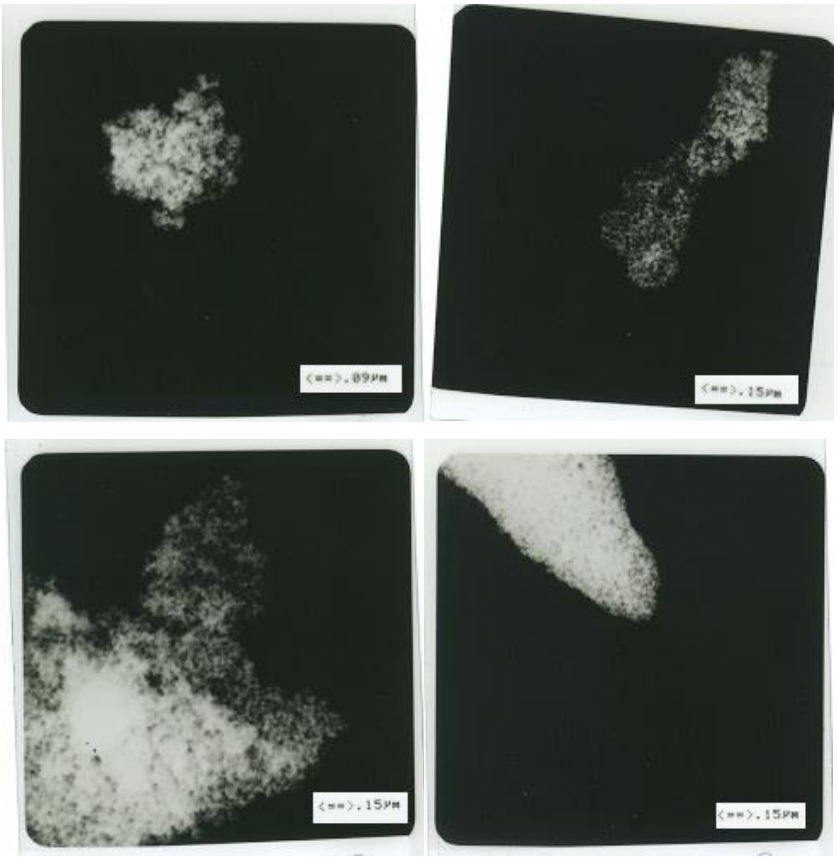

Fig. 3.63: TEM images of material $^{Amine;Azide}$Silica@SPION **36** (upper left), $^{Cy5;Azide}$Silica@SPION **36a** (upper right), $^{Cy5;ALST1}$Silica@SPION **36b** (lower left), and $^{Cy5;butyl\text{-}capped}$Silica@SPION **36c** (lower right).

Due to the images available as printouts only, picture-processing was difficult. Still, single particles can clearly be identified. However, compared to materials 36, 36a, and 36b, $^{Cy5;butyl\text{-}capped}$Silica@SPION **36c** shows a high tendency to agglomerate. The functionalization with two hydrophobic moieties, Cy5 and hexyne, leads to a higher tendency to agglomerate. The IR spectra of the functionalized silica-coated iron oxide nanoparticles $^{Amine;Azide}$Silica@SPION **36**, $^{Cy5;Azide}$Silica@SPION **36a**, $^{Cy5;ALST1}$Silica@SPION **36b**, and $^{Cy5;butyl\text{-}capped}$Silica@SPION **36c** each show signals at 3416, 2927, 2110, 1615, and 1054 cm^{-1}.The two peaks at 3416 and 1615 cm^{-1} are assigned to the amine stretching and deformation vibrations. The signal at 2927 cm^{-1} is due to the CH stretching vibrations, while the signal at 2110 cm^{-1} is assigned to the azide stretching vibrations. The signal at 1054 cm^{-1} results from the Si-O stretching vibrations. Due to the coating procedure based on the *Stöber* process, the azide and amine groups are present both on the surface as well as inside the coating layer. Thus, the surface-functionalized silica-coated superparamagnetic nanoparticles still show some resident amine and azide signals in the IR spectrum, as some groups are not accessible for modification reactions. For further characterisation, the relaxivity r_1 and r_2, the hydrodynamic radius (distribution and average) and zeta potential were measured (Tab. 3.19).

Tab. 3.19: Characterization of materials $^{Amine;Azide}$Silica@SPION **36**, $^{Cy5;Azide}$Silica@SPION **36a**, $^{Cy5;ALST1}$Silica@SPION **36b**, and $^{Cy5;butyl\text{-}capped}$Silica@SPION **36c** by DLS, zeta-potential and relaxivity measurements.

Compound	Hydrodynamic Distribution [nm]	Average Diameter [nm]	ζ [mV]	r_1[a] [L/mmol$_{Fe}$·s]	r_2[a] [L/mmol$_{Fe}$·s]
36	10% ≤ 56; 50% ≤ 132; 90% ≤ 439	165	-35.6	0.48 ± 0.05	125 ± 11
36a	10% ≤ 55; 50% ≤ 98; 90% ≤ 348	143	-33.6	0.04 ± 0.07	87 ± 7
36b	10% ≤ 159; 50% ≤ 663; 90% ≤ 2337	358	-20.0	0.16 ± 0.05	27 ± 5
36c	10% ≤ 88; 50% ≤ 467; 90% ≤ 3412	312	-29,4	0.26 ± 0.13	49 ± 5

[a] measured at 7 T

Determination of the hydrodynamic distribution gives the average hydrodynamic diameter of a material. Thus, materials $^{Amine;Azide}$Silica@SPION **36**, $^{Cy5;Azide}$Silica@SPION **36a**, $^{Cy5;ALST1}$Silica@SPION **36b**, and $^{Cy5;butyl\text{-}capped}$Silica@SPION **36c** can be organized according to their average hydrodynamic diameter ranging from 143 to 358 nm into **36a** < **36** < **36c** < **36b**. The average hydrodynamic diameter increases with the degree of functionalization of the surface from functional groups like azides/amines over Cy5-functionalized to the peptide-functionalized particle, as expected. The zeta-potential, ranging from -36 to -20 mV can be organized according to its increase into **36** < **36a**< **36c** < **36b**, showing a slight increase due to functionalization with Cy5 and hexyne, but a significant increase of about 10 mV due to conjugation to the peptide ALST1, indicating a successful attachment of the peptide to the nanoparticle surface. The relaxivity r_1 of materials $^{Amine;Azide}$Silica@SPION **36**, $^{Cy5;Azide}$Silica@SPION **36a**, $^{Cy5;ALST1}$Silica@SPION **36b**, and $^{Cy5;butyl\text{-}capped}$Silica@SPION **36c** can be organized according to r_1 increase into **36a** < **36b** < **36c** < **36**. However, the materials show r_1 values ranging from 0.04 to 0.48 L/mmol$_{Fe}$ which are not significant for any T_1 MRI measurements. This is not surprising, since superparamagnetic iron oxide nanoparticles are contrast agents for T_2 MRI measurements. Comparing the materials $^{Amine;Azide}$Silica@SPION **36**, $^{Cy5;Azide}$Silica@SPION **36a**, $^{Cy5;ALST1}$Silica@SPION **36b**, and $^{Cy5;butyl\text{-}capped}$Silica@SPION **36c** regarding their relaxivity r_2 ranging from 125 to 27 L/mmol$_{Fe}$, they can be ordered due to

their decrease to **36** > **36a** > **36c** > **36b**. The relaxivity r_2 decreases with increasing hydrodynamic diameter due a higher degree of functionalization from surface groups only to dual-functionalized particle with ALST1 and Cy5.[211] To investigate the successful attachment of the ALST1 peptide on the DND surface, compounds **36b** and **36c** were treated with 6 M hydrochloric acid, the residue was derivatized with PITC and then analyzed using HPLC according to the established method in Chapter 3.3.4. The spectra were overlaid for better identification (Fig. 3.64). The overlaid HPLC traces of $^{Cy5;ALST1}$Silica@SPION **36b** and $^{Cy5;butyl\text{-}capped}$Silica@SPION **36c** show 7 signals, which do not overlap. The R_t and the R_f values are collected and assigned in Table 3.20. For evaluation, the amounts of the amino acids were calculated using the calibration factors displayed in Table 3.6 and the absorption of the individual signals. Then, the values were normalized on the amino acid with the fewest amount, rounded to whole numbers, and compared to the expected amino acid ratio of the peptide sequence assumed to be conjugated to the nanoparticle surface and the results discussed in Chapter 3.4.4.2 for the individual peptides upon acid hydrolysis and PITC derivatization.

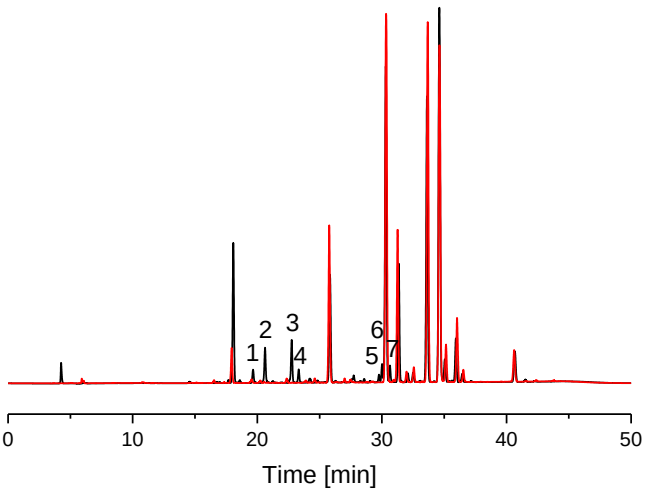

Fig. 3.64: Overlaid HPLC traces at 254 nm of compound $^{Cy5;ALST1}$Silica@SPION **36b** (black) and $^{Cy5;butyl\text{-}capped}$Silica@SPION **36c** (red) after hydrolysis with hydrochloric acid and derivatization with PITC.

Tab. 3.20: Summarized results of amino acid analysis by HPLC of material $^{Cy5;ALST1}$Silica@SPION **36b** overlaid with $^{Cy5;butyl\text{-}capped}$Silica@SPION **36c**

Peak	R_t [min]	R_f	Assignment [a]	Amount [nmol] [a]	Normalized [b]
1	19.67	1.96	serine	10	1
2	20.63	2.11	glycine	20	2
3	22.73	2.42	proline	12	1
4	23.32	2.51	alanine	17	2
5	29.72	3.47			
6	30.02	3.52			
7	30.64	3.66	leucine	18	2

[a] assigned and calculated according to Table 3.6; [b] rounded values.

The amino acid analysis by HPLC of peptide $^{Cy5;ALST1}$Silica@SPION **36b** shows the amino acids serine, glycine, proline, alanine, and leucine in a normalized amino acid ratio of 2(G) : 2(A) : 2(L) : 1(S): 1(P). The other amino acids of the sequence APSGAQRLYGFGL^{NH2} were not observed and two signals with R_f = 3.47 and R_f = 3.52 cannot be assigned. This is due to many signals of side reactions and impurities coming from the nanoparticle core itself. Nonetheless, the amino acids serine, glycine, proline, alanine, and leucine show a normalized ratio also found for the ALST1 described in Chapter 3.4.4.2, indicating successful attachment of the peptide ALST1 to the surface of the silica-coated superparamagnetic iron oxide nanoparticle by CuAAC. Using the calculated amounts of amino acids, the peptide loading is assessed to 5.2 µmol/g, indicating 26% of the surface azide groups have reacted with peptides (see Chapter 3.3.5). After reacting $^{Amine;Azide}$Silica@SPION **36** with Cy5, the particles turned from deep red to greenish-blue, indicating a successful attachment of the fluorescent dye. After conjugation with peptide **24**, the resulting $^{Cy5;ALST1}$Silica@SPION **36b** was investigating by fluorescence spectroscopy. A stable suspension in water of $^{Cy5;ALST1}$Silica@SPION **36b** was adjusted to an OD_{600} of 0.25. Then, an emission spectrum with λ_{ex} 610 nm and an excitation spectrum with λ_{em} = 690 was recorded (Fig. 3.65).

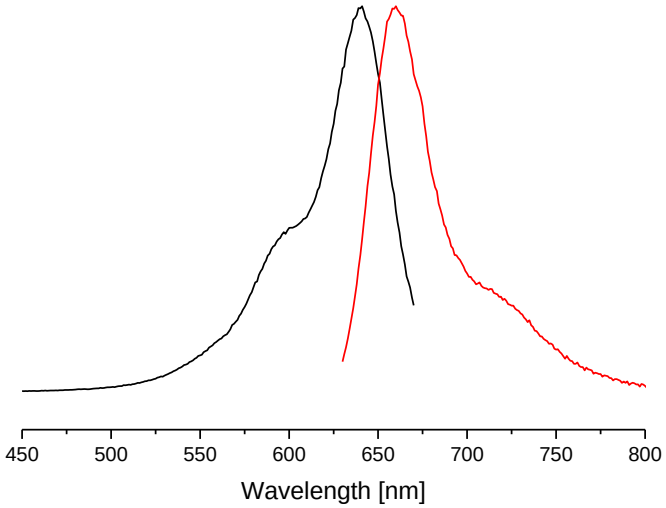

Fig. 3.65: Normalized excitations spectrum (black) and emission spectrum of material **36b** in water.

While material $^{Cy5;ALST1}$Silica@SPION **36b** showed a $\lambda(max)_{ex}$ of 640 nm and a $\lambda(max)_{em}$ of 660 nm, Cy5 itself shows a $\lambda(max)_{ex}$ of 646 nm and a $\lambda(max)_{em}$ of 670 nm. Thus, attachment to the nanoparticle surface causes a hypsochromic shift of both excitation and emission wavelength. This effect is more significant for the emission wavelength and results in a decrease of the Stokes shift from 24 to 20 nm. The combined analytical data indicate the preparation of the bifunctionalized silica-coated superparamagnetic iron oxide nanoparticles $^{Cy5;ALST1}$Silica@SPION **36b** and $^{Cy5;butyl\text{-}capped}$Silica@SPION **36c** according to Figure 3.62.

3.5.2 Cell uptake and imaging with bifunctionalized silica coated superparamagnetic iron oxide nanoparticles

The cellular uptake of SPIONs $^{Amine;Azide}$Silica@SPION **36**, $^{Cy5;Azide}$Silica@SPION **36a**, $^{Cy5;ALST1}$Silica@SPION **36b**, and $^{Cy5;butyl\text{-}capped}$Silica@SPION **36c** by mammary epithelial cell line MDA MB 231was investigated by fluorescence microscopy. The nucleus was co-stained with 4,5-diamindino-2-phenylindole (DAPI). In Figure 3.66, several oval cells can be seen with the nuclei showing up in blue. Furthermore, dark, amorphous particles next to the cells can be seen. These are assigned to agglomerated material **36**, which show no colour due to lack of a fluorophor.

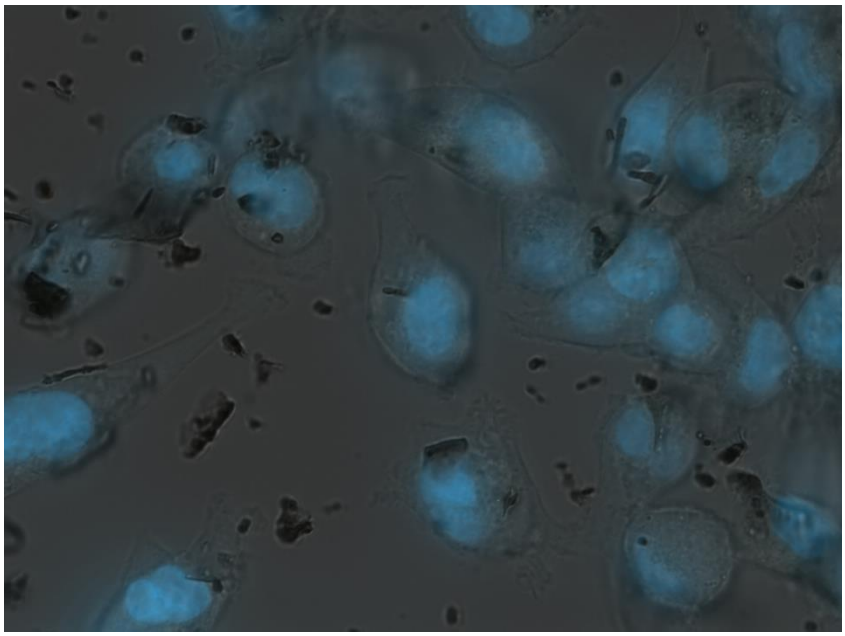

Fig. 3.66: Fluorescence microscopy image of mammary epithelial cell line MDA MB 231 incubated with $^{Amine;Azide}$Silica@SPION **36**. The cell nuclei are co-stained with DAPI and show up in a blue colour. The nuclei have a diameter of approximately 10 µm.

In Figure 3.67, several oval cells can be seen with the nuclei showing up in blue. Furthermore, few red sphere-like particles next to the cells can be seen. These are assigned to agglomerated material $^{Cy5;Azide}$Silica@SPION **36a** (top Figure) and $^{Cy5;butyl\text{-}capped}$Silica@SPION **36c** (bottom Figure), which show red fluorescence due to Cy5 attached to the materials surface. No red colour inside the cells is observed, indicating no uptake of the material $^{Cy5;Azide}$Silica@SPION **36a** and $^{Cy5;butyl\text{-}capped}$Silica@SPION **36c** respectively into the cells.

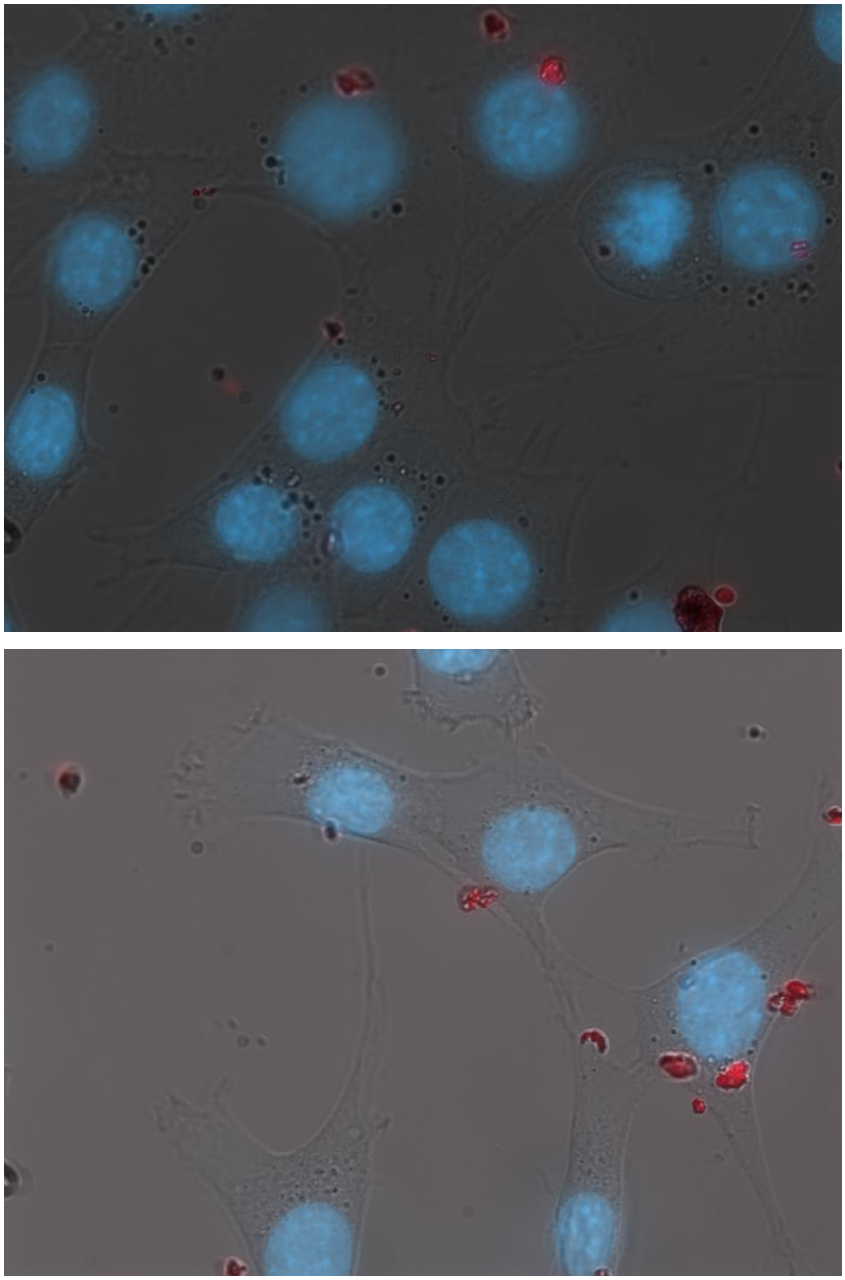

Fig. 3.67: Fluorescence microscopy image of mammary epithelial cell line MDA MB 231 incubated with $^{Cy5;Azide}$Silica@SPION **36a** (top) and $^{Cy5;butyl\text{-}capped}$Silica@SPION **36c**. The cell nuclei are co-stained with DAPI and show up in a blue colour. The nuclei have a diameter of approximately 10 µm.

In Figure 3.68, several oval cells can be seen with the nuclei showing up in blue. Furthermore, many red sphere-like particles next to and on the cells can be seen. These are assigned to agglomerated material $^{Cy5;ALST1}$Silica@SPION **36b**, which show red fluorescence due to Cy5 attached to the materials surface. The fluorescence microscopy images indicate that $^{Cy5;ALST1}$Silica@SPION **36b** is not internalized by the MDA MB 231 cells. For the final demonstration that the red fluorescent material indeed remains external, confocal fluorescence microscopy would be needed, which was not available.

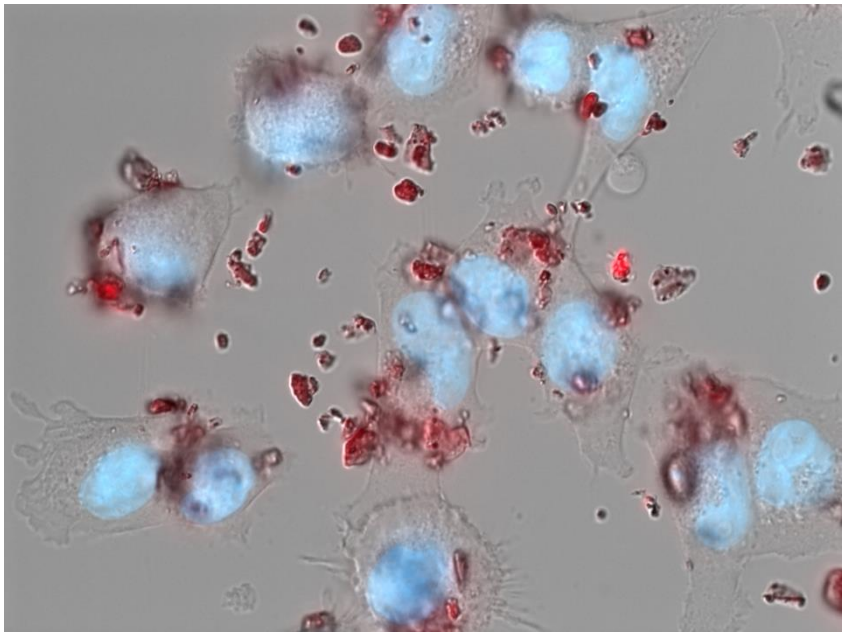

Fig. 3.68: Fluorescence microscopy image of mammary epithelial cell line MDA MB 231 incubated with $^{Cy5;ALST1}$Silica@SPION **36b**. The cell nuclei are co-stained with DAPI and show up in a blue colour. The nuclei have a diameter of approximately 10 µm.

Although conjugation of ALST1 to nanoparticles was reported to facilitate cellular uptake by several endocytotic pathways, this was not observed for material **36b**.[155-156] Probably, the strong agglomeration of the particles prevents endocytosis and therefore internalization into the cells. Thus, surface-presented ALST1 is not an effective replacement for other common modifications like PEG or chitosan, which are known to prevent agglomeration effectively.

3.6 Bifunctionalized detonation nanodiamond for imaging purposes

3.6.1 Functionalization and characterization of bifunctionalized detonation nanodiamond

Amine- and Azide-functionalized detonation nanodiamond ($^{Amine;Azide}$DND **37**) was provided by the group of *Prof. Dr. Anke Krüger* from the Institute of Organic Chemistry of the Julius-Maximilians-Universität Würzburg. The total loading of functional groups (azide and amine) was given as 0.26 mmol/g from thermogravimetric analysis (TGA). The IR spectrum of $^{Amine;Azide}$DND **37** shows a broad signal at 3378 cm^{-1}, sharp peaks at 3028, 2928, 2868 cm^{-1}, and an intense and sharp signal at 2098 cm^{-1}. Further peaks are found at 1644, 1601, 1506, 1251, and 1113 cm^{-1} (Fig. 3.69).

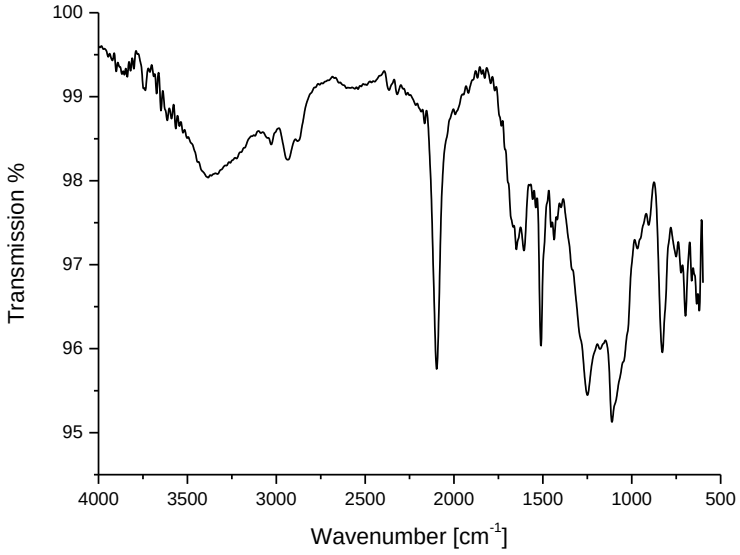

Fig. 3.69: ATR IR spectrum of $^{Amine;Azide}$DND **37**.

The signal at 3378 cm^{-1} is assigned to the amine stretching vibrations. The signals at 3028, 2928, and 2869 cm^{-1} are assigned to the aliphatic and aromatic C-H stretching vibrations of the aromatic surface linker groups. The signal at 2098 cm^{-1} is assigned to azide stretching vibrations. The signals at 1644, and 1601 is assigned to C=C stretching vibrations of graphitic surface groups. The $^{Amine;Azide}$DND **37** was separated in two batches. One was functionalized with Fmoc aminoxy acetic acid (Fmoc-Aoa) ($^{Fmoc\text{-}Aoa;Azide}$DND **38**) and the other was functionalized with the commercially available Cyanine 5 (Cy5) dye ($^{Cy5;Azide}$DND **39**). Subsequently, Fmoc was cleaved from compound $^{Fmoc\text{-}Aoa;Azide}$DND **38** using piperidine. Then, either peptide **24** or hexyne were attached to the nanodiamond surface using the copper(I)-catalysed 1,3-dipolar cycloaddition of azides and terminal alkynes. Finally, rhenium complex **23** was attached to the aminoxy group via oxime ligation to yield materials $^{[ReBr(CO)3(L)]\text{-}Aoa;ALST1}$DND **40a** and $^{[ReBr(CO)3(L)]\text{-}Aoa;butyl\text{-}capped}$DND **40b**. Material $^{Cy5;Azide}$DND **39** was either reacted with peptide **24** or hexyne via the copper(I)-catalysed 1,3-dipolar cycloaddition of azides and terminal alkynes to give compounds $^{Cy5;ALST1}$DND **39a** and $^{Cy5;butyl\text{-}capped}$DND **39b** (Fig. 3.70).

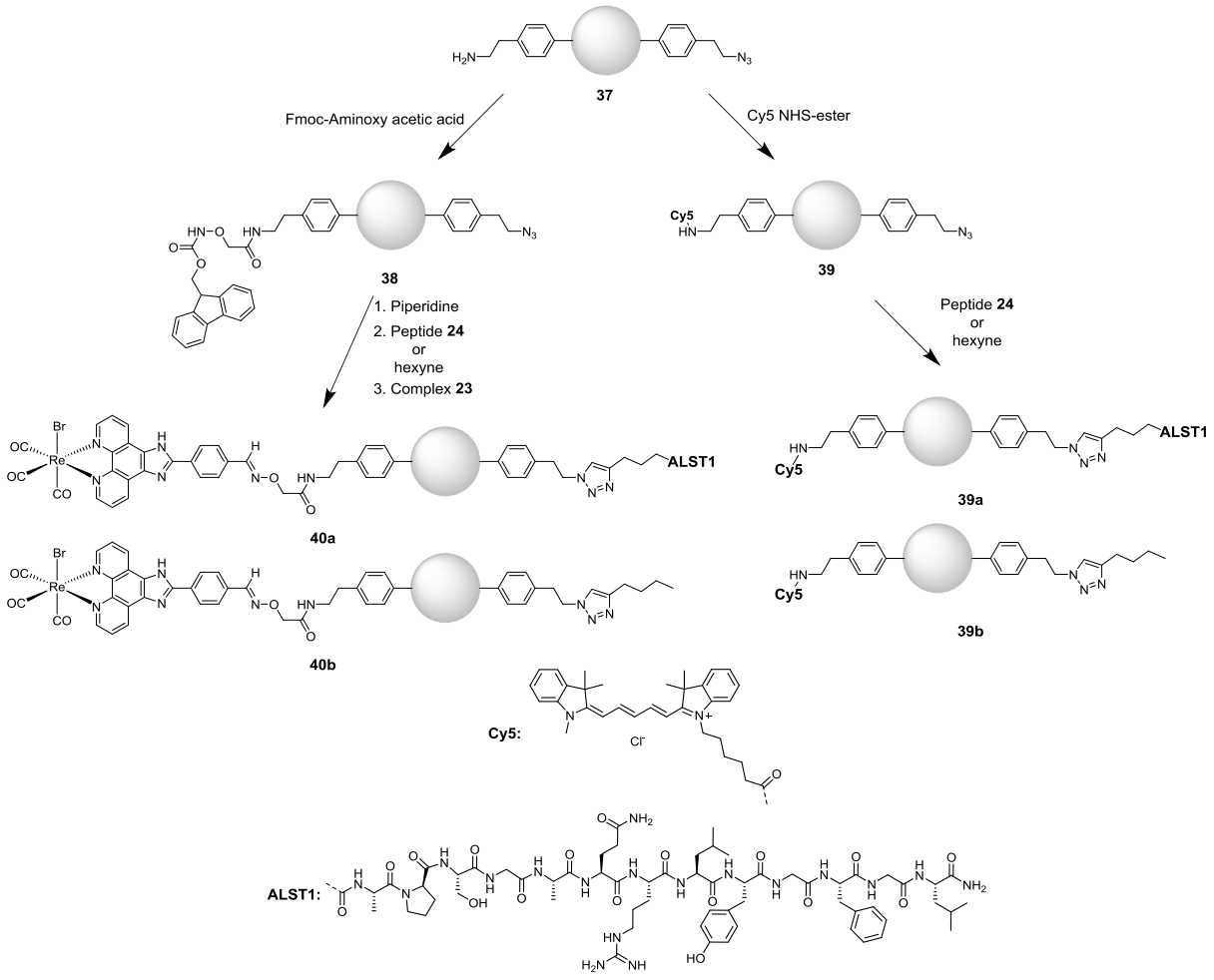

Fig. 3.70: Synthesis and of materials $^{Cy5;ALST1}$DND **39a**, $^{Cy5;butyl\text{-}capped}$DND **39b** $^{ReBr(CO)3(L)]\text{-}Aoa;ALST1}$DND **40a**, and $^{[ReBr(CO)3(L)]\text{-}Aoa;butyl\text{-}capped}$DND **40b** from $^{Amine;Azide}$DND **37**.

In the IR, 39a+b and 40a+b all show signals around 3340, 2950, and 2870 cm^{-1}, as well as from 1700 to 1600 cm^{-1}. This are assigned to amines/hydroxyl group stretching vibrations on the DND surface (3340 cm^{-1}), C-H stretching vibrations of the DND and the molecules conjugated to it (2950 and 2870 cm^{-1}) (Fig. 3.71). However, **40a** and **40b** exhibit additional signals at 2029, 1925 and 1902 cm^{-1} which are assigned to the symmetric and asymmetric carbonyl ligands of the $Re(CO)_3$ unit. Furthermore, compounds **39a** and **40a** show an intense signal at 1665 cm^{-1} compared to materials **39b** and **40b**. These are due to the amide stretching vibrations of the attached peptide.

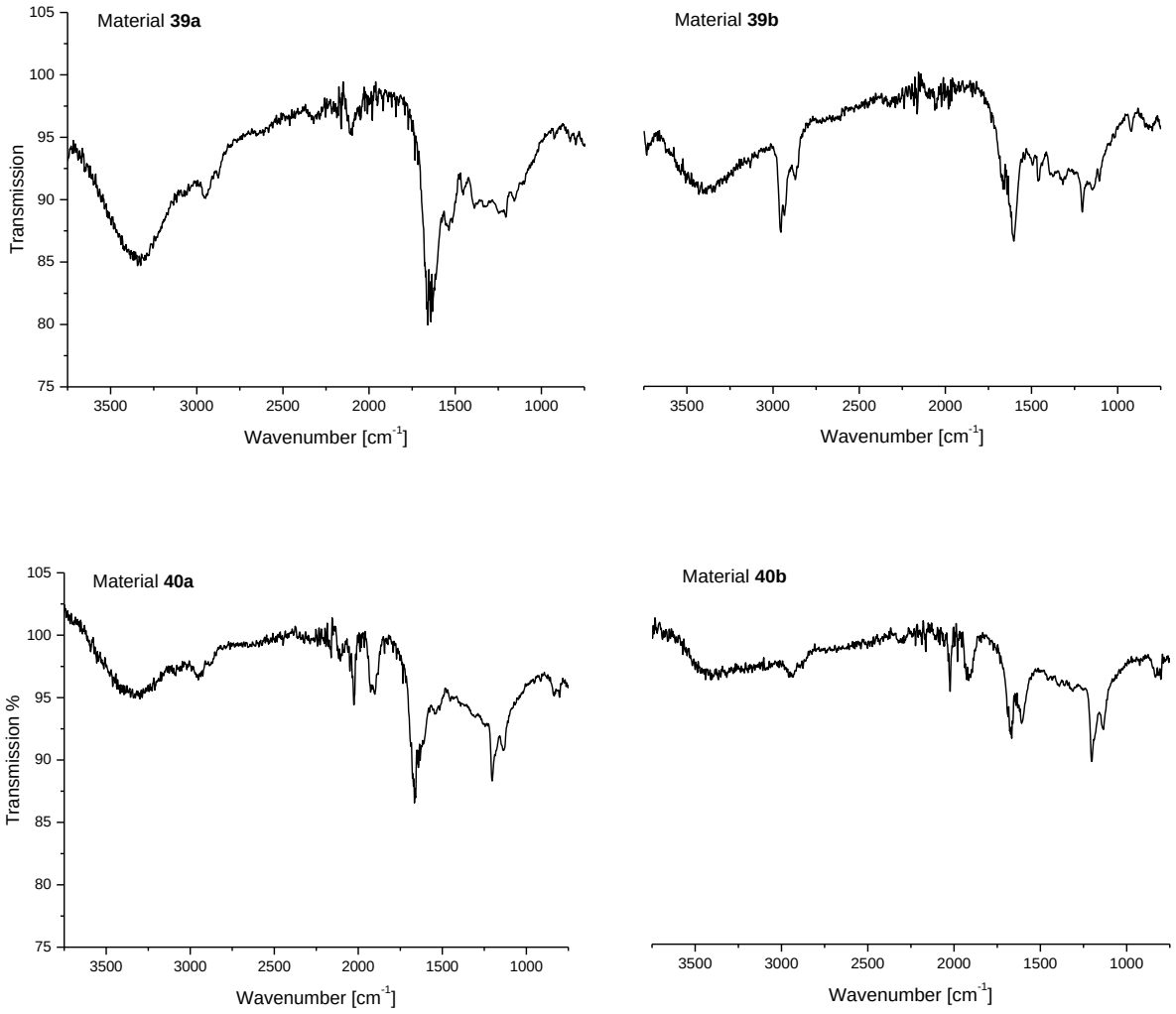

Fig. 3.71: ATR IR spectra of materials $^{Cy5;ALST1}$DND **39a**, $^{Cy5;butyl\text{-}capped}$DND **39b** $^{ReBr(CO)3(L)]\text{-}Aoa;ALST1}$DND **40a**, and $^{[ReBr(CO)3(L)]\text{-}Aoa;butyl\text{-}capped}$DND **40b**.

When investigated by TEM, $^{Amine;Azide}$DND **37**, $^{Cy5;ALST1}$DND **39a**, $^{Cy5;butyl\text{-}capped}$DND **39b** $^{ReBr(CO)3(L)]\text{-}Aoa;ALST1}$DND **40a**, and $^{[ReBr(CO)3(L)]\text{-}Aoa;butyl\text{-}capped}$DND **40b** all show amorphous particles. Due to their similarity, only the TEM pictures of material **37** are shown in Figure 3.72, while the others are shown in Chapter 7. Material **37** has a size distribution ranging from 3 to 8 nm with an average size of 5.2 nm (Fig. 3.73)

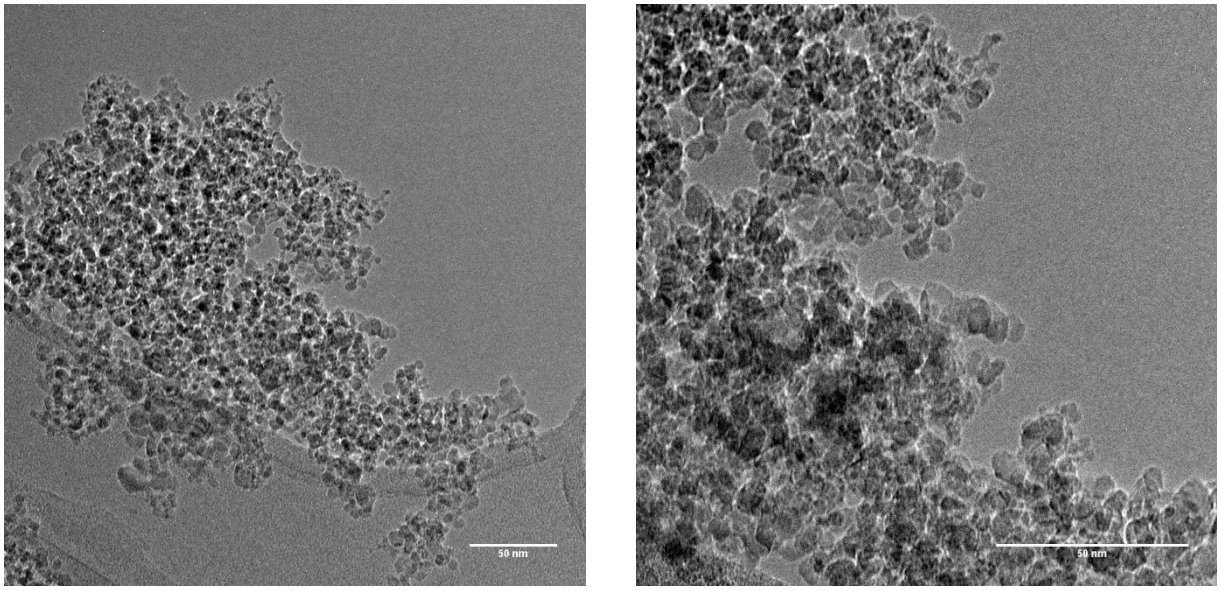

Fig. 3.72: TEM images of azide and amine functionalized detonation nanodiamond (**37**).

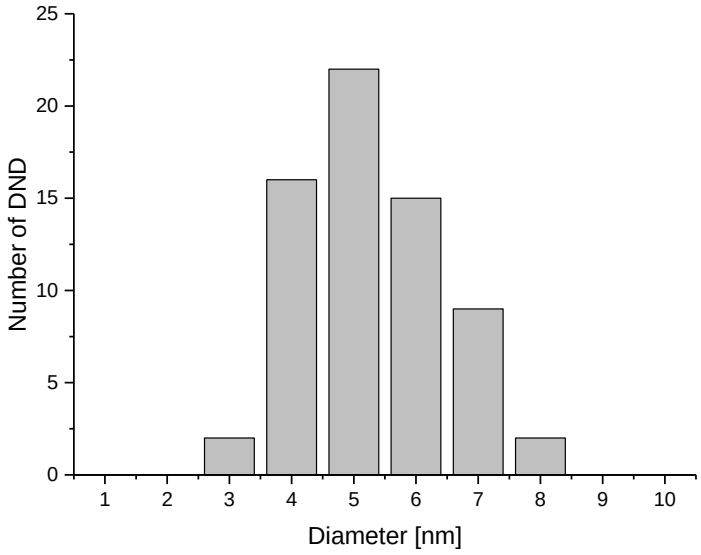

Fig. 3.73: Size distribution of $^{Amine;Azide}$DND **37**.

Materials **39a** and **40b** showed an average size of 5.2 nm, while **39b** and **40a** showed an average size of 5.3, demonstrating that the surface modifications have no significant impact on the particle size. The results of investigating materials $^{Amine;Azide}$DND **37**, $^{Cy5;ALST1}$DND **39a**, $^{Cy5;butyl\text{-}capped}$DND **39b** $^{ReBr(CO)3(L)]\text{-}Aoa;ALST1}$DND **40a**, and $^{[ReBr(CO)3(L)]\text{-}Aoa;butyl\text{-}capped}$DND **40b** with DLS are summarized in Table 3.21.

Tab. 3.21: Results of DLS and zeta potential measurements for materials $^{Amine;Azide}$DND **37**, $^{Cy5;ALST1}$DND **39a**, $^{Cy5;butyl\text{-}capped}$DND **39b** $^{ReBr(CO)3(L)]\text{-}Aoa;ALST1}$DND **40a**, and $^{[ReBr(CO)3(L)]\text{-}Aoa;butyl\text{-}capped}$DND **40b**.

Compound	Hydrodynamic Distribution [nm]	Average size [nm]	ζ [mV]
37	10% ≤ 38; 50% ≤ 60; 90% ≤ 163	53	24.2
39a	10% ≤ 67; 50% ≤ 149; 90% ≤ 406	172	24.7
39b	10% ≤ 59; 50% ≤ 129; 90% ≤ 350	163	27.5
40a	10% ≤ 66; 50% ≤ 137; 90% ≤ 457	164	24.6
40b	10% ≤ 34; 50% 62; 90% ≤ 220	128	24.8

Material **37** shows the smallest average hydrodynamic size with 53 nm. It increases from material **40b** from 128 nm to **39b**/**40a** with 164 nm to **39a**. The hydrodynamic size increases with the degree of functionalization, showing the biggest size if functionalized with ALST1. The zeta potential shows no significant change upon functionalization. To confirm the attached metal complex on the surface of compound **40a** and **40b**, they were investigated using EDX and compared to compound **35**. The spectra of compound **40a** and **40b** looked identical and showed signals at 0.28, 0.95, 1.86, 6.39, 6.93, 8.02, 8.66, 8.86, 9.99, and 10.32 keV (Fig. 3.74; 40b see Chapter 7). The assignment of the signals to corresponding transitions is given in Table 3.22.[212]

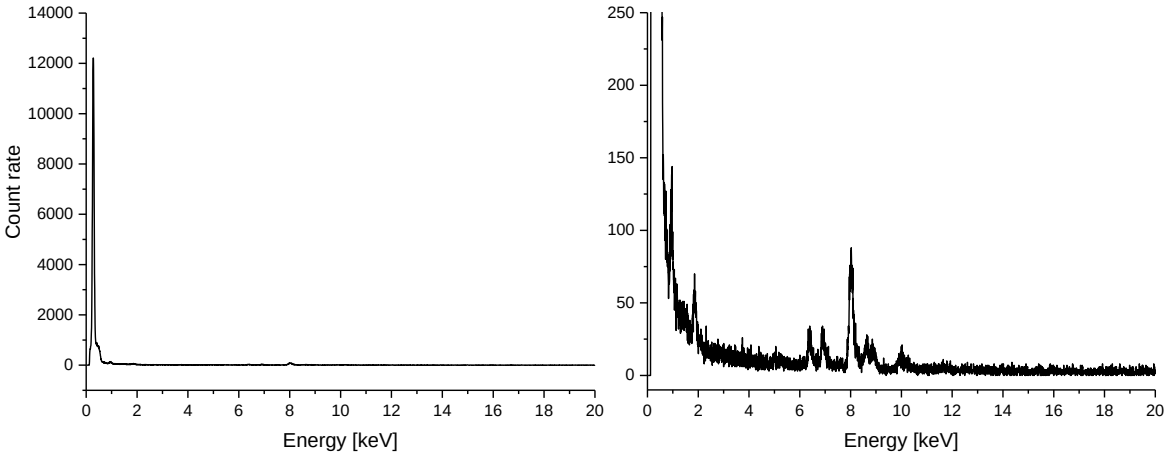

Fig. 3.74: EDX of material $^{[ReBr(CO)3(L)]\text{-}Aoa;ALST1}$DND **40a** on lacey carbon grid.

Tab. 3.22: EDX signals of materials $^{ReBr(CO)3(L)]-Aoa;ALST1}$DND **40a** and $^{[ReBr(CO)3(L)]-Aoa;butyl-capped}$DND **40b** with assignment to the corresponding element and its transition.[212]

Signal [keV]	Element	Transition
0.28	C	KL
0.95	Cu	$K_{II}M_{IV}$
1.86	Re	$M_{IV}N_{VI}$
6.39	Fe	KL_{II}
6.93	Co	KL_{III}
8.02	Cu	KL_{II}
8.66	Re	$L_{III}M_{III}$
8.86	Cu	KM_{II}
9.99	Re	$L_{II}M_{V}$
10.32	Re	$M_{I}N_{III}$

In comparison to $^{ReBr(CO)3(L)]-Aoa;ALST1}$DND **40a** and $^{[ReBr(CO)3(L)]-Aoa;butyl-capped}$DND **40b**, compound $^{Amine;Azide}$DND **37** showed signals in the EDX at 0.28, 0.95, 6.39, 6.93, 8.02, and 8.86 keV, lacking the rhenium signals observed for **40a** and **40b** (Fig. 3.75).

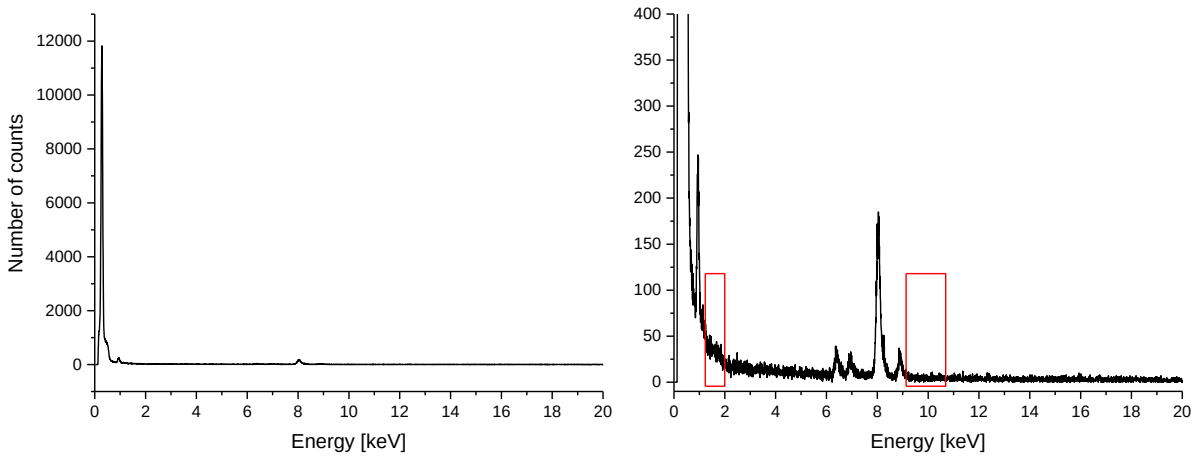

Fig. 3.74: EDX spectrum of material $^{Amine;Azide}$DND **37** on a lacey carbon grid.

The signals found in the EDX of compound $^{Amine;Azide}$DND **37** are assigned according to table 3.22 displayed before. The areas where rhenium signals would be expected are marked with red boxes. The very strong carbon signal at 0.28 eV is due to the DND itself as well as lacey carbon sample grid. The copper signal is also due to the used sample grid. The iron and cobalt signals are due to the sample chamber of the microscope. To check the successful attachment of the ALST1 peptide to the DND surface, materials **37**, **39a**, **39b**, **40a**, and **40b** were treated with 6

M hydrochloric acid for 24 h, the cleavage products were treated with PITC and then analyzed using HPLC according to the method established in Chapter 3.3.4. Material $^{Amine;Azide}$DND **37** showed 16 signals in the HPLC trace (Fig. 3.75). The R_t signals observed and calculated R_f values are given in Table 3.23. All of these signals are expected to be due to reactions with the nanoparticle $^{Amine;Azide}$DND **37**. Therefore, they have to be taken into consideration when evaluating the HPLC traces for materials **39a**, **39b**, **40a**, and **40b**. For evaluation, the amounts of the amino acids were calculated using the calibration factors displayed in Table 3.6 and the absorption of the individual signals. Then, the values were normalized on the amino acid with the fewest amount, rounded to whole numbers, and compared to the expected amino acid ratio of the peptide sequence assumed to be conjugated to the nanoparticle surface and the results discussed in Chapter 3.4.4.2 for the individual peptides upon acid hydrolysis and PITC derivatization.

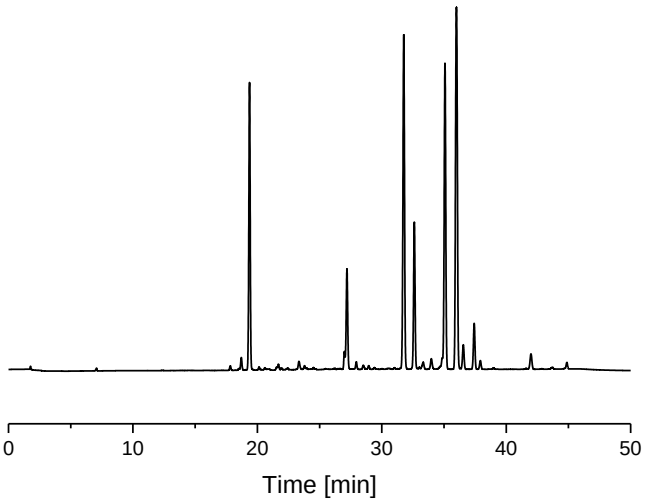

Fig. 3.75: HPLC trace at 254 nm of material **37** after digestion with 6 M hydrochloric acid and derivatization with PITC.

Tab. 3.23: Retention times R_t and retention factors R_f after digestion of $^{Amine;Azide}$DND **37** with 6 M HCl and subsequent derivatization with PITC.

Signal R_t [min]	R_f
17.82	1.52
18.68	1.64
19.37	1.74
21.72	2.08
23.26	2.29
27.22	2.86
27.95	2.94
28.44	3.03
28.88	3.09
31.78	3.50
32.59	3.62
33.33	3.72
34.01	3.82
35.06	3.97
36.04	4.11
36.53	4.18
37.41	4.30

The HPLC traces of materials $^{Cy5;ALST1}$DND **39a** and $^{Cy5;butyl\text{-}capped}$DND **39b** are overlaid in Figure 3.76. They show six signals for **39a**, which do not overlap with the signals of materials **39b**. The R_t were determined and the R_f were calculated to assign the signals to amino acids if possible (Tab. 3.24).

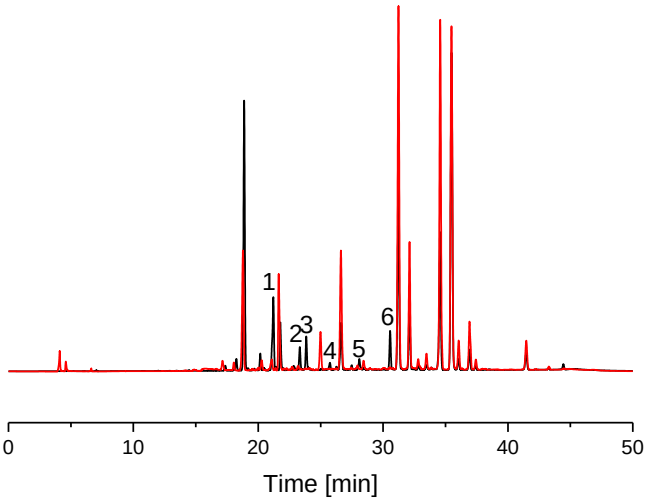

Fig. 3.76: HPLC chromatogram at 254 nm of compound **39a** (black) and **39b** (red) after digestion with 6 M hydrochloric acid and derivatization with PITC.

Tab. 3.24: Retention times R_t, Retention factors R_f, and assignments of the identifiable signals found in the overlay of the HPLC traces at 254 nm after digestion of materials **39a** and **39b** and subsequent derivatization with PITC.

Peak	R_t [min]	R_f	Assignment [a]	Amount [nmol] [a]	Normalized [b]
1	21.21	2.02	glycine	50	3
2	23.35	2.33	glutamate	19	1
3	23.87	2.40	proline	20	1
4	25.74	2.67	alanine	16	1
5	28.07	3.00	tyrosine	19	1
6	30.58	3.36			

[a] assigned and calculated according to Table 3.6; [b] rounded values.

The amino acids glycine, glutamate, proline, alanine, and tyrosine were clearly identified this way, while signal 6 (Tab. 3.24) could not be assigned to any known species. Still, a ratio of normalized G:A:Y:P:E using the calibration factors presented in Chapter 3.4.4.1 was calculated. Thus, values of 3:1:1:1:1 was found, matching the expected ratio derived from the amino acid sequence of ALST1, indicating successful conjugation of the peptide to the DND surface. Using this results, the peptide loading for material $^{Cy5;ALST1}$DND **39a** was calculated as 24 µmol/g. The HPLC traces of materials $^{[ReBr(CO)3(L)]\text{-}Aoa;ALST1}$DND **40a** and $^{[ReBr(CO)3(L)]\text{-}Aoa;butyl\text{-}capped}$DND **40b** are overlaid in Figure 3.77. They show seven signals for **40a**, which do not overlap with the signals of compound **40b**. The R_t were determined and the R_f were calculated to assign the

signals to amino acids if possible (Tab. 3.25). The amino acids glycine, glutamate, proline, alanine, and tyrosine were clearly identified this way, while signal 7 (Tab. 3.25) could not be assigned to any known species.

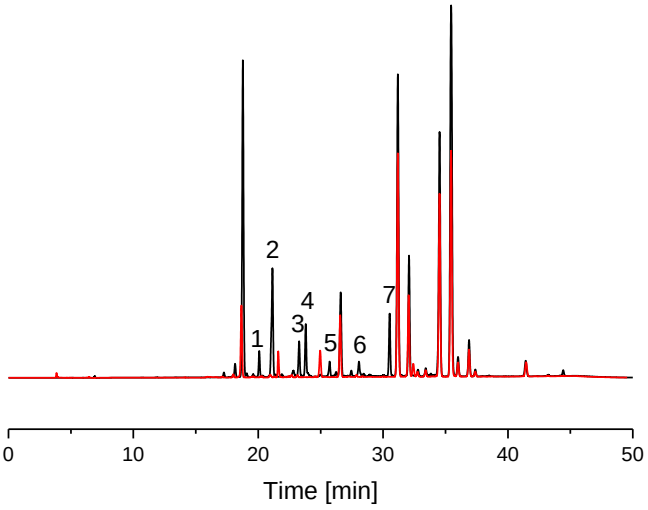

Fig. 3.77: HPLC chromatogram at 254 nm of compound **40a** (black) and **40b** (red) after digestion with hydrochloric acid and derivatization with PITC.

Tab. 3.25: Retention times R_t, Retention factors R_f, and assignments of the identifiable signals found in the overlay of the HPLC traces at 254 nm after digestion of materials **40a** and **40b** and subsequent derivatization with PITC.

Peak	R_t [min]	R_f	Assignment [a]	Amount [nmol] [a]	Normalized [b]
1	20.10	1.91	arginine	20	1
2	21.16	2.08	glycine	68	3
3	23.19	2.36	glutamate	26	1
4	23.88	2.45	proline	27	1
5	25.67	2.71	alanine	25	1
6	28.14	3.08	tyrosine	24	1
7	30.42	3.41			

[a] assigned and calculated according to Table 3.6; [b] rounded values.

Still, a ratio of normalized G:A:R:Y:P:E using the calibration factors presented in Chapter 3.4.4.1 was calculated. Thus, an amino acid ratio of 3:1:1:1:1:1 was found, matching the expected ratio for the amino acid sequence of ALST1, indicating successful conjugation of the peptide to the DND surface. Using this results, the peptide loading for material $^{[ReBr(CO)3(L)]\text{-}Aoa;ALST1}$DND **40a** was calculated as 25 µmol/g, also matching the peptide surface loading of material $^{Cy5;ALST1}$DND **39a**

3.6.2 Luminescence studies with materials $^{Cy5;ALST1}$DND and $^{[ReBr(CO)3(L)]-Aoa;ALST1}$DND

Materials $^{Cy5;ALST1}$DND **39a** and $^{[ReBr(CO)3(L)]-Aoa;ALST1}$DND **40a** were investigated by fluorescence spectroscopy to compare the luminophoric performance of Cy5 versus the metal complex [ReBr(CO)$_3$(*L*)] (**22**) attached to the nanoparticle surface. Thus, both materials were suspended in ultrapure water and a mixture of dichloromethane and methanol (1:1) and the concentration was adjusted by UV/Vis spectroscopy to an optical density OD_{600} of 0.25 at 600 nm. The excitation spectrum of **39a** was recorded at 690 nm and the emission spectrum was recorded under excitation at 620 nm. These wavelengths were chosen to avoid an overlap of the excitation and emission signal due to the small Stokes shift (Fig. 3.78).

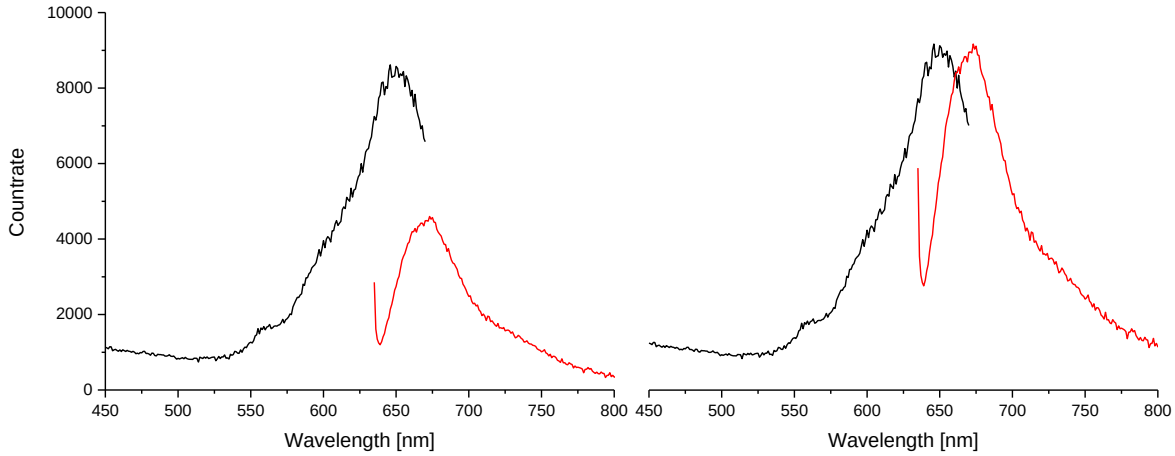

Fig. 3.78: Emission and excitation spectra of $^{Cy5;ALST1}$DND **39a** in water at an OD_{600} of 0.25. The left spectrum shows the original spectra, the right panel the normalized ones to facilitate comparison.

The lifetime of material **39a** in water was determined as < 0.4 ns by the time-correlated single-photon counting (TCSPC) method. In water, material **39a** shows an excitation maximum at 649 nm and an emission maximum at 672 nm, matching the values expected for Cy5 in aqueous solution. [190-191] Then, the experiment was repeated with compound **39a** suspended in dichloromethane/methanol (1:1) (Fig. 3.79)

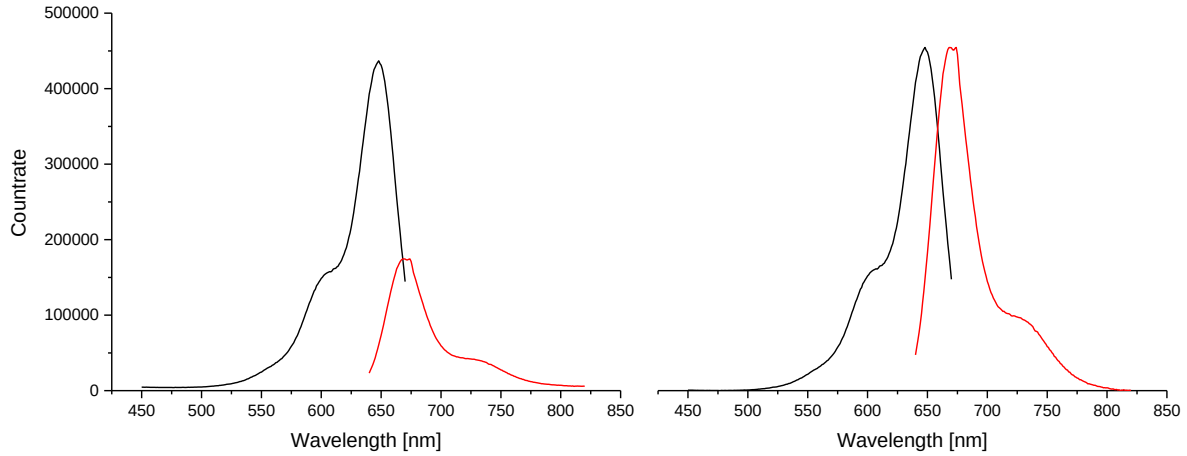

Fig. 3.79: Emission and excitation spectra of $^{Cy5;ALST1}$DND **39a** in dichloromethane/methanol (1:1) at an OD_{600} of 0.25. The left spectrum shows the original spectra, the right panel the normalized ones to facilitate comparison.

The lifetime of material **39a** in dichloromethane/methanol (1:1) was determined as 0.9 ns by the time-correlated single-photon counting (TCSPC) method. Furthermore, material **39a** shows an excitation maximum at 647 nm and an emission maximum at 671 nm, matching the values expected for Cy5 in organic solution.[190-191]

The excitation spectrum of $^{[ReBr(CO)3(L)]-Aoa;ALST1}$DND **40a** was recorded at 600 nm and the emission spectrum was recorded under excitation at 415 nm. A sharp emission at 482 nm and a broad emission at 612 nm were observed. (Fig. 3.80).

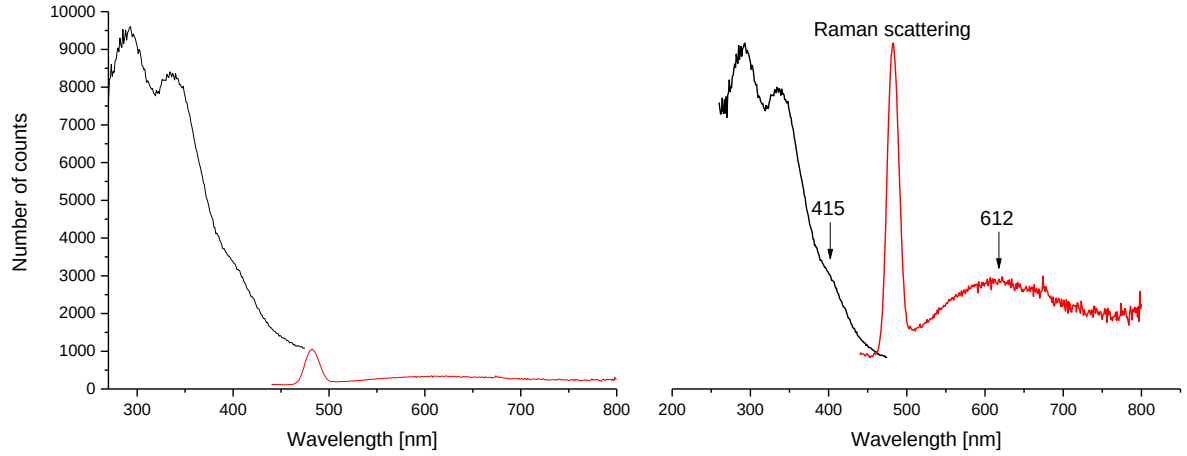

Fig. 3.80: Emission and excitation spectra of $^{[ReBr(CO)3(L)]-Aoa;ALST1}$DND **40a** in water at an OD_{600} of 0.25. The left spectrum shows the original spectra, the right panel the normalized ones to facilitate comparison.

The signal at 482 nm is due to Raman scattering of the excitation light and the signal at 612 nm to the phosphorescence of the rhenium complex **22** attached to the nanodiamond surface. In water, the fluorescence intensity was too weak for lifetimes to be determined by the time-correlated single-photon counting (TCSPC) method. The experiment was repeated with [ReBr(CO)3(L)]-Aoa;ALST1DND **40a** suspended in dichloromethane/methanol (1:1). The excitation spectrum of material **40a** was recorded at 600 nm and the emission spectrum was recorded under excitation at 415 nm. A sharp emission at 482 nm and a broad emission at 612 nm was observed. (Fig. 3.81).

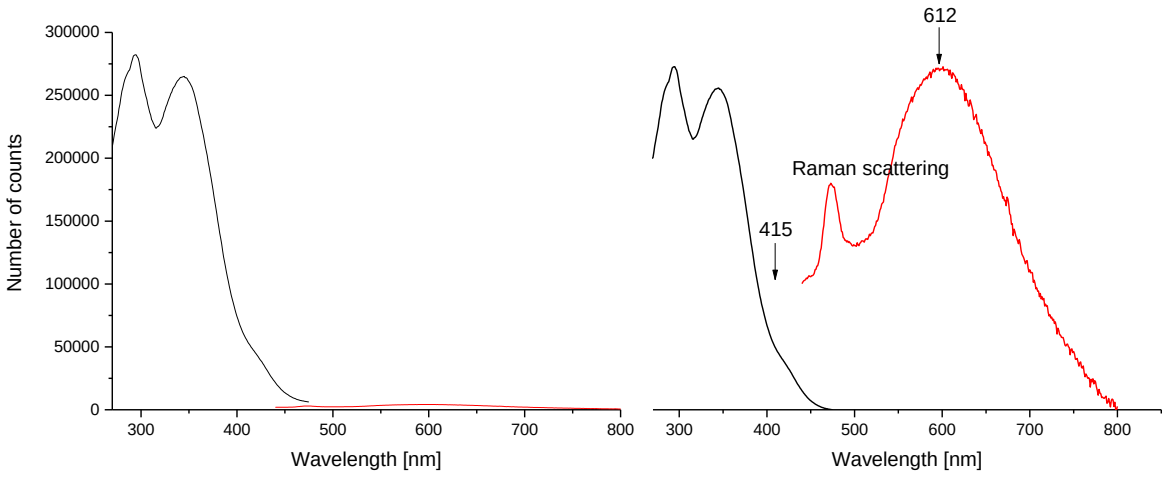

Fig. 3.81: Emission and excitation spectra of [ReBr(CO)3(L)]-Aoa;ALST1DND **40a** in dichloromethane/methanol (1:1) at an OD_{600} of 0.25. The left spectrum shows the original spectra, the right panel the normalized ones to facilitate comparison.

The signal at 482 nm is assigned to Raman scattering of the excitation light and the signal at 612 nm to the phosphorescence of the rhenium complex **22** attached to the nanodiamond surface. The phosphorescence intensity is higher than in water. Multiple lifetimes were determined by the time-correlated single-photon counting (TCSPC) method with τ_1 = 110 ns, τ_2 = 30 ns, τ_3 = 3.1 ns, and τ_4 = 0.6 ns. Due to size distribution of the detonation nanodiamond, the luminescent metal complex molecules are exposed to different environments, since the number of attached peptide and metal complexes of an individual particle changes with the size of the carrier material. These different environments of the inorganic luminophor generate several different observable lifetimes.

In summary, [ReBr(CO)$_3$(*L*)] shows a larger Stokes shift and longer lifetimes compared to the organic fluorescent dye Cy5. However, the metal complex luminophor is strongly quenched in water, making it less suitable for cell imaging than Cy5.

3.6.3 Cell uptake and imaging of bifunctionalized detonation nanodiamond

The cellular uptake of the materials $^{Amine;Azide}$DND **37**, $^{Cy5;ALST1}$DND **39a**, $^{Cy5;butyl\text{-}capped}$DND **39b** $^{[ReBr(CO)3(L)]\text{-}Aoa;ALST1}$DND **40a**, and $^{[ReBr(CO)3(L)]\text{-}Aoa;butyl\text{-}capped}$DND **40b** by mammary epithelial cell line MDA MB 231was investigated by fluorescence microscopy. The nucleus was co-stained with 4,5-diamindino-2-phenylindole (DAPI).). In Figure 3.82, several oval cells can be seen with the nuclei showing up in blue. Furthermore, gray particles can be seen covering the cell membrane. These are assigned to agglomerated material $^{Amine;Azide}$DND **37**, which show no colour due to lack of a fluorophor.

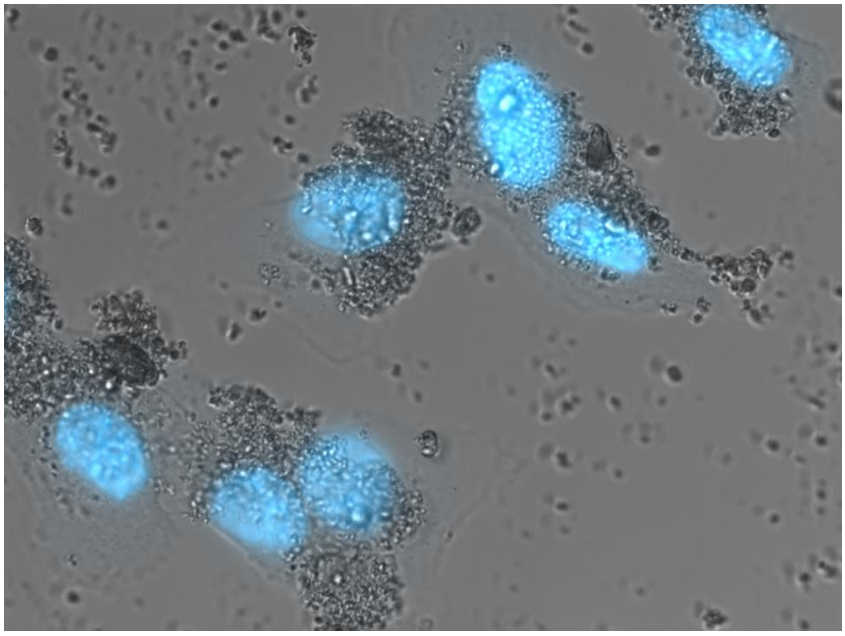

Fig. 3.82: Fluorescence microscopy image of mammary epithelial cell line MDA MB 231 incubated with $^{Amine;Azide}$DND **37**. The cell nuclei are co-stained with DAPI and show up in a blue colour. The nuclei have a diameter of approximately 10 µm.

In Figure 3.83, several oval cells can be seen with the nuclei showing up in blue. Furthermore, gray debris-like particles can be seen next to the cells. Unfortunately, materials $^{[ReBr(CO)3(L)]\text{-}Aoa;ALST1}$DND **40a** and $^{[ReBr(CO)3(L)]\text{-}Aoa;butyl\text{-}capped}$DND **40b** could not be detected by fluorescence microscopy as the emission intensity of the attached rhenium complex **22** was to low and there was no appropriate microscope filter available. Still, the images indicate agglomeration of the particles, with **40b** showing a higher tendency to agglomerate than **40a** (Fig. 3.83). This might be due to the butyl-capped azide groups which promote hydrophobic interaction.

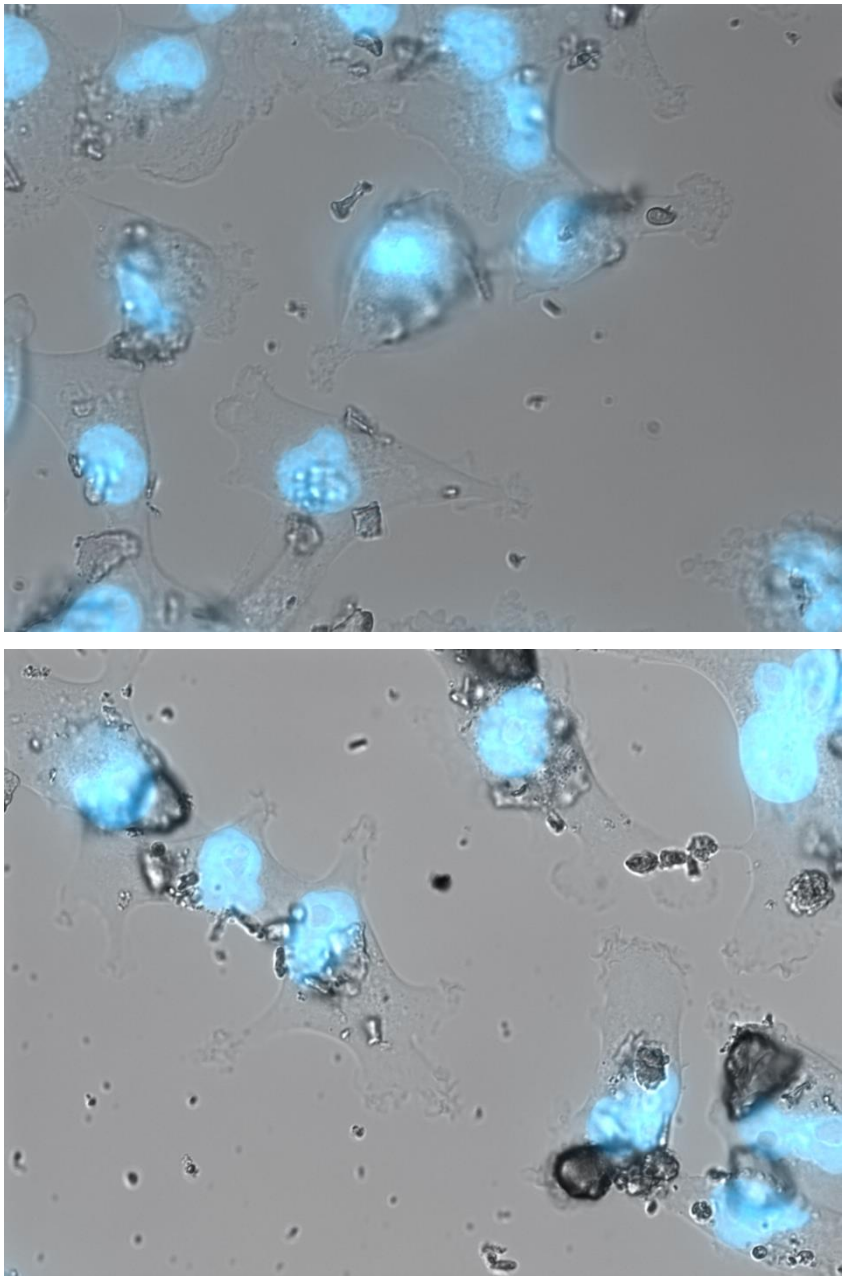

Fig. 3.83: Fluorescence microscopy image of mammary epithelial cell line MDA MB 231 incubated with $^{[ReBr(CO)3(L)]\text{-}Aoa;ALST1}$DND **40a** (top) and $^{[ReBr(CO)3(L)]\text{-}Aoa;butyl\text{-}capped}$DND **40b** (bottom). The cell nuclei are co-stained with DAPI and show up in a blue colour. The nuclei have a diameter of approximately 10 µm.

In Figure 3.84, several oval cells can be seen with the nuclei showing up in blue. Furthermore, red particles are observed next to the cells. Material $^{Cy5;ALST1}$DND **39a**, $^{Cy5;butyl\text{-}capped}$DND **39b** show red fluorescence due to the attached Cy5. However, these particles are not internalized into cells, but show agglomeration instead. As with **40a+a**, material **39b** also has a stronger tendency to agglomerate than compound **39a**. This might be due to the butyl-capped azide groups which promote hydrophobic interaction.

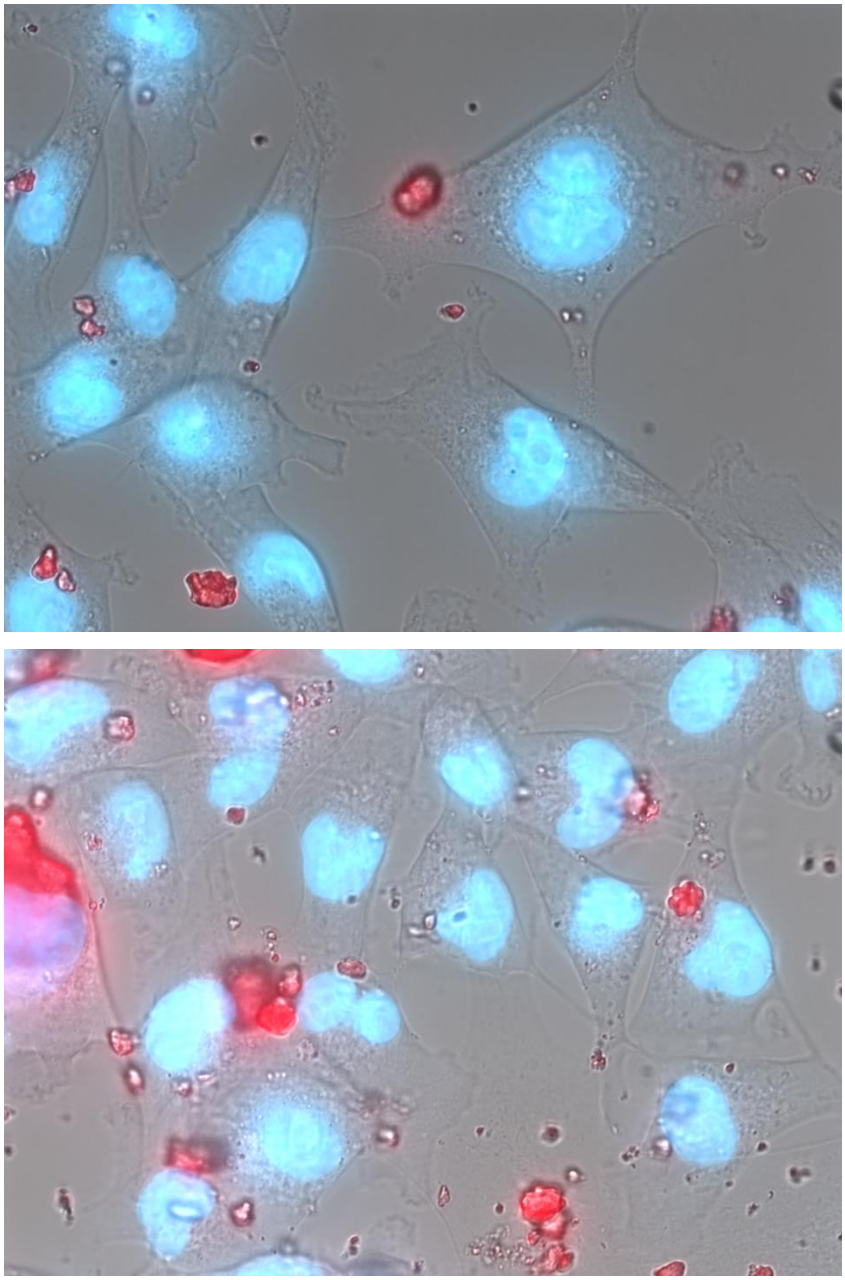

Fig. 3.84: Fluorescence microscopy image of mammary epithelial cell line MDA MB 231 incubated with $^{Cy5;ALST1}$DND **39a** (top) and $^{Cy5;butyl\text{-}capped}$DND **39b** (bottom). The cell nuclei are co-stained with DAPI and show up in a blue colour. The nuclei have a diameter of approximately 10 µm.

Apparently, the conjugation of ALST1 to the nanodiamond surface does not enhance their cellular uptake as expected from published results.[155-156] This might be due to agglomeration of the particles, which prevents endocytosis. Another reason might be that the peptide chain is aligned perpendicular on the nanodiamond surface, since they are known for strong non-covalent surface binding to proteins and peptides.[65, 88, 91, 95] Thus, the peptide is not able to interact with receptors on the cell membrane to promote cellular uptake of the particle.

4 Summary

The aim of this work was to synthesize and functionalize different bio-relevant nanomaterials like silica-coated superparamagnetic iron oxide nanoparticles (SPIONs) as contrast agents for T_2 magnetic resonance imaging (MRI) and detonation nanodiamond (DND) with the neurohormone peptide allatostatin 1 (ALST1) and a fluorescent dye. Analytical techniques for the determination and quantification of surface functional groups like amines, azides, and peptides were also developed and established.

Thus, in the first part of the work, a TGF-β_1 binding peptide and allatostatin 1 (ALST1), both supposed to act as active tumour targeting vectors, were synthesized by solid-phase peptide synthesis (SPPS) and characterized by high pressure liquid chromatography (HPLC) and mass spectrometry. Then, azide-functionalized silica nanoparticles were synthesized by the *Stöber* process and characterized by transmission electron microscopy (TEM) and infrared spectroscopy (IR). The surface loading of amine and azide groups was determined by a new protocol. The azide groups were reduced with sodium boronhydride to amine and then functionalized with Fmoc-Rink Amide linker according to a standard SPPS protocol. Upon cleavage of Fmoc by piperidine, the resulting dibenzofulvene and its piperidine adduct were quantified by UV/Vis spectroscopy and used to determine the amount of amine groups on the nanoparticle surface. Then, ALST1 and related tyrosine- and phenylalanine substituted model peptides were conjugated to the azide-functionalized silica nanoparticles by copper(I)-catalyzed azide-alkyne dipolar cycloaddition (CuAAC). The successful peptide conjugation was demonstrated by the *Pauly* reaction, which however is only sensitive to histidine- and tyrosine-containing peptides. As a more general alternative, the acid hydrolysis of the peptides to their individual amino acid building blocks followed by derivatization with phenyl isothiocyanate (PITC) allowed the separation, determination, and quantification of the constituent amino acids by HPLC.

In the second part of the work, amine- and azide-functionalized silica-coated superparamagnetic iron oxide nanoparticles (SPIONs) were synthesized by co-precipitation and subsequent silica-coated based on the *Stöber* process and characterized by TEM and IR. The amine surface loading was determined by the method already established for the pure silica systems. The azide surface loading could also be quantified by reduction with sodium boronhydride to amine groups and then conjugation to Fmoc-Rink amide linker. Upon cleavage of Fmoc with piperidine, the total amine surface loading was obtained. The amount of azide surface groups was then determined from the difference of the total amine surface loading and the amine

surface loading. Thus, it was possible to quantify both amine and azide surface groups on a single nanoparticle system. Superparamagnetic iron oxide nanoparticles (SPIONs) are potent T_2 contrast agents for magnetic resonance imaging (MRI). Due to their natural metabolism after injection into the blood stream, SPIONs mostly end up inside macrophages, liver, spleen or kidneys. To generate a potential target-specific SPION-based T_2 contrast agent for MRI, the neurohormone peptide ALST1 was conjugated by CuAAC to the azide- and amine functionalized superparamagnetic iron oxide nanoparticles, since ALST1 is supposed to target difficult-to-treat neuroendocrinic tumours due to its analogy to galanin and somastatin receptor ligands. The organic fluorescent dye cyanine 5 (Cy5) was also conjugated to the silica-coated superparamagnetic iron oxide nanoparticles (SPIONs) via a NHS-ester to the amines to enable cell uptake studies by fluorescence microscopy. These constructs were characterized by TEM, dynamic light scattering (DLS), and IR. The amino acids of the conjugated ALST1 were determined by the HPLC method as described before for peptide-modified silica nanoparticle surfaces. Then, the relaxivity r_2 was measured at 7 T. However, a r_2 value of 27 $L/mmol_{Fe}\cdot s$ for the dual ALST1-/Cy5-functionalized silica-coated SPIONs was not comparable to T_2 contrast agents in clinical use, since their relaxivity is commonly determined at 1.5 T, and no such instrument was available. However, it can be assumed that the synthesized dual ALST1-/Cy5-functionalized silica-coated SPION would show a lower r_2 at 1.5 T than at 7T. Commercial T_2 MRI contrast agents like *VSOP-C184* from *Ferropharm* show at r_2 values of about 30 $L/mmol_{Fe}\cdot s$ at 1.5 T. Still, the relaxivity of the new material has some potential for application as a T_2 contrast agent. Then, the material was used in cell uptake studies by fluorescence microscopy with the conjugated Cy5 dye as a probe. The dual ALST1-/Cy5-functionalized silica-coated SPION showed a high degree of agglomeration with no cellular uptake unlike described for ALST1-functionalized nanoparticles in literature. It is assumed that upon agglomeration of the particles, constructs form which are unable to be internalized by the cellular endocytotic pathways anymore. As a future perspective, the tendency of the particle to agglomerate should be reduced by changing the coating material to polyethylene glycol (PEG) or chitosan, which are known to be bio-compatible, bio-degradable and prevent agglomeration.

In the third part of the work, the rhenium compound $[ReBr(CO)_3(L)]$ with L = 2-phenyl-1*H*-imidazo[4,5-*f*][1,10]phenanthroline and its manganese analogue were synthesized by heating the ligand and rhenium pentacarbonyl bromide or and manganese pentacarbonyl bromide respectively, in toluene. However, $[MnBr(CO)_3(L)]$ was unstable upon illumination by UV light at 365 nm. Thus, it was dismissed for further application. The photophysical properties of

[$ReBr(CO)_3(L)$] were explored, by determination of the excited-state life time by the time-correlated single-photon counting (TCSPC) method and the quantum yield by a fluorescence spectrometer equipped with an integration sphere. A value of τ = 455 ns, a Stokes shift of 197 nm and a rather low quantum yield ϕ = 0.05 were found. Metal complexes are supposed to have superior properties compared to organic dyes due to their large Stokes shifts, long excited-state life times, and high quantum yields. Thus, amine- and azide-functionalized detonation nanodiamond (DND) as an alternative biological inert carrier system was functionalized with ALST1 to enhance its cell uptake properties. A luminescent probe for cell uptake studies using fluorescence microscopy was also attached, either based on the new rhenium complex or the commercially available organic dye Cy5, respectively. The aldehyde-functionalized rhenium complex was conjugated to the DND via oxime ligation, which is known to be a mild and catalyst-free conjugation method. The amount of peptide ALST1 on the DND was analyzed and quantified after acid hydrolysis and PITC derivatization by HPLC as described before. Then, the ALST1-/luminescent probe-functionalized DND was investigated for its photophysical properties by fluorescence spectroscopy. The Cy5-functionalized material showed a slightly lower fluorescence performance in aqueous solution than reported in literature and commercial suppliers with a life time τ < 0.4 ns and quantum yields ϕ not determinable by integration sphere due to the week signal intensity. The rhenium complex-functionalized material had a very low signal intensity in only aqueous medium, and thus determination of life times and quantum yield by fluorescence spectroscopy was not possible. After incubation with MDA-MB 231 cells, the Cy5-functionalized DND could easily be detected due to its red fluorescence. However, it was not possible to visualize the rhenium complex-functionalized DND with fluorescence microscopy due to the low fluorescence intensity of the complex in aqueous medium and the lack of proper filters for the fluorescence microscope. Cy5-functionalized DND did not show any cellular uptake in fluorescence microscopy after conjugation with ALST1. Since the nanodiamond surface is known to strongly adsorb peptides and proteins, it is assumed that the peptide chain is oriented perpendicular to the nanoparticle surface and thus not able to interact with cell membrane receptors to promote cell uptake of the particles. As a future perspective, the ALST1-promoted cellular uptake of the DND should be improved by using different linker systems for peptide conjugation to prevent adsorption of the peptide chain on the particle surface.

The new analytical methods for amino-, azide-, and peptide-functionalized nanoparticles have great potential to assist in the quantification of nanoparticle surface modifications by UV/Vis spectroscopy and HPLC. The determination of surface amine and azide groups based on the

cleavage of conjugated Fmoc-Rink amide linker and detected by UV/Vis spectroscopy is applicable to all amine-/azide-functionalized nanomaterials. However, particles which form very stable suspension with the cleavage mixture can cause quantification problems due to scattering, making an accurate quantification of dibenzofulvene and its piperidine adduct impossible. The detection of tyrosine- and histidine-containing peptides based on the *Pauly* reaction is well-suited as a fast and easy-to-perform qualitative demonstration of successful peptide surface conjugation. However, its major drawback as a colourimetric approach is that coloured particles cannot be evaluated by this method. The amino acid analysis based on HPLC after acid hydrolysis of peptides conjugated to nanoparticle surfaces to its individual building blocks and subsequent derivatization with PITC, can be used on all nanomaterials with peptide or protein surface modification. It allows detection of amino acids down to picomolar concentrations and even enables analysis of very small peptide surface loadings. However, the resulting HPLC traces are difficult to analyze.

Three new analytical methods based on UV/Vis and HPLC techniques have been developed and established. They assisted in the characterization of the synthesized DND and SPIONs with dual functionalization by ALST1 and Cy5 or [$ReBr(CO)_3(L)$], respectively. However, the nanomaterials showed no cellular uptake due to a high tendency to agglomerate. The cellular uptake should be improved and the tendency to agglomerate of the SPIONs should be reduced by changing the surface coating from silica to either PEG or chitosan. Furthermore, different linker systems for connecting peptides to DND surfaces should be synthesized and evaluated to reduce potential peptide chain adsorption.

Zusammenfassung

Das Ziel dieser Arbeit war die Synthese und Funktionalisierung biologisch relevanter Nanomaterialien wie die Silica-umhüllten superparamagnetischen Eisenoxid Nanopartikel (SPIONs) als Kontrastmittel für T_2 gewichtete Magnetresonanztomographie (MRT) und Detonantionsnanodiamant mit dem Neurohormonpeptid Allatostatin 1 (ALST1) sowie einem Fluoreszenzfarbstoff. Des Weiteren sollten analytische Methoden zur Bestimmung und Quantifizierung von funktionellen Oberflächenmodifikationen wie Amine, Azide und Peptide entwickelt und etabliert werden.

Aus diesem Grund wurden im ersten Teil der Arbeit ein TGF-β1 bindendes Peptid und Allatostatin 1 (ALST1), welche beide spezifisch Tumorgewebe anzielen, mit Hilfe der Festphasen Peptid Synthese (SPPS) hergestellt und durch HPLC und Massenspektrometrie charakterisiert. Danach wurden Azid-funktionalisierte Silica-Partikel durch den *Stöber* Prozess hergestellt und mit Hilfe von Transmissionselektronenmikroskopie (TEM) und Infrarot Spektroskopie (IR) charakterisiert. Die Oberflächenbeladung von Aminen und Aziden wurde mit einer neuen Methode bestimmt. Azidgruppen wurden mit Natriumborhydrid zu Aminen reduziert und anschließend mit dem Fmoc-Rink Amid Linker unter Verwendung des allgemeinen SPPS Verfahrens. Durch die Abspaltung von Fmoc mit Piperidin wurden Dibenzofulven und sein Piperidin-Adduct gebildet und mit Hilfe von UV/Vis Spektroskopie quantifiziert um die Oberflächenbeladung der Amino-Gruppen auf den Nanopartikeln zu bestimmen. Danach wurden ALST1 und verwandte Tyrosin- und Phenylalanin- substituierte Modellpeptide synthetisiert und durch die Kuper(I)-katalysierte Azid-Alkin dipolare Cycloaddition (CuAAC) an die Oberfläche der Silica-Partikel konjugiert. Die erfolgreiche Peptidkonjugation wurde mit Hilfe der *Pauly* Reaktion, welche jedoch ausschließlich auf Tyrosin- und Histidin-haltige Peptide und Proteine anwendbar ist, nachgewiesen. Als eine universellere Alternative wurden die Peptid-konjugierten Nanomaterialien mit konzentrierter Salzsäure hydrolysiert und anschließend mit Phenylisothiocyanat (PITC) derivatisiert, was die Trennung, Bestimmung und Quantifikation der individuellen Aminosäuren des Peptids durch HPLC ermöglichte.

In dem zweiten Teil dieser Arbeit wurden Amin- und Azid-funktionalisierte Silica-umhüllte superparamagnetische Eisenoxidnanopartikel (SPIONs) durch Co-Präzipitation und anschließender Silica-Ummantelung basierend auf dem *Stöber* Prozess synthetisiert und mit Hilfe von TEM und IR charakterisiert. Die Oberflächenbeladung der Aminogruppen wurde an Hand der bereits etablierten Methode für Silica-Partikel bestimmt. Die Oberflächenbeladung der Azidgruppen wurde quantifiziert durch deren Reduktion mit Natriumborhydrid zu

Aminogruppen und der darauf folgenden Verknüpfung mit dem Fmoc-Rink Amid Linker. Durch die Abspaltung des Fmoc mit Piperidin und dessen Quantifizierung durch UV/Vis Spektroskopie wurde so die gesamte Aminogruppen Oberflächenbeladung erhalten. Die Oberflächenbeladung mit Azidgruppen wurde dann durch die Differenz aus gesamter Amin- und tatsächlicher Amin-Oberflächenbeladung berechnet. Auf diese Weise war es möglich die Oberflächenbeladung sowohl von Aminen, als auch von Aziden an nur einem einzigen Nanopartikelsystem zu bestimmen. SPIONs können als Kontrastmittel für T_2-gewichtete MRT Messungen verwendet werden. Jedoch werden sie auf Grund ihres Metabolismus nach der Injektion ins Blutsystem von Makrophagen, Leber, Milz und Niere aufgenommen. Um ein potentielles, gewebespezifisches SPION-basiertes Kontrastmittel für T_2-gewichtete MRT Messungen zu erzeugen wurde das Neurohormonpeptid ALST1 mit Hilfe der CuAAC an die Azid-/Amin-funktionalisierten Silica-ummantelten SPIONs konjugiert, da von ALST1 eine Spezifität auf schwierig zu behandelnde neuroendokrine Tumore vermutet wird, auf Grund seiner Ähnlichkeit zu Galanin und Somastatin Rezeptorliganden. Der organische Fluoreszenzfarbstoff Cyanin 5 (Cy5) wurde ebenfalls an den Azid-/Amin-funktionalisierten Silica-ummantelten SPIONs über einen NHS-Ester konjugiert um Zellaufnahmestudien mit Hilfe von Fluoreszenzmikroskopie zu ermöglichen. Diese Materialien wurden mit TEM, dynamischer Lichtstreuung (DLS) und IR charakterisiert. Die Aminosäuren des konjugierten ALST1 wurden an Hand der bereits für Silica-Partikel beschriebenen HPLC-Methode bestimmt. Danach wurde die Relaxivität r_2 bei 7 T gemessen. Leider sind der gemessene Wert von 27 $L/mmol_{Fe}\cdot s$ für das duale System ALST1-/Cy5-functionaliserte Silica-ummantelte SPIONs nicht mit klinisch verwendete T_2 Kontrastmittel zu vergleichen, da diese bei einer Feldstärke von 1.5 T verwendet werden. Es ist jedoch anzunehmen, dass das synthetisierte Nanopartikelsystem bei 1.5 T eine geringere Relaxivität r_2 zeigen würde als bei 7 T. Jedoch zeigen kommerzielle Kontrastmittel für T_2-gewichtete MRT Messungen wie zum Beispiel *VSOP-C184* von *Ferropharm* r_2 Werte um die 30 $L/mmol_{Fe}\cdot s$. Von daher hat das neue Material durchaus Potential als Kontrastmittel für T_2-gewichtete MRT Messungen. Danach wurde das Material auf seine Zellaufnahme mit Hilfe von Fluoreszenzmikroskopie unter Verwendung des konjugierten Cy5 als Sonde untersucht. Die dualen ALST1-/Cy5-functionaliserte Silica-ummantelte SPIONs wurden mit MDA-MB 231 Zellen inkubiert, zeigten jedoch einen hohen Grad an Agglomeration, wobei große Konstrukte gebildet wurden die nicht mehr durch die zellularen Endozytosewege internalisiert werden konnten. Für weitere Anwendungen muss die Tendenz der Partikel zur Agglomeration verringert werden. Dies kann durch einen Wechsel der Hülle von Silica zu Polyethylenglykol (PEG) oder Chitosan erreicht werden, welche dafür

bekannt sind Agglomeration zu verhindern als auch biologisch kompatibel, abbaubar zu sein. Im dritten Teil der Arbeit wurde die Rheniumverbindung [$ReBr(CO)_3(L)$] mit *L* = 2-Phenyl-1*H*-imidazo[4,5-*f*][1,10]phenanthrolin und ihr Mangan-Analogon synthetisiert durch Erhitzen des Liganden und Bromopentacarbonylrhenium, beziehungsweise Bromopentacarbonyl-mangan, in Toluol. Der Komplex [$MnBr(CO)_3(L)$] wurde jedoch wegen seiner Instabilität bei Belichtung mit UV-Licht der Wellenlänge 365 nm für weitere Anwendungen verworfen. Die photophysikalischen Eigenschaften von [$ReBr(CO)_3(L)$] wurden untersucht durch die Bestimmung der Lebenszeit des angeregten Zustandes mit der *time-correlated single-photon counting* (TCSPC) Methode und die Quantenausbeute mit Hilfe eines Fluoreszenzspektrometers welches mit einer Integrationsphäre ausgerüstet war. Ein Wert von τ = 455 ns, einem *Stokes shift* von 197 nm und eine eher niedrige Quantenausbeute ϕ = 0.05 wurden ermittelt. Es wird behauptet, dass Metallkomplexe den organischen Fluoreszenzfarbstoffen überlegende *Stokes shifts*, Lebenszeiten des angeregten Zustandes sowie Quantenausbeuten haben. Aus diesem Grund wurde der Amino- und Azid-funktionalisierte DND mit ALST1, auf Grund seiner Eigenschaft die Zellaufnahme zu verstärken, funktionalisiert. Des Weiteren wurde eine Fluoreszenzsonde für Zellaufnahmestudien unter Verwendung von Fluoreszenzmikroskopie und die Partikeloberfläche konjugiert, welche entweder auf [$ReBr(CO)_3(L)$] oder Cy5 basierten. Die Aldehyd-funktionalisierte Rheniumverbindung wurde über die Oxime Ligation an den Nanopartikel konjugiert, welche als milde und Katalysator-freie Konjugationsmethode bekannt ist. Die Menge des Peptids ALST1 auf der DND Oberfläche wurde durch HPLC nach saurer Hydrolyse und Derivatisierung mit PITC wie zuvor beschrieben analysiert und quantifiziert. Danach wurden die dualen ALST1-/Lumineszenzsonde-funktionalisierten DND in Bezug auf ihre photophysikalischen Eigenschaften mit Hilfe der Fluoreszenzspektroskopie untersucht. Das Cy5-funktionaliserte Material zeigte in wässrigem Medium etwas geringere Lebenszeit des angeregten Zustandes mit $\tau < 0.4$ ns als in der Literatur beschrieben und eine nicht bestimmbare Quantenausbeute durch die Integrationssphäre auf Grund der schwachen Emissionsintensität. Das [$ReBr(CO)_3(L)$]-funktionalisierte Material zeigte eine sehr geringe Emissionsintensität in wässrigen Medium, welche es unmöglich machte die Lebenszeit des angeregten Zustandes und die Quantenausbeute zu bestimmen. Es war nicht möglich das Rhenium Komplex-funktionalisierte Material auf Grund seiner geringen Emissionsintensität in der Fluoreszenzmikroskopie nach Inkubation mit MDA-MB 231 Zellen zu visualisieren. Nach der Inkubation des Cy5-functionalisierten DND mit MDA-MB 231 Zellen, konnte das Material sehr gut auf Grund seiner roten Fluoreszenz identifiziert werden. Jedoch zeigte es keine

Internalisierung in die Zellen nach Konjugation mit ALST1. Es wird vermutet dass die Peptidkette flach auf die Nanodiamantoberfläche, welche für ihre starke, nicht-kovalente Interaktion mit Proteinen und Peptiden bekannt ist, adsorbiert ist. Für zukünftige Anwendungen muss die ALST1-vermittelte Zellaufnahme der Detonationsnanodiamanten verbessert werden. Dies kann erreicht werden durch die Verwendung anderer Linker-Systeme zur Verbrückung von Peptid und Partikeloberfläche um Adsorption zu verhindern.

Die neuen analytischen Methoden für Amino-, Azid-, und Peptid-funktionalisierte Nanopartikel haben großes Potential in der Quantifizierung von Oberflächenmodifikationen von Nanopartikeln durch HPLC und UV/Vis. Die Bestimmung von Oberflächenbeladungen von Amin- und Azidgruppen basierend auf der Abspaltung von konjugiertem Fmoc des Fmoc-Rink Amid Linkers und Detektion durch UV/Vis Spektroskopie ist anwendbar auf alle Amin- und Azid-funktionalisierten Nanomaterialien. Jedoch kann es bei Partikeln welche besonders stabilen Suspensionen mit der Abspaltlösung bilden zu Problemen in der Quantifikation von Dibenzofulven und seinem Piperidin Addukt mittels UV/Vis Spektroskopie auf Grund von Streuung kommen. Die Detektion von Tyrosin- und Histidin-enthaltenden Peptiden auf Nanopartikeloberflächen auf Grundlage der *Pauly* Reaktion ist besonders geeignet als schneller und einfach durchzuführender qualitativer Nachweis für die erfolgreiche Konjugation von Peptiden auf Nanopartikeloberflächen. Der Hauptnachteil ist jedoch, dass Partikel mit Eigenfarbe nicht verwendet werden können. Die Aminosäureanalyse auf Grundlage von HPLC nach saurer Hydrolyse von Peptid-funktionalisierten Nanomaterialien und anschließender Derivatisierung mit PITC kann für alle Peptid- oder Protein-modifizierten Nanomaterialien verwendet werden. Es ermöglicht die Detektion von bis zu pikomolaren Konzentrationen und damit die Quantifizierung sehr geringe Oberflächenbeladungen mit Peptiden und Proteinen. Jedoch sind die resultierenden HPLC Chromatogramme schwierig zu interpretieren.

Drei neue analytische Methoden auf der Grundlage von UV/Vis und HPLC Techniken wurden entwickelt und etabliert. Sie halfen bei der erfolgreichen Charakterisierung der synthetisierten DND und SPIONs mit dualer Funktionalisierung durch ALST1 und Cy5, beziehungsweise $[ReBr(CO)_3(L)]$. Jedoch zeigten die Nanomaterialien auf Grund der hohen Tendenz zur Agglomeration keine Zellaufnahme. Das weitere Vorgehen umfasst die Verbesserung der Zellaufnahme durch ersetzen der Silica-Hülle der SPIONs mit PEG oder Chitosan. Bei den DND müssen andere Linkersysteme in Betracht gezogen und dann synthetisiert werden, welche die Adsorption der Peptidkette auf der Oberfläche des Partikels verhindern.

5 Experimental section

5.1 General procedures and instrumentation

5.1.1 General instrumentation

NMR spectroscopy

NMR spectra were recorded on a *Bruker Avance 200* spectrometer (^{1}H NMR at 200.13 MHz and ^{13}C NMR at 50.33 MHz). Chemical shifts are given in ppm and were referenced relative to the solvent signal.[213] Coupling constants are given in Hz. Individual peaks are marked as singlet (s), doublet (d), triplet (t), or multiplet (m).

ESI mass spectrometry

ESI mass spectra were measured using a *Bruker micrOTOF* spectrometer. The solvent flow rate was 4 ml min^{-1} with a nebulizer pressure of 10 psi and an anhydrous gas flow rate of 5 l min^{-1} at a temperature of 300 °C. The measurements were carried out by *Prof. Dr. Ulrich Schatzschneider*.

IR spectroscopy

IR spectra of solid samples were recorded with a *Nicolet 380 FT-IR* spectrometer equipped with a *SMART iTR ATR* unit.

CHN analysis

The elemental composition of the compounds was determined using a *Vario micro cube analyser* from *Elementar Analysensysteme GmbH*.

Transmission electron microscopy

TEM and images were recorded either using the *Titan 80-300* equipped with an X-ray source and an EDX detector from *FEI Company* or with the *JOEL JEM 2100* equipped with the camera systems *TVIPS F416 4k x 4k* and Olympus *Veleta 2k x 2k*. High resolution scanning electron microscopy (hrSEM) was recorded using the *Titan 80-300*. The samples were suspended in ethanol and applied to sample carbon grids provided by the operator of the TEM system. The measurements on the *Titan-80-30* were carried out by *Prof. Dr. Martin Kamp.*

Zeta potential and dynamic light scattering

For determination of the hydrodynamic diameter and the zeta potential of the nanoparticles, a small amount of sample was suspended in ultrapure water (pH = 6.5) and kept in an ultrasonic bath for 30 min. Then, the zeta potential and hydrodynamic diameter was measured with the *Malvern Zetasizer Nanoseries Nano-ZS* using *Malvern zetasizer nano series folded capillary cells*.

5.1.2 HPLC

High pressure liquid chromatography was carried out on a *Dionex Ultimate 3000* instrument equipped with the diode array detector *DAD-3000(RS)* and a binary pump system with integrated degasser. For analytical purposes, a ReproSil 100 C18 5 µm column with a size of 250 x 4.6 mm from *Jasco* was used. For preparative purification, a column with the same filling, but a size of 250 x 10 mm from *Jasco* was employed. For all experiment, a standard ramp gradient protocol for analysis was developed which can be found in Table 5.1. The solvents were water (pump A) with 0.1% TFA and acetonitrile (pump B) with 0.1% TFA. All retentions times R_t and retention factors R_f in the experimental section are given according to this standard protocol.

Tab. 5.1: Program parameters for the standard protocol used for all analytical experiments. The program is using a ramp gradient for sample separation.

Time [min]	Flow rate [ml/min]	%ACN
0	0.6	5
40	0.6	90
50	0.6	5

For purification, the protocol was optimized for each compound. However, at a flow rate of 3.0 ml/min, R_t and R_f are comparable to the analytical data obtained for the same gradient at a flow rate of 0.6 ml/min. Results are given in retention time R_t and retention factor R_f.

5.1.3 Solid-phase peptide synthesis (SPPS)

Solid-phase peptide synthesis was carried out according to *Fmoc Solid Phase Peptide Synthesis - A Practical Approach* by Chen and White.[137] Either Fmoc Rink Amide MBHA (0.67 mmol/g) resin, H-L-His(Trt)-2CT resin (0.78 mmol/g), or Wang Amide resin (0.8 mmol/g) was used depending on the desired amino acid sequence. All resins were purchased from *Iris*

Biotech. In addition, all amino acids were used in the *L*-configuration and purchased from *Iris Biotech* as well. The synthesis was carried out in a filter syringe. The deprotection of Fmoc was carried out using piperidine (*Iris Biotech*) in *N*,*N*-dimethylformamide (*Carl Roth*) in 30% v/v. After each step, the resin was washed by adding *N*,*N*-dimethylformamide or dichloromethane to the resin, shaking it for approximately 1 min, and discarding the solvent. For the coupling, 5 eq. of amino acid (0.65 M) and coupling reagent (HOBT/HBTU 0.65 M) in DMF were added to the deprotected and washed resin. Then, 10 eq. of Diisopropylethylamine (DIPEA) was added. The coupling was carried out on an *IKA KS 130 Basic* shaker for 90 min. Completeness was monitored by the Kaiser test which monitors free primary amines.[195] For the test, two drops of a ninhydrine solution (5% w/v in ethanol), a phenol solution (80% w/v in ethanol), and a mixture of potassium cyanide (1 mM) and pyridine (2% v/v) in water were added to few resin beads and heated to 90 °C for 5 min. Blue staining of the beads due to the formation of *Ruhemann's blue* indicates incomplete coupling. However, arginine, asparagine, and glutamine give false negative results. Furthermore, serine always shows a deep red-brown colour. The peptide was cleaved from the resin using a mixture of TFA with triisopropysilane (TIS) and water as scavenger (95:2.5:2.5 v/v) in a filter syringe for at least 3 h. Subsequently, the crude peptide was isolated by precipitation with ice-cold ether (-20 °C) or evaporation of the cleavage solution in vacuum. The solid was dissolved in a mixture of acetonitrile/water, lyophilized and purified by HPLC if necessary.

5.1.4 Reduction of azide groups on nanoparticle surfaces

The nanoparticle powder was suspended in anhydrous methanol. Then, the same amount as the nanoparticles of sodium boronhydride was added. The reaction mixture was shaken for 24 h. Afterwards, the suspension was centrifuged (30 min, *Eppendorf Centrifuge 5418*, 14000 rpm), the supernatant was discarded, and the precipitate was suspended in water and centrifuged again (30 min, *Eppendorf Centrifuge 5418*, 14000 rpm). The supernatant was discarded and the obtained solid was lyophilized.

5.1.5 Determination of azide/amine nanoparticle surface loading utilizing Fmoc cleavage

For the cleavage reaction, a freshly prepared solution of piperidine in DMF (30% v/v) was used. For the calibration curve, commercially available Fmoc Rink Amide MBHA Resin (0.67 mmol/g, *Iris Biotech*) was mixed with the piperidine solution and shaken for 20 min. Then, the suspension was centrifuged (30 min, *Eppendorf Centrifuge 5418*, 14000 rpm). The supernatant

was diluted 1:10000 and it's the UV/Vis absorption was measured in a 1 ml cuvette at 301 nm (*Agilent 8453 UV/VIS spectrometer*). The amount of used resin is displayed in Table 5.2

Tab. 5.2: Amount of Fmoc Rink Amide MBHA (0.67 mmol/g) resin used to generate calibration curve of amine/azide group surface loading determination of nanoparticles.

m (Fmoc Rink Amide MBHA resin) [mg]	n (loading) [µmol]
2.25	1.50
4.77	3.19
5.26	3.52
7.79	5.21
9.62	6.44
10.37	6.94
11.58	7.75
17.04	11.41
20.54	13.76

The nanoparticles were suspended in piperidine solution (in DMF 30% v/v), shaken for 30 min and centrifuged (30 min, Eppendorf Centrifuge 5418, 14000 rpm). The supernatant was then diluted 1:100 before measuring the absorption at 301 nm (*Agilent 8453 UV/VIS spectrometer*). Using the calibration curve, the surface loading of the nanoparticle systems were calculated.

5.1.6 *Pauly* reaction for tyrosine- or histidine-containing peptides

The reaction of sulfanilic acid with tyrosine or histidine can be used for qualitative analysis of histidine- and tyrosine-containing peptides or proteins on nanoparticle surfaces. For this purpose, a number of stock solutions were prepared in advance and stored at 4 °C.

<u>0.5% (w/w) acidic sulfanilic acid solution</u>

Sulfanilic acid (0.25 mg, 1.44 mmol) was dissolved in a mixture of ultrapure water (47.3 ml) and concentrated hydrochloric acid (2.7 ml, 27 mmol)

<u>0.5% (w/w) sodium nitrate solution</u>

Sodium nitrate (250 mg, 3.62 mmol) was dissolved in ultrapure water (50 ml).

<u>10% (w/w) sodium carbonate solution</u>

Sodium carbonate (5 g, 47.16 mmol) was dissolved in ultrapure water (45 ml).

The sulfanilic acid solution and the sodium nitrate solution were mixed in a ratio of 1:1 and incubated for 1 min at room temperature. The mixture (500 µl) was then added to the peptide solution (1 ml) and incubated for 2 min. Then, the sodium carbonate solution was added (500 µl) and the mixture was incubated for 5 min at room temperature. The mixture turns reddish in the presence of tyrosine or histidine. For UV/Vis spectroscopy, the mixture was diluted 1:10 or 1:20 with water depending on the absorption, before measurement.

5.1.7 Peptide digestion, derivatization with PITC and HPLC analysis

A defined amount of peptide (weighed in using a *Mettler Toledo XA105 DualRange*) was placed in a 1.5 ml reaction vial (*Eppendorf*), dissolved in hydrochloric acid (6 M, 500 µl), and heated to 110 °C for 24 h using a *Stuart Block Heater SBH 130D*. Then, the hydrochloric acid was evaporated carefully using cooling traps and a *RZ6 vacuum pump* from *vacuubrand*. The remaining residue was suspended in a mixture of ethanol, water, triethylamine, and PITC (7:1:1:1) and shaken for 20 min. Subsequently, the solvent was evaporated using cooling traps and a *RZ6 vacuum pump from vacuubrand*. The residue was dissolved in Acetonitrile/water (1:1, 100 µl) and 60 µl were injected into the HPLC. The standard protocol described in chapter 5.1.2 was used for analysis. For amino acid calibration curves, different amounts (20 – 300 nmol) of the specific amino acid were derivatized and analysed by HPLC.

5.1.8 General photophysical and life time measurements

All measurements were made in quartz cuvettes (2 mm x 1 cm cross-section). The emission and excitation spectra were recorded using an Edinburgh Instruments FLSP920 spectrometer equipped with a double monochromator for both excitation and emission, operating in right-angle geometry mode. All spectra were fully corrected for the spectral response of the instrument. All solutions used in photophysical measurements had optical densities below 0.2 to minimize inner filter effects during fluorescence measurements. Fluorescence lifetimes were recorded using the time-correlated single-photon counting (TCSPC) method using the same FLSP920 spectrometer described above. Solutions were excited with a picosecond pulsed diode laser at wavelengths of 656, 419 or 377 nm. The full width at half maximum (FWHM) of the pulsed diode lasers was *ca.* 75–90 ps, while each instrument response function (IRF) had FWHM of *ca.* 1.0 ns, measured from the scatter of pure solvent at the excitation wavelength. Decays were recorded to 10000 counts in the peak channel with a record length of at least 1000 channels. The band pass of the monochromator was adjusted to give a signal count rate of < 20 kHz. Iterative reconvolution of the IRF with decay function(s) and non-linear least-squares

analysis were used to analyze the data. The quality of each decay fit was judged to be satisfactory based on the calculated values of the reduced χ^2 and Durbin-Watson parameters and visual inspection of the weighted residuals.

5.1.9 Stability tests of metal complexes

For dark stability, compounds **20**, **21**, and **22**, were dissolved in methanol/dichloromethane (1:1 v/v) and compound **23** in pure DMSO. Then, UV/Vis spectra were recorded overnight in 30 min intervals under exclusion of light using the kinetics mode of the *Agilent 8453 UV/VIS spectrometer*. Subsequently, the samples were illuminated at 365 nm for 30 sec and UV/Vis spectra were recorded. The illumination intervals were increased to 60 sec, 120, sec, or 300 sec when the spectrum showed no significant changes after 30 sec. When the spectrum showed no changes after an illumination interval of 300 sec, the measurement was interrupted.

5.1.10 Relaxivity measurements

The relaxivities of the superparamagnetic iron oxide nanoparticles were measured in ultrapure water at concentrations of 0.250, 0.212, 0.162, 0.125, 0.087, 0.05, 0.025, and 0.012 mM Fe, assuming that the SPIONs are γ-Fe_3O_4 using a *Bruker Biospec 70/30° instrument (7T)* equipped with a *72 mm Bruker Quadratur Birdcage*. The measurement sequences were *CPMG* for T_2 relaxation and *Inversion Recovery Look-Locker* for T_1 relaxation. The measurements were carried out by *Thomas Kampf*.

5.1.11 Cell culture

MDA MB 231 cells were harvested from exponentially growing subconfluent monolayers. The culture was maintained in 25 cm^2 culture flasks in DMEM (*Sigma Aldrich, Schnelldorf, Germany*) supplemented with heat inactivated fetal bovine serum (10%, FBS, *Invitrogen, 10270*) and antibiotics (1%, *Sigma Aldrich, Schnelldorf, Germany* at 37 °C and carbon dioxide, 5% CO_2). MDA-MB 231 cells were seeded in 4 well chamber slides (*Nunc*). The following day, a pinch of SPIONs and DND were dissolved in 1mL DMEM and treated by ultrasonication for 30 min. DND were dissolved in 10 µL DMSO prior before adding 990 µL of DMEM and prior before ultrasonication. MDA-MB 231 cells were washed with PBS and 400 µL of serum-free DMEM was added. 100 µL of particle solution were carefully given to the cells and the cells were incubated for 2h at 37 °C and 5% CO_2. Afterwards the cells were washed with PBS and then fixed with a buffered aqueous solution of 4% (V/V) formaldehyde at pH 6.9. After fixation, the cells were washed again and permeabilized with 0.1% (V/V) Triton X-100 in PBS and

stained for cell nuclei with DAPI solution, diluted 1:1000 (V/V) in water for 10 min. Samples were analyzed with an inverted epifluorescence microscope *Axio Observer Z1* (*Zeiss, Oberkochen, Germany*). The experiments were carried out by *Dr. Tessa Lühmann.*

5.2 Synthetic procedures

5.2.1 Synthesis of 2-phenyl-1*H*-imidazo[4,5-*f*][1,10]phenanthroline[179-181]

USC-TS-151-01

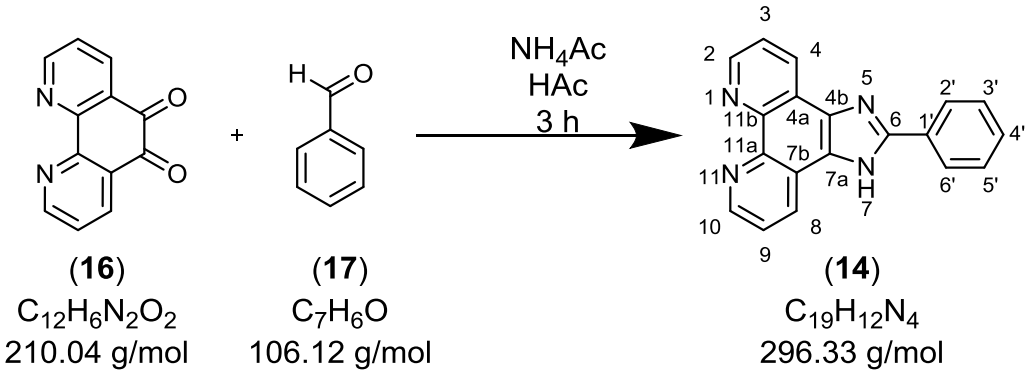

(**16**)
$C_{12}H_6N_2O_2$
210.04 g/mol

(**17**)
C_7H_6O
106.12 g/mol

(**14**)
$C_{19}H_{12}N_4$
296.33 g/mol

Ammonia acetate (2.41 g, 31 mmol), benzaldehyde (0.22 g, 2.1 mmol), and 1,10-phenantroline-5,6-dione. (0.46 g, 2.1 mmol) were heated to reflux in acetic acid (100 ml) for 3 h. After cooling to room temperature, 25% aqueous ammonia was added to the reaction mixture to precipitate the product as a bright-yellow solid. It was filtered off, washed several times with water, and dried in vacuum.

Yield: 0.45 g (1.0 mmol, 49%).

^{1}H-NMR (200.13 MHz, DMSO-d_6, ppm): δ = 9.04 (2H, dd, H2+H10, ^3J = 4.33 Hz, ^4J = 1.73 Hz), 8.94 (2H, dd, H4+H8, ^3J = 8.13 Hz, ^4J = 1.75 Hz), 8.28 (2H, dd, H2'+H6, ^3J = 8.41 Hz, ^4J = 1.53 Hz), 7.84 (2H, dd, H3+H9, ^3J = 4.53 Hz), 7.62 - 7.52 (2H, m, H3'+H4'+H5').

^{13}C-NMR (50.32 MHz, DMSO-d_6, ppm): δ = 150.56 (C6), 147.80 (C2+C10), 143.56 (C4+C8), 129.99 (C3'+C5'), 129.58 (C4), 129.00 (C2'+C6'), 126.19 (C4b+C7a), 123.27 (C3+C9).

IR (ATR, cm^{-1}): 3063 (w, ν_{C-H}, ν_{N-H}), 1546, 1459 (w, $\nu_{C=C}$).

MS (ESI$^+$, CH_3OH, *m/z*): 297.11 $[M+H]^+$, 319,09 $[M+Na]^+$, 615.20 $[2M+Na]^+$.

CHN analysis (%): calculated for $C_{19}H_{12}N_4$: C 70.77, H 4.53, and N 17.72; found: C 70.20, H 4.53, and N 17.24

5.2.2 Synthesis of 2-phenyl-1*H*-imidazo[4,5-*f*][1,10]phenanthroline[179-181]

USC-TS-089-02

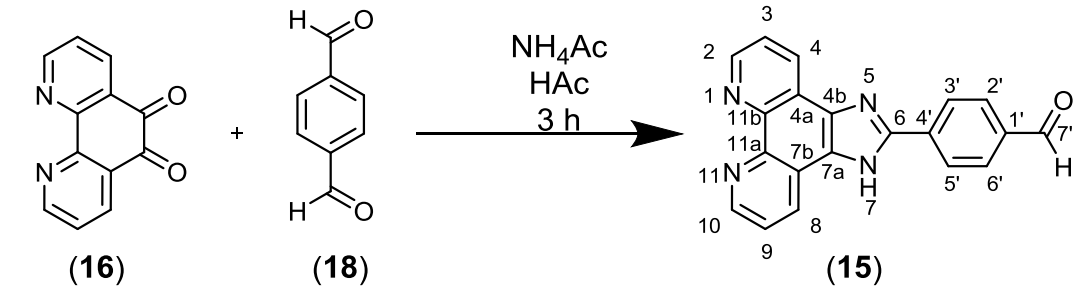

(**16**) $C_{12}H_6N_2O_2$ 210.04 g/mol

(**18**) $C_8H_6O_2$ 134.04 g/mol

(**15**) $C_{20}H_{12}N_4O$ 324.10 g/mol

Ammonia acetate (2.41 g, 31 mmol) and terephthalaldehyde (0.29 g, 2.1 mmol) were heated to reflux in concentrated acetic acid (40 ml). 1,10-Phenantroline-5,6-dione. (0.35 g, 1.6 mmol) was dissolved in warm concentrated acetic acid and added dropwise to the boiling reaction mixture, which turned from yellow to red. After heating to reflux for 3 h, a red precipitate had formed. After cooling to room temperature, it was filtered off, washed several times with water and dried in vacuum. However, the red solid was 2-(4-(1*H*-imidazo[4,5-*f*][1,10]phenanthrolin-2-yl)phenyl)-1*H*-imidazo[4,5-*f*][1,10]-phenanthroline (**19**) and not the desired product. Therefore, concentrated aqueous ammonia was added to the remaining yellow reaction mixture to precipitate a yellow-orange solid. It was washed with water several times and dried in vacuum to yield an orange powder.

Yield: 0.25 g (0.79 mmol, 48%).

^{1}H-NMR (200.13 MHz, DMSO-d_6, ppm): δ = 10.09 (1H, s, H7'), 9.04 (2H, dd, H2+H10, ^3J = 4.33 Hz, ^4J = 1.73 Hz), 8.91(2H, dd, H4+H8, ^3J = 8.13 Hz, ^4J = 1.75 Hz), 8.48 (2H, d, H3'+H5', ^3J = 8.27 Hz), 8.13 (2H, d, H2'+H6', ^3J = 8.41 Hz), 7.84 (2H, q, H3,9).

^{13}C-NMR (50.32 MHz, DMSO-d_6, ppm): The solubility in all common solvents was too poor to measure a properly resolved ^{13}C-NMR spectrum.

IR (ATR, cm^{-1}): 3046 (w, ν_{C-H}, ν_{N-H}), 1693 (m, $\nu_{C=O}$).

MS (ESI$^+$, CH_3OH, *m/z*): 325.10 $[M+H]^+$.

CHN analysis (%): calculated for $C_{20}H_{12}N_4O$: C 74.06, H 3.73, and N 17.27; found: C 73.20, H 3.81, and N 16.84

5.2.3 Synthesis of bromo(tricarbonyl)(2-phenyl-1*H*-imidazo[4,5-*f*][1,10]phen-anthroline) manganese(I)

USC-TS-157-01

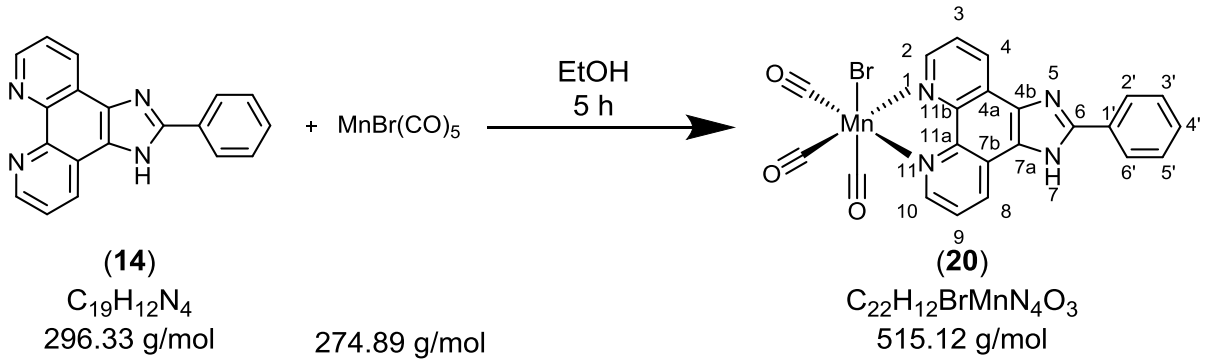

(**14**)
$C_{19}H_{12}N_4$
296.33 g/mol

274.89 g/mol

(**20**)
$C_{22}H_{12}BrMnN_4O_3$
515.12 g/mol

2-phenyl-1*H*-imidazo[4,5-*f*][1,10]phenanthroline (85 mg, 0.28 mmol) and manganese pentacarbonyl bromide (70 mg, 0.25 mmol) where heated to reflux in ethanol (40 ml) for 5 h. During the reaction, a yellow solid precipitated. It was filtered off and washed with water and ethanol to yield a bright yellow solid. Afterwards, the product was dried in vacuum.

Yield: 0.076 g (0.15 mmol, 61%).

^{1}H-NMR (200.13 MHz, DMSO-d_6, ppm): δ = 9.51 (2H, dd, H2+H10, ^3J = 4.73 Hz,), 9.16 (2H, dd, H4+H8, ^3J = 7.64 Hz,), 8.33 (2H, d, H2'+H6', ^3J = 7.13 Hz), 7.12 (2H, q, H3,9), 7.56 - 7.68 (3H, m, H3'+H4'+H5').

^{13}C-NMR (50.32 MHz, DMSO-d_6, ppm): The solubility in all common solvents was too poor to measure a properly resolved ^{13}C-NMR spectrum.

IR (ATR, cm^{-1}): 3041 (w, ν_{C-H}, ν_{N-H}), 2024, 1934, 1909 (s, $\nu_{C\equiv O}$).

MS (ESI$^+$, CH_3OH, *m/z*): 950.97 $[2M-Br]^+$.

CHN analysis (%): calculated for $C_{22}H_{12}BrMnN_4O_3$: C 51.29, H 2.35, and N 10.87; found: C 50.84, H 2.35, and N 10.87.

5.2.4 Synthesis of bromo(tricarbonyl)(4-(1*H*-imidazo[4,5-*f*][1,10]phenanthrolin-2-yl)benzaldehyde) manganese(I)

USC-TS-130-01

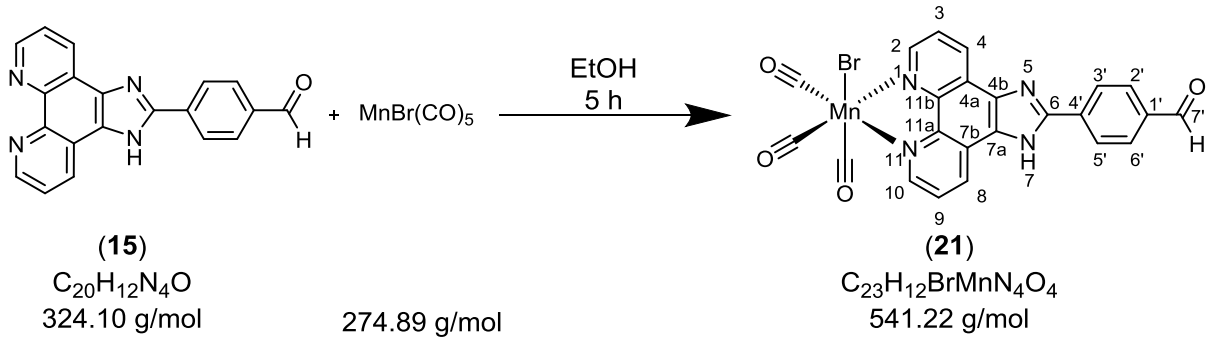

4-(1H-imidazo[4,5-f][1,10]phenanthrolin-2-yl)benzaldehyde (85 mg, 0.275 mmol) and manganese pentacarbonyl bromide (70 mg, 0.25 mmol) where heated to reflux in ethanol (40 ml) for 5 h. During the reaction, a yellow solid precipitated. It was filtered off and washed with water an ethanol to yield a bright yellow solid. Afterwards, the product was dried in vacuum.

Yield: 0.082 g (0.16 mmol, 63%).

^{1}H-NMR (200.13 MHz, DMSO-d_6, ppm): It was not possible to obtain a properly resolved ^{1}H-NMR spectrum.

^{13}C-NMR (50.32 MHz, DMSO-d_6, ppm): The solubility in all common solvents was too poor to measure a properly resolved ^{13}C-NMR spectrum.

IR (ATR, cm^{-1}): 2024, 1924, 1911 (s, $\nu_{C\equiv O}$), 1691 (s, $\nu_{C=O}$).

MS (ESI^{+}, CH_3OH, *m/z*): 379.03 $[M+Br-3CO]^{+}$.

CHN analysis (%): calculated for $C_{23}H_{12}BrMnN_4O_4$: C 50.85, H 2.23, and N 10.31; found: C 51.11, H 2.30, and N 10.20.

5.2.5 Synthesis of bromo(tricarbonyl)(2-phenyl-1*H*-imidazo[4,5-*f*][1,10]phenan-throline) rhenium(I)

USC-TS-153-01

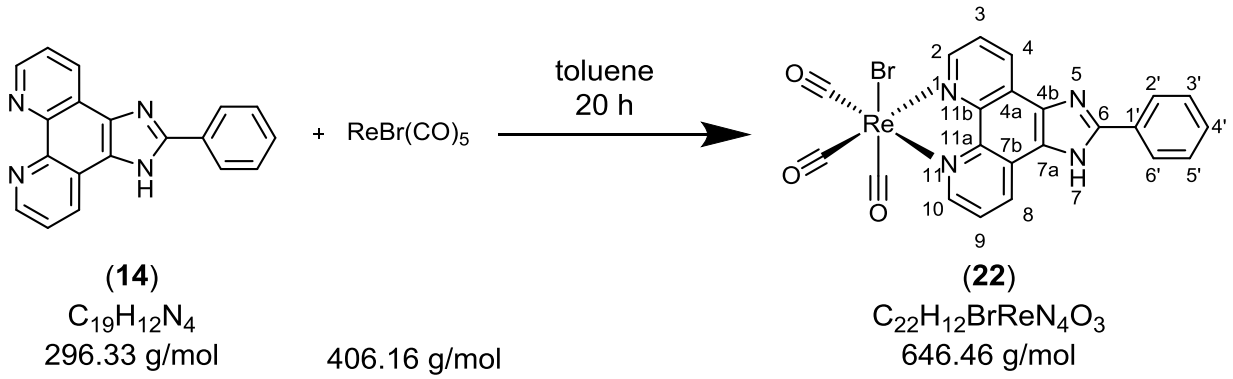

(**14**)
$C_{19}H_{12}N_4$
296.33 g/mol

406.16 g/mol

(**22**)
$C_{22}H_{12}BrReN_4O_3$
646.46 g/mol

2-phenyl-1*H*-imidazo[4,5-*f*][1,10]phenanthroline (85 mg, 0.28 mmol) and rhenium pentacarbonyl bromide (100 mg, 0.25 mmol) where heated to reflux in toluene (40 ml) for 20 h. During the reaction, a yellow solid precipitated. It was filtered off and washed with water and cold toluene to yield a bright yellow solid. Afterwards, the product was dried in vacuum.

Yield: 0.055 g (0.08 mmol, 33%).

^{1}H-NMR (200.13 MHz, DMSO-d_6, ppm): δ = 9.49 (2H, dd, H2+H10, ^3J = 5.13 Hz, ^4J = 1.25 Hz), 9.29 (2H, dd, H4+H8, ^3J = 8.29 Hz, ^4J = 1.25 Hz), 8.30 (2H, d, H2'+H6', ^3J = 6.69 Hz), 8.17 (2H, dd, H3+H9), 7.58 - 7.70 (3H, m, H3'+H4'+H5').

^{13}C-NMR (50.32 MHz, DMSO-d_6, ppm): The solubility in all common solvents was too poor to measure a properly resolved ^{13}C-NMR spectrum.

IR (ATR, cm^{-1}): 3137 (w, ν_{C-H}, ν_{N-H}), 2021, 1882 (s, $\nu_{C\equiv O}$).

MS (ESI$^+$, CH_3OH, *m/z*): 567.04 $[M-Br]^+$, 595.05 $[M-Br+N_2]^+$, 668.95 $[M-Br]^+$,

CHN analysis (%): calculated for $C_{22}H_{12}BrReN_4O_3$: C 40.10, H 1.87, and N 8.67; found: C 39.64, H 1.89, and N 8.03.

5.2.6 Synthesis of bromo(tricarbonyle)(4-(1*H*-imidazo[4,5-*f*][1,10]phenanthrolin-2-yl)benzaldehyde) rhenium(I)

USC-TS-138-01

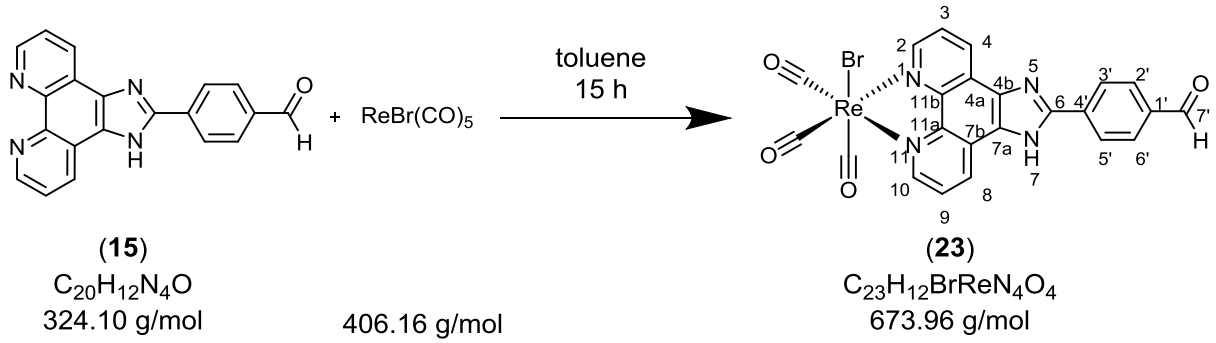

(**15**)
$C_{20}H_{12}N_4O$
324.10 g/mol

406.16 g/mol

(**23**)
$C_{23}H_{12}BrReN_4O_4$
673.96 g/mol

4-(1*H*-imidazo[4,5-*f*][1,10]phenanthrolin-2-yl)benzaldehyde (85 mg, 0.275 mmol) and rhenium pentacarbonyl bromide (100 mg, 0.25 mmol) where heated to reflux in toluene (40 ml) for 15 h. During the reaction, a greenish-yellow solid precipitated. It was filtered off and washed with water and cold toluene to yield a greenish-yellow solid. Afterwards, the product was dried in vacuum.

Yield: 0.037 g (0.05 mmol, 22%).

^{1}H-NMR (200.13 MHz, DMSO-d_6, ppm): δ = 10.13 (1H, s, H7'), 9.42 (2H, dd, H2+H10, ^3J = 5.13 Hz, ^4J = 1.27 Hz), 9.29 (2H, dd, H4+H8, ^3J = 8.31 Hz, ^4J = 1.25 Hz), 8.54 (2H, d, H3'+H5', ^3J = 8.03 Hz), 8.16 - 8.22 (4H, m, H3+H9+H2'+H6').

^{13}C-NMR (50.32 MHz, DMSO-d_6, ppm): The solubility in all common solvents was too poor to measure a properly resolved ^{13}C-NMR spectrum.

IR (ATR, cm^{-1}): 3216 (w, ν_{C-H}, ν_{N-H}), 2017, 1920, 1899 (s, $\nu_{C\equiv O}$), 1693 (s, $\nu_{C=O}$).

MS (ESI$^+$, CH_3OH, *m/z*): 697.65 $[M+Na]^+$.

CHN analysis: calculated for $C_{23}H_{12}BrReN_4O_4$: C 40.01, H 1.79, N 7.95; found: C 39.22, H 2.13, N 7.39

5.2.7 Synthesis of benzyl azide[202]

USC-XB-083-01

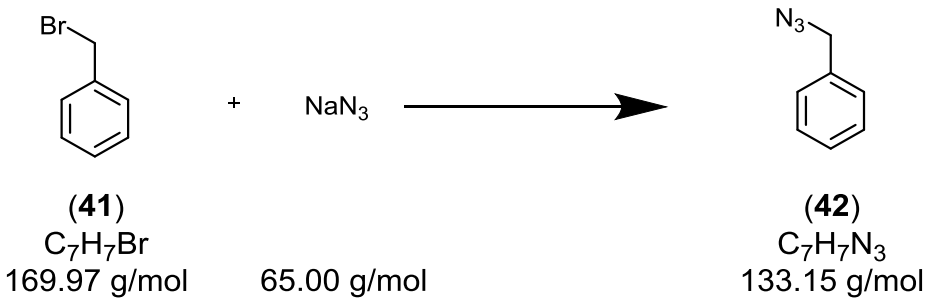

Benzyl bromide (12.1 g, 7 mmol) was added dropwise to a solution of sodium azide (6.84 g, 105 mmol) in dimethylsulfoxide (70 ml). The reaction mixture was stirred overnight. Then, it was extracted by diethyl ether. The combined organic layers were washed with water, brine and dried, over magnesium sulfate. Afterwards, the solvent was evaporated to yield a brown liquid.

Yield: 7.76 g (58 mmol, 83%).

^{1}H-NMR (200.13 MHz, $CDCl_3$, ppm): δ = 7.40 – 7.30 (5H, m, benzyl), 4.35 (2H. s, CH_2N_3).

^{13}C-NMR (50.32 MHz, $CDCl_3$, ppm): 135.48 (C1), 128.95 (C2+6), 128.42 (C3+5), 128.33 (C4), 54.92 (CH_2N_3).

IR (ATR, cm^{-1}): 2877 (s, ν_{C-H}), 2090 (s, ν_{azide}).

CHN analysis: calculated for $C_7H_7N_3$: C 63.14, H 5.30, N 31.56; found: C 63.52, H 5.34, N 30.99.

5.2.8 Synthesis of tetrakis(acetonitrile)copper(I)hexaflourophosphate[203]

USC-XB-084-01

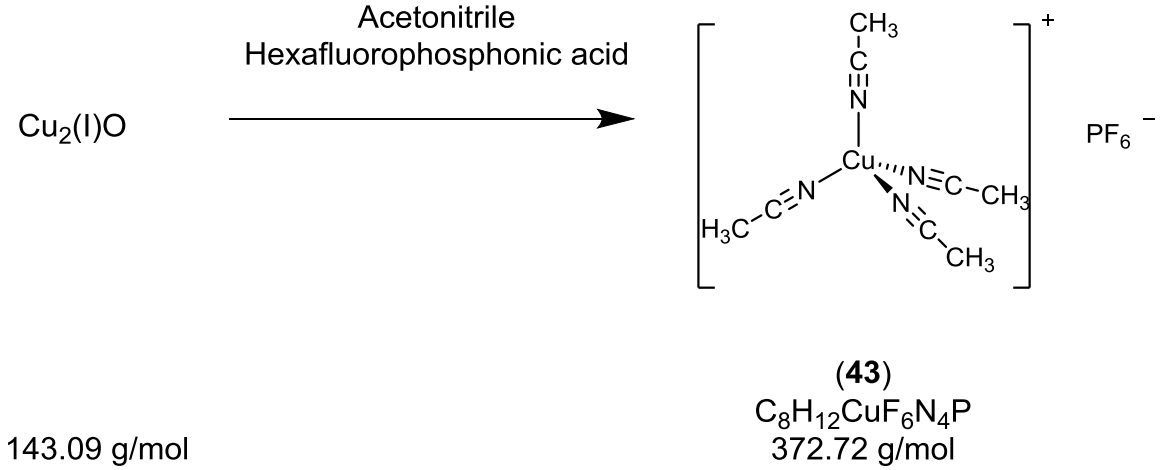

143.09 g/mol

(**43**)
$C_8H_{12}CuF_6N_4P$
372.72 g/mol

A three-neck flask was charged with copper(I) oxide (2.05 g, 14 mmol) and anhydrous acetonitrile (50 ml) under protective gas atmosphere. Then, hexafluorophosphonic acid (35.5 g, 242.5 mmol) was added dropwise. The hot reaction mixture was filtered to remove the precipitated solid and the solution was stored at -25 °C over night. The precipitated white solid was filtered of and washed with diethyl ether. Afterwards, it was dissolved in a mixture of acetonitrile (70 ml) and diethyl ether (50 ml) and stored at -25 °C to crystallize obtain the product as a white solid which was filtered off under protective gas atmosphere.

Yield: 3.36 g (9.6 mmol, 68%).

^{1}H-NMR (200.13 MHz, aceton-d_6, ppm): δ = 2.20 (s, NCC*H*$_3$).

^{13}C-NMR (50.32 MHz, aceton-d_6, ppm): 206.43 (N*C*CH$_3$), 1.68 (NC*C*H$_3$) ppm.

IR (ATR, cm^{-1}): 3007 (s, ν_{C-H}), 2943 (s, ν_{C-H}), 2274 (w, $\nu_{N\equiv C}$).

CHN analysis: calculated for $C_8H_{12}CuF_6N_4P$: C 25.78, H 3.25 N 15.03; found: C 25.51, H 3.19 N 14.98.

5.2.9 Synthesis of 1-(1-benzyl-1*H*-1,2,3-triazole-4-yl)-*N*,*N*-bis((1-benzyl-1*H*-1,2,3-triazole-5-yl)methyl)methanamine (TBTA)[204]

USC-XB-084-01

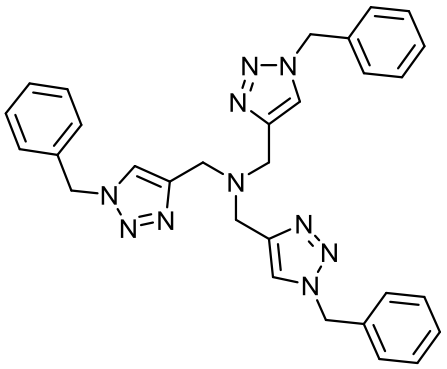

(**44**)
$C_{30}H_{30}N_{10}$
530.63 g/mol

Tetrakis(acetonitrile) copper(I) hexaflourophosphate (244 mg, 0.65 mmol) was slowly added to a mixture of tripropargyl amine (1.32 g, 10 mmol), benzyl azide (5.99 g, 45 mmol) und 2,6-Lutidin (1.07 g, 10 mmol) in anhydrous acetonitrile (15 ml) under protective gas atmosphere. The reaction mixture was cooled for 15 min at 0 °C and then stirred for 3 d. The white precipitate was filtered off and washed with acetonitrile.

Yield: 2.827 g (5.33 mmol, 53%).

^{1}H-NMR (200.13 MHz, $CDCl_3$, ppm): δ = 7.69 (3H, s, triazol), 7.33 (9H, m), 7.26 (6H. m), 5.50 (6H, s, PhC*H*$_2$), 3.72 (6H, s, N-C*H*$_2$-Triazol).

^{13}C-NMR (50.32 MHz, $CDCl_3$, ppm): 134.80, 123.19, 128.79, 128.12, 54.31.

IR (ATR, cm^{-1}): 3141 (s, $\nu_{C=C-H}$), 3060 (s, $\nu_{C=C-H}$), 2951 (s, ν_{C-H}), 2930 (s, ν_{C-H}), 2825 (m, ν_{N-CH2}).

CHN analysis: calculated for $C_{30}H_{30}N_{10}$: C 67.90, H 5.70, N 26.40; found C 67.79, H 5.74, N 26.03.

5.2.10 Synthesis of ALST1 hexynoic acid conjugate

USC-TS-066-01

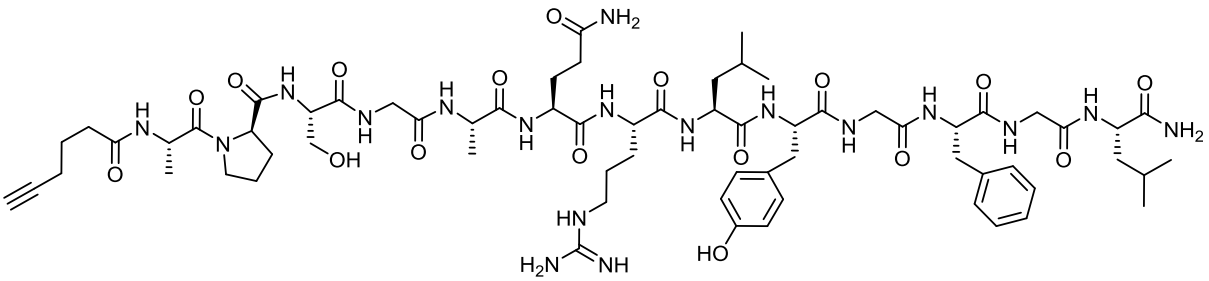

(**24**)
Hexynoic acid-APSGAQRLYGFGL-NH_2
$C_{67}H_{100}N_{18}O_{17}$
1428.75 g/mol

Fmoc Rink Amide MBHA resin (500 mg, 0.34 mmol) was the used as solid support for this reaction. HBTU (6.44 g, 17 mmol) in DMF (25 ml) and HOBT (2.60 g; 17 mmol) in DMF (25 ml) were prepared as stock solutions in advance. HOBT solution (2.5 ml) and HBTU solution (2.5 ml) were added to the solid amino acids (5 eq., 1.7 mmol, see table below) and shaken for 5 min. Afterwards, the activated amino acid was given to the deprotected resin and DIPEA (593 µl, 3.4 mmol) was added. Then, the reaction mixture was shaken for 90 min at room temperature. Between coupling and Fmoc deprotection, the resin was washed several times with DMF and dichloromethane. After sequence assembly, the peptide was cleaved from the resin according to the conditions mentioned in chapter 5.1.3. The crude peptide was purified by HPLC using following program parameters for a ramp gradient:

Time [min]	Flow rate [ml/min]	%ACN
0	3.0	5
40	3.0	90
45	3.0	5

The detection wavelengths were 220 and 254 nm. The fraction from 21.1 to 22.1 min was collected and lyophilized to yield the product as a white solid.

Amino acid building block	Amount used [mg]
Fmoc-(L)-Leucine-OH	601
Fmoc-Glycine-OH	515
Fmoc-(L)-Phenylalanine-OH	661
Fmoc-Glycine-OH	505
Fmoc-(L)-Tyrosine(tBu)-OH	779
Fmoc-(L)-Leucine-OH	598
Fmoc-(L)-Arginine(Pbf)-OH	1112
Fmoc-(L)-Glutamine(Trt)-OH	1031
Fmoc-(L)-Alanine-OH	542
Fmoc-Glycine-OH	507
Fmoc-(L)-Serine(tBu)-OH	652
Fmoc-(L)-Proline-OH	573
Fmoc-(L)-Alanine-OH	651
Hexynoic acid	188

Yield: 53 mg (0.03 mmol, 29%).

R_t (min; 220 nm): 21.57.

R_f (220 nm): 2.51.

MS (ESI^+, CH_3OH, *m/z*): 1429.75 $[M+H]^+$, 726.37 $[M+H+Na]^{2+}$.

5.2.11 Synthesis of TGF-β1 binding peptide

USC-TS-072-01

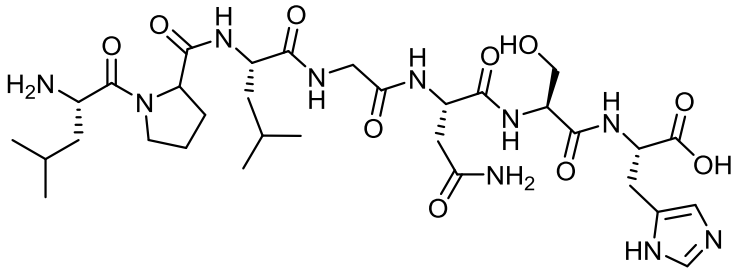

(**10**)
LPLGNSH
$C_{32}H_{52}N_{10}O_{10}$
736.82 g/mol

H-(L)-His(Trt)-2CT resin (200 mg, 0.15 mmol) was used as the solid support for this reaction. HBTU (2.95 g, 7.8 mmol) in DMF (10 ml) and HOBT (1.19 g; 7.8 mmol) in DMF (10 ml) were prepared as stock solutions in advance. HOBT solution (1 ml) and HBTU solution (1 ml) were added to the solid amino acids (5 eq., 0.75 mmol, see table below) and shaken for 5 min.

Amino acid building block	Amount used [mg]
Fmoc-(L)-Serine(tBu)-OH	300
Fmoc-(L)-Arginine(Pbf)-OH	510
Fmoc-Glycine-OH	231
Fmoc-(L)-Leucine-OH	275
Fmoc-(L)-Proline-OH	269
Fmoc-(L)-Leucine-OH	281

Afterwards, the activated amino acid was given to the deprotected resin and DIPEA (271 µl, 1.5 mmol) was added. Then, the reaction mixture was shaken for 90 min at room temperature. Between coupling and Fmoc deprotection, the resin was washed several times with DMF and

dichloromethane. After sequence assembly, a small amount of peptide was cleaved to perform HPLC and ESI MS characterization. The remaining compound was left on the resin for further modification.

R_t (min; 220 nm): 13.21.
R_f (220 nm): 1.36.
MS (ESI^+, CH_3OH, *m/z*): 737.38 $[M+H]^+$.

5.2.12 Synthesis of (3-azidopropyl)triethoxysilane

USC-XB076-01

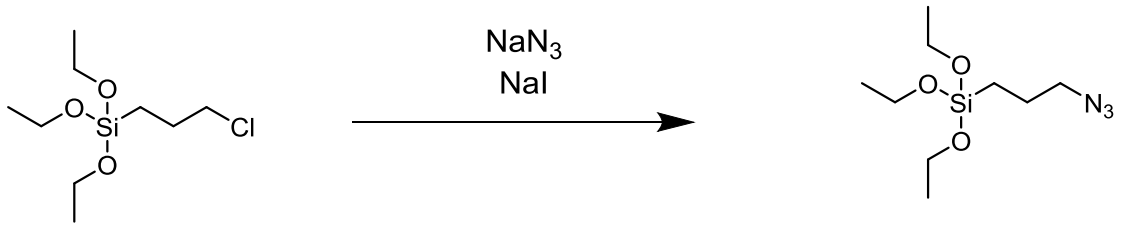

(**45**)
$C_9H_{21}ClO_3Si$
240.09 g/mol

(**46**)
$C_9H_{21}N_3O_3Si$
247.37 g/mol

3-Chloropropyltriethoxysilane (2.7 g, 11.2 mmol) was added to a solution of sodium azide (1.4 g, 22.4 mmol) and sodium iodine (0.3 mg, 0.7 mmol) in DMSO (20 ml). The reaction mixture was heated to 60 °C for 24 h. Then, n-hexane (40 ml) was added and stirred for additional 2.5 h. Then, the reaction mixture was washed with water (3 x 10 ml) and brine (10 ml). The organic fractions were dried with magnesium sulfate and evaporated to yield a colourless oil.

Yield: 2.24 g (9.1 mmol, 81%).

^{1}H-NMR (200.13 MHz, $CDCl_3$, ppm): δ = 3.82 (6H, q, $SiOCH_2$, ^3J = 7.0), 3.27 (2H, t, CH_2N_3, ^3J = 6.9), 1.79 - 1.56 (2H, m, $CH_2CH_2CH_2$), 1.23 (9H, t, CH_2CH_3, ^3J = 7.0), 0.72 . 0.63 (2H, m, $SiCH_2$).

^{13}C-NMR (50.32 MHz, $CDCl_3$, ppm): δ = 58.45 ($SiOCH_2$), 53.82 (CH_2N_3), 22.65 ($CH_2CH_2CH_2$), 18.27 (CH_3), 7.59 ($SiCH_2$)

IR (ATR, cm^{-1}): 2975, 2927 (s, ν_{C-H}), 2095 (s, ν_{azide}), 1075 (s, ν_{Si-O}).

5.2.13 Synthesis of azide-functionalized silica nanoparticles

USC-XB077-01

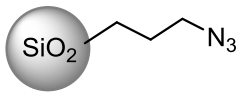

(**25**)

Sodium hydroxide (5.4 mg, 0.13 mmol) and benzethonium chloride (384.2 mg, 0.86 mmol) were dissolved in water (100 ml) and stirred for 10 min at room temperature. Then, tetraethylorthosilicate (6.88 g, 33 mmol, 7.3 ml) and (3-azidopropyl)triethoxysilane (504 mg, 2 mmol) were added dropwise and the reaction mixture was stirred for 24 h at room temperature. Subsequently, methanol (200 ml) was added and the precipitate was filtered off and dried in vacuum to yield a white powder.

Yield: 1.34 g

IR (ATR, cm^{-1}): 2105 (w, ν_{azide}), 1064 (s, ν_{Si-O}).

Average diameter (TEM, nm): 48.2

Kaiser Test: Negative; positive after reduction with $NaBH_4$.

5.2.14 Synthesis of Fmoc Rink Amide silica nanoparticle conjugate

USC-TS-095-01

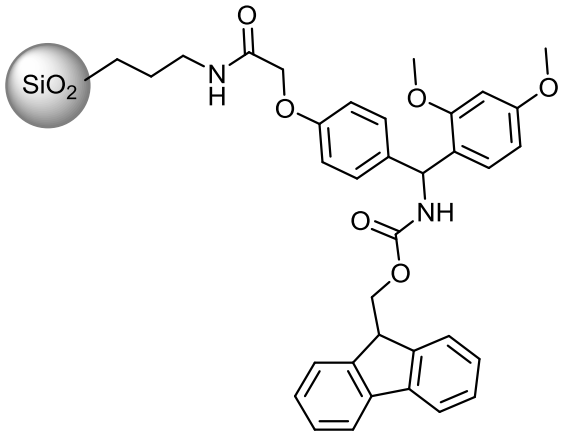

(**25c**)

$NaBH_4$-reduced azide-functionalized silica nanoparticles (100 mg) were mixed with HOBT (32.4 mg, 43 mmol), HBTU (81.6 mg, 43 mmol), and Fmoc Rink Amide linker (215.4 mg, 43 mmol) and suspended in DMF (1 ml). Then, DIPEA (75 µl, 86 mmol) was added and the suspension was shaken for 1.5 h. The white suspension was centrifuged (45 min, *Eppendorf Centrifuge 5418*, 14000 rpm) and the supernatant was discarded. The white solid was washed three times with dichloromethane, three times with DMF and three times with water. For each step, the solid was suspended in the solvent and centrifuged (20 min, *Eppendorf Centrifuge 5418*, 14000 rpm). The supernatant was discarded. Subsequently, the product was lyophilized to yield a white powder.

Yield: 1.34 g

IR (ATR, cm^{-1}): 2105 (w, ν_{azide}), 1659 (s, ν_{amide}), 1064 (s, ν_{Si-O}).

5.2.15 Synthesis of hexynoic acid-LYGFGL-NH_2

USC-TS-084-03

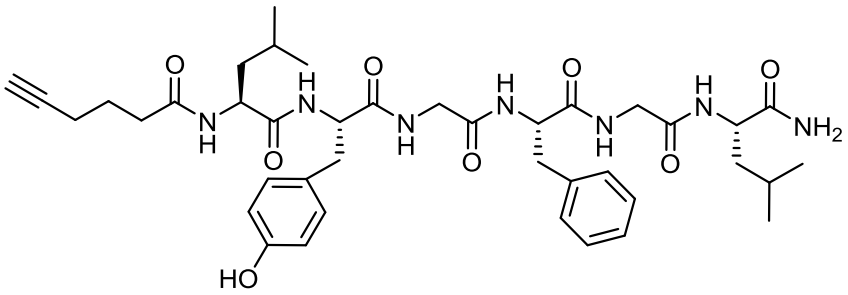

(**24a**)
Hexynoic acid-LYGFGL-NH_2
$C_{40}H_{55}N_7O_8$
761.41 g/mol

Wang-Amide resin (300 mg, 0.2 mmol) was used as the solid support for this reaction. HBTU (3.81 g, 10.0 mmol) in DMF (15 ml) and HOBT (1.53 g; 10 mmol) in DMF (15 ml) were prepared as stock solutions in advance. HOBT solution (1.5 ml) and HBTU solution (1.5 ml) were added to the solid amino acid (5 eq., 0.75 mmol, see table below) and shaken for 5 min.

Amino acid building block	Used amount [mg]
Fmoc-(L)-Leucine-OH	355
Fmoc-Glycine-OH	298
Fmoc-(L)-Phenylalanine-OH	398
Fmoc-Glycine-OH	300
Fmoc-(L)-Tyrosine(tBu)-OH	462
Fmoc-(L)-Leucine-OH	350
Hexynoic acid	111

Afterwards, the activated amino acid was given to the deprotected resin and DIPEA (350 µl, 2.0 mmol) was added. Then, the reaction mixture was shaken for 90 min at room temperature. Between coupling and Fmoc deprotection, the resin was washed several times with DMF and dichloromethane. After sequence assembly, Fmoc was removed and the peptide was cleaved

from the resin according to the conditions mentioned in chapter 5.1.2. However, it was not possible to precipitate the peptide. Thus, the cleavage mixture was evaporated to dryness. The crude peptide was purified by HPLC using following program parameters for a ramp gradient:

Time [min]	Flow rate [ml/min]	%ACN
0	3.0	5
30	3.0	70
33	3.0	5

The detection wavelengths were 220 and 254 nm. The fraction from 25.0 to 26.2 min was collected and lyophilized to yield the product as a white solid.

R_t (min; 220 nm): 25.46.

R_f (220 nm): 3.62.

MS (ESI^+, CH_3OH, *m/z*): 784.40 $[M+Na]^+$; 1545.81 $[2M+Na]^+$

5.2.16 Synthesis of hexynoic acid-LYGGGL-NH_2

(USC-TS-085-03)

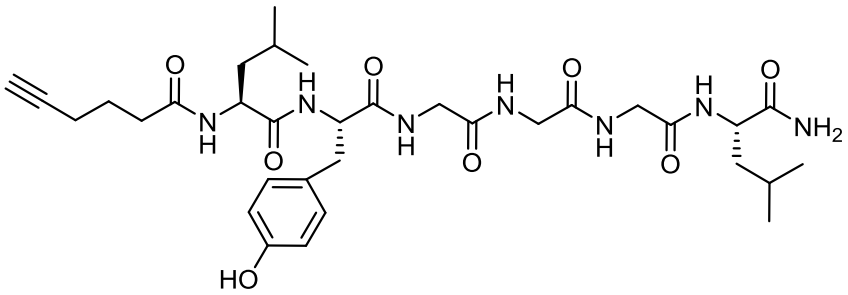

(**24b**)
Hexynoic acid-LYGGGL-NH_2
$C_{33}H_{49}N_7O_8$
761.41 g/mol

Wang-Amide resin (300 mg, 0.2 mmol) was used as the solid support for this reaction. HBTU (3.81 g, 10.0 mmol) in DMF (15 ml) and HOBT (1.53 g; 10 mmol) in DMF (15 ml) were prepared as stock solutions in advance. HOBT solution (1.5 ml) and HBTU solution (1.5 ml) were added to the solid amino acid (5 eq., 0.75 mmol, see table below) and shaken for 5 min.

Amino acid building block	Used amount [mg]
Fmoc-(L)-Leucine-OH	355
Fmoc-Glycine-OH	298
Fmoc-Glycine-OH	301
Fmoc-Glycine-OH	300
Fmoc-(L)-Tyrosine(tBu)-OH	462
Fmoc-(L)-Leucine-OH	350
Hexynoic acid	111

Afterwards, the activated amino acid was given to the deprotected resin and DIPEA (350 µl, 2.0 mmol) was added. Then, the reaction mixture was shaken for 90 min at room temperature. Between coupling and Fmoc deprotection, the resin was washed several times with DMF and

dichloromethane. After sequence assembly, Fmoc was removed and the peptide was cleaved from the resin according to the conditions mentioned in chapter 5.1.2. However, it was not possible to precipitate the peptide. Thus, the cleavage mixture was evaporated to dryness. The crude peptide was purified by HPLC using following program parameters for a ramp gradient:

Time [min]	Flow rate [ml/min]	%ACN
0	3.0	5
30	3.0	70
33	3.0	5

The detection wavelengths were 220 and 254 nm. The fraction from 20.6 to 21.5 min was collected and lyophilized to yield the product as a white solid.

R_t (min; 220 nm): 21.77.

R_f (220 nm): 2.90.

MS (ESI^+, CH_3OH, *m/z*): 694.35 $[M+Na]^+$; 1365.72 $[2M+Na]^+$

5.2.17 Synthesis of hexynoic acid-LGGFGL-NH_2

(USC-TS-086-03)

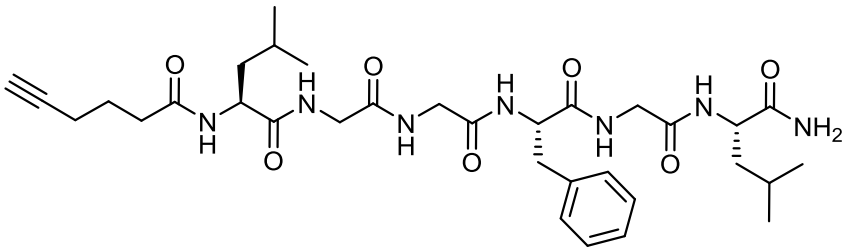

(**24c**)
Hexynoic acid-LGGFGL-NH_2
$C_{33}H_{49}N_7O_7$
655.37 g/mol

Wang-Amide resin (300 mg, 0.2 mmol) was used as the solid support for this reaction. HBTU (3.81 g, 10.0 mmol) in DMF (15 ml) and HOBT (1.53 g; 10 mmol) in DMF (15 ml) were prepared as stock solutions in advance. HOBT solution (1.5 ml) and HBTU solution (1.5 ml) were added to the solid amino acid (5 eq., 0.75 mmol, see table below) and shaken for 5 min.

Amino acid building block	Used amount [mg]
Fmoc-(L)-Leucine-OH	355
Fmoc-Glycine-OH	298
Fmoc-(L)-Phenylalanine-OH	400
Fmoc-Glycine-OH	300
Fmoc-Glycine-OH	301
Fmoc-(L)-Leucine-OH	350
Hexynoic acid	111

Afterwards, the activated amino acid was given to the deprotected resin and DIPEA (350 µl, 2.0 mmol) was added. Then, the reaction mixture was shaken for 90 min at room temperature. Between coupling and Fmoc deprotection, the resin was washed several times with DMF and dichloromethane. After sequence assembly, Fmoc was removed and the peptide was cleaved

from the resin according to the conditions mentioned in chapter 5.1.2. However, it was not possible to precipitate the peptide. Thus, the cleavage mixture was evaporated to dryness. The crude peptide was purified by HPLC using following program parameters for a ramp gradient:

Time [min]	Flow rate [ml/min]	%ACN
0	3.0	5
33	3.0	75
36	3.0	5

The detection wavelengths were 220 and 254 nm. The fraction from 24.0 to 24.6 min was collected and lyophilized to yield the product as a white solid.

R_t (min; 220 nm): 30.89.

R_f (220 nm): 4.05.

MS (ESI^+, CH_3OH, *m/z*): 678.36 $[M+Na]^+$; 1333.72 $[2M+Na]^+$

5.2.18 Synthesis of hexynoic acid-LTGVGL-NH_2

(USC-TS-091-03)

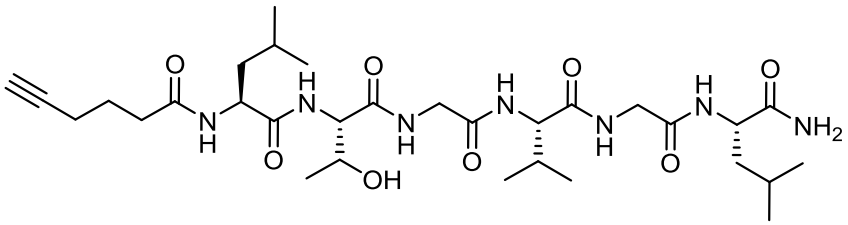

(**24d**)
Hexynoic acid-LTGVGL-NH_2
$C_{31}H_{53}N_7O_8$
651.40 g/mol

Wang-Amide resin (300 mg, 0.2 mmol) was used as the solid support for this reaction. HBTU (3.81 g, 10.0 mmol) in DMF (15 ml) and HOBT (1.53 g; 10 mmol) in DMF (15 ml) were prepared as stock solutions in advance. HOBT solution (1.5 ml) and HBTU solution (1.5 ml) were added to the solid amino acid (5 eq., 0.75 mmol, see table below) and shaken for 5 min.

Amino acid building block	Used amount [mg]
Fmoc-(L)-Leucine-OH	355
Fmoc-Glycine-OH	298
Fmoc-(L)-Valine-OH	341
Fmoc-Glycine-OH	300
Fmoc-Glycine-OH	301
Fmoc-(L)-Threonine(tBu)-OH	399
Hexynoic acid	111

Afterwards, the activated amino acid was given to the deprotected resin and DIPEA (350 µl, 2.0 mmol) was added. Then, the reaction mixture was shaken for 90 min at room temperature. Between coupling and Fmoc deprotection, the resin was washed several times with DMF and dichloromethane. After sequence assembly, Fmoc was removed and the peptide was cleaved from the resin according to the conditions mentioned in chapter 5.1.2. However, it was not

possible to precipitate the peptide. Thus, the cleavage mixture was evaporated to dryness. The crude peptide was purified by HPLC using following program parameters for a ramp gradient:

Time [min]	Flow rate [ml/min]	%ACN
0	3.0	5
40	3.0	90
45	3.0	5

The detection wavelengths were 220 and 254 nm. The fraction from 32.7 to 34.0 min was collected and lyophilized to yield the product as a white solid.

R_t (min; 220 nm): 33.17.

R_f (220 nm): 4.44.

MS (ESI^+, CH_3OH, *m/z*): 674.38 $[M+Na]^+$; 1325.77 $[2M+Na]^+$

5.2.19 Synthesis of ALST1-functionalized silica nanoparticle

USC-TS-121-05

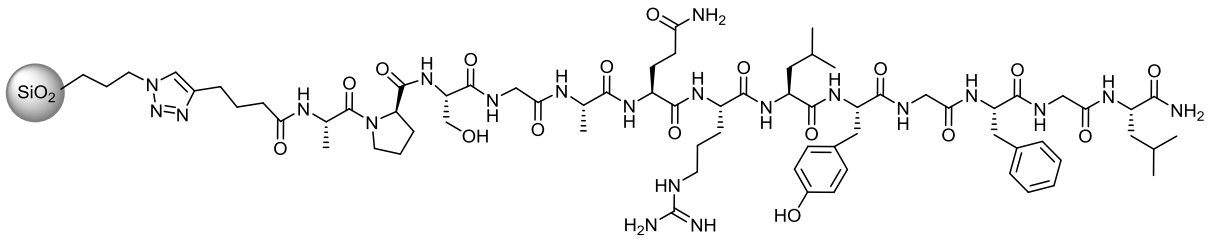

(**35**)

Triethylamine (30 ml), copper(I) iodine (2.2 mg, 0.015 mmol), and TBTA (6.8 mg, 0.015 mmol) were suspended in an ultrasonic bath and subsequently degassed by freeze-pump-thaw. Afterwards, azide-functionalised silica nanoparticles (50 mg), and ALST1-hexynoic acid conjugate (1.22 mg, 0.85 µmol) were suspended in the degassed TEA/Cu(I)/TBTA solution and shaken for 3 d. Then, the particles were centrifuged (15 min, *Eppendorf Centrifuge 5418*, 14000 rpm). The supernatant was discarded, and the particles were washed with TEA (1x), 0.1 M EDTA solution (3x), acetonitrile (2x), and ultrapure water (2x). For each washing step, the particles were suspended in the appropriate solvent, centrifuged (15 min, *Eppendorf Centrifuge 5418*, 14000 rpm), and the supernatant discarded. The solid was lyophilized to yield the product as a white powder.

Yield: 0.049 g

IR (ATR, cm^{-1}): 2956, 2892 (w, $\nu_{C\text{-}H,}$ $\nu_{c\text{-}c}$), 2105 (w, ν_{azide}), 1662 - 1462 (w, $\nu_{amide,}$ $\nu_{c=c}$), 1064 (s, $\nu_{Si\text{-}O}$).

Pauly reaction: positive, particles turn deep red.

5.2.20 Synthesis of LYGFGL^{NH2} functionalized silica nanoparticle

USC-TS-121-01

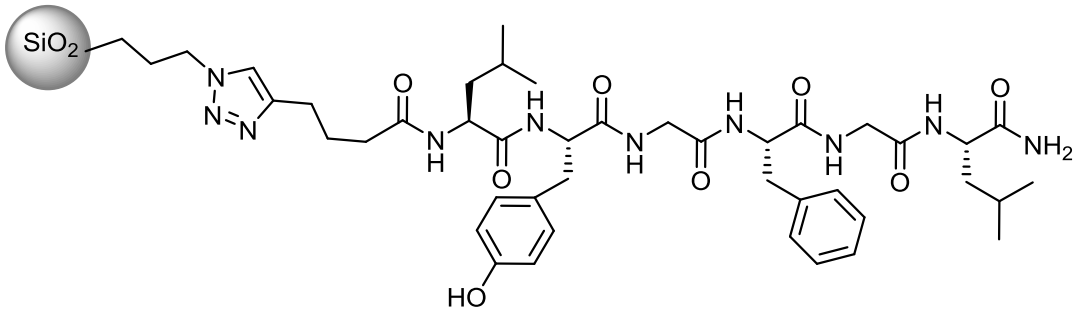

(**35a**)

The synthesis was carried out according to the procedure described in chapter 5.2.19. Azide-functionalised silica nanoparticles (50 mg), and hexynoic acid-LYGFGL^{NH2} (0.65 mg, 0.85 µmol) were suspended in the degassed TEA/Cu(I)/TBTA solution and shaken for 3 d. The isolation and purification of the particles were carried out according to the procedure described in chapter 5.2.19. The product was a white powder.

Yield: 0.050 g

IR (ATR, cm^{-1}): 2956, 2892 (w, $\nu_{C-H,}$ ν_{c-c}), 2105 (w, ν_{azide}), 1662 - 1462 (w, ν_{amide}, $\nu_{c=c}$,$\omega_{Triazole}$), 1064 (s, ν_{Si-O}).

Pauly reaction: positive, particles turn deep red.

5.2.21 Synthesis of LYGGGL^{NH2} functionalized silica nanoparticle

USC-TS-121-02

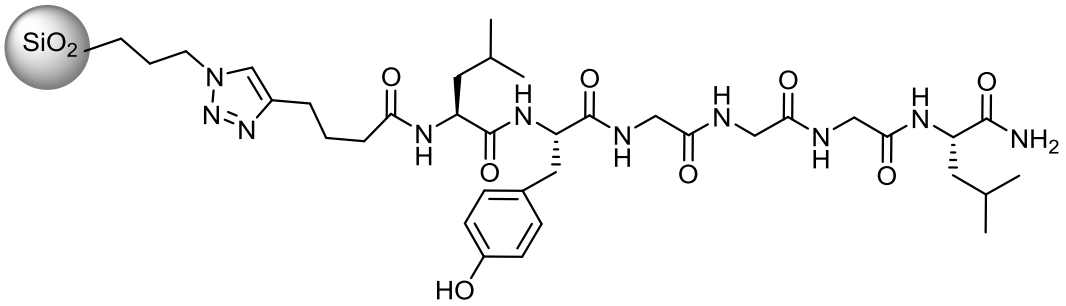

(**35b**)

The synthesis was carried out according to the procedure described in chapter 5.2.19. Azide-functionalised silica nanoparticles (50 mg), and hexynoic acid-LYGGGL^{NH2} (0.57 mg, 0.85 µmol) were suspended in the degassed TEA/Cu(I)/TBTA solution and shaken for 3 d. The isolation and purification of the particles were carried out according to the procedure described in chapter 5.2.19. The product was a white powder.

Yield: 0.050 g

IR (ATR, cm^{-1}): 2956, 2892 (w, $\nu_{C-H,}$ ν_{c-c}), 2105 (w, ν_{azide}), 1662 - 1462 (w, ν_{amide}, $\nu_{c=c}$, $\omega_{Triazole}$)1064 (s, ν_{Si-O}).

Pauly reaction: positive, particles turn red-orange.

5.2.22 Synthesis of LGGFGL^{NH2} functionalized silica nanoparticle

USC-TS-121-03

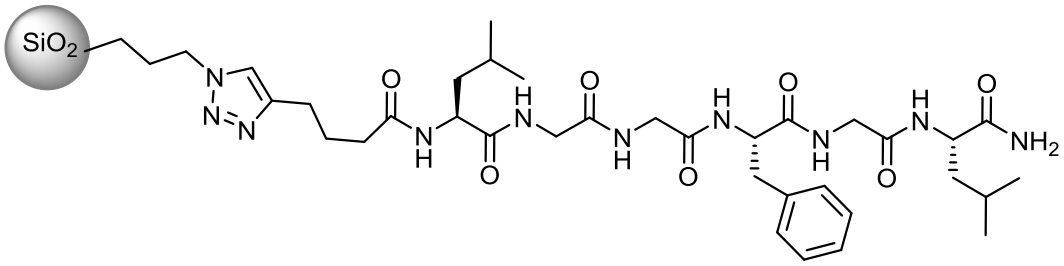

(**35c**)

The synthesis was carried out according to the procedure described in chapter 5.2.19. Azide-functionalised silica nanoparticles (50 mg), and hexynoic acid-LGGFGL^{NH2} (0.56 mg, 0.85 µmol) were suspended in the degassed TEA/Cu(I)/TBTA solution and shaken for 3 d. The isolation and purification of the particles were carried out according to the procedure described in chapter 5.2.19. The product was a white powder.

Yield: 0.050 g

IR (ATR, cm^{-1}): 2956, 2892 (w, $\nu_{C-H,}$ ν_{c-c}), 2105 (w, ν_{azide}), 1662 - 1462 (w, $\nu_{amide,}$ $\nu_{c=c,}$ $\omega_{Triazole}$)1064 (s, ν_{Si-O}).

Pauly reaction: negative, particles remained white.

5.2.23 Synthesis of LTGVGL^{NH2} functionalized silica nanoparticle

USC-TS-121-04

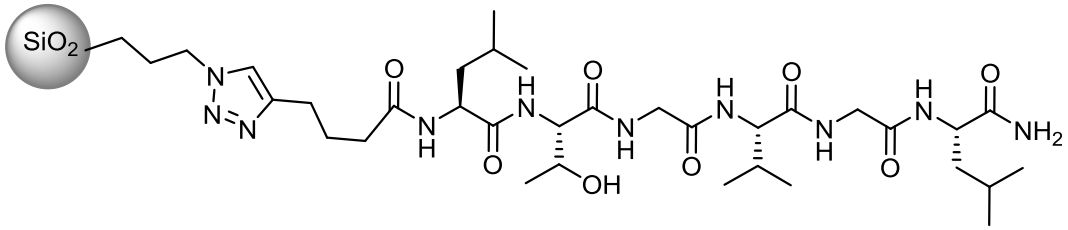

(**35d**)

The synthesis was carried out according to the procedure described in chapter 5.2.19. Azide-functionalised silica nanoparticles (50 mg), and hexynoic acid-LTGVGL^{NH2} (0.65 mg, 0.85 µmol) were suspended in the degassed TEA/Cu(I)/TBTA solution and shaken for 3 d. The isolation and purification of the particles were carried out according to the procedure described in 5.2.19. The product was a white powder.

Yield: 0.050 g

IR (ATR, cm^{-1}): 2956, 2892 (w, $\nu_{C-H,}$ ν_{c-c}), 2105 (w, ν_{azide}), 1662 - 1462 (w, $\nu_{amide,}$ $\nu_{c=c,}$ $\omega_{Triazole}$)1064 (s, ν_{Si-O}).

Pauly reaction: negative, particles remained white.

5.2.24 Synthesis of amino- and azide-functionalized silica-coated superparamagnetic iron oxide nanoparticles

USC-TS-143-01

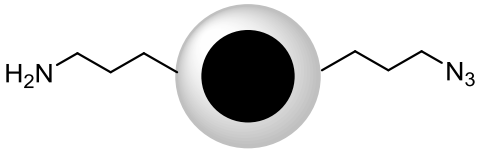

(**36**)
$^{Amine;Azide}$Silica@SPION

Iron(II)sulfate heptahydrate (3.75 g, 13.49 mmol) and iron(III)sulfate hexahydrate (2.30 g, 4.52 mmol) were dissolved in water (500 ml). Then, pH 3 was adjusted with 25% aqueous ammonia and stirred for 30 min. Subsequently, the pH was adjusted to 11.4 with 25% aqueous ammonia and stirred for additional 30 min. The particles were collected using a neodym magnet placed underneath the beaker. The black solid was washed with 25% aqueous ammonia and the particle suspension was centrifuged 30 min (*Hettich Rotana 460*, 2000 rpm). The supernatant was discarded and the black solid was lyophilized. Then, it was suspended in a solution of citric acid in ultrapure water (57 ml, 0.02 M). The pH was adjusted to 5.25 with 25% aqueous ammonia and heated to 80 °C for 90 min. After cooling to room temperature, the suspension was adjusted to pH 10.1 with 25% aqueous ammonia and centrifuged 30 min (*Hettich Rotana 460*, 2000 rpm). The precipitate was discarded and the supernatant was collected and centrifuged again (30 min, *Eppendorf Centrifuge 5418*, 14000 rpm). The supernatant was discarded. The black precipitate was collected and lyophilized.

The coating mixture was prepared by addition of tetraethylorthosilicate (848 µl, 4 mmol), (3-aminopropyl) trimethoxysilane (18 µl, 0.08 mmol) and (3-azidopropyl)triethoxysilane (18 µl, 0.07 mmol) into ethanol (4 ml). Then, coating mixture (679 µl) was added to a suspension of citrate-coated SPIONs (65 mg) in a potassium hydroxide solution (2.5 ml; pH = 12). The suspension was shaken for 1 h and subsequently centrifuged (10 min, *Eppendorf Centrifuge 5418*, 14000 rpm). Then, the dark red precipitate was washed with potassium hydroxide solution (pH = 12), and water and lyophilized to yield a dark red powder.

Yield: 251 mg

Amine loading (µmol/g): 61.0 ± 1.8

Azide loading (µmol/g): 21.3 ± 3.9

IR (ATR, cm^{-1}): 3416 (b, ν_{amine}), 2927(w, ν_{C-H}), 2110 (w, ν_{azide}), 1615 (w, δ_{amine}), 1054(s, $\nu_{Si-O,}$).

Hydrodynamic size distribution (DLS, nm): 10% ≤ 56; 50% ≤ 132; 90% ≤ 439

Zeta potential (mV): -35.6

Relaxivity r_2 (L $mmol_{Fe}^{-1}$ s^{-1}): 125 ± 11

5.2.26 Synthesis of Cy5- and azide-functionalized silica-coated superparamagnetic iron oxide nanoparticles

USC-TS-176-01

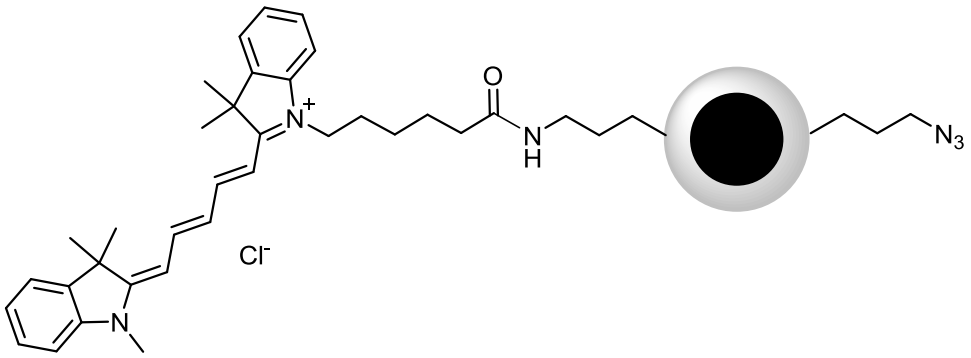

(**36a**)

$^{Cy5;Azide}$Silica@SPION

Azide- and amine-functionalized silica-coated superparamagnetic iron oxide nanoparticles (90 mg) were suspended in a solution of sodium hydrogen carbonate (4.5 ml, pH = 8.3). Then, Cy5 (1.5 mg, 2.4 µmol) in DMF (500 µl) was added and the reaction mixture was shaken for 24 h at room temperature. Subsequently, the greenish-blue suspension was centrifuged (45 min, *Eppendorf Centrifuge 5418*, 14000 rpm) and washed several times with DMF and water until the supernatant became completely colourless. The remaining dark-green solid was suspended in water and lyophilized to yield a dark greenish-blue powder.

Yield: 76 mg

IR (ATR, cm^{-1}): 3416 (b, ν_{amine}), 2927(w, ν_{C-H}), 2110 (w, ν_{azide}), 1650-1600 (w, $\delta_{amine,}$ ν_{amide}), 1054(s, $\nu_{Si-O,}$).

Hydrodynamic size distribution (DLS, nm): 10% ≤ 55; 50% ≤ 98; 90% ≤ 348

Zeta potential (mV): -33.6

Relaxivity r_2 (L $mmol_{Fe}^{-1}$ s^{-1}): 87 ± 7

5.2.27 Synthesis of Cy5- and ALST1-functionalized silica-coated superparamagnetic iron oxide nanoparticles

USC-TS-177-01

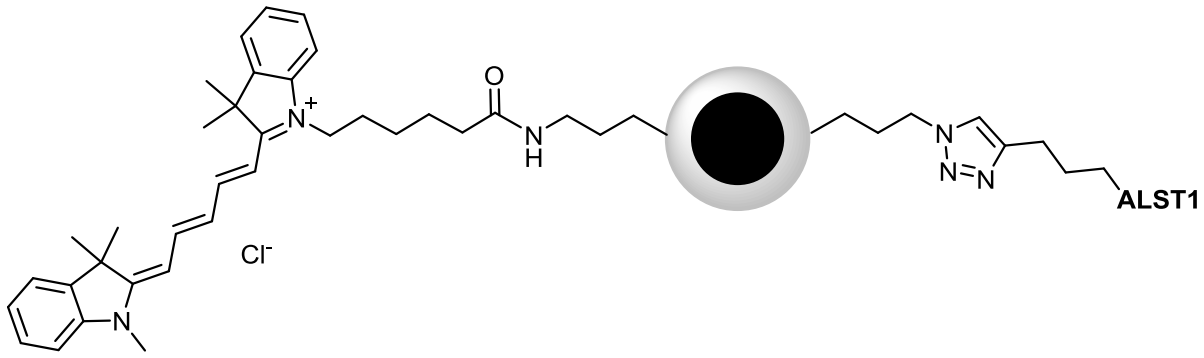

(**36b**)

$^{Cy5;ALST1}$Silica@SPION

Triethylamine (30 ml), copper(I) iodine (2.2 mg, 0.015 mmol), and TBTA (6.8 mg, 0.015 mmol) were suspended in an ultrasonic bath and subsequently degassed using freeze-pump-thaw. Afterwards, Cy5- and azide-functionalized silica-coated SPIONs (20 mg) and ALST1 hexynoic acid conjugate (8.5 mg, 0.05 mmol) were suspended in the degassed TEA/Cu(I)/TBTA solution and shaken for 3 d. Then, the particles were centrifuged (30 min, *Eppendorf Centrifuge 5418*, 14000 rpm). The supernatant was discarded and the particles were washed with TEA (1x), 0.1 M EDTA solution (3x), acetonitrile (2x), and ultrapure water (2x). For each washing step, the particles were suspended in the appropriate solvent, centrifuged (30 min, *Eppendorf Centrifuge 5418*, 14000 rpm), and the supernatant was discarded. The solid was lyophilized to yield the product as a greenish-blue powder.

Yield: 18 mg

IR (ATR, cm^{-1}): 3416 (b, ν_{amine}), 2927(w, ν_{C-H}), 2110 (w, ν_{azide}), 1650-1600 (w, $\delta_{amine,}$ $\nu_{amide,,}$ $\omega_{Triazole}$), 1054(s, $\nu_{Si-O,}$).

Hydrodynamic size distribution (DLS, nm): 10% ≤ 158; 50% ≤ 663; 90% ≤ 2337

Zeta potential (mV): -20.0

Relaxivity r_2 (L $mmol_{Fe}^{-1}$ s^{-1}): 27 ± 5

5.2.28 Synthesis of Cy5- and butyl-capped functionalized silica-coated superparamagnetic iron oxide nanoparticles

USC-TS-178-01

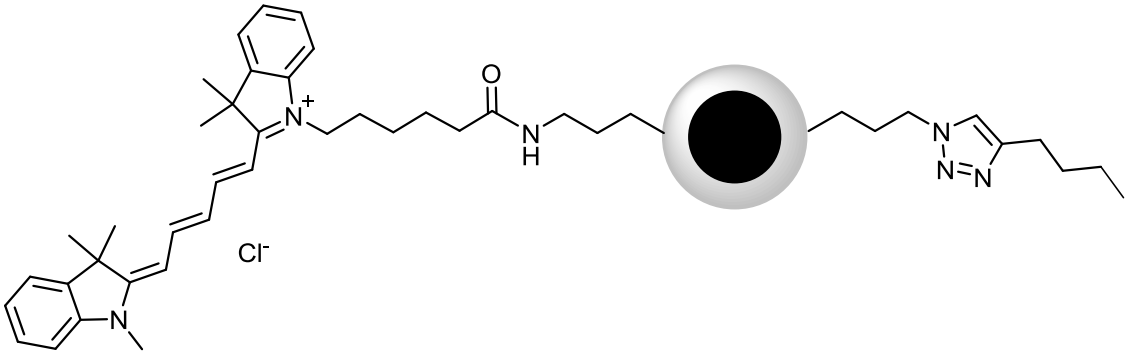

(**36c**)
Cy5;butyl-capped Silica@SPION

Triethylamine (30 ml), copper(I) iodine (2.2 mg, 0.015 mmol), and TBTA (6.8 mg, 0.015 mmol) were suspended in an ultrasonic bath and subsequently degassed using freeze-pump-thaw. Afterwards, Cy5- and azide-functionalized silica-coated SPIONs (20 mg) and 1-hexyne (5 µl, 0.08 mmol) were suspended in the degassed TEA/Cu(I)/TBTA solution and shaken for 3 days. Then, the particles were centrifuged (30 min, *Eppendorf Centrifuge 5418*, 14000 rpm). The supernatant was discarded and the particles were washed with TEA (1x), 0.1 M EDTA solution (3x), acetonitrile (2x), and ultrapure water (2x). For each washing step, the particles were suspended in the appropriate solvent, centrifuged (30 min, *Eppendorf Centrifuge 5418*, 14000 rpm), and the supernatant was discarded. The solid was lyophilized to yield the product as greenish-blue powder.

Yield: 12 mg

IR (ATR, cm^{-1}): 3416 (b, ν_{amine}), 2927(w, ν_{C-H}), 2110 (w, ν_{azide}), 1650-1600 (w, $\delta_{amine,}$ $\nu_{amide,,}$ $\omega_{Triazole}$), 1054(s, $\nu_{Si-O,}$).

Hydrodynamic size distribution (DLS, nm): 10% ≤ 88; 50% ≤ 467; 90% ≤ 3412

Zeta potential (mV): -29.4

Relaxivity r_2 ($L\ mmol_{Fe}^{-1}\ s^{-1}$): 49 ± 5

5.2.29 Synthesis of Aoa- and azide-functionalized detonation nanodiamond

USC-TS-179-01

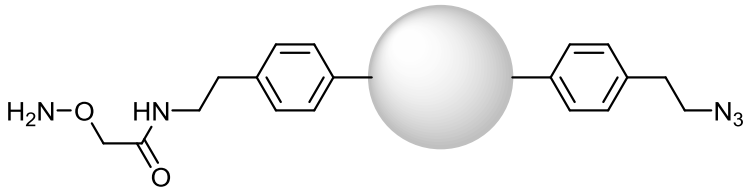

(**38a**)
Aoa;ALST1DND

Azide- and amine-functionalized DND (30 mg) was suspended with HOBT hydrate (25 mg, 0.13 mmol), HBTU (50 mg, 0.13 mmol), Fmoc-Aoa (18 mg, 0.05 mmol), and DIEPA (60 µl, 6.1 mmol) in DMF (2 ml). The brown suspension was shaken for 2 h. Then, it was centrifuged (45 min, *Eppendorf Centrifuge 5418*, 14000 rpm) and the supernatant was discarded. The brown solid was washed with DMF (3x), ultrapure water (2x), and lyophilized to yield a brown solid. Then, the material was suspended in a solution of piperidine in DMF (30%) and shaken for 30 min. Then, the suspension was centrifuged (45 min, *Eppendorf Centrifuge 5418*, 14000 rpm). The cleavage was monitored using UV/Vis spectroscopy using the absorption at 301 nm of the supernatant. For this purpose, the deprotection step was repeated until the supernatant showed no absorption at 301. Subsequently, the brown solid was washed with DMF (3x), water (2x) and lyophilized to yield the compound as a brown powder.

Yield: 30 mg

5.2.30 Synthesis of Cy5- and azide-functionalized detonation nanodiamond

USC-TS-180-01

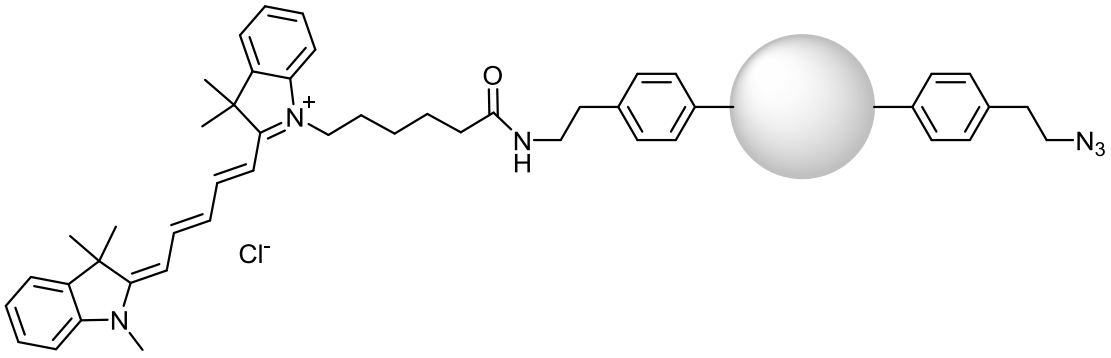

(**39**)
Cy5;Azide DND

Azide- and amine-functionalized DND (30 mg) were suspended in a solution of sodium hydrogen carbonate (900 µl, pH = 8.3). Then, Cy5 (0.5 mg, 0.8 µmol) in DMF (500 µl) were added and the reaction mixture was shaken for 24 h at room temperature. Subsequently, the greenish-blue suspension was centrifuged (45 min, *Eppendorf Centrifuge 5418*, 14000 rpm) and washed several times with DMF and water until the supernatant became completely colourless. The remaining dark-green solid was suspended in water and lyophilized to yield a dark greenish-blue powder.

Yield: 30 mg

5.2.31 Synthesis of Cy5- and ALST-functionalized detonation nanodiamond

USC-TS-183-01

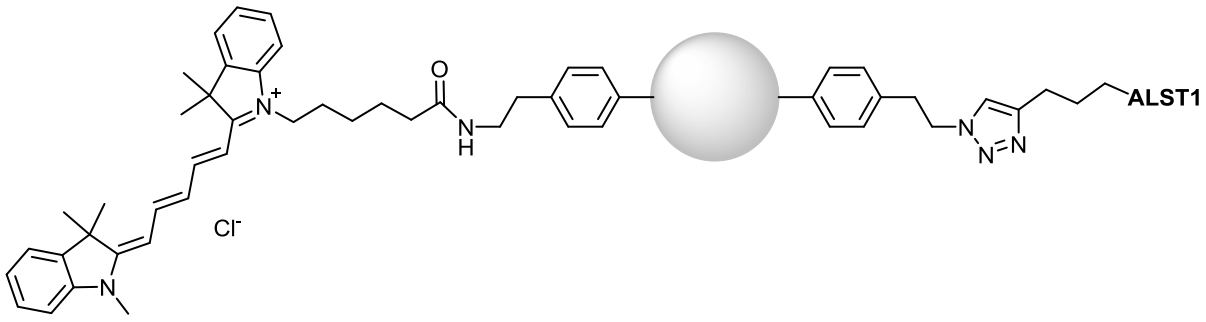

(**39a**)
Cy5;ALST1DND

Triethylamine (30 ml), Cu(I)I (2.2 mg, 0.015 mmol), and TBTA (6.8 mg, 0.015 mmol) were suspended in an ultrasonic bath and subsequently degassed by freeze-pump-thaw. Afterwards, Cy5- and azide-functionalized DND (15 mg) and ALST1 hexynoic acid conjugate (4.0 mg, 0.025 mmol) were suspended in the degassed TEA/Cu(I)/TBTA solution and shaken for 3 d. Then, the particles were centrifuged (30 min, *Eppendorf Centrifuge 5418*, 14000 rpm). The supernatant was discarded, and the particles were washed with TEA (1x), 0.1 M EDTA solution (3x), acetonitrile (2x), and ultrapure water (2x). For each washing step, the particles were suspended in the appropriate solvent, centrifuged (30 min, *Eppendorf Centrifuge 5418*, 14000 rpm), and the supernatant was discarded. The solid was lyophilized to yield the product as greenish-blue powder.

Yield: 12 mg

IR (ATR, cm^{-1}): 3416 (b, $\nu_{amine,\ O\text{-}H}$), 2950, 2870 (w, $\nu_{C\text{-}H}$), 1665 (w, ν_{amide})

Average diameter (TEM, nm): 5.2

Hydrodynamic size distribution (DLS, nm): 10% ≤ 67; 50% ≤ 149; 90% ≤ 406

Zeta potential (mV): 24.7

5.2.32 Synthesis of Cy5- and butyl-capped functionalized detonation nanodiamond

USC-TS-184-01

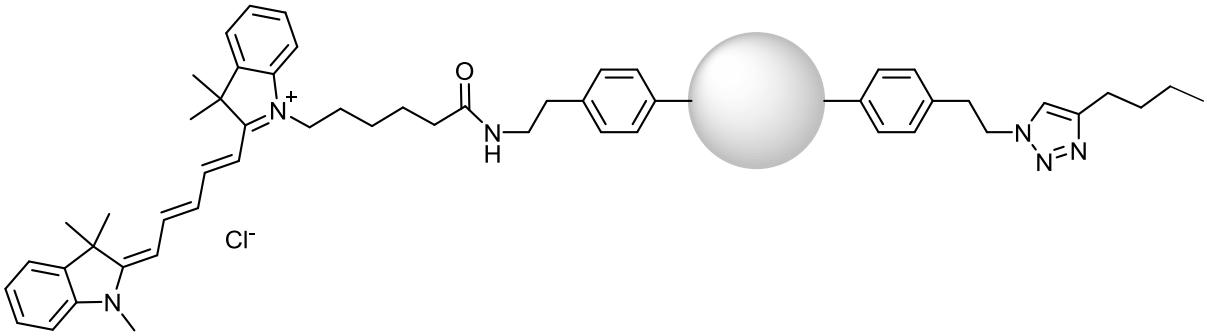

(**39b**)
Cy5;butyl-capped DND

The synthesis was carried out according to the procedure described in chapter 5.2.31. Cy5- and azide-functionalized DND (15 mg) and 1-hexyne (5 µl, 0.08 mmol) were suspended in the degassed TEA/Cu(I)/TBTA solution and shaken for 3 d. The isolation and purification of the particles were carried out according to the procedure described in chapter 5.2.31. The product was a greenish-blue powder.

Yield: 10 mg

IR (ATR, cm^{-1}): 3416 (b, $\nu_{amine,\ O\text{-}H}$), 2950, 2870 (w, $\nu_{C\text{-}H}$), 1665 (w, ν_{amide})

Average diameter (TEM, nm): 5.3

Hydrodynamic size distribution (DLS, nm): 10% ≤ 59; 50% ≤ 129; 90% ≤ 350

Zeta potential (mV): 27.5

5.2.33 Synthesis of bromo[(tricarbonyle)(2-phenyl-1*H*-imidazo[4,5-*f*][1,10]phenanthroline)]rhenium(I)- and ALST1-functionalized detonation nanodiamond

USC-TS-181-02

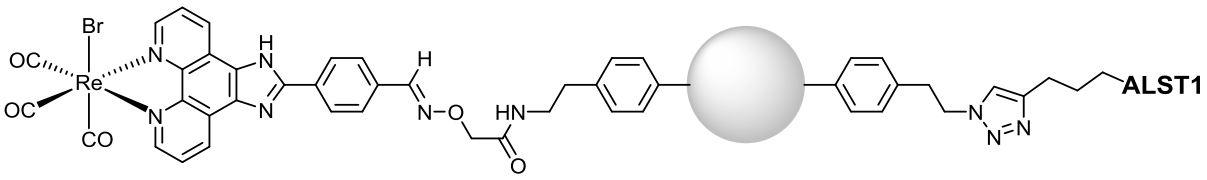

(**40a**)
[ReBr(CO)3(L)]-Aoa;ALST1DND

The copper(I)-catalysed 1,3-dipolar azide-alkyne cycloaddition of ALST1 with the azide group on the DND surface was carried out according to the protocol described in chapter 5.2.31. The Aoa- and azide-functionalized DND (15 mg) and ALST1 hexynoic acid conjugate (4.0 mg, 0.025 mmol) were suspended in the degassed TEA/Cu(I)/TBTA solution and shaken for 3 d. The isolation and purification of the particles were carried out according to the procedure described in chapter 5.2.31. The product was a brown powder. Subsequently, the material was suspended in mixture (1:1) of DMF and acetate buffer (pH = 4.7) and bromo[(tricarbonyle)(4-(1*H*-imidazo[4,5-*f*][1,10]phenanthrolin-2-yl)benzaldehyde)]rhenium(I) (5 mg, 7.5 µmol) was added. The reaction mixture was shaken for 24 h. Afterwards, the suspension was centrifuged (30 min, *Eppendorf Centrifuge 5418*, 14000 rpm), washed with DMF (3x), acetonitrile (2x), and water (3x) and lyophilized to yield the product as a brown solid.

Yield: 10 mg

IR (ATR, cm^{-1}): 3416 (b, $\nu_{amine,\ O\text{-}H}$), 2950, 2870 (w, $\nu_{C\text{-}H}$), 2029, 1925, 1902 (ν_{CO}), 1665 (w, ν_{amide})

Average diameter (TEM, nm): 5.3

Hydrodynamic size distribution (DLS, nm): 10% ≤ 66; 50% ≤ 137; 90% ≤ 457

Zeta potential (mV): 24.6

EDX (keV): 0.28 (C), 0.95 (Cu), 1.86 (Re), 6.39 (Fe), 6.93 (Co), 8.02 (Cu), 8.66 (Re), 8,86 (Cu), 9.99 (Re), 10.32 (Re).

5.2.34 Synthesis of bromo[(tricarbonyle)(2-phenyl-1*H*-imidazo[4,5-*f*][1,10]phenanthroline)]rhenium(I)- and butyl-capped functionalized detonation nanodiamond

USC-TS-182-02

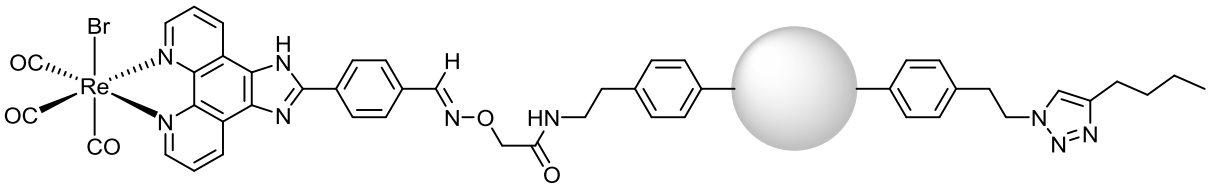

(**40b**)
[ReBr(CO)3(L)]-Aoa;butyl-capped$_{DND}$

The copper(I)-catalysed 1,3-dipolar azide-alkyne cycloaddition of 1-hexyne with the azide group on the DND surface was carried out according to the protocol described in chapter 5.2.31. Aoa and azide functionalized DND (15 mg) and 1-hexyne (5 µl, 0.08 mmol) were suspended in the degassed TEA/Cu(I)/TBTA solution and shaken for 3 d. Then, the particles were centrifuged (30 min, Eppendorf Centrifuge 5418, 14000 rpm). The isolation and purification of the particles were carried out according to the procedure described in chapter 5.2.31. The product was a brown powder. Subsequently, the material was suspended in mixture (1:1) of DMF and acetate buffer (pH = 4.7) and bromo[(tricarbonyle)(4-(1*H*-imidazo[4,5-*f*][1,10]phenanthrolin-2-yl)benzaldehyde)]rhenium(I) (5 mg, 7.5 µmol) was added. The reaction mixture was shaken for 24 h. Afterwards, the suspension was centrifuged (30 min, *Eppendorf Centrifuge 5418*, 14000 rpm), washed with DMF (3x), acetonitrile (2x), and water (3x) and lyophilized to yield the product as a brown solid.

Yield: 10 mg

IR (ATR, cm^{-1}): 3416 (b, $\nu_{amine,\ O\text{-}H}$), 2950, 2870 (w, $\nu_{C\text{-}H}$), 2029, 1925, 1902 (ν_{CO}), 1665 (w, ν_{amide})

Average diameter (TEM, nm): 5.2

Hydrodynamic size distribution (DLS, nm): 10% ≤ 24; 50% ≤ 62; 90% ≤ 220

Zeta potential (mV): 24.8

EDX (keV): 0.28 (C), 0.95 (Cu), 1.86 (Re), 6.39 (Fe), 6.93 (Co), 8.02 (Cu), 8.66 (Re), 8,86 (Cu), 9.99 (Re), 10.32 (Re).

6 References

[1] B. F. G. Johnson, *Top. Catal.* **2003**, *24*.

[2] D. Bazin, *Top. Catal.* **2002**, *18*, 79-84.

[3] L. C. Grabow, M. Mavrikakis, *Angew. Chem. Int. Ed.* **2008**, *47*, 7390–7392.

[4] T. Atanasijevic, A. Jasanoff, *Nat. Prot.* **2007**, *2*, 2581-2589.

[5] T. L. Doane, C. Burda, *Chem. Soc. Rev.* **2012**, *41*, 2885-2911.

[6] V. V. Mody, M. I. Nounou, M. Bikram, *Adv. Drug Deliv. Rev.* **2009**, *61*, 795–807.

[7] L. Y. T. Chou, K. Ming, W. C. W. Chan, *Chem. Soc. Rev.* **2011**, *40*, 233–245.

[8] A.-H. Lu, E. L. Salabas, F. Schüth, *Angew. Chem. Int. Ed.* **2007**, *46*, 1222–1244.

[9] B. L. Cushing, V. L. Kolesnichenko, C. J. O'Connor, *Chem. Rev.* **2004**, *104*, 3893-3946.

[10] B. Jeong, S. W. Kim, Y. H. Bae, *Adv. Drug Deliv. Rev.* **2002**, *54*, 37 –51.

[11] G. Schottner, *Chem. Mater.* **2001**, *13*, 3422-3435.

[12] L. L. Hench, J. K. West, *Chem. Rev.* **1990**, *90*, 33-72.

[13] J. H. Schulman, D. P. Riley, *J. Colloid Sci.* **1948**, *3*, 383-405.

[14] A. K. Ganguli, T. Ahmad, S. Vaidya, J. Ahmed, *Pure Appl. Chem.* **2008**, *80*, 2451-2477.

[15] M. Rajamathi, R. Seshadri, *Curr. Opin. Solid State Mat.* **2002**, *6*, 337–345.

[16] G. Demazeau, *J. Mater. Sci.* **2008**, *43*, 2104–2114.

[17] M. Niederberger, G. Garnweitner, N. Pinna, G. Neri, *Prog. Solid. State Chem.* **2005**, *33*, 59-70.

[18] S. M. Moghimi, A. C. Hunter, J. C. Murray, *Nanomedicine* **2005**, *19*, 311-330.

[19] L. Zhang, F. X. Gu, J. M. Chan, A. Z. Wang, R. S. Langer, O. C. Farokhzad, *Clinic. Pharm. and Therap.* **2008**, *83*, 761-769.

[20] C. Zhou, M. Long, Y. Qin, X. Sun, J. Zheng, *Angew. Chem. Int. Ed.* **2011**, *50*, 3168–3172.

[21] F. Alexis, E. Pridgen, L. K. Molnar, O. C. Farokhzad, *Mol. Pharm.* **2008**, *5*, 505–515.

[22] M. A. Dobrovolskaia, P. Aggarwal, J. B. Hall, S. E. McNeil, *Mol. Pharm.* **2008**, *5*, 487–495.

[23] S. M. Moghimi, C. Hunter, J. C. Murray, *Pharmacol. Rev.* **2001**, *53*, 283–318.

[24] H. Maeda, J. Wua, T. Sawa, Y. Matsumura, K. Horic, *J. Control. Release* **2000**, *65*, 271–284.

[25] H. Maeda, *Adv. Enzyme Regul.* **2001**, *41*, 189–207.

[26] H. Maeda, G. Y. Bharate, J. Daruwalla, *Eur. J. Pharm. Biopharm.* **2009**, *71*, 409–419.

[27] L. Brannon-Peppas, J. O. Blanchette, *Adv. Drug Deliv. Rev.* **2004**, *56*, 1649– 1659.

[28] K. Cho, X. Wang, S. Nie, Z.Chen, D. M. Shin, *Clin. Cancer Res.* **2008**, *14*, 1310-1316.

[29] D. Peer, J. M. Karp, S. Hong, Omid C. Farokhzad, R. Margalit, R. Langer, *Nat. Nanotechnol.* **2007**, *2*, 751-561.

[30] R. Haag, F. Kratz, *Angew. Chem. Int. Ed.* **2006**, *118*, 218–1237.

[31] H. Maeda, *Bioconjugate Chem.* **2010**, *21*, 797–802.

[32] S. Bhattacharyya, R. A. Kudgus, R. Bhattacharya, P. Mukherjee, *Pharm. Res.* **2010**, *28*, 237–259.

[33] K. Schwarz, D. B. Milne, *Nature* **1972**, *239*, 333-334.

[34] E. M. Carlisle, *Science* **1972**, *178*, 619-621.

[35] J. D. Birchall, *Chem. Soc. Rev.* **1995**, *24*, 351-357.

[36] J. D. Birchall, C. Exley, J. S. Chappell, M. J. Phillips, *Nature* **1989**, *338*, 146-148.

[37] B. Quartly, G. Esselmont, A. Taylor, M. Dobrota, *Food Chem. Toxicol.* **1993**, *31*, 543-548.

[38] J. D. Birchall, J. P. Bellia, N. B. Roberts, *Coord. Chem. Rev.* **1995**, *149*, 231-240.

[39] B. Fubini, A. Hubbard, *Free Radical Biol. Med.* **2003**, *34*, 1507–1516.

[40] W. Stöber, A. Fink, E. Bohn, *J. Colloid Interface Sci.* **1968**, *26*, 62-69.

[41] F. Erogbogbo, K.-T. Yong, I. Roy, G. Xu, P. N. Prasad, M. T. Swihart, *ACS Nano* **2008**, *2*, 873–878.

[42] J. H. Warner, A. Hoshino, Kenji Yamamoto, R. D. Tilley, *Angew. Chem. Int. Ed.* **2005**, *44*, 4550–4554.

[43] M. V. Wolkin, J. Jorne, P. M. Fauchet, G. Allan, C. Delerue, *Phys. Rev. Lett.* **1999**, *82*, 197-200.

[44] G. Dördelmann, H. Pfeiffer, A. Birkner, U. Schatzschneider, *Inorg. Chem.* **2011**, *50*, 4362–4367.

[45] K. Nozawa, H. Gailhanou, L. Raison, P. Panizza, H. Ushiki, E. Sellier, J. P. Delville, M. H. Delville, *Langmuir* **2005**, *21*, 1516–1523.

[46] I. I. Slowing, B. G. Trewyn, S. Giri, V. S.-Y. Lin, *Adv. Funct. Mater.* **2007**, *17*, 1225–1236.

[47] C. Barbe, J. Bartlett, L. Kong, K. Finnie, H. Quiang, M. Larkin, S. Calleja, *Adv. Mater.* **2004**, *16*, 1959-1966.

[48] J. M. Rosenholm, C. Sahlgren, M. Linden, *Nanoscale* **2010**, *2*, 1870–1883.

[49] Y. J. Wong, L. Zhu, W. S. Teo, Y. W. Tan, Y. Yang, C. Wang, H. Chen, *J. Am. Chem. Soc.* **2011**, *133*, 11422–11425.

[50] Z. Li, J. C. Barnes, A. Bosoy, J. F. Stoddart, J. I. Zink, *Chem. Soc. Rev.* **2012**, *41*, 2590-2605.

[51] A. Corma, *Chem. Rev.* **1997**, *97*, 2373-2419.

[52] H. P. Rim, K. H. Min, H. J. Lee, S. Y. Jeong, S. C. Lee, *Angew. Chem. Int. Ed.* **2011**, *123*, 1-6.

[53] S. Wang, *Micropor. Mesopor. Mat.* **2009**, *117*, 1–9.

[54] Y. Jiao, Y. Sun, B. Chang, D. Lu, W. Yang, *Chem. Eur. J.* **2013**, *19*, 15410 – 15420.

[55] A. Burns, H. Ow, U. Wiesner, *Chem. Soc. Rev.* **2006**, *35*, 028–1042.

[56] V. Salgueiriño-Maceira, M. A. Correa-Duarte, *Adv. Mater.* **2007**, *19*, 4131–4144.

[57] C.-R. Li, A.-L. Ji, L. Gao, Z.-X. Cao, *Adv. Mater.* **2009**, *21*, 4652–4657.

[58] R. Bardhan, S. Lal, A. Joshi, N. J. Halas, *Acc. Chem. Res.* **2011**, *44*, 936–946.

[59] B. H. Yang, Y. Zhuang, H. Hu, X. Du, Cuixia Zhang, X. Shi, H. Wu, S. Yang, *Adv. Funct. Mater.* **2010**, *20*, 1733–1741.

[60] M. Pumera, *Chem. Soc. Rev.* **2010**, *39*, 4146–4157.

[61] J. Yao, Y. Sun, M. Yang, Y. Duan, *J. Mater. Chem.*, **2012**, *22*, 14313-14330.

[62] J. Hu, T. W. Odom, C. M. Lieber, *Acc. Chem. Res.* **1999**, *32*, 435-446.

[63] P. M. Ajayan, *Chem. Rev.* **1999**, *99*, 1787-1799.

[64] R. H. Baughman, A. A. Zakhidov, W. A. d. Heer, *Science* **2002**, *297*, 787-794.

[65] A. Krueger, *Adv. Mater.* **2008**, *20*, 2445–2449.

[66] X. Zhang, W. Hu, J. Li, L. Tao, Y. Wei, *Toxicol. Res.* **2012**, *1*, 62–68.

[67] N. Mohan, C.-S. Chen, H.-H. Hsieh, Y.-C. Wu, H.-C. Chang, *Nano Lett.* **2010**, *10*, 3692–3699.

[68] A. M. Schrand, H. Huang, C. Carlson, J. J. Schlager, E. O. sawa, S. M. Hussain, L. Dai, *J. Phys. Chem. B* **2007**, *111*, 2-8.

[69] L. Marcon, F. Riquet, D. Vicogne, S. Szunerits, J.-F. Bodart, R. Boukherroub, *J. Mater. Chem.* **2010**, *20*, 8064–8069.

[70] C. Medina, M. J. Santos-Martinez, A. Radomski, O. I. Corrigan, M. W. Radomski, *Brit. J. Pharmacol.* **2007**, *150*, 552–558.

[71] M. Horie, L. K. Komaba, H. Kato, A. Nakamura, K. Yamamoto, S. Endoh, K. Fujita, S. Kinugasa, K. Mizuno, Y. Hagihara, Y. Yoshida, H. Iwahashi, *Diam. Relat. Mater.* **2012**, *24*, 15–24.

[72] A. M. Schrand, L. Dai, J. J. Schlager, S. M. Hussain, E. Osawa, *Diam. Relat. Mater.* **2007**, *16*, 2118–2123.

[73] Y. Yuan, Y. Chen, J.-H. Liu, H. Wang, Y. Liu, *Diam. Relat. Mater.* **2009**, *18*, 95–100.

[74] S.-J. Yu, M.-W. Kang, H.-C. Chang, K.-M. Chen, Y.-C. Yu, *J. Am. Chem. Soc.* **2005**, *127*, 17604-17605.

[75] T. Meinhardt, PhD thesis, Julius-Maximilians-Universität Würzburg **2011**.

[76] N. V. Novikov, *Diam. Relat. Mater.* **1999**, *8*, 1427-1432.

[77] P. DeCarli, J. Jamieson, *Science* **1961**, *133*, 1821-1822.

[78] G. Burkard, H. Tamura, Y. Tanabe, A. B. Sawaoka, *Appl. Phys. Lett.* **1995**, *66*, 3131-3133.

[79] O. A. Shenderova, D. M. Gruen, *Ultrananocrystalline Diamanod: Synthesis, Properties and Applications*, William Andrew Publishing, New York, **2006**.

[80] O. A. Shenderova, V. V. Zhirnov, D. W. Brenner, *Crit. Rev. Solid State Mater. Sci.* **2002**, *27*, 227-356.

[81] A. Krüger, *Neue Kohlenstoffmaterialien*, Teubner Verlag, Wiesbaden, **2007**.

[82] M. Frenklach, R. Kematick, D. Huang, W. Howard, K. E. Spear, A. W. Phelps, R. Koba, *J. Appl. Phys.* **1989**, *66*, 395-399.

[83] K. Niwase, T. Tanaka, Y. Kakimoto, K. N. Ishihara, P. H. Shingu, *Mater. Trans. JIM* **1995**, *36*, 282-288.

[84] A. M. Schrand, S. C. Hens, O. A. Shenderova, *Crit. Rev. Solid State Mater.* **2009**, *34*, 18-74.

[85] X.-W. Fang, J.-D. Mao, E. M. Levin, K. Schmidt-Rohr, *J. Am. Chem. Soc.* **2009**, *16*, 1426-1435.

[86] V. F. Loktev, V. I. Makalski, I. V. Stoyanova, A. V. Kalinkin, V. A. Likholobov, *Carbon* **1990**, *29*, 817-819.

[87] T. Tsubota, O. Hirabayashi, S. N. S. Ida, M. Nagata, Y. Matsumoto, *Diam. Relat. Mater.* **2002**, *11*, 1360-1365.

[88] V. N. Khabasheskua, J. L. Margravea, E. V. Barrera, *Diam. Relat. Mater.* **2005**, *14*, 859–866.

[89] Y. Liu, Z. Gu, J. L. Margrave, V. N. Khabashesku, *Chem. Mater.* **2004**, *16*, 3924-3930.

[90] B. V. Spitsyn, J. L. Davidson, M. N. Gradoboev, T. B. Galushko, N. V. Serebryakova, T. H. Karpukhina, I. I. Kulakova, N. N. Melnik, *Diam. Relat. Mater.* **2006**, *15*, 296-299.

[91] A. Krueger, *Chem. Eur. J.* **2008**, *14*, 1382 – 1390.

[92] A. Krüger, Y. Liang, G. Jarre, J. Stegk, *J. Mater. Chem.* **2006**, *16*, 2322-2328.

[93] R. Martin, P. C. Heydorn, M. Alvaro, H. Garcia, *Chem. Mater.* **2009**, *21*, 4505-4514.

[94] D. Steinmüller-Nethl, F. R. Kloss, M. Najam-Ul-Haq, M. Rainer, K. Larsson, C. Linsmeier, G. Köhler, C. Fehrer, G. Lepperdinger, X. Liu, N. Memmel, E. Bertel, C. W. Huck, R. Gassner, G. Bonn, *Biomaterials* **2006**, *27*, 4547-4556.

[95] A. S. Barnard, *Analyst* **2009**, *134*, 1751–1764.

[96] A. C. Ferrari, J. Robertson, *Phil. Trans. R. Soc. Lond. A* **2004**, *362*, 2477–2512.

[97] T. Meinhardt, D. Lang, H. Dill, A. Krueger, *Adv. Funct. Mater.* **2011**, *21*, 494–500.

[98] G. Jarre, PhD thesis, Julius-Maximilians-Universität Würzburg **2011**.

[99] G. Dördelmann, T. Meinhardt, T. Sowik, A. Krueger, U. Schatzschneider, *Chem. Commun.* **2012**, *48*, 11528-11530.

[100] V. S. Bondar, I. O. Pozdnyakova, A. P. Puzyr, *Phys. Solid State* **2004**, *46*, 758-760.

[101] I. Kiflawi, J. Bruley, *Diam. Relat. Mater.* **2000**, *9*, 87-93.

[102] C. D. Clark, C. A. Norris, *J. Phys. C: Solid State Phys.* **1970**, *3*, 651-658.

[103] C. D. Clark, C. A. Norris, *J. Phys. C: Solid State Phys.* **1971**, *4*, 333-336.

[104] A. E. Aleksenskii, V. Y. Osipov, A. Y. Vul, Y. B. Ber, A. B. Smirnov, V. G. Melekhin, *Phys. Solid State* **2001**, *43*, 145–150.

[105] F. Jelezko, C. Tietz, A. Gruber, I. Popa, A. Nizovtsev, S. Kilin, J. Wrachtrup, *Single Mol.* **2001**, *4*, 255-260.

[106] A. Lenef, S. C. Rand, *Physical Rev.* **1996**, *53*, 13441-13455.

[107] N. B. Manson, R. L. McMurtrie, *J. Lumin.*, *127*, 98–103.

[108] M. Mahmoudi, S. Sant, B. Wang, S. Laurent, T. Sen, *Adv. Drug Deliv. Rev.* **2011**, *63*, 24–46.

[109] A. K. Gupta, M. Gupta, *Biomaterials* **2005**, *26*, 3995–4021.

[110] T. Neuberger, B. Schöpf, H. Hofmann, M. Hofmann, B. v. Rechenberg, *J. Magn. Magn. Mater.* **2005**, *293*, 483–496.

[111] J. S. Weinstein, C. G. Varallyay, E. Dosa, S. Gahramanov, B. Hamilton, W. D. Rooney, L. L. Muldoon, E. A. Neuwelt, *J. Cerebr. Blood F. Met.* **2010**, *30*, 15-35.

[112] R. Massart, *IEEE T. Magn.* **1981**, *17*, 1247–1248.

[113] J. Gao, H. Gu, B. Xu, *Acc. Chem. Res.* **2009**, *42*, 1097-1107.

[114] Y. Sahoo, H. Pizem, T. Fried, D. Golodnitsky, L. Burstein, C. N. Sukenik, G. Markovich, *Langmuir* **2001**, *17*, 7907–7911.

[115] M. Mahmoudi, M. A. Shokrgozar, A. Simchi, M. Imani, A. S. Milani, P. Stroeve, H. Vali, U. O. Hafeli, S. Bonakdar, *J. Phys. Chem. C* **2009**, *113*, 2322–2331.

[116] M. Mahmoudi, A. Simchi, M. Imani, M. A. Shokrgozar, K. Azadmanesh, F. Azari, *Adv. Engin. Mat.* **2009**, *11*, B243–B250.

[117] M. Mahmoudi, A. Simchi, M. Imani, A. S. Milani, P. Stroeve, *Nanotechnology* **2009**, *20*, 1-8.

[118] I. Lynch, *Physica A* **2007**, *373*, 511–520.

[119] A. E. Nel, I. Madler, D. Velegol, T. Xia, E. M. V. Hoek, P. Somasundaran, F. Klaessig, V. Castranova, M. Thompson, *Nat. Mater.* **2009**, *8*, 543–557.

[120] A. Nel, T. Xia, L. Madler, N. Li, *Science* **2006**, *311*, 622–627.

[121] I. W. Hamley, *Angew. Chem. Int. Ed.* **2003**, *42*, 1692–1712.

[122] K. C. Souza, J. D. Ardisson, E. M. B. Sousa, *J. Mater. Sci.: Mater. Med.* **2009**, *20*, 507–512.

[123] J. Kandzia, M. J. D. Anderson, W. Mullerruchholtz, *Immunobiology* **1983**, *165*, 289–290.

[124] A. Antonelli, C. Sfara, L. Mosca, E. Manuali, M. Magnani, *J. Nanosci. Nanotech.* **2008**, *8*, 2270–2278.

[125] C. P. Bean, *J. Appl. Phys.* **1955**, *26*, 1381-1383.

[126] S. Chikazumi, S. Taketomi, M. Ukita, M. Mizukami, H. Miyajima, M. Setogawa, Y. Kurihara, *J. Magn. Magn. Mater.* **1987**, *65*, 245-251.

[127] M. A. Brown, R. C. Smelka, *MRI: Basic principles and Apllications*, 4 ed., Wiley, New Jersey, **2010**.

[128] C. Sun, J. S. H. Lee, M. Zhang, *Adv. Drug Deliv. Rev.* **2008**, *60*, 1252–1265.

[129] P. Caravan, *Chem. Soc. Rev.* **2006**, *35*.

[130] Y.-w. Jun, J.-H. Lee, J. Cheon, *Angew. Chem. Int. Ed.* **2008**, *47*, 5122–5135.

[131] S. Laurent, D. Forge, M. Port, A. Roch, C. Robic, L. V. Elst, R. N. Muller, *Chem. Rev.* **2008**, *108*, 2064–2110.

[132] R. B. Merrifield, *J. Am. Chem. Soc.* **1963**, *85*, 2149–2154.

[133] R. B. Merrifield, *Science* **1986**, *232*, 341–347.

[134] S. L. Pedersen, A. P. Tofteng, L. Malik, K. J. Jensen, *Chem. Soc. Rev.* **2012**, *41*, 1826–1844.

[135] L. A. Carpino, G. Y. Han, *J. Am. Chem. Soc.* **1970**, *92*, 5748–5749.

[136] L. A. Carpino, G. Y. Han, *J. Org. Chem.* **1972**, *37*, 3404–3409.

[137] W. C. Chan, P. D. White, *Fmoc Solid Phase Peptide Synthesis - A Practical Approach*, Oxford University Press, New York, **2004**.

[138] I. Coin, M. Beyermann, M. Bienert, *Nature Prot.* **2007**, *2*, 3247-3256.

[139] A. Isidro-Llobet, M. Alvarez, F. Albericio, *Chem. Rev.* **2009**, *109*, 2455–2504.

[140] E. Valeur, M. Bradley, *Chem. Soc. Rev.* **2009**, *38*, 606–631.

[141] C. J. Sherr, *Science* **1996**, *274*, 1672-1677.

[142] S. B. Baylin, J. E. Ohm, *Nat. Rev. Canc.* **2006**, *6*, 107-116.

[143] S. W. Lowe, A. W. Lin, *Carcinogenesis* **2000**, *21*, 485-495.

[144] A. E. Frankel, R. J. Kreitman, E. A. Sausville, *Clin. Cancer Res.* **2000**, *6*, 326–334.

[145] J. C. Reubi, *Endocrine Rev.* **2003**, *24*, 389–427.

[146] A. V. Schally, A. Nagy, *Europ. J. Endocrin.* **1999**, *141*, 1–14.

[147] J. J. J. M. Donners, G. A. Silva, H. A. Behanna, S. G. Anthony, U.S. Patent 7,544,661 B2, **2009**.

[148] J. Yue, K. M. Mulder, *Pharmacology & Therapeutics* **2001**, *91*, 1– 34.

[149] C. Duvernelle, V. Freund, N. Frossard, *Pulmonary Pharmacology & Therapeutics* **2003**, *16*, 181–196.

[150] M. Reiss, *Microbes and Infect.* **1999**, *1*, 1327−1347.

[151] S. N. Giri, D. M. Hyde, R. K. Braun, W. Gaarde, J. R. Harper, M. D. Pierschbacher, *Biochem. Pharm.* **1997**, *54*, 1205-1216.

[152] H. Fakhrai, O. Dorigo, D. L. Shawler, H. Lin, D. Mercola, K. L. Black, I. Royston, R. E. Sobol, *Proc. Natl. Acad. Sci. USA* **1996**, *93*, 2909-2914.

[153] H. Vizthum, U. Homberg, H. Agricola, *J. Comp. Neurol.* **1996**, *369*, 419-437.

[154] K. Reichenwald, G. C. Unnithan, N. T. Davis, H. Agricola, R. Feyereisen, *P. Natl. Acad. Sci. USA* **1994**, *91*, 11894-11898.

[155] A. Anas, T. Okuda, N. Kawashima, K. Nakayama, T. Itoh, M. Ishikawa, V. Biju, *ACS Nano* **2009**, *3*, 2419–2429.

[156] V. Biju, D. Muraleedharan, K.-i. Nakayama, Y. Shinohara, T. Itoh, Y. Baba, M. Ishikawa, *Langmuir* **2007**, *23*, 10254-10261.

[157] N. Birgul, C. Weise, H.-J. Kreienkamp, D. Richter, *EMBO J.* **1999**, *18*, 5892–5900.

[158] C. Lenz, M. Willliamson, C. J. P. Grimmelikhuijzen, *Biochem. Biophys. Res. Commun.* **2000**, *273*, 571–577.

[159] A. Berger, R. Santic, C. Hauser-Kronberger, F. H. Schilling, P. Kogner, M. Ratschek, A. Gamper, N. Jones, W. Sperl, B. Kofler, *Neuropeptide hormones* **2005**, *39*, 353–359.

[160] S. Schulz, S. U. Pauli, S. Schulz, M. Händel, K. Dietzmann, R. Firsching, V. Höllt, *Clin. Cancer Res.* **2000**, *6*, 1865–1874.

[161] F. Boomsma, U. M. Bhaggoe, M. A. Schalekamp, *Clin. Chim. Acta* **1995**, *239*, 57–63.

[162] E. Baggaley, J. A. Weinstein, J. A. G. Williams, *Coord. Chem. Rev.* **2012**, *256*, 1762–1785.

[163] N. Johnsson, K. Johnsson, *Am. Chem. Soc. Chem. Biol.* **2007**, *2*, 31-38.

[164] L. Bachmann, D. M. Zezell, A. D. Ribeiro, L. Gomes, A. S. Ito, *Appl. Spectrosc. Rev.* **2006**, *41*, 575-590.

[165] V. Fernandez-Moreira, F. L. Thorp-Greenwood, M. P. Coogan, *Chem. Commun.* **2010**, *46*, 186–202.

[166] J. R. Lakowicz, *Principles of Fluorescence Spectroscopy*, Springer, New York, **2006**.

[167] U. Mahmood, C. H. Tung, A. Bogdanov, R. Weissleder, *Radiology* **1999**, *213*, 866-870.

[168] A. Barbieri, G. Accorsi, N. Armaroli, *Chem. Commun.* **2008**, *19*, 2185–2193.

[169] F. Barigelletti, D. Sandrini, M. Maestri, V. Balzani, A. v. Zelewsky, L. Chassot, P. Jolliet, U. Maeder, *Inorg. Chem.* **1988**, *27*, 3644-3647.

[170] J. Brooks, Y. Babayan, S. Lamansky, P. I. Djurovich, I. Tsyba, R. Bau, M. E. Thompson, *Inorg. Chem.* **2002**, *41*, 3055-3066.

[171] P. K.-M. Siu, D.-L. Ma, C.-M. Che, *Chem. Commun.* **2005**, 1025-1027.

[172] S. W. Botchway, M. Charnley, J. W. Haycock, A. W. Parker, D. L. Rochester, J. A. Weinstein, J. A. G. Williams, *P. Natl. Acad. Sci. USA.*, **2008**, *105*, 16071–16076.

[173] A. Juris, V. Balzani, F. Barigellatti, S. Campagna, P. Belser, A. v. Zelewsky, *Coord. Chem. Rev.* **1998**, *84*, 85-227.

[174] M. S. Lowry, W. R. Hudson, R. A. Pascal, S. Bernhard, *J. Am. Chem. Soc.* **2004**, *126*, 14129–14135.

[175] D. J. Stufkens, A. Vlcek, *Coord. Chem. Rev.* **1998**, *177*, 127–179.

[176] A. Juris, V. Balzani, F. Barigelletti, S. Campagna, P. Belser, A. v. Zelewsky, *Coord. Chem. Rev.* **1988**, *84*, 85–277.

[177] M. Bartholoma, J. Valliant, K. P. Maresca, J. Zubieta, *Chem. Commun.* **2009**, *5*, 493-512.

[178] E. Boros, U. O. Hafeli, B. O. Patrick, M. J. Adam, C. Orvig, *Bioconjugate Chem.* **2009**, *20*, 1002-1009.

[179] H. Chao, R.-H. Li, C.-W. Jiang, H. Li, L.-N. Ji, X.-Y. Li, *Dalton Trans.* **2001**, 1920-1926.

[180] H. Tang, H. Tang, Z. Zhang, C. Cong, K. Zhang, *J. Mater. Sci: Mater. Electron* **2009**, *20*, 597–603.

[181] C. Zhong, H. Huang, A. He, H. Zhang, *Dyes and Pigments* **2008**, *77*, 578-583.

[182] J. O. Edwards, R. G. Pearson, *J. Am. Chem. Soc.* **1962**, *84*, 16-24.

[183] W. P. Jencks, J. Carriuolo, *J. Am. Chem. Soc.* **1960**, *82*, 675-681.

[184] R. E. Mewis, S. J. Archibald, *Coord. Chem. Rev.* **2010**, *254*, 1686–1712.

[185] S. Bodige, F. M. MacDonnell, *Tetrahedron Lett.* **1997**, *38*, 8159-8816.

[186] P. Govender, S. Pai, U. Schatzschneider, G. S. Smith, *Inorg. Chem.* **2013**, *52*, 5470−5478.

[187] R. Alberto, R. Motterlini, *Dalton Trans.* **2007**, 1651–1660.

[188] R. Motterlini, L. E. Otterbein, *Nature Reviews* **2010**, *8*, 728-744.

[189] U. Schatzschneider, *Inorg. Chim. Acta* **2011**, *374*, 19–23.

[190] K. Umezawa, A. Matsui, Y. Nakamura, D. Citterio, K. Suzuki, *Chem. Eur. J.* **2009**, *15*, 1096 – 1106.

[191] Z. Huang, D. Ji, A. Xia, *Colloids and Surfaces A: Physicochem. Eng. Aspects* **2005**, *257*, 203–209.

[192] A. Köhler, J. S. Wilson, R. H. Friend, *Adv. Mater.* **2002**, *14*, 701-707.

[193] Q. Zhao, F. Li, C. Huanga, *Chem. Soc. Rev.* **2010**, *39*, 3007–3030.

[194] M. Meldal, C. W. Tornoe, *Chem. Rev.* **2008**, *108*, 2952-3015.

[195] E. Kaiser, R. L. Colescott, C. D. Bossinger, P. I. Cook, *Anal. Biochem.* **1970**, *34*, 595-598.

[196] J. L. Steinbacher, C. C. Landry, *Langmuir* **2014**, *30*, 4396−4405.

[197] Y. Wang, F. Caruso, *Chem. Commun.* **2004**.

[198] H.-W. Marquart, *Neue Deutsche Biographie, Vol. 20*, Duncker & Humblot, Berlin, **2001**.

[199] O. Pieroni, A. Fissi, J. L. Houben, *Die Makromolekulare Chemie* **1975**, *176*, 3201-3209.

[200] R. Huisgen, *Angew. Chem. Int. Ed.* **1963**, *2*, 633-645.

[201] K. V. Gothelf, K. A. Jorgensen, *Chem. Rev.* **1998**, *98*, 863-909.

[202] S. Alvarez, M. Alvarez, *Synthesis* **1997**, 413-414.

[203] G. Kubas, *Inorg. Synth.* **1990**, *28*, 68-69.

[204] T. Chan, R. Hilgraf, K. Sharpless, V. Folkin, *Org. Lett.* **2004**, *6*, 2853-2855.

[205] D. H. Spackman, W. H. Stein, S. Moore, *Anal. Chem.* **1958**, *30*, 1185-1189.

[206] E. L. V. Harris, in *New Protein Techniques*, Springer, **1988**, pp. 33-47.

[207] G. B. Irvine, in *Basic Protein and Peptide Protocols, Vol. 32*, Springer, **1994**, pp. 257-265

[208] D. Voet, J. G. Voet, C. W. Pratt, *Lehrbuch der Biochemie*, Wiley, Weinheim, **2002**.

[209] B. A. Bindlingmeyer, S. A. Cohen, T. L. Tarvin, *J. Chromatogr.* **1984**, *336*, 93-104.

[210] L. R. Heinrikson, S. C. Meredeith, *Anal. Biochem.* **1984**, *136*, 65-74.

[211] M. Rohrer, H. Bauer, J. Mintorovitch, M. Requardt, H.-J. Weinmann, *Investig. Rad.* **2005**, *40*, 715-724.

[212] J. A. Bearden, *Rev. Mod. Phys.* **1967**, *39*, 78-124.

[213] H. E. Gottlieb, V. Kotlyar, A. Nudelman, *J. Org. Chem.* **1997**, *62*, 7512-7515.

7 Appendix

7.1 HPLC traces of amino acid analysis and calibration curves

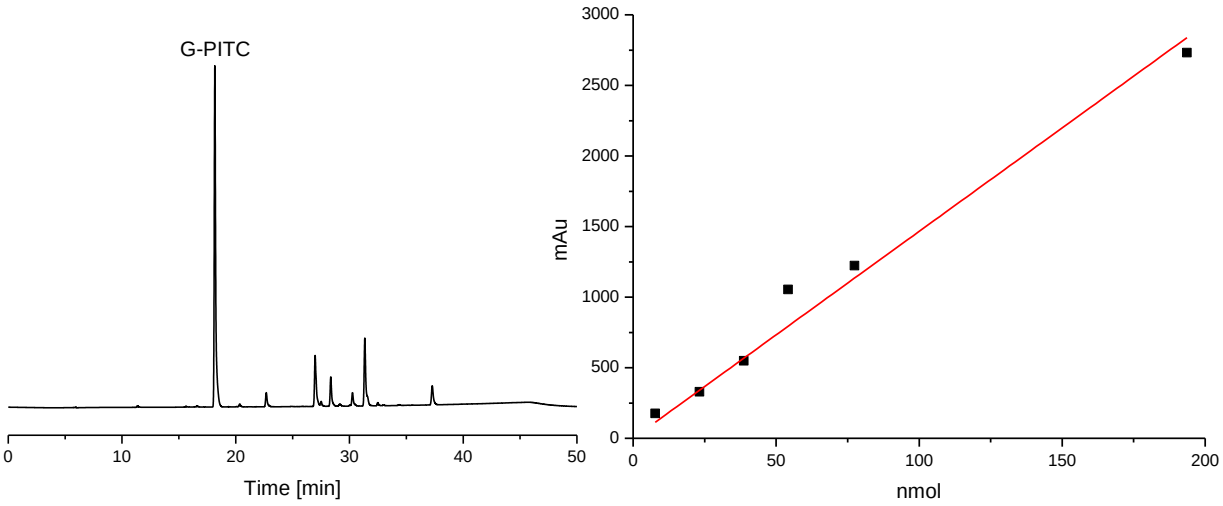

Calibration curve of PITC derivatized glycine (G-PITC)

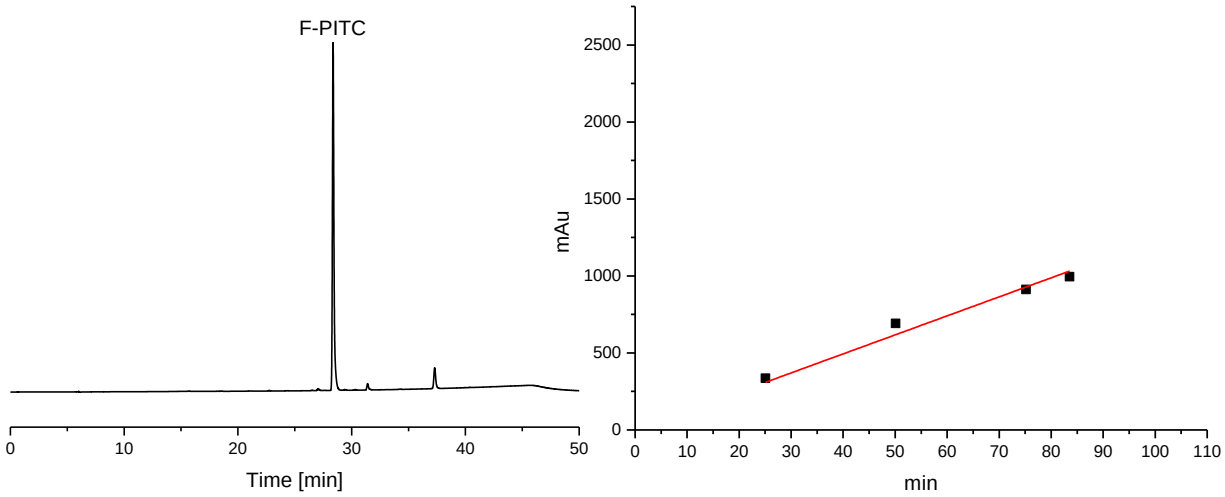

Calibration curve of PITC derivatized phenylalanine (F-PITC)

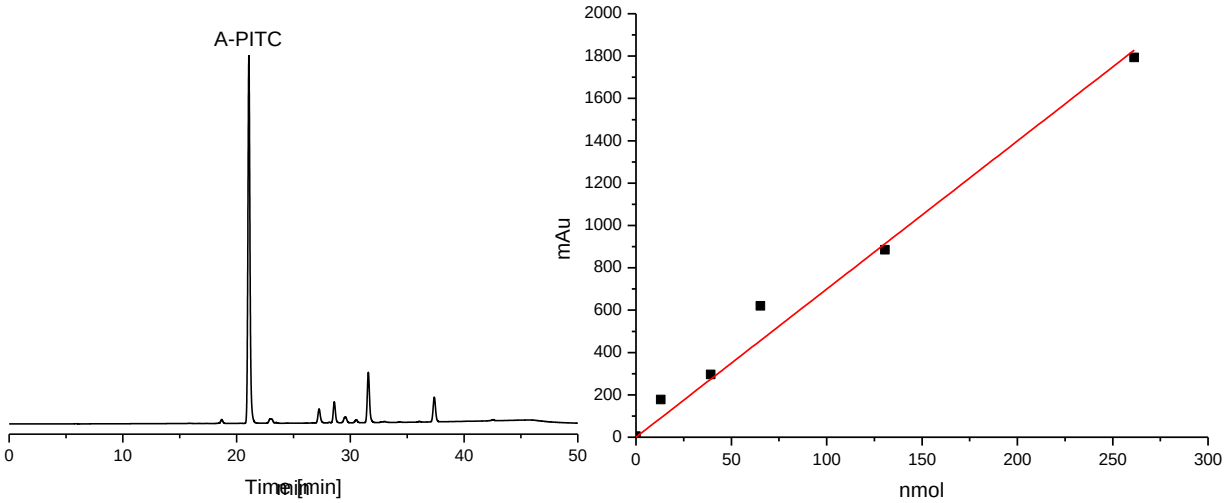

Calibration curve of PITC derivatized alanine (A-PITC)

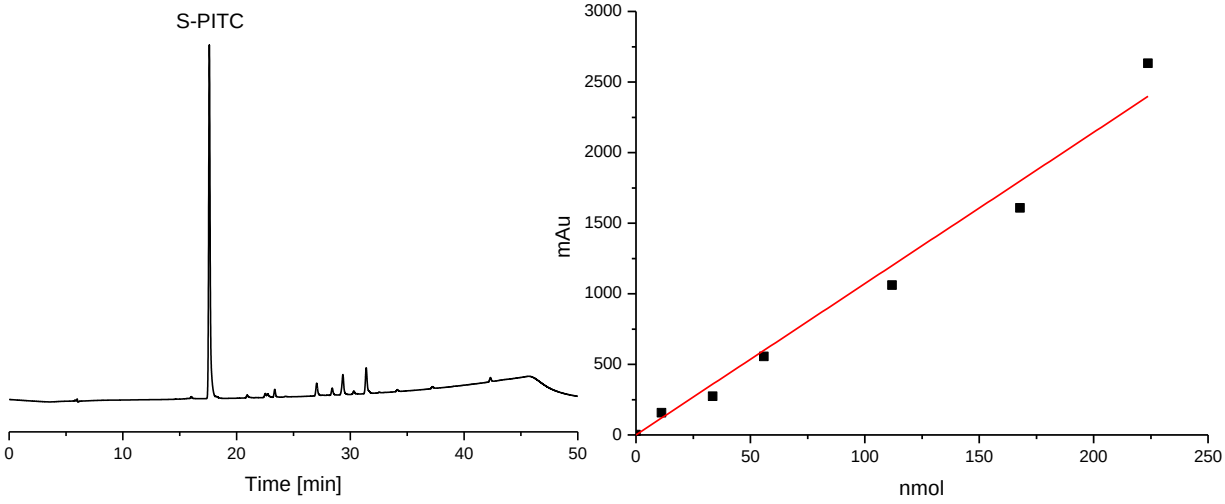

Calibration curve of PITC derivatized serine (S-PITC)

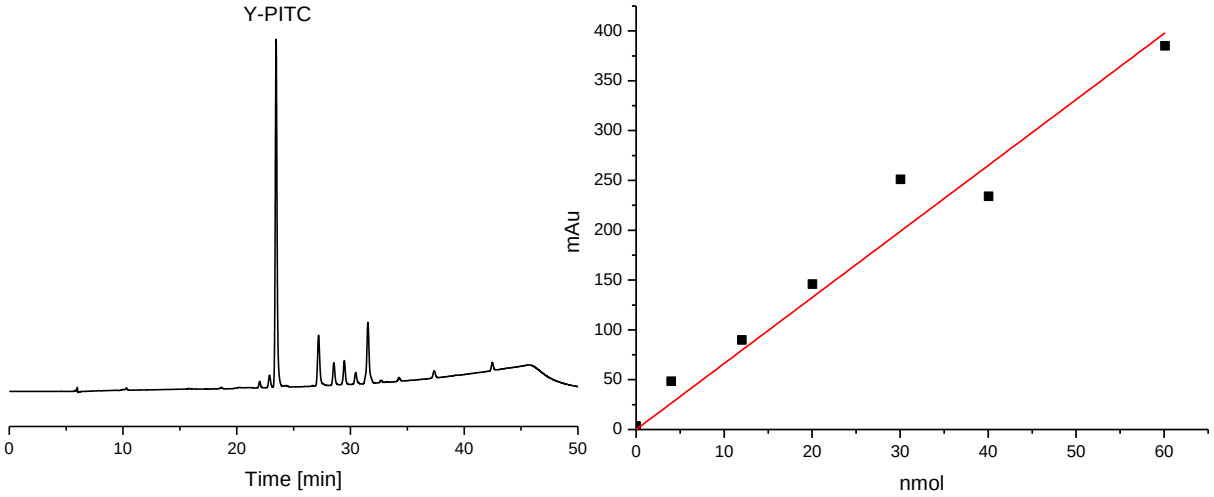

Calibration curve of PITC derivatized tyrosine (Y-PITC)

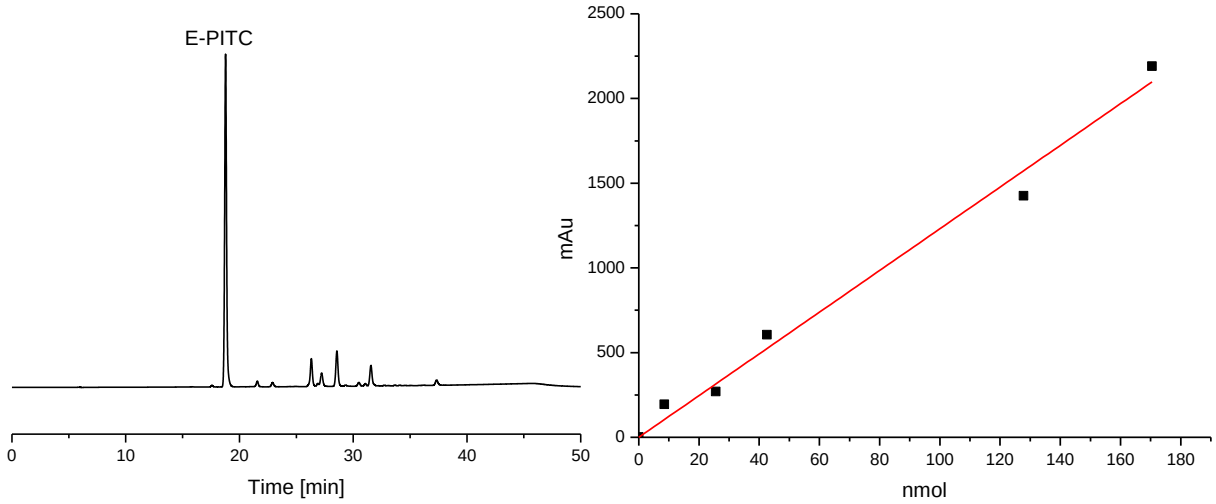

Calibration curve of PITC derivatized glutamate (E-PITC)

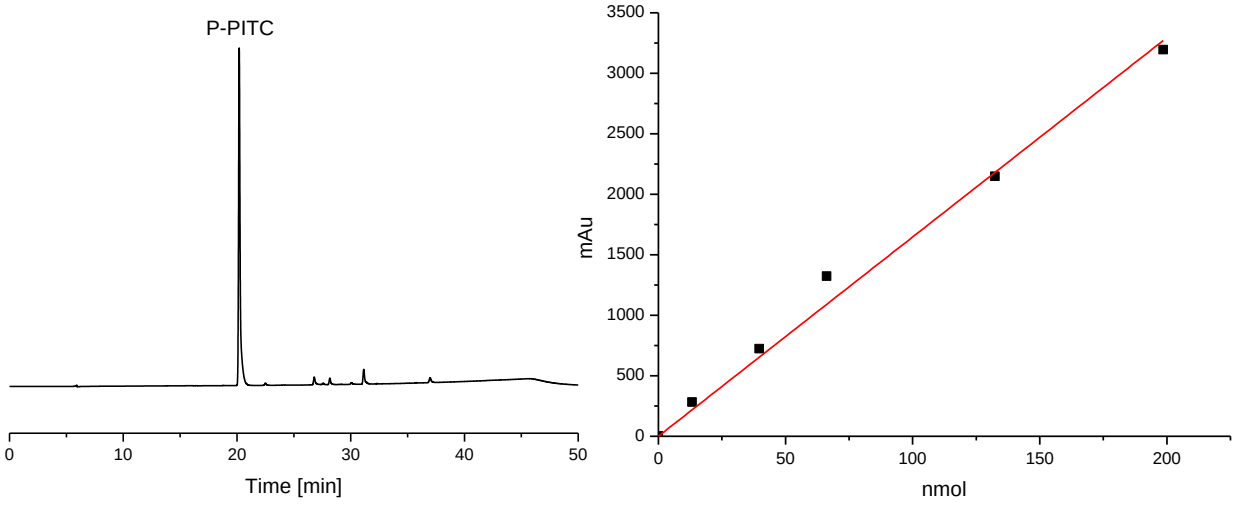

Calibration curve of PITC derivatized proline (P-PITC)

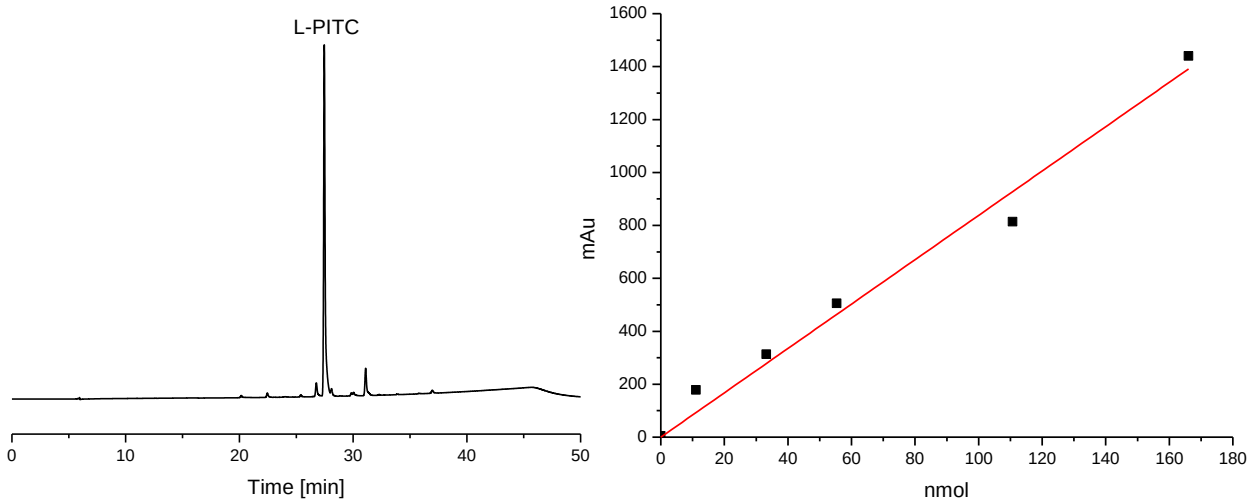

Calibration curve of PITC derivatized leucine (L-PITC)

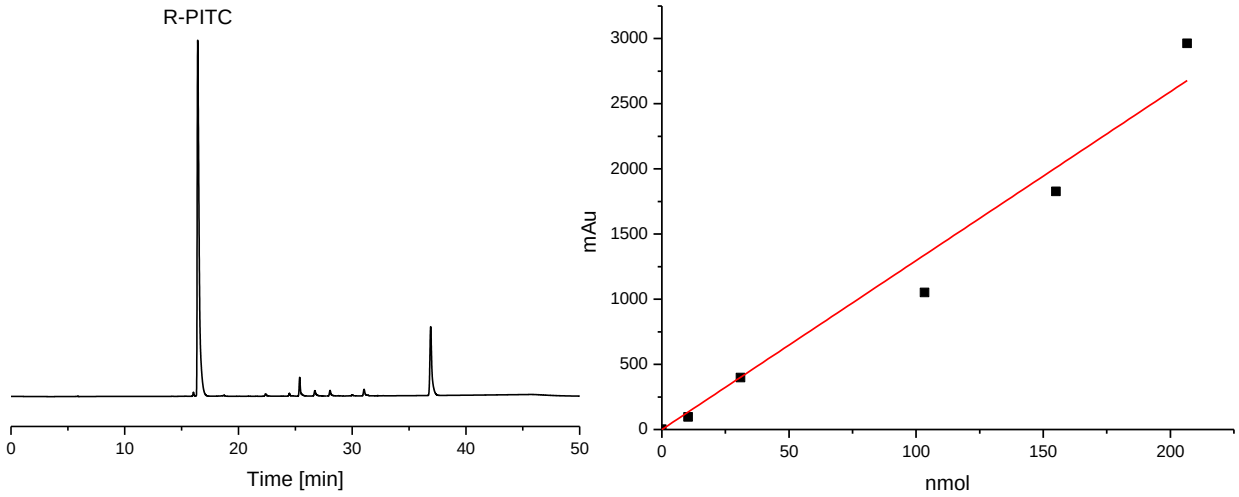

Calibration curve of PITC derivatized arginine (R-PITC)

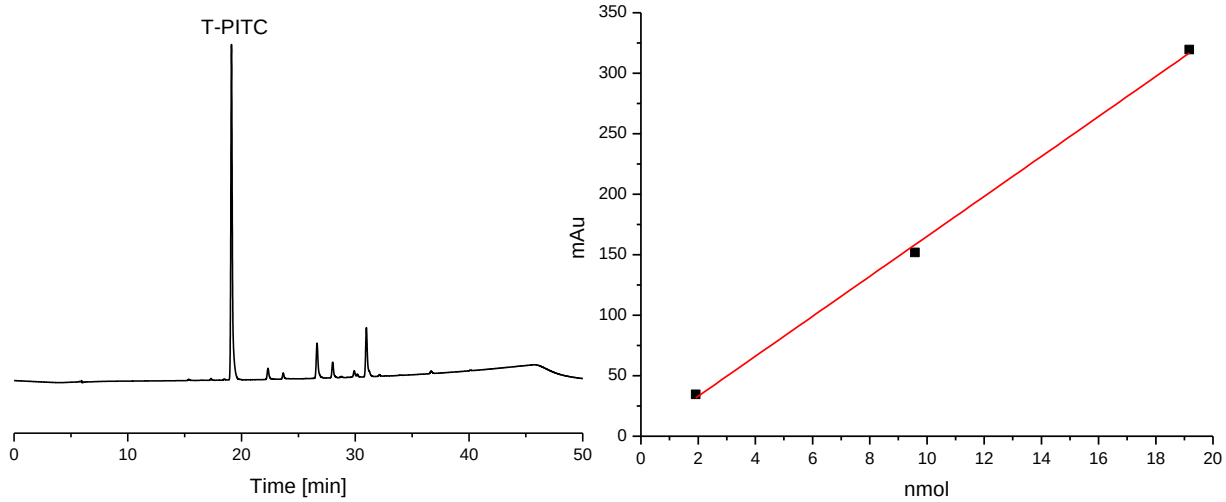

Calibration curve of PITC derivatized threonine (T-PITC)

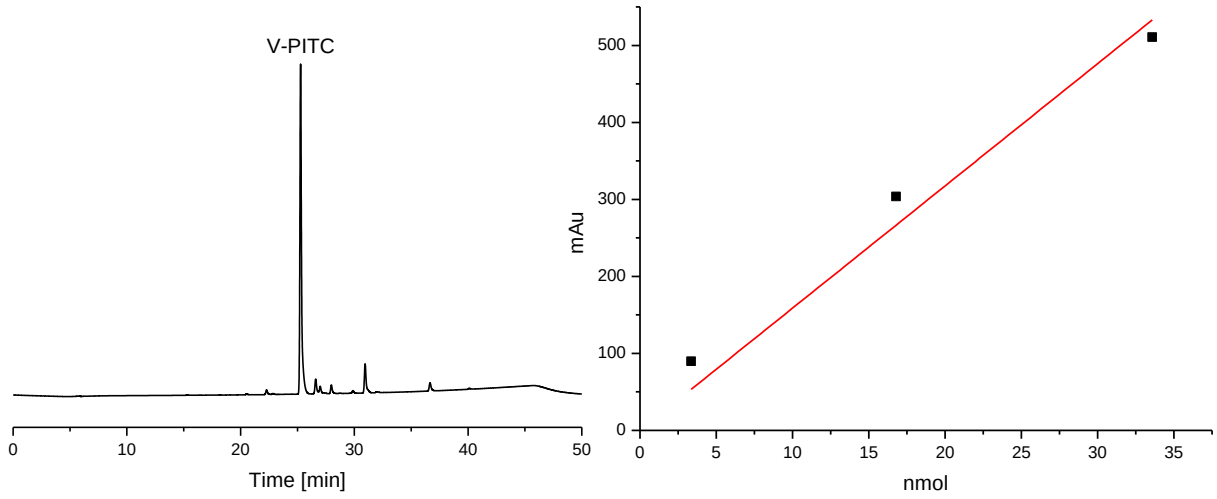

Calibration curve of PITC derivatized valine (V-PITC)

7.2 TEM images and size distributation of compounds 39a, 39b, 40a, and 40b

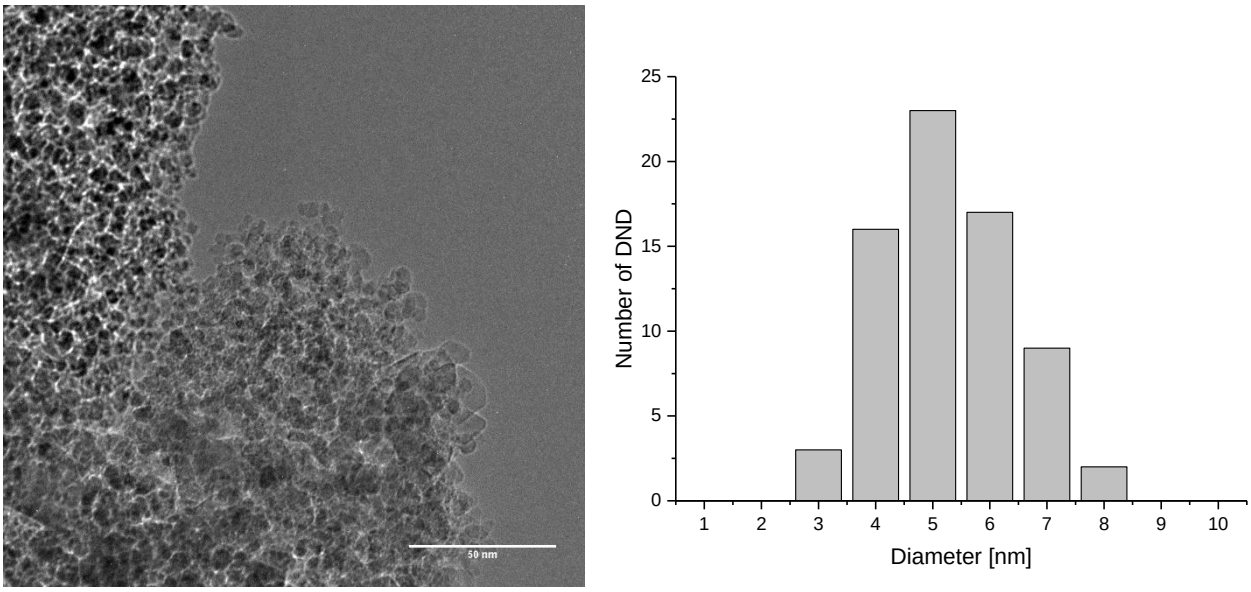

TEM image and size distribution of compound **39a**. The average size is 5.2 nm

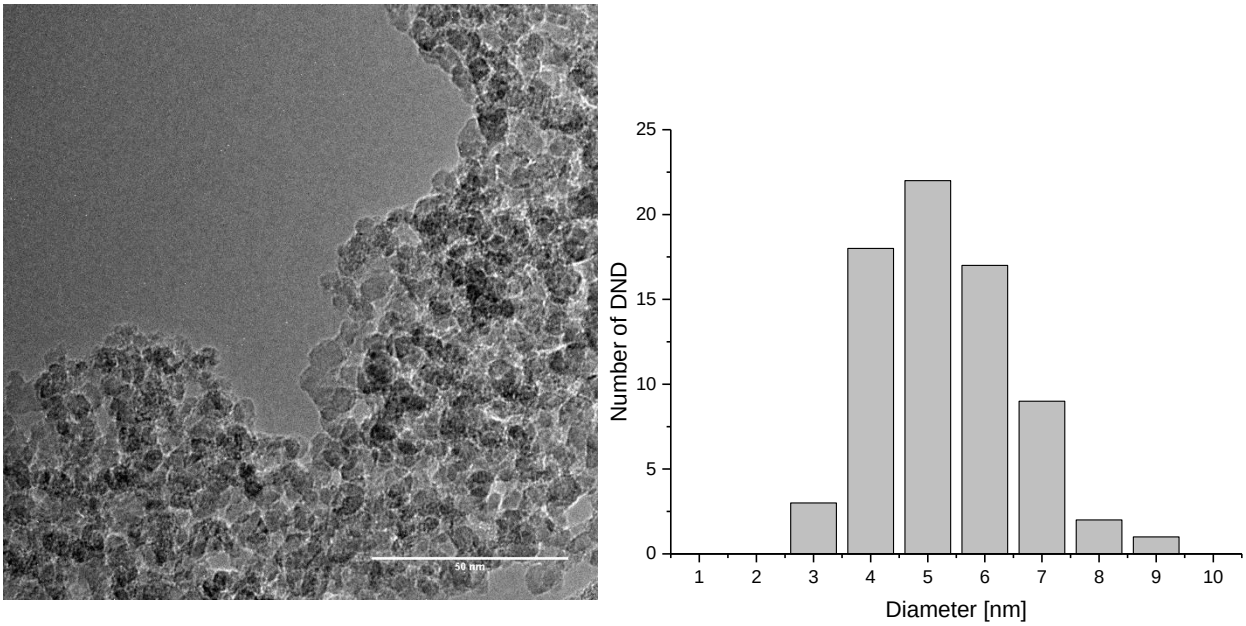

TEM image and size distribution of compound **39b**. The average size is 5.3 nm

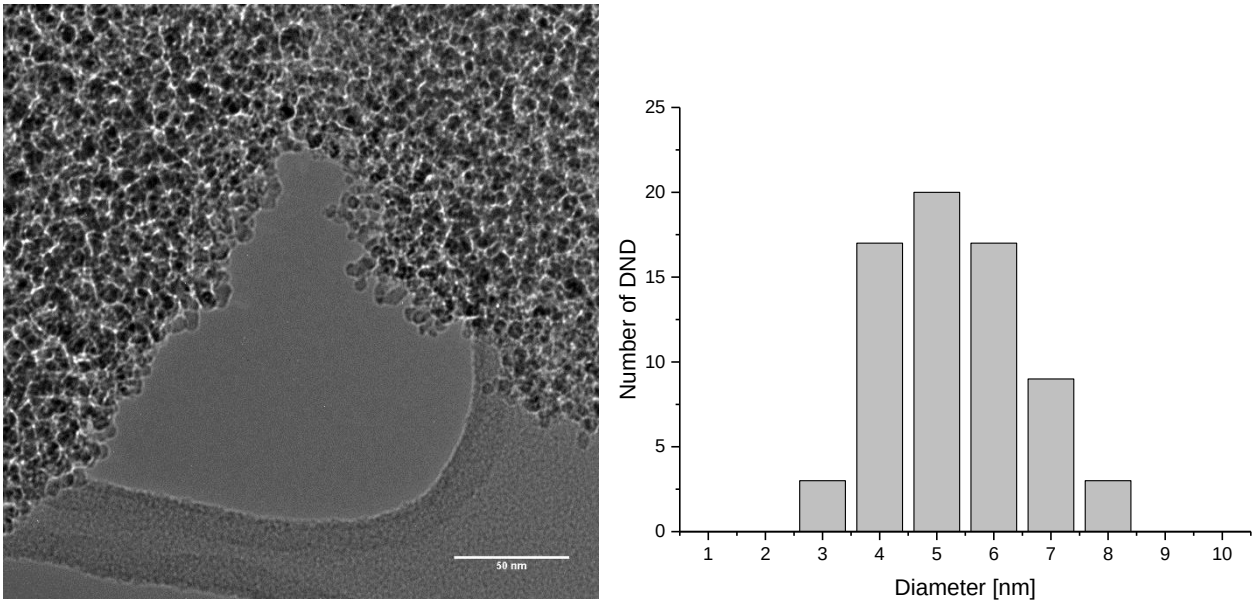

TEM image and size distribution of compound **40a**. The average size is 5.3 nm

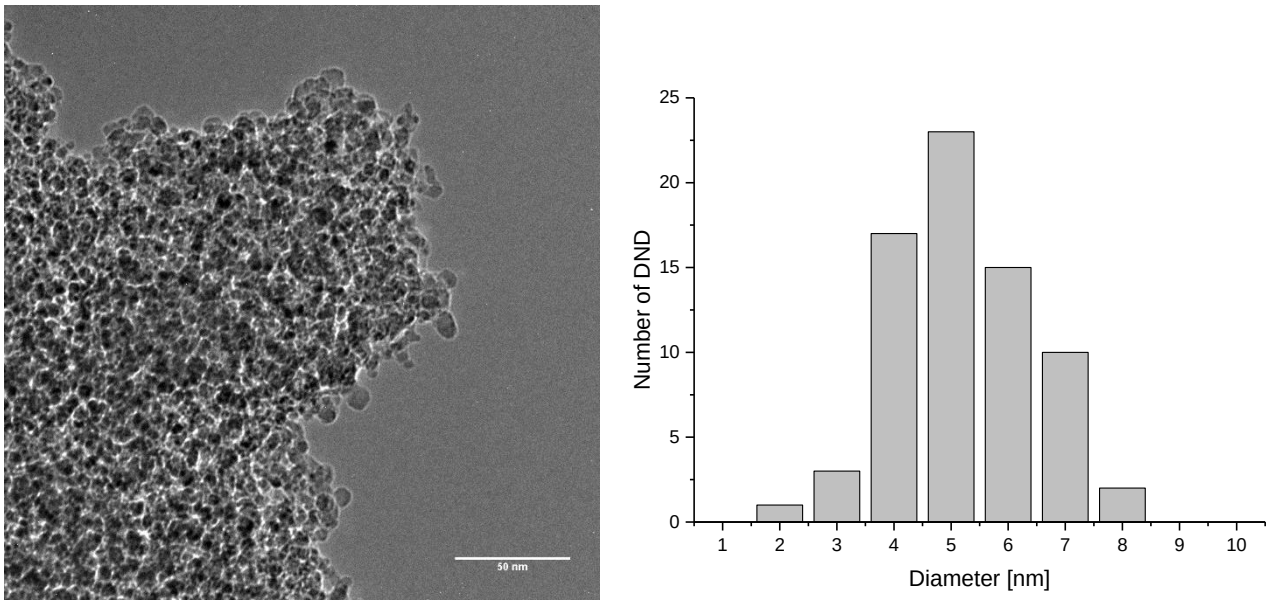

TEM image and size distribution of compound **40b**. The average size is 5.2 nm

7.3 EDX of compound 40b

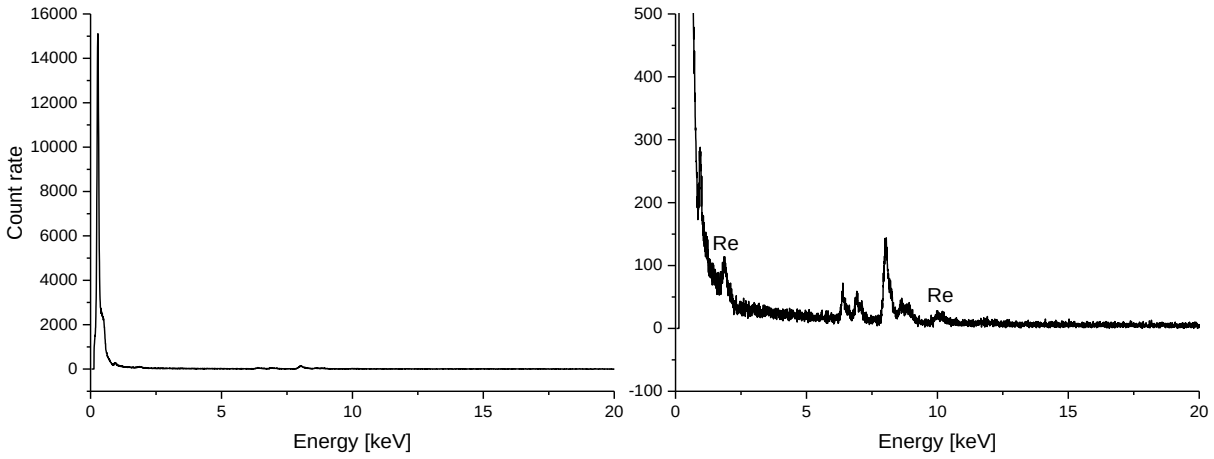

7.4 Photophysical data

The samples were dissolved in either water (H_2O) or dichloromethane/methanol (1:1), (D/M). When multiple lifetimes are given, the percentage to the whole lifetime is given as well. The fitted lifetimes were estimated as good with a χ^2 value < 1.3 and a Durbin Watson factor < 1.90.

	$^{Cy5;ALST1}$Silica@SPION **36b**		$^{Cy5;ALST1}$DND **39a**		$^{[ReBr(CO)3(L)]\text{-}Aoa;ALST1}$DND **40a**	
Solvent	H_2O	D/M	H_2O	D/M	H_2O	D/M
τ_1 [ns]	0.4 (92%)	1.0 (40%)	< 0.4 (60%)	0.9 (99%)		110 (61%)
τ_2	1.5 (8%)	< 0.4 (60%)		2.8 (1%)		30 (16%)
τ_3						3.1 (14%)
τ_4						0.6 (9%)
χ^2	1.27	1.26	N/A	1.22		1.18
Durbin Watson	1.72	1.68	N/A	1.73		1.89

7.5 ^{1}H-NMR of 2-(4-(1*H*-imidazo[4,5-*f*][1,10]phenanthrolin-2-yl)phenyl)-1*H*-imidazo[4,5-*f*][1,10]-phenanthroline (19)

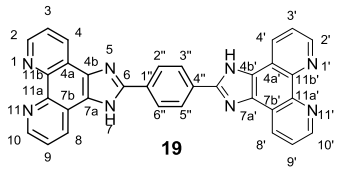

19

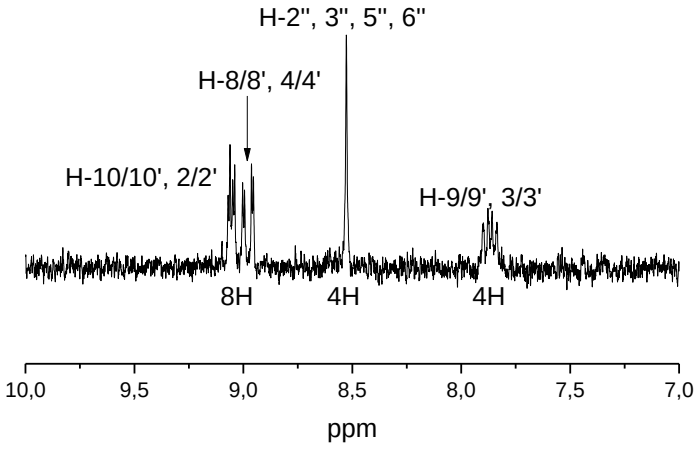

200 Hz ^{1}H-NMR spectrum of 2-(4-(1*H*-imidazo[4,5-*f*][1,10]phenanthrolin-2-yl)phenyl)-1*H*-imidazo[4,5-*f*][1,10]-phenanthroline (**19**) in DMSO-d_6.

7.6 *Pauly* reaction of peptides 24, 24b, and 24d

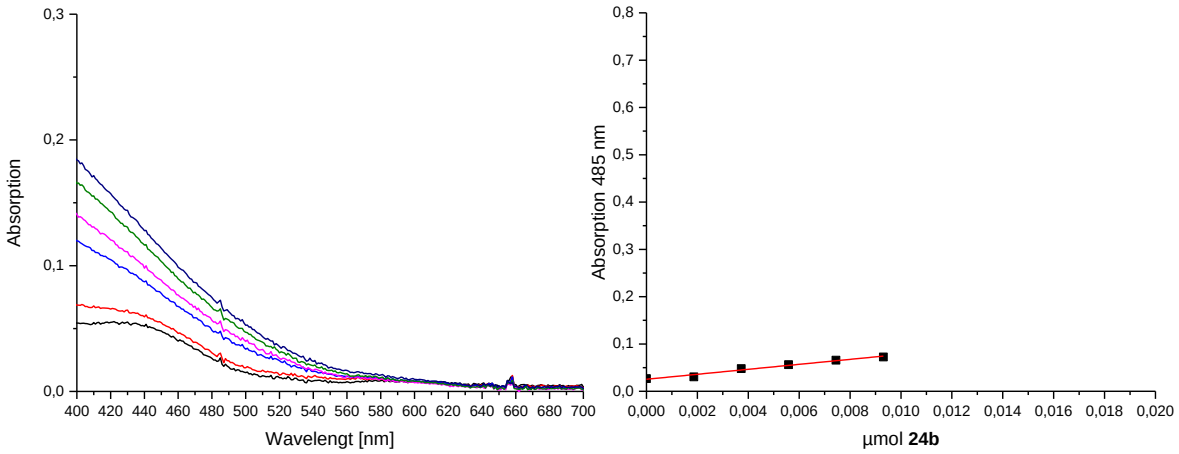

Left: change in absorption of solution in *Pauly* reaction upon increasing concentration of **24b**. Right: change of absorption at 435 nm with increasing concentration of **24b** in the *Pauly* reaction. The amount of substance of **24b** is plotted against the absorption at 435 nm.

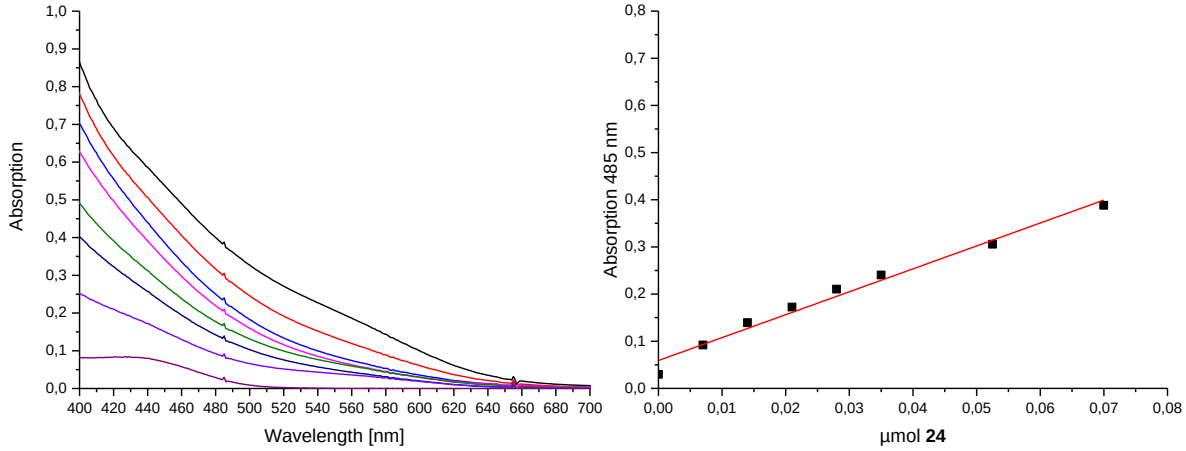

Left: change in absorption of solution in *Pauly* reaction upon increasing concentration of **24**. Right: change of absorption at 435 nm with increasing concentration of **24** in the *Pauly* reaction. The amount of substance of **24** is plotted against the absorption at 435 nm.

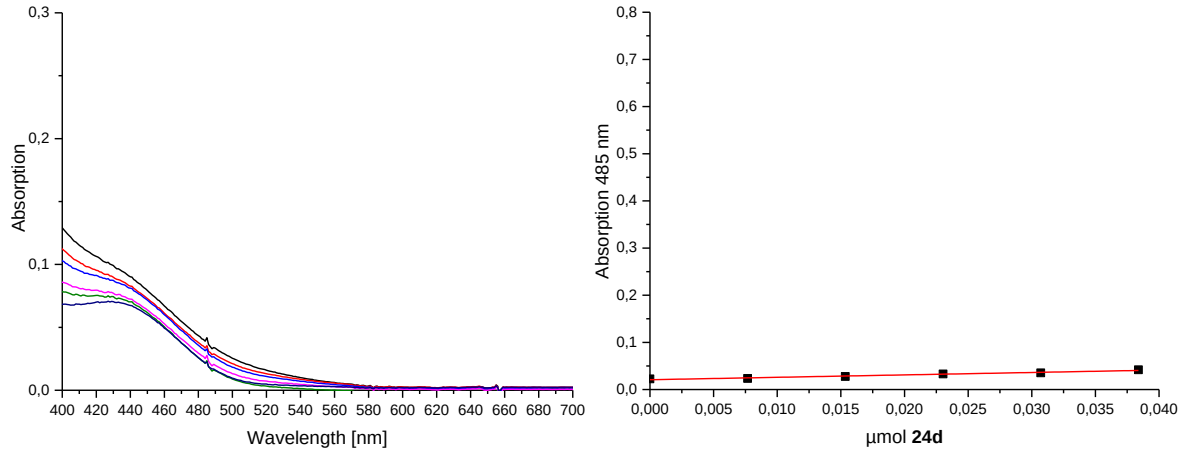

Left: change in absorption of solution in *Pauly* reaction upon increasing concentration of **24d**. Right: change of absorption at 435 nm with increasing concentration of **24d** in the *Pauly* reaction. The amount of substance of **24d** is plotted against the absorption at 435 nm.

7.7 HPLC traces of peptide analysis of functionalized silica nanoparticles

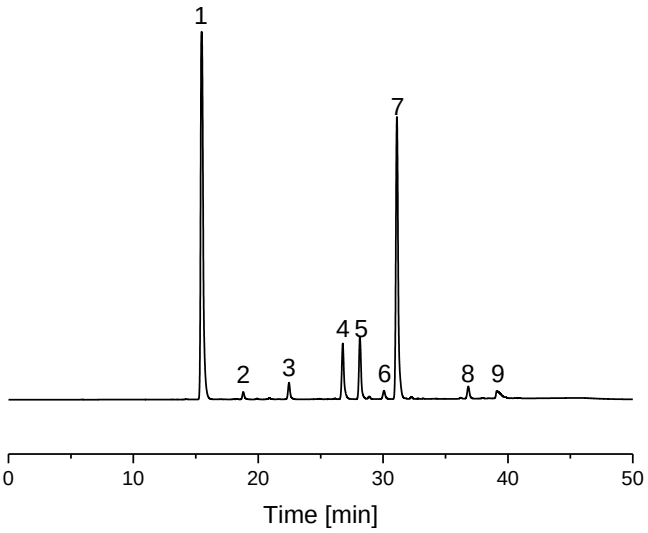

HPLC trace at 254 nm of material **25** after digestion with hydrochloric acid and derivatization with PITC.

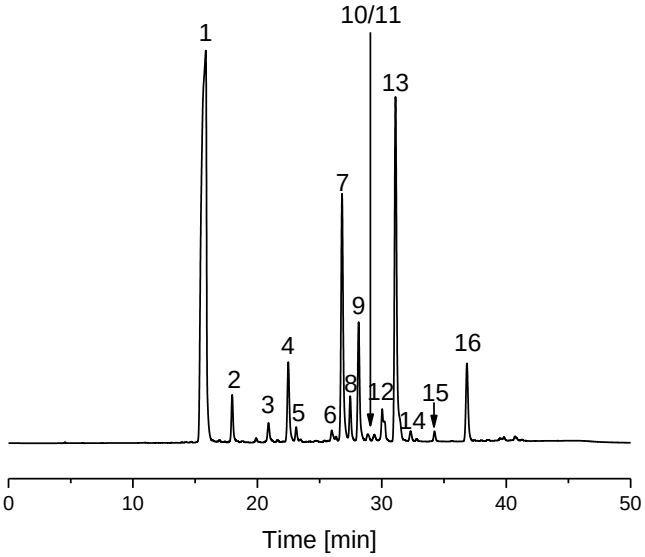

HPLC trace at 254 nm of material **35a** after digestion with hydrochloric acid and derivatization with PITC.

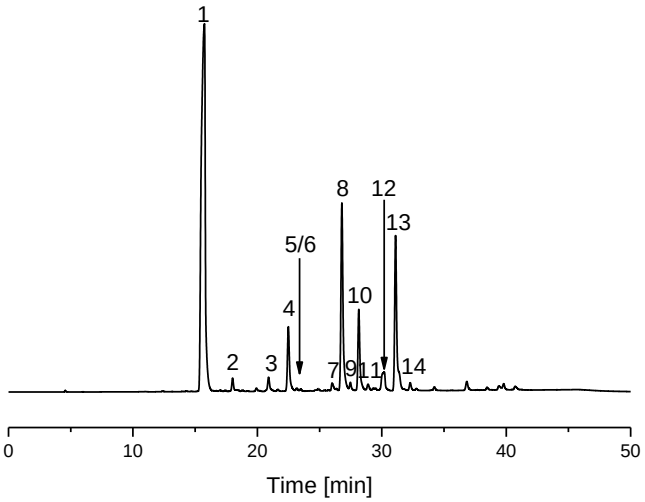

HPLC trace at 254 nm of material **35b** after digestion with hydrochloric acid and derivatization with PITC.

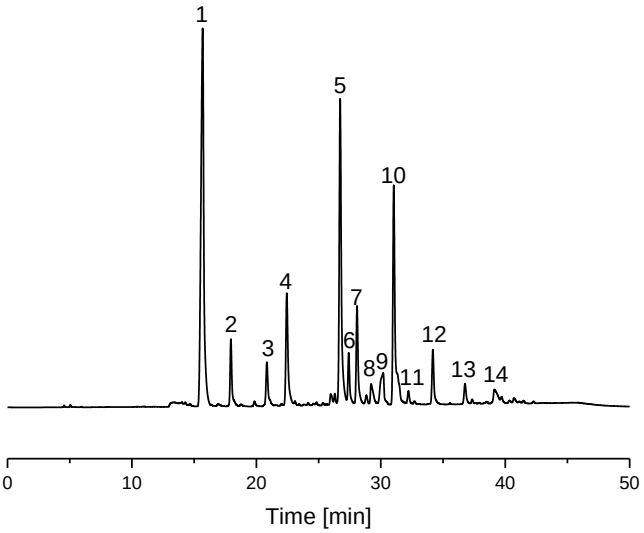

HPLC trace at 254 nm of material **35c** after digestion with hydrochloric acid and derivatization with PITC.

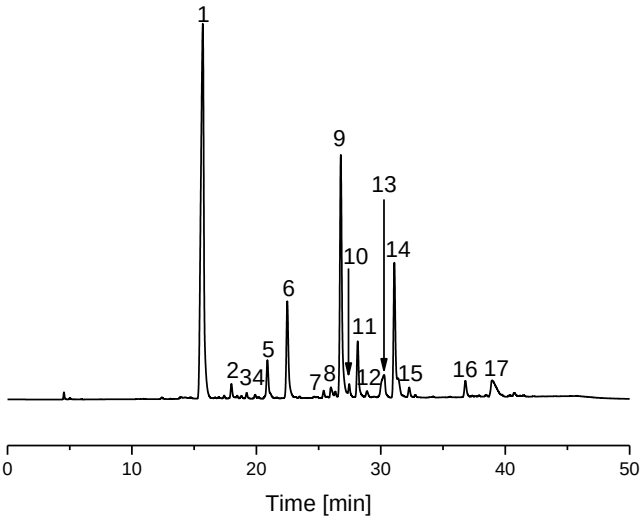

HPLC trace at 254 nm of material **35d** after digestion with hydrochloric acid and derivatization with PITC.

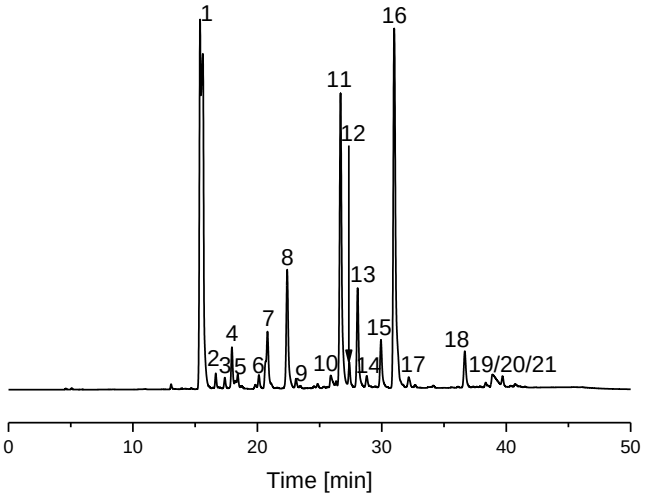

HPLC trace at 254 nm of material **35** after digestion with hydrochloric acid and derivatization with PITC.